frontiers | Research Topics

New techniques for modeling, prognosis, diagnosis, and treatment of human knee pathology

Edited by
Abdelwahed Barkaoui, Bernardo Innocenti and João Manuel R. S. Tavares

Published in
Frontiers in Bioengineering and Biotechnology

ISSN 1664-8714
ISBN 978-2-8325-5872-0
DOI 10.3389/978-2-8325-5872-0

About Frontiers

Frontiers is more than just an open access publisher of scholarly articles: it is a pioneering approach to the world of academia, radically improving the way scholarly research is managed. The grand vision of Frontiers is a world where all people have an equal opportunity to seek, share and generate knowledge. Frontiers provides immediate and permanent online open access to all its publications, but this alone is not enough to realize our grand goals.

Frontiers journal series

The Frontiers journal series is a multi-tier and interdisciplinary set of open-access, online journals, promising a paradigm shift from the current review, selection and dissemination processes in academic publishing. All Frontiers journals are driven by researchers for researchers; therefore, they constitute a service to the scholarly community. At the same time, the *Frontiers journal series* operates on a revolutionary invention, the tiered publishing system, initially addressing specific communities of scholars, and gradually climbing up to broader public understanding, thus serving the interests of the lay society, too.

Dedication to quality

Each Frontiers article is a landmark of the highest quality, thanks to genuinely collaborative interactions between authors and review editors, who include some of the world's best academicians. Research must be certified by peers before entering a stream of knowledge that may eventually reach the public - and shape society; therefore, Frontiers only applies the most rigorous and unbiased reviews. Frontiers revolutionizes research publishing by freely delivering the most outstanding research, evaluated with no bias from both the academic and social point of view. By applying the most advanced information technologies, Frontiers is catapulting scholarly publishing into a new generation.

What are Frontiers Research Topics?

Frontiers Research Topics are very popular trademarks of the *Frontiers journals series*: they are collections of at least ten articles, all centered on a particular subject. With their unique mix of varied contributions from Original Research to Review Articles, Frontiers Research Topics unify the most influential researchers, the latest key findings and historical advances in a hot research area.

Find out more on how to host your own Frontiers Research Topic or contribute to one as an author by contacting the Frontiers editorial office: frontiersin.org/about/contact

New techniques for modeling, prognosis, diagnosis, and treatment of human knee pathology

Topic editors

Abdelwahed Barkaoui — International University of Rabat, Morocco

Bernardo Innocenti — Université libre de Bruxelles, Belgium

João Manuel R. S. Tavares — University of Porto, Portugal

Citation

Barkaoui, A., Innocenti, B., Tavares, J. M. R. S., eds. (2025). *New techniques for modeling, prognosis, diagnosis, and treatment of human knee pathology*. Lausanne: Frontiers Media SA. doi: 10.3389/978-2-8325-5872-0

Table of contents

frontiers | Frontiers in Bioengineering and Biotechnology

TYPE Editorial
PUBLISHED 14 May 2024
DOI 10.3389/fbioe.2024.1412924

OPEN ACCESS

EDITED AND REVIEWED BY
Markus O. Heller,
University of Southampton, United Kingdom

*CORRESPONDENCE
Abdelwahed Barkaoui,
aabarkaoui@gmail.com

RECEIVED 06 April 2024
ACCEPTED 03 May 2024
PUBLISHED 14 May 2024

CITATION
Barkaoui A, Innocenti B and Tavares JMRS (2024), Editorial: New techniques for modelling, prognosis, diagnosis, and treatment of human knee pathology.
Front. Bioeng. Biotechnol. 12:1412924.
doi: 10.3389/fbioe.2024.1412924

Editorial: New techniques for modelling, prognosis, diagnosis, and treatment of human knee pathology

Abdelwahed Barkaoui[1]*, Bernardo Innocenti[2] and João Manuel R. S. Tavares[3]

[1]Université Internationale de Rabat, Sale, Morocco, [2]Université Libre de Bruxelles, Brussels, Belgium, [3]Faculdade de Engenharia, Universidade do Porto, Porto, Portugal

KEYWORDS

knee, biomechancis, diagnostic, pronostic, pathologies and risk prevention

Editorial on the Research Topic
New techniques for modelling, prognosis, diagnosis, and treatment of human knee pathology

Pathologies of the human knee represent a significant challenge for healthcare professionals, affecting individuals' quality of life and incurring substantial costs for healthcare systems. These conditions can result from various factors, such as sports injuries, age-related wear and tear, or underlying medical conditions. Over recent years, significant advancements in the modelling, prognosis, diagnosis, and treatment of these knee pathologies have been driven by technological progress and a better understanding of knee physiology and biomechanics. These advancements have led to the development of more precise and personalized techniques to improve clinical outcomes and patient recovery. By combining state-of-the-art medical imaging, biomechanical analysis, and innovative therapeutic approaches, healthcare professionals are better equipped than ever to diagnose and effectively treat knee pathologies, enabling patients to regain optimal functionality and improved quality of life.

The guest editors are delighted to present this Research Topic of Frontiers in Bioengineering and Biotechnology - Biomechanics, dedicated to "New Techniques for Modelling, Prognosis, Diagnosis, and Treatment of Human Knee Pathology", which brings together a diverse range of expertise to explore the challenges and opportunities in the complex field of knee biomechanics.

The knee, one of the most essential and complex joints in the human body, faces various challenges, notably osteoarthritis, a degenerative disease that can devastate quality of life. With a growing prevalence of knee osteoarthritis and its significant socioeconomic consequences, it is imperative to develop innovative approaches for early detection, prevention, and effective treatment of this condition.

Under this perspective, this Research Topic focuses on the latest advances in the field, highlighting progress in modelling, prognosis, diagnosis, and treatment of knee pathologies. The 11 contributions from authors representing five countries (Spain, China, United Kingdom, Germany, and Chile), give a comprehensive understanding of the field from different angles.

These contributions encompass several Research Topic, including the influence of tension-band plates on mechanical loading and their effects on the femoral growth plate, alongside motion capture's role in detecting kinematic abnormalities in osteoarthritis patients.

Additionally, studies delve into foot biomechanics using dual fluoroscopic imaging, the impact of patellar morphology on knee gait, ligament laxity, and finite element analysis of posterior tibial plate fixation. Further investigations compare machine learning and deep learning for predicting knee biomechanics, explore tibial shock attenuation with non-Newtonian fluid material footwear, and introduce intraoperative sensor technology in the knee domain.

The included contributions can be summarized as:

- Wang et al. investigated markerless motion capture's effectiveness in identifying kinematic abnormalities in knee osteoarthritis (KOA) during the Functional Movement Screen (FMS) and daily activities, suggesting the FMS, particularly knee flexion and trunk angles during in-line lunge, as potential indicators for KOA assessment.
- Peng et al. examined knee joint loading during badminton lunges at various distances and foot positions using dual fluoroscopic imaging, revealing increased knee flexion and ground reaction forces with longer lunges, and larger knee translation and torque with externally rotated foot positions, indicating potential injury risks.
- Wang et al. explored the relationship between patella morphology, transverse alignment, and knee gait in healthy Chinese adults over 40, finding no significant association between patella morphology/transverse alignment and knee gait parameters, but highlighting the femoral-tibial angle's influence on the knee adduction moment.
- Wu et al. assessed knee laxity in patients with ACL injury using a digital arthrometer, indicating significantly lower stiffness in the ACL injury group than controls, particularly in later loading stages, suggesting potential diagnostic value for knee laxity assessment.
- Hu et al. aimed to improve the fixation of posterolateral tibial plateau fractures (PTPF) using various screw fixation methods, with biomechanical tests showing superior strength in two-screw fixation compared to single-screw fixation, supported by finite element analysis.
- Shao et al. compared non-Newtonian (NN) shoes with ethylene vinyl acetate (EVA) shoes in cushioning and reducing sports injuries, revealing NN shoes' superior cushioning during exercise, particularly in high-temperature conditions.
- Stoddart et al. examined different knee arthroplasty techniques' effects on bone load transfer, indicating higher strain shielding with total knee arthroplasty (TKA) compared to partial knee arthroplasty (PKA) and potential long-term bone health implications.
- Zhang et al. compared deep learning with conventional machine learning methods in predicting knee biomechanics post-total knee arthroplasty, demonstrating deep learning's superior accuracy and potential for precise alignment assessment.
- Valente et al. investigated the impact of tibiofemoral alignment and contact point locations on knee contact forces in individuals with varus malalignment, highlighting contact points' significant influence on knee forces during different activities.
- Ge et al. assessed inter-prosthetic pressures post-Oxford unicompartmental knee arthroplasty and their correlation with lower limb alignment, revealing correlations between pressures at specific knee angles and postoperative alignment parameters.
- Hucke et al. studied the mechanical influence of tension-band plates used in correcting knee malalignment through guided growth therapy, showing heterogeneous stress distribution in the growth plate, with implants inducing static stress in the insertion region and altering cyclic loading, affecting growth rates, with potential implications for preventing malalignment recurrence.

These articles illustrate the diversity of approaches and methodologies used to address the complex challenges of knee pathologies from various angles, including mechanical, biomedical, digital, and experimental. They thus underscore the growing importance of research in this domain. The Research Topic addressed in this Research Topic go beyond mere academic research; they contribute significantly to understanding the biomechanical behavior of the knee joint and its pathologies, particularly in early detection and prediction of knee osteoarthritis.

In conclusion, this Research Topic provides a captivating overview of recent progress in the field of knee biomechanics. The guest editors thank the editors, authors, and reviewers for contributing to this stimulating Research Topic, hope this Research Topic will inspire new ideas, collaborations, and advancements in the fight against knee pathologies, and look forward to future developments in this domain.

Author contributions

AB: Conceptualization, Investigation, Methodology, Validation, Writing–original draft, Writing–review and editing. BI: Conceptualization, Investigation, Validation, Writing–review and editing. JT: Investigation, Supervision, Validation, Writing–review and editing.

Funding

The author(s) declare that no financial support was received for the research, authorship, and/or publication of this article.

Conflict of interest

The authors declare that the research was conducted in the absence of any commercial or financial relationships that could be construed as a potential conflict of interest.

The author(s) declared that they were an editorial board member of Frontiers, at the time of submission. This had no impact on the peer review process and the final decision.

Publisher's note

frontiers | Frontiers in Bioengineering and Biotechnology

TYPE Original Research
PUBLISHED 21 June 2023
DOI 10.3389/fbioe.2023.1165963

OPEN ACCESS

EDITED BY
Abdelwahed Barkaoui,
International University of Rabat,
Morocco

REVIEWED BY
Zahra Trad,
UMR5295 Institut de Mecanique et d'Ingenierie de Bordeaux (I2M), France
Khaled Harrar,
University of Boumerdés, Algeria
Jean-Louis Milan,
Aix-Marseille Université, France

*CORRESPONDENCE
Lucie Hucke,
lucie.hucke@fb2.fra-uas.de
Andreas Wittek,
wittek@fb2.fra-uas.de

†PRESENT ADDRESS
Jana Holder,
Department of Sport and Exercise Sciences, University of Salzburg,
Salzburg, Austria

RECEIVED 14 February 2023
ACCEPTED 07 June 2023
PUBLISHED 21 June 2023

CITATION
Hucke L, Holder J, van Drongelen S, Stief F, Gámez AJ, Huß A and Wittek A (2023), Influence of tension-band plates on the mechanical loading of the femoral growth plate during guided growth due to coronal plane deformities.
Front. Bioeng. Biotechnol. 11:1165963.
doi: 10.3389/fbioe.2023.1165963

Influence of tension-band plates on the mechanical loading of the femoral growth plate during guided growth due to coronal plane deformities

Lucie Hucke[1,2]*, Jana Holder[3†], Stefan van Drongelen[3,4], Felix Stief[3,4], Antonio J. Gámez[2], Armin Huß[1] and Andreas Wittek[1]*

[1]Peronalized Biomedical Engineering Laboratory, Frankfurt University of Applied Sciences, Frankfurt am Main, Germany, [2]Department of Mechanical Engineering and Industrial Design, School of Engineering, University of Cádiz, Cádiz, Spain, [3]Department of Orthopedics (Friedrichsheim), University Hospital Frankfurt, Goethe University Frankfurt, Frankfurt am Main, Germany, [4]Dr. Rolf M. Schwiete Research Unit for Osteoarthritis, Department of Orthopedics (Friedrichsheim), University Hospital Frankfurt, Goethe University Frankfurt, Frankfurt am Main, Germany

Introduction: Correction of knee malalignment by guided growth using a tension-band plate is a common therapy to prevent knee osteoarthritis among other things. This approach is based on the Hueter-Volkmann law stating that the length growth of bones is inhibited by compression and stimulated by tension. How the locally varying mechanical loading of the growth plate is influenced by the implant has not yet been investigated. This study combines load cases from the gait cycle with personalized geometry in order to investigate the mechanical influence of the tension-band plates.

Methods: Personalized finite element models of four distal femoral epiphyses of three individuals, that had undergone guided growth, were generated. Load cases from the gait cycles and musculoskeletal modelling were simulated with and without implant. Morphological features of the growth plates were obtained from radiographs. 3D geometries were completed using non-individual Magnetic Resonance Images of age-matched individuals. Boundary conditions for the models were obtained from instrumented gait analyses.

Results: The stress distribution in the growth plate was heterogenous and depended on the geometry. In the insertion region, the implants locally induced static stress and reduced the cyclic loading and unloading. Both factors that reduce the growth rate. On the contralateral side of the growth plate, increased tension stress was observed, which stimulates growth.

Discussion: Personalized finite element models are able to estimate the changes of local static and cyclic loading of the growth plate induced by the implant. In future, this knowledge can help to better control growth modulation and avoid the return of the malalignment after the treatment. However, this requires models that are completely participant-specific in terms of load cases and 3D geometry.

Abbreviations: FE, Finite Element; GP, Growth plate; KCF, Knee contact force; OI, Osteogenic Index; RoL, Ring of Lacroix.

KEYWORDS

growth plate, guided growth, finite element analysis, knee model, tension-band plate, stress distribution

1 Introduction

Frontal plane malalignment of the knee axis can lead to permanent unphysiological loading of the knee joint, one of the most common causes for knee osteoarthritis (Sharma et al., 2001). It can occur in one or both knees and does not have to be equally severe. A preventive therapy is the correction of the malalignment by guiding growth of bones in adolescence. Longitudinal growth of bones originates from the growth plate (GP), which changes its shape during growth until it has a complex geometry in adolescence. Presumably its shape is an adaption to the mechanical loading (Thomson, 1902; Castro-Abril et al., 2016; Stamos und Weaver, 2020; Stamos und Berthaume, 2021). The GP geometry in adolescents consists of four different compartments, the anterior medial quadrant, the anterior lateral quadrant, the posterior medial quadrant, and the posterior lateral quadrant. These are separated by a central ridge, a medial and a lateral ridge (cf. Lippiello et al., 1989; Liu et al., 2013) (Figure 1B). The GP consists of a specialized type of non-vascularized hyaline cartilage from which newly formed bone is pushed out in the direction of the diaphysis (Figure 1C) (Kronenberg, 2003) which results in a gradual transition of material properties from soft, cartilage-like tissue in the GP itself, to ossified regions ("transition zone," cf. Sadeghian et al., 2020). It is surrounded in the transverse plane by the Ring of Lacroix (RoL), a fibrous layer that constrains the GP radially (Brighton, 1978; Piszczatowski, 2011).

The so-called "guided growth" therapy is based on the Hueter-Volkmann law. It states that static compression inhibits growth, while reduced compression can lead to accelerated growth (Gottliebsen et al., 2016; Hüter 1862a; (Huter, 1862b); Mehlman et al., 1997; Volkmann 1862). In addition Frost (1979) found that physiologically alternating compression and tension can also lead to an increase of the growth rate. Guided growth is performed by a minimal invasive surgical intervention called "temporary hemiepiphysiodesis". The implant, a metal plate, is fixed at the GP with two screws, one in the metaphyseal and one in the epiphyseal bone (Figure 1A). This leads to a reduced growth rate on the implant side, while the normal length growth continues contralaterally, resulting in an outgrowth of the malalignment. After implant removal, normal length growth continues on both sides (Stevens, 2007; Gottliebsen et al., 2013; Gottliebsen et al., 2016). Although, the axis correction initially is successful in most of the patients, the original malalignment returns in many cases. There is still limited knowledge about this so-called rebound phenomenon and potential risk factors are not well defined and controversially reported in literature, despite a high incidence (up to 69%) (Farr et al., 2018; Stief et al., 2021b). Therefore, a deeper understanding of the growth modulation mechanism is necessary, to better understand this rebound phenomenon. To date, the success of the guided growth treatment depends on the existing residual growth and the right timing of the removal of the implant. To determine the optimal time point, there are different approaches. The clinical standard is the malalignment test, where the mechanical leg axis and the deviation of the center of the knee joint from said axis is measured on radiograph images in the frontal plane (Vogt et al., 2014). Especially in borderline cases, when the malalignment test does not reveal a clear medical indication for or against the guided growth intervention, knee joint moments from instrumented gait analysis are additionally assessed. (Böhm et al., 2015; Stief et al., 2021a). In particular, the knee adduction moment is a commonly used surrogate measure for medial and lateral compartment knee loading. It was statistically associated to osteoarthritis severity and progression. A valgus malalignment was shown to reduce the knee adduction moment and therefore at the time of removal of the implant it should no longer differ from an age-matched control group (Holder et al., 2020). Calculating knee joint contact forces requires the additional use of musculoskeletal simulation software. While calculation of joint reaction forces using inverse dynamics

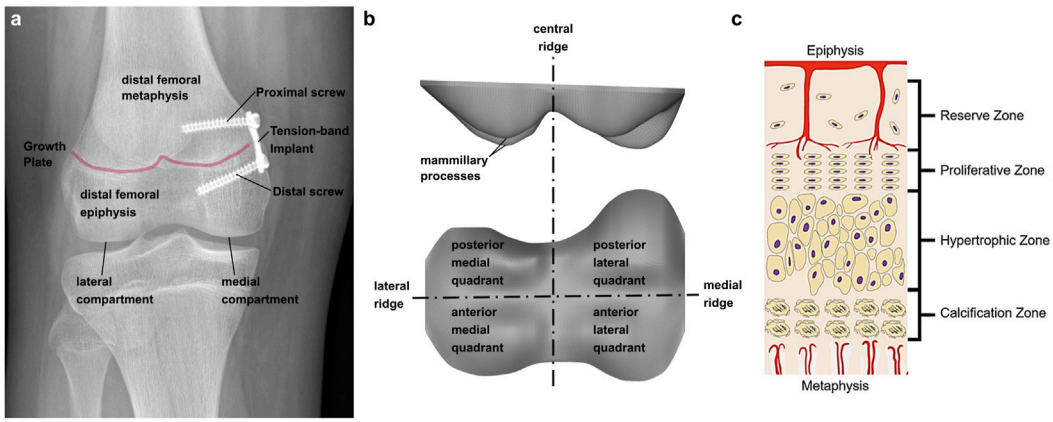

FIGURE 1
(A) Implant positioning at the tibio-femoral joint. Two screws, proximal and distal of the growth plate, fix the implant; **(B)** terminology of growth plate anatomy; **(C)** Growth plate zones in an epiphyseal growth plate; Reprinted from D'Andrea et al. (2021) with permission from John Wiley and Sons.

represents the reaction to external loads, only musculoskeletal modelling enables to additionally consider the contribution of the internal loads, mainly generated by muscles during walking (Lerner et al., 2015; Rajagopal et al., 2016), and are more representative of cartilage loading (Dell'Isola et al., 2017). Holder et al. (2020) used the data obtained by instrumented gait analysis to generate participant-individual multi-body models in OpenSim und calculated the medial and lateral knee contact forces (KCF), considering the influence of the muscle forces.

The described approaches consider the global mechanical loading of the whole knee joint in the form of resulting moments and forces. They do not investigate how these global loads on the knee translate into a load on the soft tissue in the growth plate, from which growth originates. Due to the complex geometry of the distal femoral growth plate, a balanced 'global' load does not necessarily mean a balanced or uniform local load on the tissue. This local loading of the growth plate tissue is exactly where the implant intervenes, since the joint momentum and the medial and lateral knee contact forces do not change with implantation. The finite element (FE) method that was used in this study is appropriate to analyze locally varying mechanical loading of tissue regions with complex, irregular geometries and its dependency on external loads and boundary conditions. To our knowledge the current study is the first that applies the FE method to investigate how tension-band plates change the distribution, type and size of mechanical stresses in the juvenile growth plate. This knowledge is a necessary precondition for analyzing and modelling differences of length growth of bones as a response to changes in mechanical loading.

FE models of the distal femoral GP are rare in literature. Most studies assume a simplified geometry. Mainly, linear elastic material properties are assumed, which show a wide range of the Young´s Modulus from 0.2 up to 1,157 MPa with an accumulation around 6 MPa. The Poisson-Ratio varies between 0.1 and 0.5 but is mostly assumed to be 0.48. (Piszczatowski, 2011; Yadav et al., 2017; Sadeghian et al., 2021; Stamos und Berthaume, 2021).

Schneider et al. (2018) inversely estimated the forces exerted by tension-band plates from the bending of the screws. The model focused on the material and geometrical properties of the screws and used a simplified cubic geometrical model of the trabecular bone with an embedded plane GP. Gao et al. (2017) used two cubic models of the trabecular bone with a "flat" and an "m-shaped" GP. The focus of this model was to investigate how the "global" forces are affecting the local cells at different depths of the tissue. Using geometrically simplified mechanical models with different morphological parameters, several studies have shown that GP morphology is an important factor influencing the transfer of joint loading to the stress distribution in the GP tissue itself (Piszczatowski, 2012; Castro-Abril et al., 2015; Guevara et al., 2015; Stamos und Berthaume, 2021). Stamos und Berthaume (2021) investigated the relations between GP morphology, type of biomechanical loading and resulting GP stresses in a comparative study between human and chimpanzee motion patterns. In order to predict the effect of mechanical loading on bone growth, several FE studies (cf. Carriero et al., 2011; Piszczatowski, 2012; Yadav et al., 2017; Sadeghian et al., 2021) apply the Osteogenic Index (OI that was proposed by Carter und Wong (1988); Stevens et al. (1999)). The OI is a linear combination of the maximum octahedral shear stress (stimulation) and the minimum hydrostatic stress (inhibition) adjusted by experimental data. It was developed to predict the endochondral growth and ossification in long bones in children from 8 weeks to approximately 2 years after birth. Since this model is not validated–though often used–for other age groups and, moreover, several, mutually contradictory versions of the OI have been proposed since the first use, the authors of this study decided not to use the OI or similar indices. This is discussed in more detail in the discussion section.

Although it is known that the mechanical loading situation at the knee joint during gait can affect the development of the leg axis (Stokes et al., 2002), the influence of guided growth on the mechanical loading of the GP tissue has not yet been studied using personalized FE analyses, and thus a geometrical complex GP. Furthermore, a differentiation between static and cyclic compression was not considered in previous studies. Therefore, the objective of this study was to analyze the influence of tension-band plates on the mechanical loading on the GP in terms of locally varying stress distributions in the plate itself. For this purpose, FE models of patients undergoing frontal plane leg axis correction by guided growth were generated at different stages of the treatment. Characteristic load cases were obtained from the results of instrumented gait analyses and multi-body simulations that had been performed for a previous study by Holder et al. (2020). Characteristic geometrical features of the individual GP at different stages of the treatment were derived from radiographs and used to generate 3D models with adequate morphological complexity even though available data did not allow for fully participant-individual 3D models. To the best of our knowledge, this is the first time the FE method was used to assess the loading of the GP due to the implant. Our hypothesis is, that the implant reduces the growth rate by increasing the static compression and reducing the cyclic changes of dynamic loading during gait on the implant side.

2 Materials and methods

2.1 Participants

In the present study, three patients with a pathological valgus alignment of at least one knee and a clinical indication for a temporary hemiepiphysiodesis were included (Table 1). Clinical indications for the in- and explantation of the implant were based on static weight bearing full-length radiographs of the legs in the frontal plane. Additionally, an instrumented gait analysis was performed a few days before implantation and explantation. Participants and their parents gave written informed consent to participate in this study, as approved by the local ethics committee (182/16) and in accordance with the Declaration of Helsinki.

2.2 Gait analysis and musculoskeletal modelling

In order to assess the dynamic mechanical loading on the GP the results of instrumented gait analysis and multi-body simulations from a previous study by Holder et al. (2020) were used as boundary conditions for the FE analyses. The gait analysis and musculoskeletal modelling was performed before and after guided growth as described in detail in

TABLE 1 Study participant's characteristics. The static mechanical axis angle (MAA) is the angle between the mechanical femur axis and the mechanical tibia axis in the frontal plane. Negative values of MAA indicate a valgus malalignment, positive values a varus malalignment. Table includes the thickness of the growth plate preoperative and postoperative: at the beginning of the treatment, a constant thickness was assumed, at the end of the treatment (explantation of the implant), the thickness was measured on the implant side and on the contralateral side.

Patient	P1		P2	P3
Sex	Female		Male	Male
Analyzed leg	Left	Right	Right	Right
Preoperative				
Age in years	11		13	14
Height in cm	162.5		169.3	175.0
Body weight in kg	74.2		71.0	60.8
MAA in °	−5	−3	−6	−10
Thickness growth plate in mm	1.43	1.35	1.51	1.39
Postoperative				
Age in years	13		15	15
Height in cm	167.8		178.5	180.0
Body weight in kg	91.3		88.5	70.9
MAA in °	−3	1	3	−2
Thickness growth plate in mm implant side/opposite side	0.47/0.66	0.46/0.72	0.69/1.20	0.5/0.76

Holder et al. (2020). Kinematic data were collected using an 8-camera motion capture system (MX 10, VICON Motion Systems, Oxford, UK) while participants walked barefoot. Ground reaction forces were recorded synchronously using two force plates (Advanced Mechanical Technology, Inc., Watertown, MA, United States) situated at the mid-point of the walkway. A custom-made lower body protocol was used for improvement of the reliability and accuracy described in a previous study Stief et al. (2013). In addition to the standardized Plug in-Gait marker set (Kadaba et al., 1990), reflective markers were attached on the medial malleolus, medial femoral condyle and greater trochanter. The statically measured midpoints between the medial and lateral malleolus and condyle markers defined the centers of rotation of the ankle and knee joints (Stief et al., 2013). The center of the hip joint was calculated with a standardized geometrical prediction method using regression equation (Davis et al., 1991) which is common in the clinical gait community (Stief, 2018). Three to five dynamic trials with a clear foot-force plate contact were selected for further processing.

For subsequent generation of a musculoskeletal model in OpenSim (version 3.3), marker and force plate data were processed using the MOtoNMS toolbox (version 3) in Matlab (version 2022a, The MathWorks, Inc., Natick, MA, United States). The full body model by Lerner et al. (2015) was used. This model includes 18 body segments and 92 muscle-tendon actuators and allows for the separate calculation of medial and lateral KCFs. The model was linearly scaled based on the marker positions to fit the participant's body mass and height. The participant-specific mechanical axis angle, as obtained from full-length standing anteroposterior radiograph was implemented. Inverse kinematics and inverse dynamics, were calculated within OpenSim for all participants. A static optimization implementation that incorporates tendon compliance and passive muscle forces was used to solve for muscle activations, with a cost function that minimized the sum of squared muscle activation (Seagers et al., 2022). The computed medial and lateral KCFs were time normalized to the full duration of the stance phase, beginning with the foot strike and ending with the foot off (Holder et al., 2020).

2.3 Finite element model

2.3.1 3D geometries and FE discretization

To create a geometrical three-dimensional (3D) model of the distal femoral GP of each participant, characteristic parameters were measured manually in radiographs using Fusion 360 (Fusion 360, Autodesk, San Rafael, United States): width and thickness, axis malalignment, edge steepness, location of vertices of valleys and ridges, radii at the vertices, and implant positioning in the frontal plane. To determine the thickness the shortest distance between the proximal and distal border of the growth plate was measured at a location where it was clearly visible. For the axis malalignment, the mechanical leg axis connecting the ankle joint and the hip joint was defined and the deviation of the knee joint center from the axis was measured (Figure 2A). For reference a line connecting the outwards, upper points of the GP was introduced (Line b, Figure 2B), the length of this line was considered the width. The edge steepness was measured by the angle of a straight tangential line at the edge of the GP and the Line b (Figure 2B). The radii (Figure 2D) and location of vertices of valleys and ridges (Figure 2C) were defined by placing points at the locations and fitting a circle on the local shape of vertices and ridges. Vertices and steepness were measured for the anterior and posterior part of the GP separately, based on the assumption that the distal structures lie posterior. The implant positioning in the frontal plane (Figures 2H, I) was measured by the angles between the screws and a vertical line. Additionally, the

10.3389/fbioe.2023.1165963

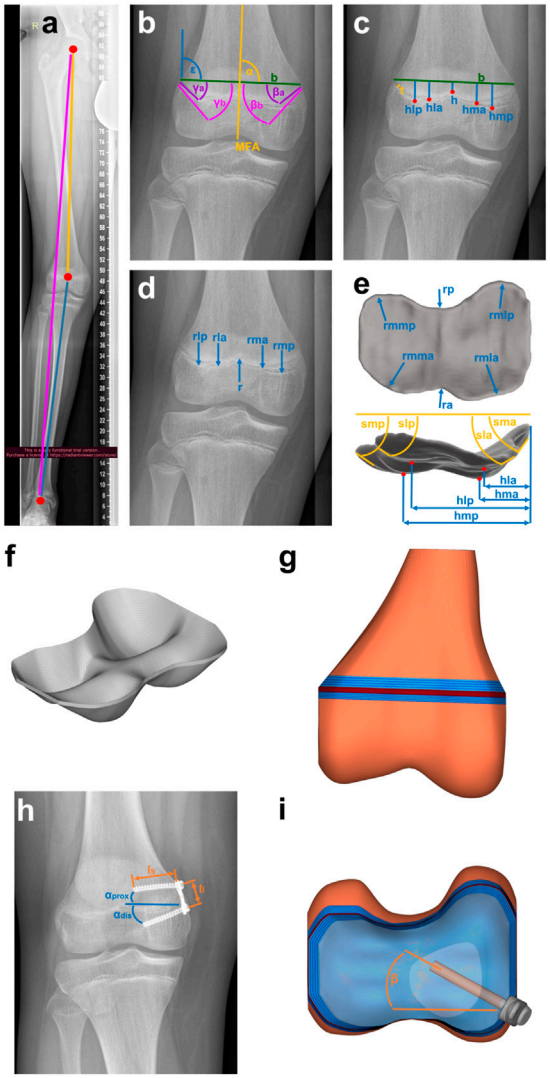

FIGURE 2
Creating the geometry based on clinical data: **(A–E)** Characteristic parameters of the growth plate and the knee, such as **(A)** malalignment, **(B)** edge steepness measured with angles medially β′ and laterally,γ′ each anterior,a′ and posterior, p′, **(C)** location of vertices, h′ laterally, l′ and medially, m′ each anterior, a′ and posterior, p′, width, b′ and thickness, t′, **(D)** radii, r′ laterally, l′ and medially, m′ each anterior, a′ and posterior, p′ and **(E)** additional parameters from 3D-MRI-data (Lustig und Vasanawala, 2022) such as the radii in the transversal plane, rm′, r′ laterally, l′ and medially, m′ each anterior, a′ and posterior, p′. This leads to **(F)** the 3D-Mesh of growth plate, implemented in **(G)** FE-Mesh of distal femur. **(H)** Implant parameters such as screw length, l_S, implant length, li′ and screw angles,α_{prox}′, α_{dis}′ are measured and implemented in **(G)** FE-Mesh of the distal femur with **(I)** the implant included.

screw length and the implant size were measured. To minimize the random error of manual measurement, a total of five measurements for each radiographic image were performed in a random order of patients and by the same person and the mean value was used. To complete the 2D radiograph image data into a 3D geometry, radii and edge steepness in the transversal plane were measured on open source Magnetic Resonance Images (MRI) data (Lustig und Vasanawala, 2022) (Figure 2E).

A cloud with a total of 59 points was generated from the measured parameters. These points were interpolated in two steps using a shape preserving piecewise cubic interpolation (Matlab function PCHIP). Using Hypermesh Desktop (HyperMesh 2017; Altair HyperWorks, Troy, Michigan, United States), the resulting surface was discretized into quad elements with an edge length of 0.75 mm. This 2D mesh was dragged to the measured thickness of each GP. A 3D mesh of hexaeder and wedge elements (C3D6, C3D8), which was organized in 5 to 6 layers over the thickness (Figure 2F), resulted. A convergence study was performed to determine the optimal element size, as shown in the Supplementary Material (Section 1).

The computed medial and lateral KCFs were concentrated forces that pass through the joint axis of the knee. Since the GP consists of a very soft material, it was not possible to apply the forces directly to it, this would have led to infinitely high stresses at one point (singularity). Therefore, the GPs were embedded in an idealized distal femur geometry that allowed the application of the medial and lateral KCFs onto the bone in sufficient distance to transform concentrated loads into realistically distributed stresses acting on the GP. Femoral bone geometry was the same for all participants. The idealized distal femur geometry consisted of the medial and lateral joint compartments, the distal femoral trabecular bone, distal and proximal transition zones between GP, bone, and the RoL (Figure 2G). The RoL is a fibrous tissue that lies circumferentially around the GP. Without the RoL, the GP would be pressed out between the epiphyseal and metaphyseal femur and thus change its shape at the edge. This would cause notch effects, i.e., singularities, in the peripheral region of the GP. Discontinuities in stiffness also lead to stress artefacts in the peripheral regions, which were prevented by considering the transition zones (Sadeghian et al., 2020) in the model. The effects of the different components on the stress distribution are shown in the Supplementary Material, Section 2 and Supplementary Figures S6, S7. As the thickness of the distal and proximal transition zones, 3 and 5 mm were chosen (Sadeghian et al., 2020; Castro-Abril et al., 2015; Figure 2G). The RoL was modelled by 4-node shell elements (S4). The implant and the screws were discretized by 8-node brick elements and 4-node tetrahedron elements (C3D4/C3D8). All used element types are linear and of full integration type. For the execution of the simulations the Solver Abaqus 6.14 (Dassault Systèmes Simulia Corp., Vélizy-Villacoublay, France) was used (Table 2). The angle of the screws in the transversal plane was calculated by comparing the length of the projection of the screws on the frontal plane measured from the radiographs and the known true length of the screws reported by the surgeon (Figures 2H, I). All GP parameters were measured at two time points, before implantation and before explantation. From these measurements four different FE-models, M1 to M4, of each knee were created, representing different stages of treatment: M1 and M2 model the knee at the start of treatment before and after implantation of the tension-band plate. M3 and M4 refer to the end of treatment before and after explantation (Figure 3). For all components, linear elastic material properties with Young´s Modulus of 6 MPa for the GP, 2,942 MPa for the trabecular bone, 775 MPa for the RoL and 110,000 MPa for the implant and the screws were used. The transition zone has a stepwise increasing Young´s Modulus from GP to bone. The Poisson-Ratio was 0.48 for the GP and 0.3 for the other components (Table 2).

TABLE 2 Mesh and material properties of FE-model. With two given element types, underlined element types are the mainly used ones for each component. The used solver was Abaqus 6.14. Material properties are linear elastic.

Part	Element type	E-Modulus [MPa]	Poisson-ratio	Source
Growth Plate	C3D6/C3D8	6	0.48	Yadav et al., 2017
Transition Zone	C3D6/C3D8	6–2,942	0.3	-
Trabecular Bone	C3D4/C3D8	2,942	0.3	Yadav et al., 2017
Perichondrial Ring	S4	775	0.3	Fishkin et al., 2006
Implant	C3D4/C3D8	110,000	0.3	-
Screws	C3D4/C3D8	110,000	0.3	-

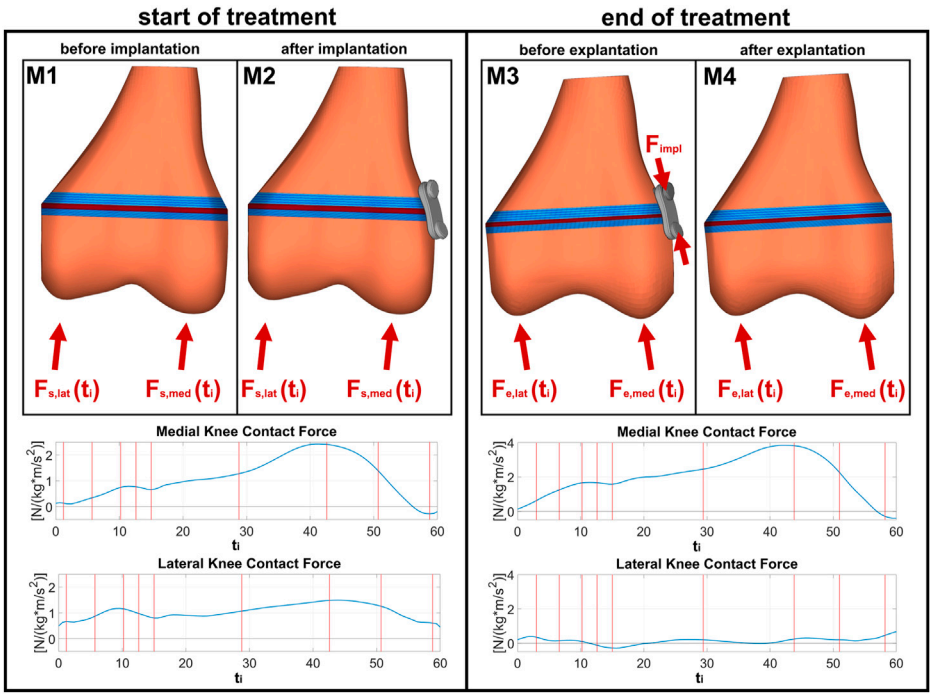

FIGURE 3
FE models for different stages of treatment: M1 and M2 are models before and after implantation at the start of the treatment, with the same boundary conditions obtained from corresponding individual instrumented gait analyses; M3 and M4 are models before and after explantation at the end of the treatment, with now changed boundary conditions due to growth and correction of malalignment.

2.3.2 Load cases und boundary conditions

In the following, the terminus "load case" stands for the different loads at different points of the gait cycle, whereas the terminus "stage" stands for the different stages of treatment: start and end of treatment. For each of the four FE-models stress distributions in the GP were evaluated for nine different characteristic load cases throughout the stance phase of the gait cycle (cf. e.g., Perry und Burnfield, 2010): initial contact, end of loading response, mid stance, terminal stance (maximum KCF), pre-swing, and four intermediate cases in the middle between (Figure 3). For each load case, medial and lateral KCF vectors obtained from the joint reaction analysis were applied as quasistatic loads. The only difference between models M1 and M2 as well as between M3 and M4 was the existence of the implant. In M2 the implant is stress free, whereas in M3 the implant is under pre-tension stresses due to the bone growth. Schneider et al. (2018) have reported implant forces ranging from 129 to 1002 N. For the present study, the minimum force (129 N), mean of all the reported forces (485.1 N), and the maximum force (1002 N) were chosen for all participants. In order to apply this to the models, the augmented iterative design algorithm by Rausch et al. (2017) was used.

An additional study was conducted, in which one load case (terminal stance of P2) was applied to the models M1 of the patients P1 R, P2 R and P3 R. P1 L was excluded since it was a left knee. The

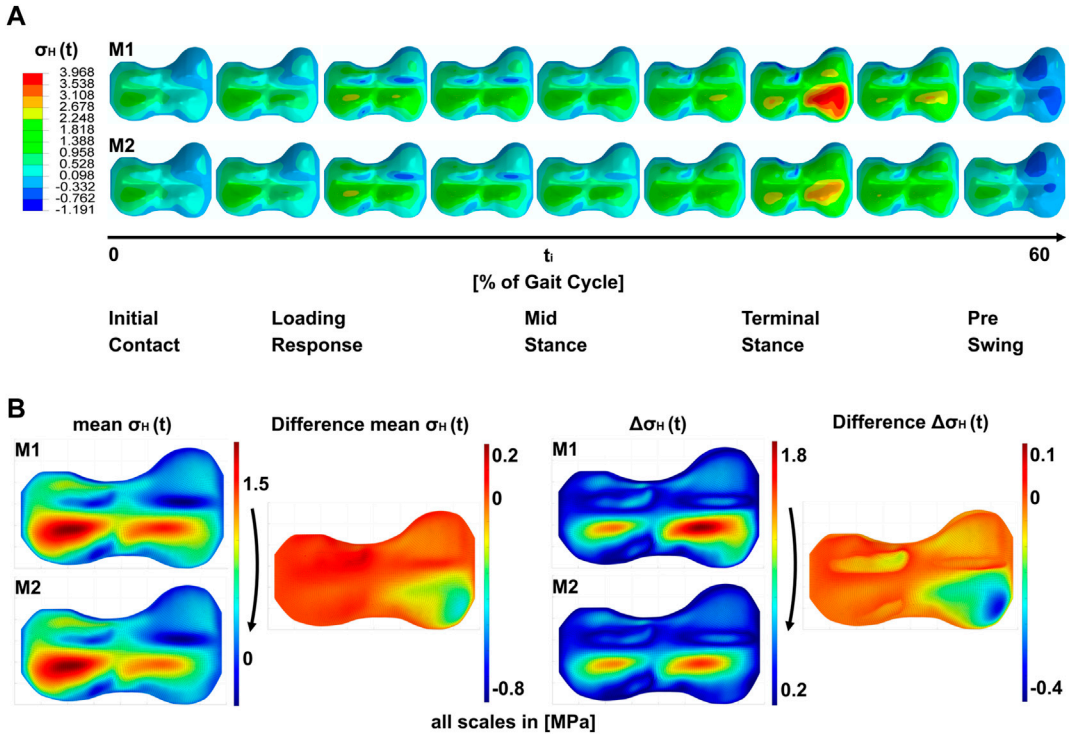

FIGURE 4
Results of the simulations; **(A)** shows a timeline of hydrostatic stresses in the growth plate during the stance phase of the gait cycle for models M1 and M2. i.e., both models are identical with regard to load cases and geometry, but differ in the absence or presence of the implant (M1 and M2, respectively). **(B)** shows the peak-to-peak amplitude $\Delta\sigma_H$ (t) over the gait cycle and the mean σ_H (t) over the gait cycle. Both shown for M1 and M2. Right to this the difference plots between M1 and M2 are shown.

aim of this study was to show the influence of the GP geometry on the stress distribution in the GP under the same boundary conditions.

2.4 Stress metrics

To account for the different influences of compression, tension and shear, the hydrostatic and octahedral shear stress distributions in the GP were calculated from the Cauchy stress tensor using an in-house Matlab script.

The hydrostatic stress was calculated as

$$\sigma_{Hi} = -\frac{1}{3}\mathrm{tr}\,(\boldsymbol{\sigma}_i) \tag{1}$$

with $\boldsymbol{\sigma}_i$ being the stress tensor. And the octahedral shear stress as

$$\sigma_{Si} = \sqrt{-\frac{1}{3}\left[\mathrm{tr}^2\,(\boldsymbol{\sigma}_i{}^{Dev}) - \mathrm{tr}\,(\boldsymbol{\sigma}_i{}^{Dev^2})\right]} \tag{2}$$

with $\boldsymbol{\sigma}_i{}^{Dev}$ being the deviatoric stress tensor of $\boldsymbol{\sigma}_i$:

$$\boldsymbol{\sigma}_i{}^{Dev} = \boldsymbol{\sigma}_i - \frac{1}{3}\mathrm{tr}\,(\boldsymbol{\sigma}_i)\boldsymbol{I}. \tag{3}$$

$\boldsymbol{I}$ is the Identity Tensor.

The results of the simulations (Figure 4) are the stress distributions in the GP for each load case throughout the gait cycle examined at four stages of the treatment (M1–M4, Figure 4A). The peak-to-peak-amplitudes and the mean of the stress metrics σ_{Si} and σ_{Hi} were calculated over the gait cycle for each model and each element. The peak-to-peak-amplitudes show the cyclic change of the loading of the growth plate during gait whereas the mean represents the static loading of the growth plate. For a better visualization of the impact of the implant, the difference of each value from before and after implantation at the start of treatment (M1 to M2) (Figure 4B) and from before and after explantation (M3 to M4) at the end was calculated.

3 Results

Simulations show a heterogeneous distribution of stresses over the GP (Figure 4A). In all models that are not affected by pretension of the implant at the end of treatment, the area of the ridges showed the lowest absolute values of σ_H and σ_S. Anterior to the medial and lateral ridge, between the ridges and the vertices, the highest pressure stresses occurred, especially during terminal stance. Tension was present especially at the anterior periphery of the GP and posterior to the medial and lateral ridges. The stress distribution in the GP followed the distribution of the external forces. If the medial KCF became very high, this was reflected in increased medial stresses. This was particularly clear in the

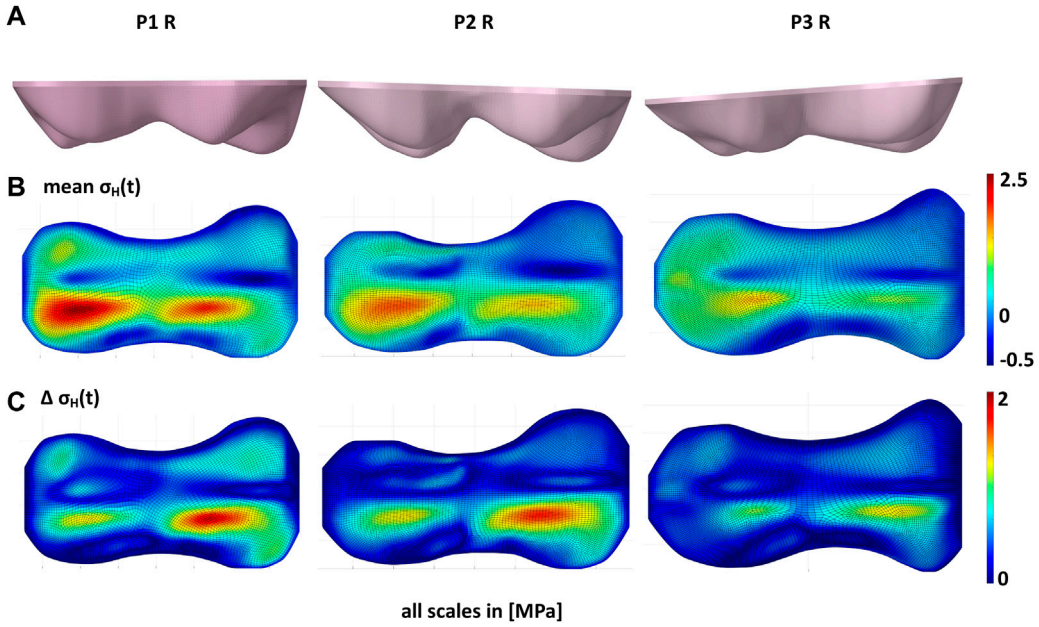

FIGURE 5
Influence of growth plate geometry on the stress distribution in the growth plate. **(A)** shows the different growth plate geometries of the right knees of patients P1, P2, and P3. With the same loads **(B)** shows that the mean of hydrostatic stresses over the gait cycle ($\sigma_H(t)$) is significantly higher in P1. The same applies to **(C)** the peak-to-peak-amplitudes ($\sigma_H(t)$), although the difference is not so pronounced here.

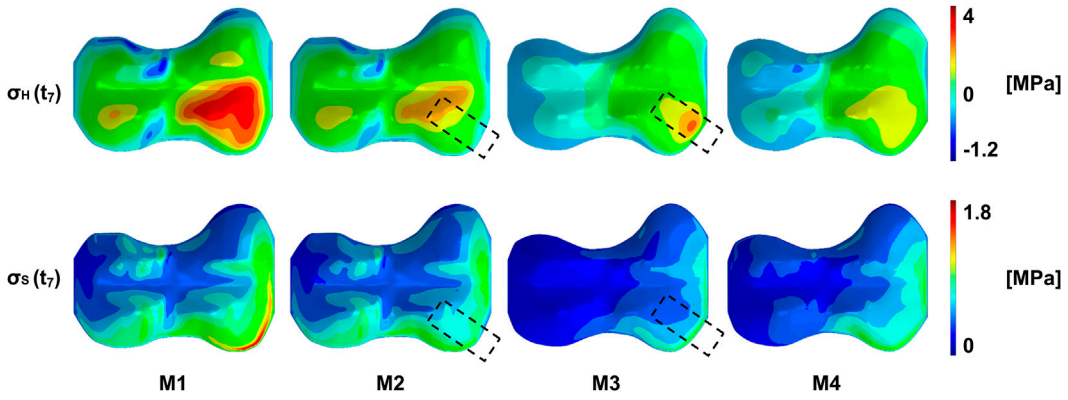

FIGURE 6
Exemplary representation of the stress distribution of the growth plate of patient P2 R at a point in time in the terminal stance phase. From left to right the same load case is shown at different stages during the treatment: M1/M2–start of treatment without/with implant, respectively, M3/M4–end of treatment without/with prestressed implant, respectively. On top, the pattern of the pressure stresses is shown, with the highest compression stresses in the anterior quadrants. This pattern can be seen, as long as the implant is not under prestresses. Here (M3), high pressure stresses appear in the implant area. After explantation, the original pattern returns with a different distribution of pressure stresses. A similar pattern can be seen on the bottom with the octahedral shear stresses. More detailed figures can be found in the supplementary material.

terminal stance (Figure 4A). Furthermore, the magnitude of stress in the GP was dependent on the GP geometry. When we compared different models with different GP geometries, but the same boundary conditions, the resulting stress distributions qualitatively remained the same between the GPs compared, but the magnitude of the stresses σ_H and σ_S changed considerably. This was particularly evident between GPs with different angles relative to the femoral axis (Figure 5).

At the start of the treatment, right after implantation, the overall pattern of stress distribution remained unchanged, but a decrease of the absolute stress values could be observed, on the implant side. This is exemplarily shown in Figure 6 for the terminal stance phase of P2 R. In the case of P1 L and P1 R, the implant reduced the stresses on the entire medial side, with the greatest effect directly at the implant (Supplementary Figures 16, 17). In P2 R and P3 R, the implant was anterior, so the main change was observed directly at the implant, with

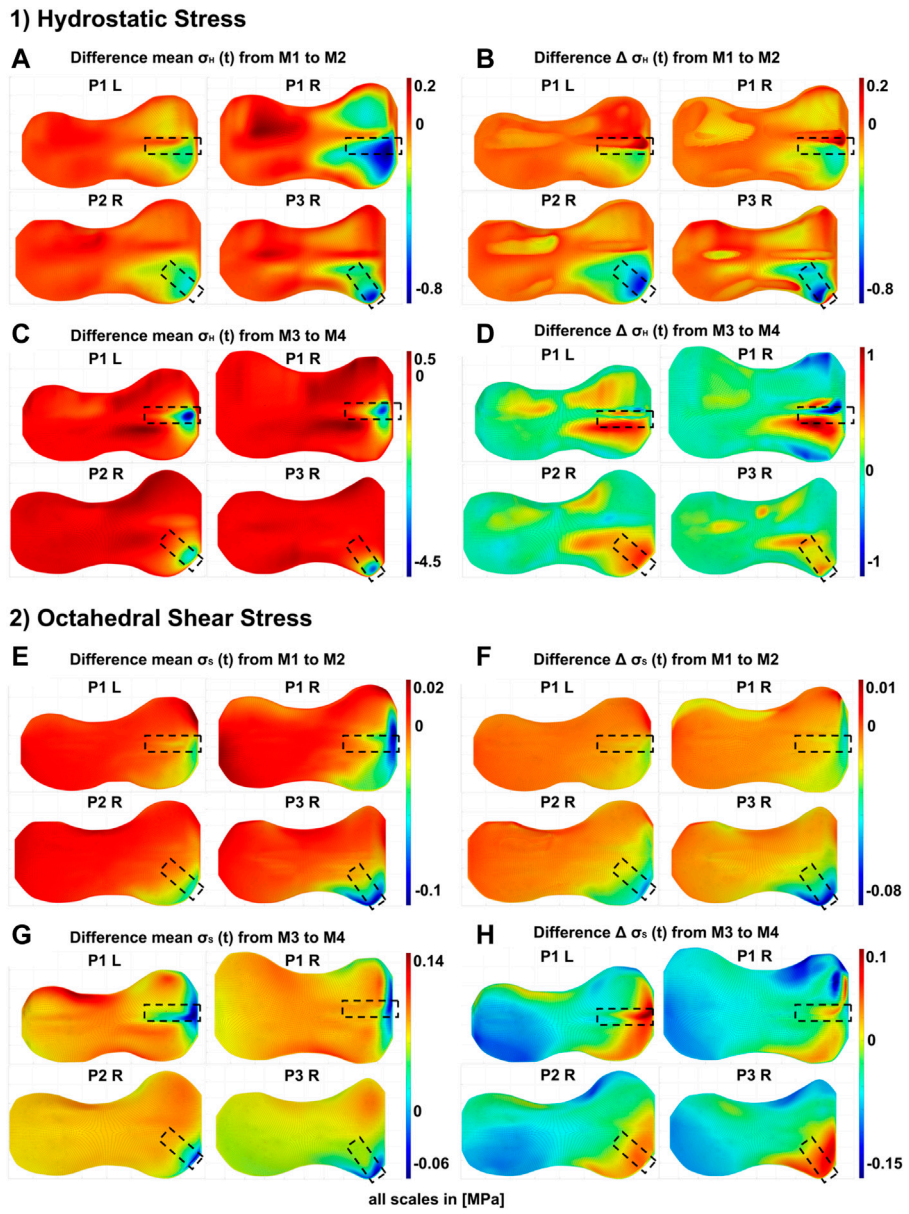

FIGURE 7
Differences in the GP stress distributions resulting from the presence or absence of the implant at different stages of the treatment: M1/M2–start of treatment without/with implant, respectively, M3/M4–end of treatment without/with prestressed implant, respectively. 1) Differences of hydrostatic stresses in the growth plate; the figure shows the difference of M1 and M2 for each patient (P1 to P3, R = right knee, L = left knee) in **(A)** Peak-to-peak amplitudes $\Delta\sigma_H(t)$ and **(B)** for ***mean*** $\sigma_H(t)$. It shows the difference of M3 and M4 for each patient in **(C)** Peak-to-peak amplitudes $\Delta\sigma_H(t)$ and **(D)** for ***mean*** $\sigma_H(t)$. 2) Differences of octahedral shear stresses in the growth plate; the figure shows the difference of M1 and M2 for each patient in **(E)** Peak-to-peak amplitudes $\Delta\sigma_S(t)$ and **(F)** for ***mean*** $\sigma_S(t)$. It shows the difference of M3 and M4 for each patient in **(G)** Peak-to-peak amplitudes $\Delta\sigma_S(t)$ and **(H)** for ***mean*** $\sigma_S(t)$.

only small changes in the rest of the medial half (Supplementary Figures 18, 19). At the end of the treatment, when the implant is under pretension, high pressure and shear stresses were observed in the area of the implant. The implant also had an effect on the lateral side, where tension stresses occurred in the whole half of the growth plate (Figure 6, Supplementary Figures 16–23, M3). While the tension stresses in M1 and M2 had a higher magnitude, but where also only occurring locally and depending on the gait phase, tension stresses in M3 covered the whole half of the GP and occurred over the whole gait cycle. After explantation, the initial pattern returned, but with more balanced medial and lateral stresses, and an overall decrease in absolute stress values (Figure 6). The exact pattern depends on the individual geometry and loading conditions.

Figure 7 shows the changes in the stress distributions that were induced by adding or removal of the implant. At the beginning of the treatment, the implant has the biggest influence in the quadrant where it was placed. Here it reduced the cyclic as well as the static loading. On the contralateral side, the implant resulted in no or small increases

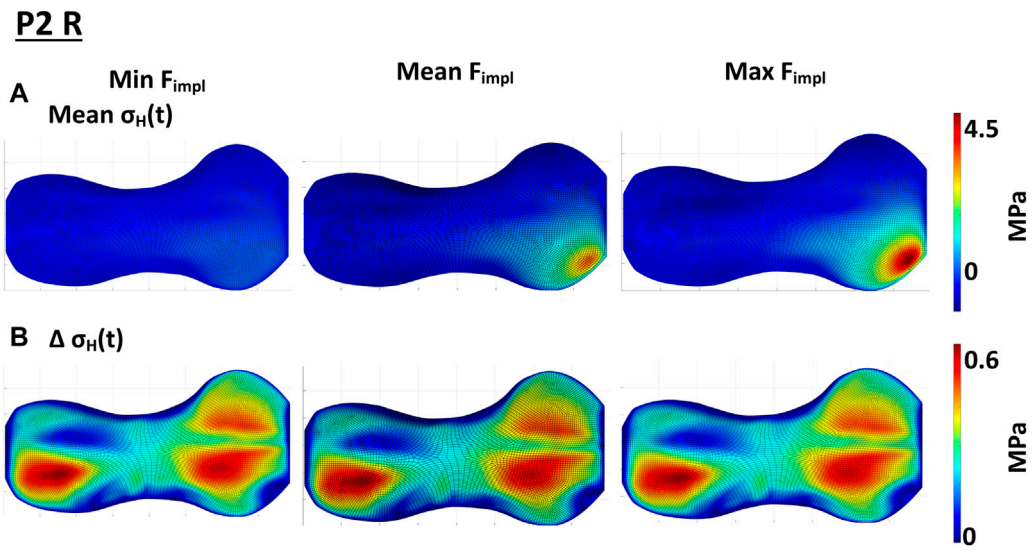

FIGURE 8
Influence of the implant force on the static compressive stress distribution; **(A)** shows the change in ***mean*** $\sigma_H(t)$ over the gait cycle when varying the implant force. With the minimal implant force after Schneider et al. (2018) the implant has little to no influence on the stress distribution in the growth plate. The higher the implant force gets, the higher the compressive stress in the growth plate and the bigger the area of influence. **(B)** shows, that the magnitude of the implant force does not have an influence on $\Delta\sigma_H(t)$ over the gait cycle.

in static loading. The cyclic loading was reduced throughout the GP, although significantly less than in the direct area of influence of the implant. Depending on the location of implantation the area of influence is slightly different, although it has the main influence on the anterior medial quadrant and a smaller influence on the posterior medial quadrant (Figures 7A, B, E, F).

At the end of the treatment, as a result of the removal of the implant, pressure and shear stresses where significantly reduced, i.e., the implant induced high pressure and shear stresses locally. Outside the direct area of influence of the implant, either no change or a slight increase with implant removal was observed. The influence on the dynamic stress was more extensive. In P1 L and P1 R, the main changes were seen in the anterior medial quadrant, with some still significant changes in the posterior medial quadrant. In P2 R and P3 R, the implant mainly changed stresses on the anterior medial quadrant. The removal of the implant led to an increase in cyclic change of loading, i.e., the implant decreased the cyclic change of loading during the treatment. Other areas where not changed by implant removal. An exception is P1 R, where the removal of the implant locally decreased the cyclic load changes in small areas. However, the general trend here follows the stress distribution of the other participants.

The variation of the magnitude of the pretention force exerted by the implant at the end of treatment (cf. Section 2.3.2) influenced on the size of the affected GP area and magnitude of the stresses. Exemplary results for P2 R are shown in Figure 8, the results for all included knees can be found in Supplementary Figures S25–S29. The higher the implant force acting on the GP, the higher are also the local pressure stresses and the bigger the area of influence. While the implant with the minimal implant force only had a small influence on the static loading, the highest implant force also led to the highest static loading of the GP. This effect seemed not to be linear (Figure 8A, Supplementary Figures S24–S27). The magnitude of the implant force showed only negligible influence on the cyclic loading in the GP (Figure 8B, Supplementary Figures S24–S27).

4 Discussion

To the best of our knowledge, this is the first numerical finite element study, which used participant-individual load cases combined with a personalized, although not fully individual geometry of the distal femoral GP in order to investigate the heterogenous stress distribution in the GP and the mechanical influence of tension band implants on it in detail.

To evaluate the influence of the tension band implant on the mechanical loading of the juvenile GP, four different models of each of the four different knees were build, representing different stages of the treatment. The model geometries, based on radiographs, were not fully participant-individual, but represented a realistic and characteristic geometry of the distal femoral GP. Boundary conditions and load cases were obtained from instrumented gait analyses of three different participants and subsequent patient-specific musculoskeletal modelling using OpenSim that were available from a previous study (Holder et al., 2020). The goal of this prospective study was to investigate the difference between medial or lateral KCF before and after temporary hemiepiphysiodesis in patients with valgus malalignment compared to a typically developed control group and to determine if a linear relationship exists between the static radiographic mechanical axis angle and the KCFs.

An investigation carried out as part of this study showed that the geometry of the GP has a significant influence on the stress distribution in the GP. Under the same boundary and loading conditions, the stresses in the GP were significantly different for different geometries. This was mainly related to the magnitude of the stresses, rather than the qualitative distribution in the GP, as all GPs showed similar geometrical or morphological features with different degrees of expression.

Due to these recurring geometric features, the stress distributions follow a pattern. The highest pressure stresses were found in both anterior quadrants, close to the medial and lateral ridges, at the steep area. The highest tension stresses were on the other side of the ridges in the posterior quadrants and in the front area of the GP (Figures 4, 5). This indicates that the ridge works as a lever, depending on the joint reaction forces. This assumption is supported by the observation that high pressure stresses in one place in the GP went hand in hand with high tension stresses on the other side of the ridge. This was observed in the diagonal and in the sagittal direction (Figure 4, Supplementary Figures S8–S23). The assumption that the ridges work as a lever was strengthened by a numerical parameter study by Piszczatowski (2012). Eight different geometries and five different arbitrarily chosen load cases were investigated using cylindrical models with the different GP geometries embedded. The RoL was considered as a soft solid body around the cylinder. Although the models were simplified, two load cases in particular, each with two geometries, show similar characteristics to the growth plates we investigated: A wave-shaped growth plate under diagonal loads was evaluated, which was comparable to the simulation of each model in terminal stance. In Piszczatowski (2012) as well as in this study, the stress maxima were observed in the steeply sloping areas of the geometry. On the other side of the ridge, the stress minimum could be identified, suggesting the ridge acts as a lever.

Figure 6 shows the differences in the stress distribution that result from adding or removing the implant, whereas geometry, boundary conditions and external loading remained unchanged. This allowed to isolate the influence of the implant in exemplary cases. Hereby, the peak-to-peak-amplitudes represented the cyclic change of the loading, the mean stresses over the gait cycle showed the static loading. With the insertion of the implant, the cyclic loading and unloading was reduced locally (Figures 7B, 7F), as well as the static compression (Figures 7A, 7E). At the end of the treatment, the prestressed implant reduced the cyclic change of loading and increased the static compressive stresses in the area of the implant (cf. changes between M3 and M4 as shown in Supplementary Figures S8–S15). The effect size regarding the compressive stresses depended on the implant force. The higher the force, the higher the increase in static pressure stresses and the bigger the influence area of the implant (Figure 8). Both, reduced cyclic loading and increased static compressive stresses, were factors that are considered to reduce the growth rate according to Hueter-Volkman (Hüter, 1862a; Huter, 1862b; Volkmann, 1862; Mehlman et al., 1997; Gottliebsen et al., 2016) and Frost (Frost, 1979). These findings confirm our initial hypothesis stated above (cf. Section 1). Surprisingly, the implant initially reduced the static loads on the GP since part of the loading was transferred from epiphysis to metaphysis via the plate instead of the GP. Since it also reduced the cyclic loading at the beginning, a growth inhibiting and a growth stimulating factor were observed for this stage of treatment.

The implant did not only have an impact on the stress distribution on the joint side where it was placed. Right before explantation of the prestressed implant an increase in tension stresses on the contralateral side of the GP was observed. Since tension stresses are believed to increase the growth rate, this would mean, that axis correction by the implant is not only achieved by suppressing growth on one side, but also by promoting growth on the other side of the GP.

Few studies have been conducted using FE modelling to understand the influence of the mechanical loading of the respective GP and the surrounding structures on the stress distribution in the GP. Hereby, mainly growth models were investigated, all of them used different versions of the OI to connect the mechanical loading with the resulting growth. Carter und Wong (1988) studied the role of mechanical loading in development of diarthrodial joints in human fetuses, with the aim to develop a hypothesis on how to describe the behavior of the GP tissue sufficiently. Therefore, simplified geometries and load cases were used in the FE-model, which consisted of the joint bones and cartilage of infantile subjects. In contrast to the current study, perichondrial structures were not included. A constructed gait cycle was simulated as discrete load steps and the contact forces were applied on nodes in the contact area of the joint, as was also done in this study. Since the fluid flow between the cartilage and the growth plate is slow, the assumption of a linear elastic, nearly incompressible model was considered sufficient to investigate the influence of mechanical loads on the tissue. The same material model was applied in this study. The model predicted the ossification center and the development of the growth plate in infantile joints.

Carriero et al. (2011) used a similar approach and investigated the effect of altered gait due to cerebral palsy on the proximal femoral morphology in later developmental stages. Here, transition zones with gradually increasing Young´s Modulus from the GP to the bone were added to improve the simulation stability, as we did in our model. They also make sense when compared to the biological structure, as the GP becomes harder gradually across its layers.

Yadav et al. (2017) studied the influence of muscle groups on the proximal femoral growth in able bodied children between the ages of 6 and 11 years old. Using previously described methods the study used nine load cases representing the stance phase of the gait cycle, as was also done in this study. The direction of growth was considered in the direction of the maximum principal stress for each element and the growth was applied by thermal expansion of the outer growth plate layer. Although a model of the whole femur was studied, the distal femoral GP was not included in the model. Only the influence of muscles in healthy children was investigated.

Close to the aforementioned studies Sadeghian et al. (2021) investigated the endochondral ossification in long bones using a phalanx joint. A distinction between calcified and non-calcified cartilage was made. This model could predict the ossification of postnatal cartilage in the phalanx joint.

None of the discussed studies investigated the distal femoral GP in adolescents. Since the geometry of the GP is highly

irregular our results are hard to compare to these studies. To investigate the connection between mechanical loading and growth all aforementioned studies used the OI, but all in a different way. The OI always consists of the octahedral shear stress as the growth increasing factor and the hydrostatic stress as the growth inhibiting factor. Carter und Wong (1988) used the sum of OI over all load cases and first proposed an experimental constant weighting of the hydrostatic stress. Sadeghian et al. (2021) used the same approach but calculated the OI for each element in each load step and used the mean OI over all load steps for each element. Carriero et al. (2011) and Yadav et al. (2017) each used the minimum hydrostatic stress and maximum octahedral shear stress over all load cases and used a weighting factor for both stresses, so that the mechanical contribution to growth is half as the biological contribution. Piszczatowski (2011) used two different approaches of the OI and the main principal stresses to evaluate the results. Since formulation and use of the OI for predicting bone growth is inconsistent and not validated, we decided to restrict this study to the evaluation of the distributions of compressive and deviatoric stresses. Future work of our group will aim at validation of the OI for adolescents. Furthermore, none of the studies differentiated between static and cyclic compression.

In contrast to the aforementioned studies, part of our model was the RoL. It is part of the perichondrium and encloses the GP in the circumferential direction. Biologically, the circumferential growth of the bone originates from these structures, therefore they also contain stem cells. Mechanically, it prevents the growth plate from being pushed out of the bone and reduces high stresses at the edges. A short numerical sensitivity study was conducted to show the influence of the RoL and the transitions zones. This can be found in the supplementary material, Section 2 and Supplementary Figures S6, S7.

Castro-Abril et al. (2015) investigated the influence of the geometry and force application on the stress distribution in the proximal femoral growth plate and how this influenced a slipped capital femoral epiphysis. To do so, a numerical parameter study was conducted, varying the physeal-diaphysis angle, body mass, RoL, physical activity and GP thickness. The RoL was modelled according to Piszczatowski (2012). Castro-Abril et al. (2015) was able to show whether or not the RoL is considered has a greater influence on the stress distribution and thereby also the growth, than the position and shape of the growth plate or the force application. Due to the complex geometry of the distal femoral growth plate, this cannot necessarily be transferred to our model, but it was shown that the RoL should not be neglected in a mechanical investigation of the structure.

Schneider et al. (2018) conducted the first study investigating the implant and its screws, but did not investigate the effect of the implant on the stress distribution in the GP. They used the screw bending observed on radiographed images at the end of the guided growth treatment to determine the resulting forces on the implant. Although the validation model used was geometrically simplified, the bending and the stress curve in the screws could be represented well. In comparison to this study, the implant screws showed qualitatively the same bending as in our model and thus are likely to be able to represent the loading of the GP induced by the implant.

4.1 Limitations

As already stated above, the exemplarily presented models were not fully participant-individual, meaning that the calculated stress distributions did not allow for the prediction of future growth in the individual case. Geometrical parameters in the frontal plane were measured in the radiograph images, parameters in the transversal and sagittal plane were added from age matched MRI-data (Lustig und Vasanawala, 2022). This led to not fully participant-specific models of the distal femoral GP, which however incorporated typical morphological features and had a realistic geometrical complexity. Due to this geometry, the computed stress patterns were heterogeneous and contained not only pressure, but also tension stresses, although the applied forces were solely compression forces. The material properties of the models were not participant-specific. In contrast, linear elastic properties with parameters based on literature were used. Also, the implant forces applied to the implant in Model M3 were not participant-specific. Instead the mean, minimum and maximum value of the calculated screw forces by Schneider et al. (2018) were used. The positioning of the implant inside the model was based on radiograph images in the frontal plane and thus the parameters in the transversal plane had to be estimated. Within the RoL lies Ranvier's Groove, which was not considered in our model.

The developed model is a participant-specific but not a participant-individual model. It can be used to investigate the typical effect of tension-band plates on the stress distribution in the growth plate, but it does not allow predictions about the course of treatment or the occurrence of a rebound effect after treatment in the individual case. Future work will include fully patient-specific modelling.

5 Conclusion

The current study demonstrates the capability of finite element analyses that model the interplay of the complex GP morphology and realistic loading conditions from experimental gait analysis to show stress distribution in the GP and the implant's influence, for a given geometry and given material parameters. With untouched loading and geometry between two models, the insertion/exertion of the implant changes the stress distribution in the GP drastically. In order to allow for clinical predictions, these models have to be fully participant-individual with regard to GP morphology and load cases. This together with patient examinations during and after the treatment can show, if these models will be able to determine the implant removal time point, predict further growth, and estimate the risk of the occurrence of rebound.

Data availability statement

The data analyzed in this study is subject to the following licenses/restrictions: Clinical data of patients under the age of 18 years, generated by clinical partner (see authors list). Requests to access these datasets should be directed to FS, felix.stief@kgu.de.

Ethics statement

The studies involving human participants were reviewed and approved by the Ethics commission of the Goethe University Hospital Frankfurt am Main in Germany, Approved 21.09.2018, reference number "Geschäftszeichen: 182/16." Written informed consent to participate in this study was provided by the participants' legal guardian/next of kin.

Author contributions

LH and AW contributed to the conception and design of the study. JH, SD, and FS collected the medical data. LH conducted the study with help of AW, AH, and AG. LH performed steps of finite element preprocessing, modelling, analysis and post processing of the analysis results. LH, JH, FS, and AW were involved in the interpretation and discussion of the results. LH and AW wrote sections of the manuscript. All authors contributed to the article and approved the submitted version.

Acknowledgments

We thank Sonia Vincenti, Hochschule Offenburg, for conducting the FE Analysis during her internship at the Frankfurt University of Applied Sciences, that showed the influence of the geometry on the stress distribution in the GP.

Conflict of interest

The authors declare that the research was conducted in the absence of any commercial or financial relationships that could be construed as a potential conflict of interest.

Publisher's note

Supplementary material

The Supplementary Material for this article can be found online at: https://www.frontiersin.org/articles/10.3389/fbioe.2023.1165963/full#supplementary-material

References

Böhm, Harald, Stief, Felix, Sander, Klaus, Hösl, Matthias, and Döderlein, Leonhard (2015). Correction of static axial alignment in children with knee varus or valgus deformities through guided growth: Does it also correct dynamic frontal plane moments during walking? *Gait Posture* 42 (3), 394–397. doi:10.1016/j.gaitpost.2015.06.186

Brighton, Carl T. (1978). Structure and function of the Growth Plate. *Clin. Orthop. Relat. Res.* 136, 22–32. doi:10.1097/00003086-197810000-00003

Carriero, Alessandra, Jonkers, Ilse, and Shefelbine, Sandra J. (2011). Mechanobiological prediction of proximal femoral deformities in children with cerebral palsy. *Comput. methods biomechanics Biomed. Eng.* 14 (3), 253–262. doi:10.1080/10255841003682505

Carter, Dennis R., and Wong, M. (1988). The role of mechanical loading histories in the development of diarthrodial joints. *J. Orthop. Res.* 6 (6), 804–816. doi:10.1002/jor.1100060604

Castro-AbrilAlfonso, Héctor, Gutiérrez, M. L., and Alexander, Diego (2016). Proximal femoral growth plate mechanical behavior: Comparison between different developmental stages. *Comput. Biol. Med.* 76, 192–201. doi:10.1016/j.compbiomed.2016.07.011

Castro-AbrilHector, A., Galván, Fernando, and Garzón-Alvarado, Diego A. (2015). Geometrical and mechanical factors that influence slipped capital femoral epiphysis: A finite element study. *J. Pediatr. Orthop. Part B* 24 (5), 418–424. doi:10.1097/BPB.0000000000000195

D'AndreaChristian, R., Alfraihat, Ausilah, Singh, Anita, Anari, Jason B., Cahill, Patrick J., et al. (2021). Part 1. Review and meta-analysis of studies on modulation of longitudinal bone growth and growth plate activity: A macro-scale perspective. *J. Orthop. Res.* 39 (5), 907–918. doi:10.1002/jor.24976

Davis, Roy B., Õunpuu, Sylvia, Tyburski, Dennis, and Gage, James R. (1991). A gait analysis data collection and reduction technique. *Hum. Mov. Sci.* 10 (5), 575–587. doi:10.1016/0167-9457(91)90046-Z

Dell'Isola, A., Smith, S. L., Andersen, M. S., and Steultjens, M. (2017). Knee internal contact force in a varus malaligned phenotype in knee osteoarthritis (KOA). *Osteoarthr. Cartil.* 25 (12), 2007–2013. doi:10.1016/j.joca.2017.08.010

Farr, Sebastian, Alrabai, Hamza M., Meizer, Elisabeth, Ganger, Rudolf, and Radler, Christof (2018). Rebound of frontal plane malalignment after tension band plating. *J. Pediatr. Orthop.* 38 (7), 365–369. doi:10.1097/BPO.0000000000000846

Fishkin, Zair, Armstrong, Douglas G., Shah, Hardik, Patra, Abani, and Mihalko, William M. (2006). Proximal femoral physis shear in slipped capital femoral epiphysis-a finite element study. *J. Pediatr. Orthop.* 26 (3), 291–294. doi:10.1097/01.bpo.0000217730.39288.09

Frost, H. M. (1979). A chondral modeling theory. *Calcif. tissue Int.* 28 (3), 181–200. doi:10.1007/BF02441236

Gao, Jie, Williams, John L., and Roan, Esra (2017). Multiscale modeling of growth plate cartilage mechanobiology. *Biomechanics Model. Mechanobiol.* 16 (2), 667–679. doi:10.1007/s10237-016-0844-8

Gottliebsen, Martin, Shiguetomi-Medina, J., and Rahbek, Ole, (2016). Guided growth: Mechanism and reversibility of modulation. *J. children's Orthop.* 10 (6), 471–477. doi:10.1007/s11832-016-0778-9

Gottliebsen, M., Møller-Madsen, B., Stødkilde-Jørgensen, H., and Rahbek, O. (2013). Controlled longitudinal bone growth by temporary tension band plating: An experimental study. *bone and Jt. J.* 95-B (6), 855–860. doi:10.1302/0301-620X.95B6.29327

Guevara, J. M., Moncayo, M. A., Vaca-González, J. J., Gutiérrez, M. L., Barrera, L. A., and Garzón-Alvarado, D. A. (2015). Growth plate stress distribution implications during bone development: A simple framework computational approach. *Comput. methods programs Biomed.* 118 (1), 59–68. doi:10.1016/j.cmpb.2014.10.007

Holder, Jana, Feja, Zoe, van Drongelen, Stefan, Adolf, Stefanie, Böhm, Harald, Meurer, Andrea, et al. (2020). Effect of guided growth intervention on static leg alignment and dynamic knee contact forces during gait. *Gait Posture* 78, 80–88. doi:10.1016/j.gaitpost.2020.03.012

Hüter, C. (1862a). Anatomische Studien an den Extremitätengelenken Neugeborener und Erwachsener. *Virchows Arch.* 25, 572–599.

Hüter, C. (1862b). Anatomische Studien an den Extremitätengelenken Neugeborener und Erwachsener. *Virchows Arch.* 26, 484–519.

Kadaba, M. P., Ramakrishnan, H. K., and Wootten, M. E. (1990). Measurement of lower extremity kinematics during level walking. *J. Orthop. Res.* 8 (3), 383–392. doi:10.1002/jor.1100080310

Kronenberg, Henry M. (2003). Developmental regulation of the growth plate. *Nature* 423 (6937), 332–336. doi:10.1038/nature01657

Lerner, Zachary F., DeMers, Matthew S., Delp, Scott L., and Browning, Raymond C. (2015). How tibiofemoral alignment and contact locations affect predictions of medial and lateral tibiofemoral contact forces. *J. biomechanics* 48 (4), 644–650. doi:10.1016/j.jbiomech.2014.12.049

Lippiello, L., Bass, R., and Connolly, J. F. (1989). Stereological study of the developing distal femoral growth plate. *J. Orthop. Res.* 7 (6), 868–875. doi:10.1002/jor.1100070613

Liu, Raymond W., Armstrong, Douglas G., Levine, Ari D., Gilmore, Allison, Thompson, George H., and Cooperman, Daniel R. (2013). An anatomic study of the distal femoral epiphysis. *J. Pediatr. Orthop.* 33 (7), 743–749. doi:10.1097/BPO.0b013e31829d55bf

Lustig, Michael, and Vasanawala, Shreyas (2022). MRI data. Unter mitarbeit von Anita flynn, frank ong, gabriel nahum, joseph cheng, michael lustig, joyce toh, patrick virtue, shahab amin, shreyas Vasanawala, umar tariq. UC berkeley; stanford's lucile packard children's hospital. Online verfügbar unter http://mridata.org/, zuletzt aktualisiert am 22.08.2022.

Mehlman, C. T., Araghi, A., and Roy, D. R. (1997). Hyphenated history: The hueter-volkmann law. *Am. J. Orthop. (Belle Mead, N.J.)* 26 (11), 798–800.

Perry, Jaqueline, and Burnfield, Judith (2010). Gait analysis. Normal and pathological function. *J. Sports Sci. Med.* 9.

Piszczatowski, Szczepan (2012). Geometrical aspects of growth plate modelling using Carter's and Stokes's approaches. *Acta Bioeng. Biomech.* 14 (1), 93–106.

Piszczatowski, Szczepan (2011). Material aspects of growth plate modelling using Carter's and Stokes's approaches. *Acta Bioeng. biomechanics* 13 (3), 3–14.

Rajagopal, Apoorva, Dembia, Christopher L., DeMers, Matthew S., Delp, Denny D., Hicks, Jennifer L., and Delp, Scott L. (2016). Full-body musculoskeletal model for muscle-driven simulation of human gait. *IEEE Trans. bio-medical Eng.* 63 (10), 2068–2079. doi:10.1109/TBME.2016.2586891

Rausch, Manuel K., Genet, Martin, and Humphrey, Jay D. (2017). An augmented iterative method for identifying a stress-free reference configuration in image-based biomechanical modeling. *J. biomechanics* 58, 227–231. doi:10.1016/j.jbiomech.2017.04.021

Sadeghian, S. Mahsa, Lewis, Cara L., and Shefelbine, Sandra J. (2020). Predicting growth plate orientation with altered hip loading: Potential cause of cam morphology. *Biomechanics Model. Mechanobiol.* 19 (2), 701–712. doi:10.1007/s10237-019-01241-2

Sadeghian, S. Mahsa, Shapiro, Frederic D., and Shefelbine, Sandra J. (2021). Computational model of endochondral ossification: Simulating growth of a long bone. *Bone* 153, 116132. doi:10.1016/j.bone.2021.116132

Schneider, Manuel, Buschbaum, Jan, Joeris, Alexander, Röhrle, Oliver, Dwyer, Jonathan, Hunter, James B., et al. (2018). Biomechanical investigation of two long bone growth modulation techniques by finite element simulations. *J. Orthop. Res.* 36 (5), 1398–1405. doi:10.1002/jor.23762

Seagers, Kirsten, Uhlrich, Scott D., Kolesar, Julie A., Berkson, Madeleine, Kaneda, Janelle M., Beaupre, Gary S., et al. (2022). Changes in foot progression angle during gait reduce the knee adduction moment and do not increase hip moments in individuals with knee osteoarthritis. *J. biomechanics* 141, 111204. doi:10.1016/j.jbiomech.2022.111204

Sharma, L., Song, J., Felson, D. T., Cahue, S., Shamiyeh, E., and Dunlop, D. D. (2001). The role of knee alignment in disease progression and functional decline in knee osteoarthritis. *JAMA* 286 (2), 188–195. doi:10.1001/jama.286.2.188

Stamos, Peter A., and Weaver, Timothy D. (2020). Ontogeny of the distal femoral metaphyseal surface and its relationship to locomotor behavior in hominoids. *Am. J. Phys. Anthropol.* 172 (3), 462–474. doi:10.1002/ajpa.24036

Stamos, Peter A., and Berthaume, Michael A. (2021). The effects of femoral metaphyseal morphology on growth plate biomechanics in juvenile chimpanzees and humans. *Interface focus* 11 (5), 20200092. doi:10.1098/rsfs.2020.0092

Stevens, Peter M. (2007). Guided growth for angular correction: A preliminary series using a tension band plate. *J. Pediatr. Orthop.* 27 (3), 253–259. doi:10.1097/BPO.0b013e31803433a1

Stevens, S. S., Beaupré, G. S., and Carter, D. R. (1999). Computer model of endochondral growth and ossification in long bones: Biological and mechanobiological influences. *J. Orthop. Res.* 17 (5), 646–653. doi:10.1002/jor.1100170505

Stief, Felix, Holder, Jana, Böhm, Harald, and Meurer, Andrea (2021a). Dynamische Analyse der Gelenkbelastung bei Beinachsendeformitäten in der Frontalebene: Stellenwert der instrumentellen Ganganalyse. *Der Orthopade* 50 (7), 528–537. doi:10.1007/s00132-021-04121-9

Stief, Felix, Holder, Jana, Böhm, Harald, and Meurer, Andrea (2021b). Häufigkeit und Prädiktoren für einen Rebound nach operativer Achskorrektur in der Frontalebene: Eine Literaturübersicht. *Der Orthopade* 50 (7), 548–558. doi:10.1007/s00132-021-04118-4

Stief, Felix (2018). "Variations of marker sets and models for standard gait analysis," in *Bertram Müller und Sebastian I. Wolf (Hg.): Handbook of Human Motion. Unter Mitarbeit von Gert-Peter Brüggemann, Andrew S. McIntosh, W. Scott Selbie, Zhigang Deng und Freeman Miller. 1. Aufl* (Berlin, Germnay: Springer), 509–526.

Stokes, Ian A., Mente, Peter L., Iatridis, James C., Farnum, Cornelia E., and Aronsson, David D. (2002). Enlargement of Growth Plate chondrocytes modulated by sustained mechanical loading. *JBJS* 84 (10), 1842–1848. doi:10.2106/00004623-200210000-00016

Thomson, A. (1902). The relation of structure and function as illustrated by the form of the lower epiphysial suture of the femur. *J. Anat. Physiology* 36 (2), 95–105.

Vogt, B., Schiedel, F., and Rödl, R. (2014). Guided growth in children and adolescents. Correction of leg length discrepancies and leg axis deformities. *Der Orthopade* 43 (3), 267–284. doi:10.1007/s00132-014-2270-x

Volkmann, R. (1862). Chirurgische Erfahrungen über Knochenverbiegungen und Knochenwachstum. *Arch. Path. Anat.* 24 (24), 512–540. doi:10.1007/bf01879454

Yadav, P., Shefelbine, S. J., Pontén, E., and Elena, M. (2017). Influence of muscle groups' activation on proximal femoral growth tendency. *Biomechanics Model. Mechanobiol.* 16 (6), 1869–1883. doi:10.1007/s10237-017-0925-3

frontiers | Frontiers in Bioengineering and Biotechnology

TYPE Original Research
PUBLISHED 09 August 2023
DOI 10.3389/fbioe.2023.1210713

OPEN ACCESS

EDITED BY
Abdelwahed Barkaoui,
International University of Rabat,
Morocco

REVIEWED BY
Nicola Mondanelli,
University of Siena, Italy
Taysir Rezgui,
University of Carthage, Tunisia

*CORRESPONDENCE
Bailiang Wang,
bailiang_wang@outlook.com
Wanshou Guo,
wanshou_guo@outlook.com

†These authors have contributed equally to this work and share first authorship

RECEIVED 24 April 2023
ACCEPTED 01 August 2023
PUBLISHED 09 August 2023

CITATION
Ge J, Sun X, Liu C, Zhang Q, Wang B and Guo W (2023), Intraoperative sensor technology quantifies inter-prosthesis pressure for predicting lower limb alignment after Oxford unicompartmental knee arthroplasty. *Front. Bioeng. Biotechnol.* 11:1210713. doi: 10.3389/fbioe.2023.1210713

Intraoperative sensor technology quantifies inter-prosthesis pressure for predicting lower limb alignment after Oxford unicompartmental knee arthroplasty

Juncheng Ge[1,2†], Xiaowei Sun[2,3†], Changquan Liu[2,3†], Qidong Zhang[2], Bailiang Wang[2*] and Wanshou Guo[1,2*]

[1]Department of Orthopaedic Surgery, Peking University China-Japan Friendship School of Clinical Medicine, Beijing, China, [2]Department of Orthopaedic Surgery, China-Japan Friendship Hospital, Beijing, China, [3]China-Japan Friendship Hospital, Institute of Clinical Medical Sciences, Chinese Academy of Medical Sciences and Peking Union Medical College, Beijing, China

Purpose: The aim of this study is to quantify inter-prosthetic pressures at different knee angles in Oxford unicompartmental knee arthroplasty (OUKA) and its correlation with postoperative lower limb alignment.

Methods: This study included 101 patients (122 knees) who underwent OUKA from March 2022 to July 2022. The previously designed matrix flexible force sensor was used to measure the inter-prosthesis pressure of different knee joint angles during the UKA operation, and the force variation trend and gap balance difference were obtained. The correlation between inter-prosthesis pressure and postoperative lower limb alignment index including hip-knee-ankle angle (HKAA) and posterior tibial slope (PTS) was analyzed. The effect of PTS change (ΔPTS) on the inter-prosthesis pressure and the range of motion (ROM) of the knee joint was analyzed. Radiographic and short-term clinical outcomes of included patients were assessed.

Results: The inter-prosthesis pressure of the different knee joint angles during the operation was not consistent. The mean inter-prosthesis pressure and gap balance difference were 73.68.28 ± 41.65N and 36.48 ± 20.58N. The inter-prosthesis pressure at 0° and 20° was positively correlated with postoperative HKAA ($p < 0.001$). ΔPTS was positively correlated with the pressure at the end of knee extension and negatively correlated with the pressure at the end of knee flexion ($p < 0.001$). The HKAA, ROM, degree of fixed knee flexion deformity, and knee society score of the included patients were significantly improved compared with those before the operation ($p < 0.001$).

Conclusion: The inter-prosthesis pressure measured at the knee extension position can predict postoperative HKAA to some degree. Changes in PTS will affect the inter-prosthesis pressure at the end of flexion and end of knee extension, but this change is not related to the range of motion of the knee joint.

KEYWORDS

Oxford unicompartmental knee arthroplasty (UKA), limb alignment, posterior tibial slope (PTS), pressure sensor, hip-knee-ankle angle (HKAA)

1 Introduction

Oxford unicompartmental knee arthroplasty (OUKA) is an effective treatment for end-stage knee osteoarthritis, especially for anteromedial osteoarthritis, with the advantages of less trauma and faster recovery (Mohammad et al., 2018; Hansen et al., 2019; Walker et al., 2019). OUKA repairs the diseased knee joint through osteotomy and prosthesis filling, and restores the tension of the soft tissue around the knee joint (especially the medial collateral ligament). The restoration of soft tissue tension is closely related to the effect of surgery and the dynamic stability of the knee joint. However, whether it is total knee arthroplasty (TKA) or UKA, the intraoperative judgment of soft tissue tension mostly depends on the operator's experience, and it is difficult to be directly quantified. In some respects, the use of sensors to measure inter-prosthesis pressure can indirectly reflect soft tissue tension. Sensor technology has been reported to balance the medial-lateral space and the flexion-extension space in TKA, allowing for more precise surgery (Chow et al., 2018; van der Linde et al., 2018). The potential benefit of sensors is the ability to obtain real *in vivo* measurements, and smart implants embedded with sensor technology offer the opportunity to improve surgical outcomes (Kelmers et al., 2023). For OUKA, the soft tissue tension and the balance of flexion and extension are particularly important (Heyse et al., 2016; Kwon et al., 2020). Unfortunately, there are few reports of sensor technology used in OUKA [(Mentink et al., 2017; Becker et al., 2013)], and the standard of flexion-extension gap balance has not been established.

Lower limb alignment is an important indicator, it can reflect whether the mechanical support structure of the knee joint has recovered after UKA. Postoperative coronal lower extremity alignment (i.e., hip-knee-ankle angle, HKAA) is directly related to surgical outcome, particularly long-term outcome. Intraoperative overfilling of the medial compartment can lead to valgus and accelerate degeneration of the lateral compartment, which is the commonest reason for UKA failure (Slaven et al., 2020; Slaven et al., 2021; Kamenaga et al., 2022). The optimal coronal alignment after medial UKA is considered to be neutral or mildly varus (Inoue et al., 2016; Plancher et al., 2022), and the causes of valgus may be related to the following: inaccurate determination of inter-prosthetic pressures during surgery; or surgeons implanting an oversized spacer for fear of dislocation (Ro et al., 2018; Misir et al., 2020). On the sagittal plane, the posterior tibial slope (PTS) has a significant impact on the surgical effect and prosthesis life (Hernigou and Deschamps, 2004; Gulati et al., 2009; Suero et al., 2012; Lee et al., 2014). A large number of studies have shown that changes in PTS can significantly affect the flexion-extension gap and postoperative range of motion in cruciate-retaining total knee arthroplasty. However, there are still very limited studies on the impact of PTS changes on inter-prosthesis pressure during UKA surgery and postoperative motor function (Takayama et al., 2016; Koh et al., 2021; Khow et al., 2022).

To help the operator to evaluate the soft tissue tension more accurately during the operation, we used a pressure sensor to measure the inter-prosthesis pressure of different knee angles during the OUKA operation. At the same time, we further analyzed its correlation with postoperative lower limb alignment.

2 Materials and methods

2.1 General information

This study prospectively enrolled 101 patients (122 knees) undergoing OUKA from March 2022 to July 2022. The prosthesis used in all patients was the phase III Oxford mobile-bearing prosthesis, hybrid type (Biomet, Bridgend, United Kingdom). The basic information about the included patients is shown in Table 1.

Inclusion criteria were radiographically diagnosed isolated medial compartment osteoarthritis or idiopathic osteonecrosis, fixed flexion deformity <15°, knee range of motion (ROM) greater than 90°, and varus deformity <15°. Patients with any of the following criteria were excluded from the study: 1) knee osteoarthritis involving the lateral compartment; 2) inflammatory arthritis; 3) incomplete clinical and radiological records. The study was approved by the ethics committee (approval number:2020-50-K28) and was in accordance with the Declaration of Helsinki. All the patients included in the studies have signed the informed consent.

2.2 Sensor

According to the characteristics of the OUKA prosthesis, a force sensor has been customised for inter-prosthetic pressure measurement. The pressure sensing area of this sensor is consistent with the shape of the tibial prosthesis, with a thickness of 0.12 mm, a sensing area of 45 × 22 mm^2, and a total of 197 force-measuring points (Figure 1). The structure of the sensor is that the electrodes are sprayed in two pieces flexible materials vertically and horizontally, and the middle is lined with pressure-sensitive materials (Figure 2). A matrix network is formed by crossing horizontally and vertically, which can convert different pressures on the network nodes into resistance values, and finally output specific pressure values through the transducer. The data acquisition frequency can be up to 20Hz and the measuring range is 500N/cm^2. We evaluated the accuracy and repeatability of this sensing technology through cadaver specimen measurements in the early stage and found that the error between the calibration value and the measured value

TABLE 1 Patient demographics.

Demographic	
No. of cases	101 (122 knees)
Gender (Male/female)	17/84
Age	66.75 ± 5.96
Side (L/R)	54/68
BMI(body mass index)	27.63 ± 3.74
Size of femoral component (XS/S/M/L)	4/92/22/4
Size of tibial component (AA/A/B/C/D/E)	9/41/45/23/2/2
Size of polyethylene bearing (3/4/5/6)	56/43/17/15

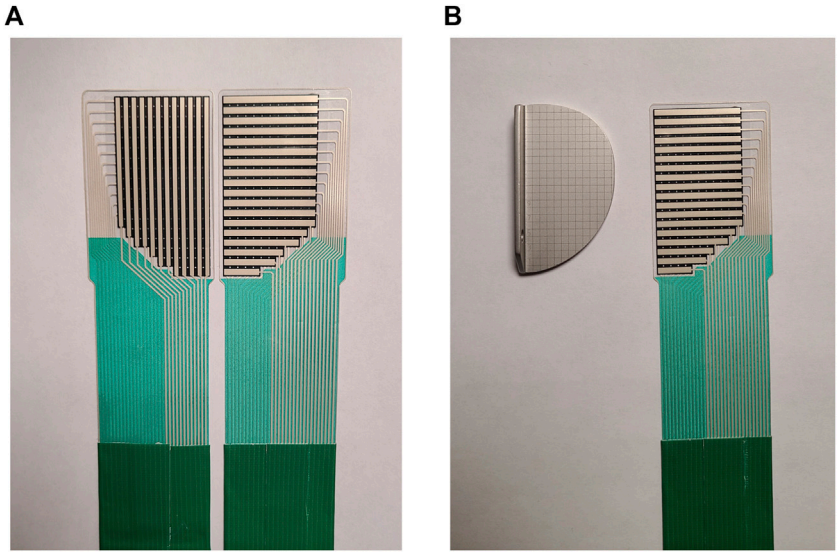

FIGURE 1
(A) Pressure sensors designed for the Oxford unicompartmental knee arthroplasty (anterior view and posterior view). The superior is a matrix sensing area with 197 measurement points and the inferior outputs pressure data via a transducer connected to a PC. **(B)** The pressure measuring area of the sensor corresponds to the shape of the tibial prosthesis (on the left is the trial mould of the tibial prosthesis, on the right is the customized sensor).

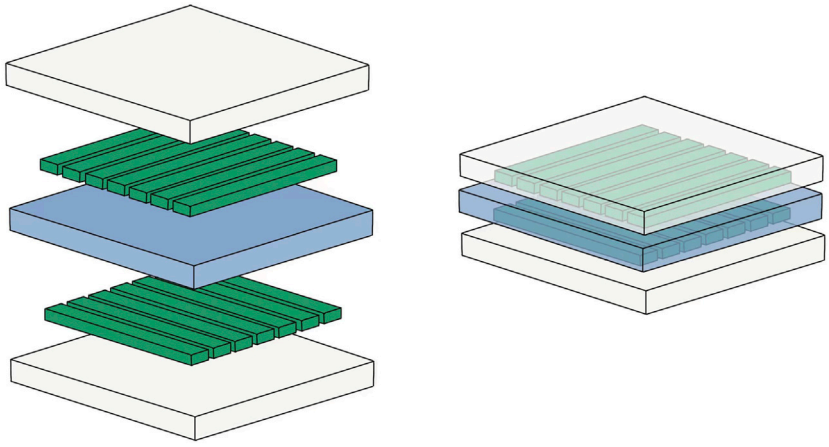

FIGURE 2
Model diagram of the sensor structure: the white transparent layer refers to the insulating layer; the central blue layer refers to the pressure-sensitive material; the green columns on both sides refer to the electrodes.

was within 1%, and the error/mean ratio of repeated measurements was also 1% Below: indicates good accuracy and repeatability (Sun et al., 2021; Sun et al., 2022). Teflon (Polytetrafluoroethylene) tape (0.1 mm in thickness) was used to fix it to reduce the influence of shear force, and a STERRAD low-temperature sterilizer (Johnson&Johnson, Inc, United States) was used for hydrogen peroxide plasma low-temperature disinfection, and data calibration was performed before and after disinfection. It was found that low-temperature disinfection below 60°C had no significant effect on data acquisition, which is consistent with another common resistive matrix sensor (Agins et al., 2003).

2.3 Surgery and intraoperative measurements

All operations on included patients were performed by the same group of surgeons, and the chief surgeon was a senior expert with a total of more than 2,000 UKA operations. The surgery is performed under general or spinal anesthesia. A medial parapatellar approach was selected. First, the tibial osteotomy was performed under extramedullary guidance, with the posterior tilt angle set at 7° in principle. If the pre-operative lateral x-ray shows that the original PTS is too large or too small, it should be adjusted to an appropriate situation. Femoral side preparation begins with the identification of

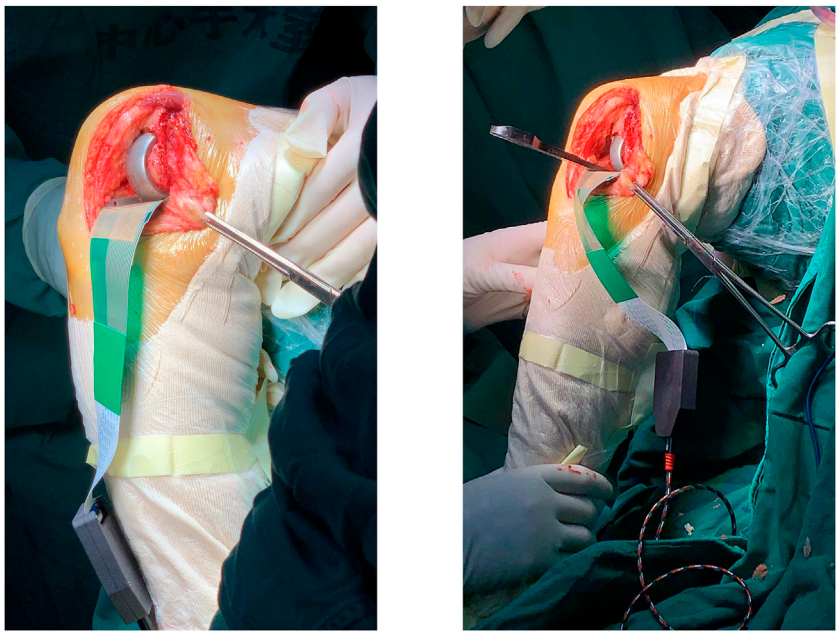

FIGURE 3
Intraoperative pressure measurement: the sensor is attached to the surface of the tibial prosthesis trial mould, while the femoral prosthesis trial mould and gap block are placed.

the component positioning holes, followed by the posterior condylar osteotomy. A mould was fitted to test the differences in flexion and extension gaps. Grinding the distal femur until the 20° extension gap was confirmed to be in balance with the 90° flexion gap. Then, a slot is made in the tibial osteotomy surface for the tibial prosthesis keel. Finally, a trial mould was fitted to confirm proper ligament tension and knee stability. At the same time, check that the knee can be fully extended to 0° without hyperextending. The sensor was fixed on the surface of the tibial prosthesis trial mold with Teflon tape (0.12 mm thickness), and a space block of appropriate size was placed. The sensor was connected to the sensor and PC, and the pressure between the prosthesis test mold and the space block was recorded at the knee joints of 120°, 90°, 60°, 45°, 20°, and 0° respectively (Figure 3). The data is acquired by self-developed multi-array pressure sensor acquisition software and recorded in a txt file for statistical analysis. The data acquisition frequency was set at 10 Hz for 5 s. For each angle a total of 50 data were obtained and the mean value was taken as the inter-prosthetic pressure.

2.4 Clinical and radiographic evaluation

Clinical evaluation: All patients were followed up for at least 6 months. The following indicators were collected before surgery and at the last follow-up: knee joint range of motion (ROM), residual fixed flexion deformity (fixed flexion degree, FFD) when the knee joint was fully extended (if there was no residual flexion deformity, is recorded as 0°), and Knee Society Score (KSS).

Radiographic evaluation: Standard frontal, lateral, and full-length weight-bearing X-ray films of the knee joint were taken before the operation and within 1 week after the operation. The measurement indicators include: preoperative posterior tibial slope (PTS_{pre}) defined as the angle between the vertical line of the tibial axis on the lateral view of the knee joint and the tibial plateau; postoperative posterior tibial slope (PTS_{post}), defined as the angle between the vertical line of the tibial axis on the postoperative lateral film and the tangent line of the tibial prosthesis; hip-knee-ankle angle (HKAA), defined as the center of the hip-knee joint on the full-length film of the lower limb he angle between the line and the knee-ankle center line (Figure 4).

2.5 Calculation method

Measure the inter-prosthesis pressure of the knee joint at 0°, 20°, 45°, 60°, 90°, and 120° of knee flexion, and record them as $F_{0°}$, $F_{20°}$, $F_{45°}$, $F_{60°}$, $F_{90°}$, $F_{120°}$. Continuous variable are presented as mean ± standard deviation. Since the Oxford unicompartmental knee arthroplasty requires the balance of the inter-prosthesis pressure between 20° and 90° of knee flexion, we calculated the average value of the inter-prosthesis pressure of 20°, 45°, 60°, and 90° of knee flexion as the mean inter-prosthesis pressure (F_{mean}). In order to reduce the influence of inter-prosthesis pressure differences on the results, the inter-prosthesis pressure at the end of knee extension is expressed as the ratio of the inter-prosthesis pressure at 0° of knee extension (the knee joint is fully extended) to the average inter-prosthesis pressure, and the formula is:

$$F_{extension} = \frac{F_{0°}}{F_{mean}} \times 100\%$$

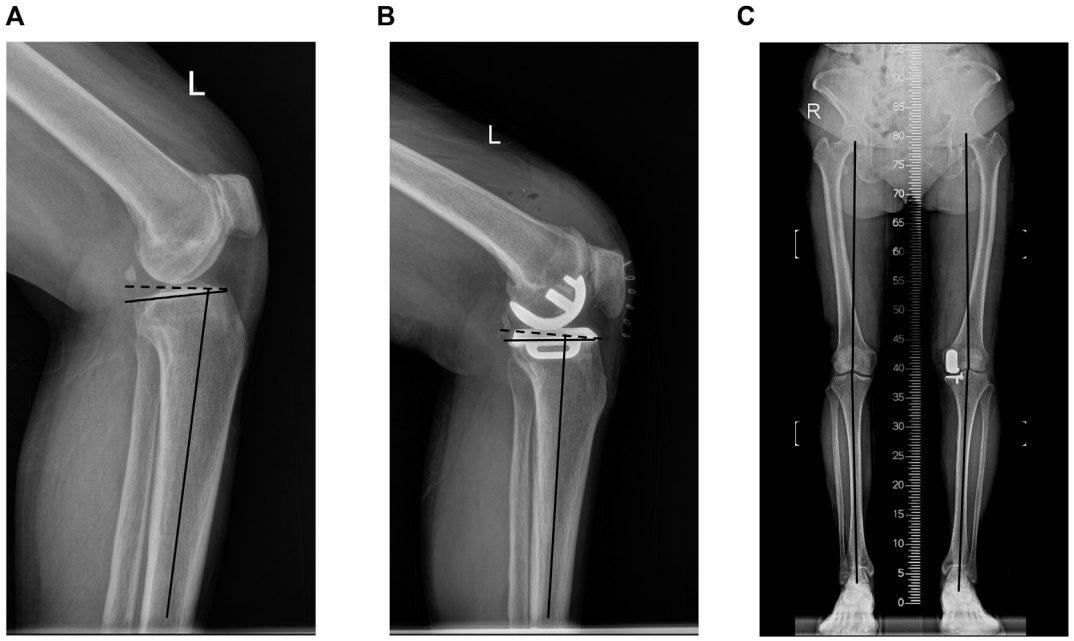

FIGURE 4
(A) Preoperative posterior tibial slope. **(B)** Postoperative posterior tibial slope. **(C)** hip–knee–ankle angle (HKAA).

Similarly, the formula for the inter-prosthesis pressure at the end of the knee flexion is:

$$F_{flexion} = \frac{F_{120°}}{F_{mean}} \times 100\%$$

The gap balance difference is defined as $F_{balance}$, and the calculation formula is:

$$F_{balance} = F_{20°} - F_{90°}$$

The calculation formula for the change of tibial retroversion before and after the operation is:

$$\Delta PTS = PTS_{post} - PTS_{pre}$$

Negative values indicate that postoperative PTS decreased compared with preoperative, while positive values indicated that postoperative PTS increased compared with preoperative.

2.6 Statistical analysis

Statistical analysis was performed using SPSS statistics25 (IBM Corp, Armonk, NY). The continuous variables were presented as means and standard deviations (SD), while the categorical variables were given as frequencies. The Pearson correlation coefficient test was used to evaluate the relationship between the inter-prosthesis pressure at various angles of the knee joint during the operation and the postoperative HKAA. At the same time, the correlation between $F_{extension}$, $F_{flexion}$, and ΔPTS, the correlation between ΔPTS and postoperative ROM, FFD, and the correlation between $F_{extension}$ and ROM were also evaluated by Pearson correlation coefficient test. Preoperative and postoperative imaging indicators (HKAA, PTS) and clinical evaluation indicators (ROM, FFD, KSS) were compared by independent sample *t*-test, and $p < 0.05$ was considered statistically significant.

3 Results

3.1 Variation trend of inter-prosthesis pressure in different knee joint angles and gap balance difference distribution

The inter-prosthesis pressures in the knee joint space during operation were: $F_{0°}$: 83.03 ± 49.94N, $F_{20°}$: 87.51 ± 44.43N, $F_{45°}$: 85.54 ± 50.86N, $F_{60°}$: 70.66 ± 47.15N, $F_{90°}$: 51.03 ± 33.67N, $F_{120°}$: 29.48 ± 26.40N. After calculation, the average inter-prosthesis pressure is: 73.68.28 ± 41.65N; after adjusting the average pressure, the relative pressure of $F_{extension}$ is 115.02% ± 64.72%, and the relative pressure of $F_{flexion}$ is 42.64% ± 27.96%. $F_{balance}$ is 36.48 ± 20.58N (Figure 5).

3.2 Correlation between inter-prosthesis pressure and lower limb alignment

Inter-prosthesis pressure at 0° was positively correlated with postoperative HKAA in the Pearson correlation coefficient test ($r = 0.448$, $p < 0.001$). There was also a positive correlation between the inter-prosthesis pressure at 20° and postoperative HKA ($r = 0.302$, $p < 0.001$), while the inter-prosthesis pressure at other angles did not correlate with postoperative HKAA (Figure 6; Table 2).

In terms of sagittal alignment, ΔPTS was positively correlated with $F_{extension}$ ($r = 0.442$, $p < 0.001$), and negatively correlated with $F_{flexion}$ ($r = -0.311$, $p < 0.001$) (Figure 7). Further analysis found that

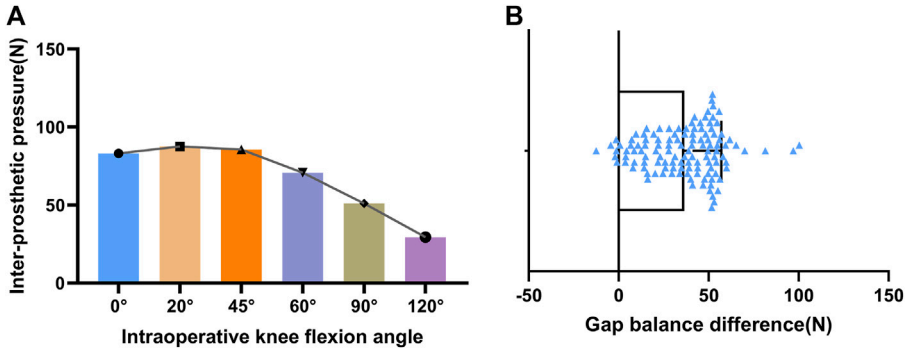

FIGURE 5
(A) variation trend of inter-prosthesis pressure in different knee joint angles. **(B)** gap balance difference distribution.

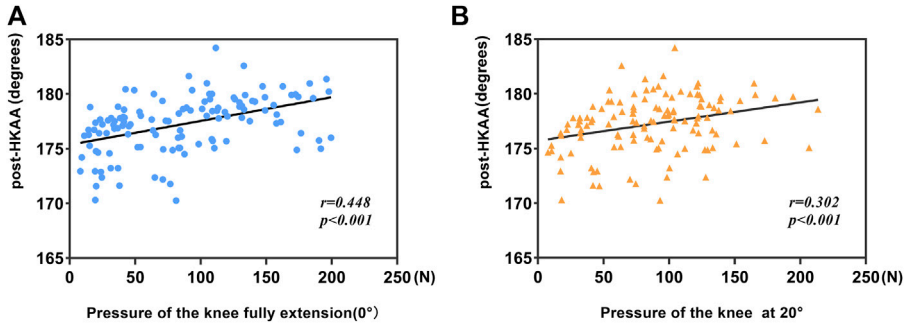

FIGURE 6
(A) Correlation between postoperative HKAA and pressure at 0°. **(B)** Correlation between postoperative HKAA and pressure at 20°.

TABLE 2 Correlation between inter-prosthetic pressure at different angles and postoperative HKAA.

Variables	Post-HKAA (postoperative hip–knee–ankle angle)	
	r	*p-value*
$F_{0°}$	0.448	< 0.001
$F_{20°}$	0.302	< 0.001
$F_{45°}$	0.092	0.316
$F_{60°}$	0.110	0.230
$F_{90°}$	0.132	0.148
$F_{120°}$	0.036	0.696

ΔPTS have no correlation with postoperative ROM (r = 0.047, $p > 0.05$).

3.3 Radiological and clinical outcomes

The UKA operation of the included patients was carried out smoothly, and no infection, bearing dislocation, or other complications occurred. Postoperative HKAA was significantly increased compared with preoperative ($p < 0.05$), PTS was not significantly different from preoperative, ROM was significantly improved compared with preoperative ($p < 0.001$), and FFD was significantly improved compared with preoperative ($p = 0.001$). Postoperative KSS clinical score and functional score were significantly improved compared with preoperative ($p < 0.001$) (Table 3).

4 Discussion

This study is the first to use sensor technology to describe the change of inter-prosthesis pressure in different knee angles in OUKA. At the same time, the difference in inter-prosthesis pressure was used to quantify the gap balance. Through the analysis of inter-prosthesis pressure and postoperative lower limb alignment index, we found that the inter-prosthesis pressure at 0° and 20° is related to postoperative HKAA, which can reflect postoperative HKAA to some degree. The change of PTS will lead to the change of the inter-prosthesis pressure between the end of knee extension and knee flexion. The excessive increase of PTS will not increase the range of motion of the knee joint after surgery but may lead to limitation of knee extension.

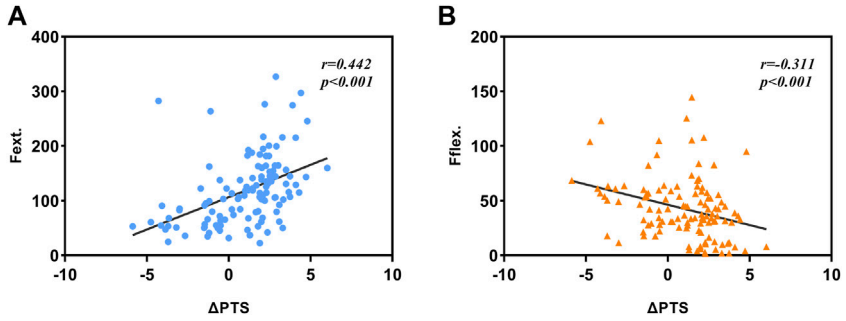

FIGURE 7
(A) Correlation between ΔPTS and $F_{extension}$. **(B)** Correlation between ΔPTS and $F_{flexion}$.

TABLE 3 Comparison of radiological and clinical outcomes.

	Preoperative	Postoperative	*p*-value
HKAA	172.32 ± 3.40	177.25 ± 2.58	<0.001
PTS	8.27 ± 3.08	8.59 ± 1.84	0.329
ROM	117.98 ± 9.08	123.97 ± 6.48	<0.001
FFD	3.18 ± 4.15	0.66 ± 1.81	<0.001
KSS clinical score	48.25 ± 7.73	88.34 ± 4.24	<0.001
functional score	47.09 ± 2.93	80.33 ± 4.44	<0.001

HKAA = hip-knee-ankle angle; PTS = posterior tibial slope; ROM = range of motion; FFD = fixed flexion deformity; KSS = knee society score.

In this study, we measured the OUKA inter-prosthesis pressure achieved by a surgeon who performed more than 2,000 OUKA operations and operated in strict accordance with the standard surgical procedures and initially formed a multi-angle inter-prosthesis pressure reference. The inter-prosthesis pressure is minimal at deep flexion of the knee joint, increases gradually as the joint is extended, reaches a peak at 20°–45°, and further decreases at full extension. This may be due to the single-radius design of the Oxford UKA prosthesis, while the radius and center of the human femoral condyle flexion-extension articular surface are not the same (Lu et al., 2021). After installation of the prosthesis, the spherical surface of the single-radius femoral prosthesis will partially exceed the original articular surface when the knee is flexed to a certain degree (probably 20°–45°), so there may induce an increase in the inter-prosthesis pressure in the middle of flexion. While the pressure at 0° is higher than 60°, it may be caused by the soft tissue around the knee joint being stretched after the knee joint is fully extended (Zhou et al., 2018).

Postoperative valgus malalignment with overcorrection (HKAA>180°) after UKA is the most common cause of increased lateral compartment load and leading to osteoarthritis progression (Murray et al., 1998; Pandit et al., 2016; Zhang et al., 2019). However, in addition to the use of navigation or robotic surgery (Innocenti and Bori, 2021; Kort et al., 2022), in traditional surgery, judging whether the force line is everted still relies solely on the surgeon's visual inspection. According to our research results, there is a positive correlation between the inter-prosthesis pressure of the knee joint at 0° and 20° and postoperative HKAA, while the pressure at other angles has no correlation. The straightened inter-prosthesis pressure directly measures the inter-prosthesis pressure in the straightened state, which can reflect the degree of correction of the force line of the lower limbs to a certain extent. However, many factors may affect the gap pressure during knee extension (Innocenti et al., 2014). For example, in the knee joint with flexion deformity before the operation, the tension of the posterior joint capsule is often high, so that the gap contact force is generally higher when the knee is extended (Malavolta and Kley, 2021). Except at 0° and 20°, the position of the knee at other angles is close to or in flexion. At this point, the tibial plateau is in contact with the posterior femoral condyle, rather than the distal femoral articular surface. The soft tissues surrounding the knee joint are also in a relatively relaxed state. Inter-prosthetic pressures in this state are therefore difficult to predict the hip-knee-ankle angle (HKAA), which is measured during knee extension.

Gap balancing is an important surgical technique step in the OUKA procedure. The purpose is to keep the soft tissue around the knee joint in proper tension during the flexion and extension process of the knee joint, so as to avoid instability during the postoperative knee joint movement. The ideal balance of the flexion-extension gap should be the same inter-prosthesis pressure in flexion-extension gap, but this process will inevitably be affected by many factors, such as the patient's position. At the same time, we found that the gap balance difference within a certain range will not affect the early clinical effect of patients after surgery (Ge et al., 2023).

PTS changes affect the biomechanics of the lower limb and the clinical outcome after UKA. The Oxford unicompartmental prosthesis

did not consider the anatomical difference of the knee joint, and the PTS was uniformly set at 7°. But in fact, the distribution of PTS individuation is very wide. By observing the CT examination results of 2031 patients with medial UKA, Nunley found that the preoperative PTS distribution ranged from −9.6° to 16.8°, which has a very wide distribution (Nunley et al., 2014), and the standard 7° retroversion may have a great change in some patients. Excessive PTS angles can gradually increase the stress of the posteromedial tibial cortex and cancellous bone, increasing the risk of prosthetic loosening, posterior tibial collapse, and even anterior cruciate ligament rupture (Aleto et al., 2008; Gulati et al., 2009; Suero et al., 2012). Most of the previous studies focused on the impact of postoperative PTS on the clinical effect of UKA, but the conclusions were not consistent. Clarius et al. found that 88% of postoperative PTS after UKA were within the recommended range, but whether it exceeded the recommended range did not seem to affect the short-term clinical outcomes of patients (Clarius et al., 2010). However, Hernigou et al. found that postoperative PTS exceeding 7° would increase the UKA revision rate (Hernigou and Deschamps, 2004). Aleto et al. found that in patients with posterior tibial plateau collapse, the average postoperative PTS was 12° ± 2°, which was significantly greater than that in the control group (Aleto et al., 2008). In terms of knee joint mobility, Inui et al. found that postoperative PTS increase was associated with high postoperative knee flexion, and the postoperative clinical effect of the high-flexion knee joint was better, especially the patient-reported effect (Inui et al., 2020). These inconsistent results may be due to investigators' excessive focus on postoperative PTS. The PTS in its natural state should be considered during the operation to avoid excessive changes that may lead to poor postoperative clinical results. This study, it found that changes in the PTS affect the extension and flexion gaps. Excessively increasing the PTS may cause the extension gap to be too tight, which is not conducive to the knee extension exercise of postoperative patients. However, the reduction of PTS will lead to a too-tight flexion gap, which is not conducive to the patient's deep knee flexion. At the same time, increasing the PTS did not increase the knee range of motion in patients.

Our study also has some limitations. This study is based on the collection of surgical data from the same orthopedic surgeon, and the establishment of standards for gap pressure and gap balance requires large samples and multi-center data collection. The collection of pressure data is carried out on the trial model, and the final tibial side prosthesis needs to be fixed with bone cement. The thickness of bone cement may affect the pressure value between the actual prosthesis, but in this study, Teflon tape and the sensor itself have a certain thickness, which can offset the effect of the bone cement to some extent.

5 Conclusion

In this study, a customized sensor was used to measure the inter-prosthesis pressure during OUKA surgery, and the results showed that the inter-prosthesis pressure was not consistent at different angles. At the same time, we further explored the relationship between pressure and lower limb alignment after OUKA and found that the inter-prosthesis pressure measured in the extended position can predict postoperative HKAA to a certain extent. Changes in PTS will affect the inter-prosthesis pressure at the end of knee flexion and knee extension, but this change is not related to the range of motion of the knee joint.

Data availability statement

The original contributions presented in the study are included in the article/Supplementary Material, further inquiries can be directed to the corresponding authors.

Ethics statement

The studies involving human participants were reviewed and approved by the institutional review board of China-Japan Friendship Hospital. The patients/participants provided their written informed consent to participate in this study.

Author contributions

JG and WG designed the study. JG, XS, and CL did the data collection and the data analysis. JG wrote the article. QZ, BW, and WG revised the article. All authors contributed to the article and approved the submitted version.

Funding

Open access funding by University of Lausanne.

Conflict of interest

The authors declare that the research was conducted in the absence of any commercial or financial relationships that could be construed as a potential conflict of interest.

Publisher's note

References

Agins, H. J., Harder, V. S., Lautenschlager, E. P., and Kudrna, J. C. (2003). Effects of sterilization on the tekscan digital pressure sensor. *Med. Eng. Phys.* 25 (9), 775–780. doi:10.1016/s1350-4533(03)00119-x

Aleto, T. J., Berend, M. E., Ritter, M. A., Faris, P. M., and Meneghini, R. M. (2008). Early failure of unicompartmental knee arthroplasty leading to revision. *J. Arthroplasty* 23 (2), 159–163. doi:10.1016/j.arth.2007.03.020

Becker, R., Mauer, C., Stärke, C., Brosz, M., Zantop, T., Lohmann, C. H., et al. (2013). Anteroposterior and rotational stability in fixed and mobile bearing unicondylar knee arthroplasty: A cadaveric study using the robotic force sensor system. *Knee Surg. Sports Traumatol. Arthrosc.* 21 (11), 2427–2432. doi:10.1007/s00167-012-2157-5

Chow, J., Law, T. Y., and Roche, M. (2018). Sensor-based soft tissue balancing in total knee arthroplasty. *Adv. Exp. Med. Biol.* 1093, 327–334. doi:10.1007/978-981-13-1396-7_25

Clarius, M., Hauck, C., Seeger, J. B., Pritsch, M., Merle, C., and Aldinger, P. R. (2010). Correlation of positioning and clinical results in Oxford uka. *Int. Orthop.* 34 (8), 1145–1151. doi:10.1007/s00264-009-0881-3

Ge, J., Liu, C., Sun, X., Zhang, Q., Ji, B., and Guo, W. (2023). Gap balance difference of unicompartmental knee arthroplasty between hanging leg and supine leg position: A prospective cohort study. *Int. Orthop.* 47 (3), 745–753. doi:10.1007/s00264-022-05680-y

Gulati, A., Chau, R., Simpson, D. J., Dodd, C. A. F., Gill, H. S., and Murray, D. W. (2009). Influence of component alignment on outcome for unicompartmental knee replacement. *Knee* 16 (3), 196–199. doi:10.1016/j.knee.2008.11.001

Hansen, E. N., Ong, K. L., Lau, E., Kurtz, S. M., and Lonner, J. H. (2019). Unicondylar knee arthroplasty has fewer complications but higher revision rates than total knee arthroplasty in a study of large United States databases. *J. Arthroplasty* 34 (8), 1617–1625. doi:10.1016/j.arth.2019.04.004

Hernigou, P., and Deschamps, G. (2004). Posterior slope of the tibial implant and the outcome of unicompartmental knee arthroplasty. *J. Bone Jt. Surg. Am.* 86 (3), 506–511. doi:10.2106/00004623-200403000-00007

Heyse, T. J., El-Zayat, B. F., De Corte, R., Scheys, L., Chevalier, Y., Fuchs-Winkelmann, S., et al. (2016). Balancing uka: Overstuffing leads to high medial collateral ligament strains. *Knee Surg. Sports Traumatol. Arthrosc.* 24 (10), 3218–3228. doi:10.1007/s00167-015-3848-5

Innocenti, B., Bilgen, Ö. F., Labey, L., van Lenthe, G. H., Sloten, J. V., and Catani, F. (2014). Load sharing and ligament strains in balanced, overstuffed and understuffed uka. A validated finite element analysis. *J. Arthroplasty* 29 (7), 1491–1498. doi:10.1016/j.arth.2014.01.020

Innocenti, B., and Bori, E. (2021). Robotics in orthopaedic surgery: Why, what and how? *Arch. Orthop. Trauma Surg.* 141 (12), 2035–2042. doi:10.1007/s00402-021-04046-0

Inoue, A., Arai, Y., Nakagawa, S., Inoue, H., Yamazoe, S., and Kubo, T. (2016). Comparison of alignment correction angles between fixed-bearing and mobile-bearing uka. *J. Arthroplasty* 31 (1), 142–145. doi:10.1016/j.arth.2015.07.024

Inui, H., Taketomi, S., Yamagami, R., Kawaguchi, K., Nakazato, K., and Tanaka, S. (2020). Necessary factors to achieve deep flexion for asian populations after Oxford unicompartmental knee arthroplasty. *J. Knee Surg.* 33 (3), 294–300. doi:10.1055/s-0039-1678539

Kamenaga, T., Hiranaka, T., Hida, Y., Nakano, N., Kuroda, Y., Tsubosaka, M., et al. (2022). Lateral osteoarthritis progression is associated with a postoperative residual tibiofemoral subluxation in Oxford uka. *Knee Surg. Sports Traumatol. Arthrosc.* 30 (9), 3236–3243. doi:10.1007/s00167-021-06729-y

Kelmers, E., Szuba, A., King, S. W., Palan, J., Freear, S., Pandit, H. G., et al. (2023). Smart knee implants: An overview of current technologies and future possibilities. *Indian J. Orthop.* 57 (5), 635–642. doi:10.1007/s43465-022-00810-5

Khow, Y. Z., Liow, M. H. L., Lee, M., Chen, J. Y., Lo, N. N., and Yeo, S. J. (2022). Posterior condylar offset and posterior tibial slope targets to optimize knee flexion after unicompartmental knee arthroplasty. *Knee Surg. Sports Traumatol. Arthrosc.* 30 (3), 822–831. doi:10.1007/s00167-021-06453-7

Koh, Y-G., Park, K-M., Kang, K., Kim, P. S., Lee, Y. H., Park, K. K., et al. (2021). Finite element analysis of the influence of the posterior tibial slope on mobile-bearing unicompartmental knee arthroplasty. *Knee* 29, 116–125. doi:10.1016/j.knee.2021.01.004

Kort, N., Stirling, P., Pilot, P., and Müller, J. H. (2022). Robot-assisted knee arthroplasty improves component positioning and alignment, but results are inconclusive on whether it improves clinical scores or reduces complications and revisions: A systematic overview of meta-analyses. *Knee Surg. Sports Traumatol. Arthrosc.* 30 (8), 2639–2653. doi:10.1007/s00167-021-06472-4

Kwon, H. M., Kang, K-T., Kim, J. H., and Park, K. K. (2020). Medial unicompartmental knee arthroplasty to patients with a ligamentous deficiency can cause biomechanically poor outcomes. *Knee Surg. Sports Traumatol. Arthrosc.* 28 (9), 2846–2853. doi:10.1007/s00167-019-05636-7

Lee, S. Y., Bae, J. H., Kim, J. G., Jang, K. M., Shon, W. Y., Kim, K. W., et al. (2014). The influence of surgical factors on dislocation of the meniscal bearing after Oxford medial unicompartmental knee replacement: A case-control study. *Bone Jt. J.* 96-B (7), 914–922. doi:10.1302/0301-620X.96B7.33352

Lu, F., Sun, X., Wang, W., Zhang, Q., and Guo, W. (2021). Anthropometry of the medial femoral condyle in the Chinese population: The morphometric analysis to design unicomparmental knee component. *BMC Musculoskelet. Disord.* 22 (1), 95. doi:10.1186/s12891-021-03979-2

Malavolta, M., and Kley, K. (2021). Kinematic alignment-management of deformities and flexion contractures. *Orthopade* 50 (3), 173–178. doi:10.1007/s00132-020-03970-0

Mentink, M. J. A., Van Duren, B. H., Murray, D. W., and Gill, H. S. (2017). A novel flexible capacitive load sensor for use in a mobile unicompartmental knee replacement bearing: An *in vitro* proof of concept study. *Med. Eng. Phys.* 46, 44–53. doi:10.1016/j.medengphy.2017.05.002

Misir, A., Uzun, E., Kizkapan, T. B., Gunay, A. E., Ozcamdalli, M., and Husrevoglu, K. (2020). Lateral and patellofemoral compartment osteoarthritis progression after medial unicompartmental knee arthroplasty: A five-to 10-year follow-up study. *Knee* 27 (4), 1135–1142. doi:10.1016/j.knee.2020.05.021

Mohammad, H. R., Strickland, L., Hamilton, T. W., and Murray, D. W. (2018). Long-term outcomes of over 8,000 medial Oxford phase 3 unicompartmental knees-a systematic review. *Acta Orthop.* 89 (1), 101–107. doi:10.1080/17453674.2017.1367577

Murray, D. W., Goodfellow, J. W., and O'Connor, J. J. (1998). The Oxford medial unicompartmental arthroplasty: A ten-year survival study. *J. Bone Jt. Surg. Br.* 80 (6), 983–989. doi:10.1302/0301-620x.80b6.0800983

Nunley, R. M., Nam, D., Johnson, S. R., and Barnes, C. L. (2014). Extreme variability in posterior slope of the proximal tibia: Measurements on 2395 Ct scans of patients undergoing uka? *J. Arthroplasty* 29 (8), 1677–1680. doi:10.1016/j.arth.2014.03.024

Pandit, H., Spiegelberg, B., Clavé, A., McGrath, C., Liddle, A. D., and Murray, D. W. (2016). Aetiology of lateral progression of arthritis following Oxford medial unicompartmental knee replacement: A case-control study. *Musculoskelet. Surg.* 100 (2), 97–102. doi:10.1007/s12306-015-0394-8

Plancher, K. D., Brite, J. E., Briggs, K. K., and Petterson, S. C. (2022). Pre-arthritic/kinematic alignment in fixed-bearing medial unicompartmental knee arthroplasty results in return to activity at mean 10-year follow-up. *J. Bone Jt. Surg. Am.* 104 (12), 1081–1089. doi:10.2106/JBJS.21.00801

Ro, K-H., Heo, J-W., and Lee, D-H. (2018). Bearing dislocation and progression of osteoarthritis after mobile-bearing unicompartmental knee arthroplasty vary between asian and western patients: A meta-analysis. *Clin. Orthop. Relat. Res.* 476 (5), 946–960. doi:10.1007/s11999.0000000000000205

Slaven, S. E., Cody, J. P., Sershon, R. A., Ho, H., Hopper, R. H., and Fricka, K. B. (2021). Alignment in medial fixed-bearing unicompartmental knee arthroplasty: The limb has a leg up on the component. *J. Arthroplasty* 36 (12), 3883–3887. doi:10.1016/j.arth.2021.08.015

Slaven, S. E., Cody, J. P., Sershon, R. A., Ho, H., Hopper, R. H., and Fricka, K. B. (2020). The impact of coronal alignment on revision in medial fixed-bearing unicompartmental knee arthroplasty. *J. Arthroplasty* 35 (2), 353–357. doi:10.1016/j.arth.2019.09.038

Suero, E. M., Citak, M., Cross, M. B., Bosscher, M. R. F., Ranawat, A. S., and Pearle, A. D. (2012). Effects of tibial slope changes in the stability of fixed bearing medial unicompartmental arthroplasty in anterior cruciate ligament deficient knees. *Knee* 19 (4), 365–369. doi:10.1016/j.knee.2011.07.004

Sun, X., Hernigou, P., Zhang, Q., Zhang, N., Wang, W., Chen, Y., et al. (2021). Sensor and machine learning-based assessment of gap balancing in cadaveric unicompartmental knee arthroplasty surgical training. *Int. Orthop.* 45 (11), 2843–2849. doi:10.1007/s00264-021-05176-1

Sun, X., Wang, Q., Ge, J., Wang, W., Guo, W., and Zhang, Q. (2022). Sensor assessment of gap balance in mobile-bearing unicompartmental knee arthroplasty. *J. Vis. Exp.*, 185. doi:10.3791/63711

Takayama, K., Matsumoto, T., Muratsu, H., Ishida, K., Araki, D., Matsushita, T., et al. (2016). The influence of posterior tibial slope changes on joint gap and range of motion in unicompartmental knee arthroplasty. *Knee* 23 (3), 517–522. doi:10.1016/j.knee.2016.01.003

van der Linde, J. A., Beath, K. J., and Leong, A. K. L. (2018). The reliability of sensor-assisted soft tissue measurements in primary total knee arthroplasty. *J. Arthroplasty* 33 (8), 2502–2505.e12. doi:10.1016/j.arth.2018.03.067

Walker, T., Hetto, P., Bruckner, T., Gotterbarm, T., Merle, C., Panzram, B., et al. (2019). Minimally invasive Oxford unicompartmental knee arthroplasty ensures excellent functional outcome and high survivorship in the long term. *Knee Surg. Sports Traumatol. Arthrosc.* 27 (5), 1658–1664. doi:10.1007/s00167-018-5299-2

Zhang, Q., Zhang, Q., Guo, W., Gao, M., Ding, R., and Wang, W. (2019). Risk factors of postoperative valgus malalignment in mobile-bearing medial unicompartmental knee arthroplasty. *Arch. Orthop. Trauma Surg.* 139 (2), 241–248. doi:10.1007/s00402-018-3070-2

Zhou, H., Trudel, G., Uhthoff, H. K., and Laneuville, O. (2018). Range of extension correlates with posterior capsule length after knee remobilization. *Med. Sci. Sports Exerc* 50 (12), 2401–2408. doi:10.1249/MSS.0000000000001741

frontiers | Frontiers in Bioengineering and Biotechnology

TYPE Original Research
PUBLISHED 01 September 2023
DOI 10.3389/fbioe.2023.1254661

OPEN ACCESS

EDITED BY
Bernardo Innocenti,
Université libre de Bruxelles, Belgium

REVIEWED BY
Francesco Travascio,
University of Miami, United States
Edoardo Bori,
Université libre de Bruxelles, Belgium

*CORRESPONDENCE
Giordano Valente,
giordano.valente@ior.it

RECEIVED 07 July 2023
ACCEPTED 22 August 2023
PUBLISHED 01 September 2023

CITATION
Valente G, Grenno G, Dal Fabbro G, Zaffagnini S and Taddei F (2023), Medial and lateral knee contact forces during walking, stair ascent and stair descent are more affected by contact locations than tibiofemoral alignment in knee osteoarthritis patients with varus malalignment.
Front. Bioeng. Biotechnol. 11:1254661.
doi: 10.3389/fbioe.2023.1254661

Medial and lateral knee contact forces during walking, stair ascent and stair descent are more affected by contact locations than tibiofemoral alignment in knee osteoarthritis patients with varus malalignment

Giordano Valente[1]*, Giulia Grenno[1], Giacomo Dal Fabbro[2], Stefano Zaffagnini[2] and Fulvia Taddei[1]

[1]Bioengineering and Computing Laboratory, IRCCS Istituto Ortopedico Rizzoli, Bologna, Italy, [2]2nd Orthopedics and Trauma Unit, IRCCS Istituto Ortopedico Rizzoli, Bologna, Italy

Introduction: Knee OA progression is related to medial knee contact forces, which can be altered by anatomical parameters of tibiofemoral alignment and contact point locations. There is limited and controversial literature on medial-lateral force distribution and the effect of anatomical parameters, especially in motor activities different from walking. We analyzed the effect of tibiofemoral alignment and contact point locations on knee contact forces, and the medial-lateral force distribution in knee OA subjects with varus malalignment during walking, stair ascending and stair descending.

Methods: Fifty-one knee OA subjects with varus malalignment underwent weight-bearing radiographs and motion capture during walking, stair ascending and stair descending. We created a set of four musculoskeletal models per subject with increasing level of personalization, and calculated medial and lateral knee contact forces. To analyze the effect of the anatomical parameters, statistically-significant differences in knee contact forces among models were evaluated. Then, to analyze the force distribution, the medial-to-total contact force ratios were calculated from the fully-informed models. In addition, a multiple regression analysis was performed to evaluate correlations between forces and anatomical parameters.

Results: The anatomical parameters significantly affected the knee contact forces. However, the contact points decreased medial forces and increased lateral forces and led to more marked variations compared to tibiofemoral alignment, which produced an opposite effect. The forces were less medially-distributed during stair negotiation, with medial-to-total ratios below 50% at force peaks. The anatomical parameters explained 30%–67% of the variability in the knee forces, where the medial contact points were the best predictors of medial contact forces.

Discussion: Including personalized locations of contact points is crucial when analyzing knee contact forces in subjects with varus malalignment, and especially the medial contact points have a major effect on the forces rather than

tibiofemoral alignment. Remarkably, the medial-lateral force distribution depends on the motor activity, where stair ascending and descending show increased lateral forces that lead to less medially-distributed loads compared to walking.

KEYWORDS

knee osteoarthritis, knee contact forces, knee contact points, musculoskeletal modeling, stair negotiation, knee force distribution

1 Introduction

The onset and progression of knee osteoarthritis (OA) and the consequent degenerative process in the articular cartilage are related, among biological and mechanical risk factors, to the knee contact forces (KCF) of the medial compartment, where the major percentage of the total contact force is transferred (Miyazaki, 2002; Andriacchi and Mündermann, 2006; Felson, 2013). In particular, recent studies showed how medial contact force (MCF) correlates with joint damage and symptom severity (Dell'Isola et al., 2017; Yamagata et al., 2021). Therefore, reducing the MCF has been the focus of several studies to slow down the progression of OA and cartilage damage by using non-invasive strategies such as gait modifications and gait retraining (Fregly et al., 2009; Richards et al., 2018), and joint preserving surgery such as high tibial osteotomy (Whatling et al., 2020; De Pieri et al., 2022).

Musculoskeletal modeling represents a state-of-the-art tool to predict KCF and their distribution in the knee, although the complexity and amount of data required limit its applications (Fregly et al., 2012; Imani Nejad et al., 2020). Therefore, the knee adduction moment has often been used as a surrogate of MCF; however, the level of correlation with MCF is still controversial (Kutzner et al., 2013; Walter et al., 2015), suggesting that the knee adduction moment is not able to explain the variability in the MCF that determines the onset and progression of knee OA, and does not provide any information about the KCF distribution.

KCFs can be altered by joint morphology and limb alignment, which hence represent risk factors for the progression of knee OA (Felson, 2013). The major anatomical parameters of the knee that influence the predictions of medial and lateral KCF include tibiofemoral alignment in the frontal plane (TFA) and contact point (CP) locations, i.e., the centers of pressure between femur and tibia (Gerus et al., 2013; Lerner et al., 2015).

In general, varus TFA was suggested to increase MCF, although the level of correlation found between MCF and TFA is variable. Measurements on patients with total knee replacement showed both marked (Halder et al., 2012) and weak significant correlation between peak MCF and TFA during single-support activities (Kutzner et al., 2017; Trepczynski et al., 2021), and no significant correlation in double-support activities (Kutzner et al., 2017). Perturbation analyses via musculoskeletal modeling showed an increase in peak MCF of 7.7% body-weight (BW)/deg in a total knee replacement patient (Lerner et al., 2015), and 6% BW/deg in both healthy and knee OA patients during walking (Saliba et al., 2017). Varus TFA resulted in significantly increased MCF from 3° upwards in healthy subjects using altered musculoskeletal models (Van Rossom et al., 2019), however a recent modeling study found no significant correlation between KCF and TFA during walking in a cohort of OA patients with a mean 6.3° ± 3.9°varus TFA (Zeighami et al., 2021).

Regarding knee CPs, recent studies showed how CP locations have a significant effect on the prediction of KCF and their distribution. Perturbation analyses showed a decrease in MCF up to 6% BW/mm by shifting the CPs medially while maintaining a constant contact width (Lerner et al., 2015), and up to 4% BW/mm decrease in MCF when increasing medial CPs (Saliba et al., 2017). In addition, significant correlation between peak MCF and CP locations was found in both knee OA and healthy subjects during walking (Zeighami et al., 2021; 2018). CPs are located at the minimum joint space width in the medial and lateral compartments of the knee, and they are typically measured via radiographs, which is the most widespread imaging technique for measuring joint space width and diagnosing OA. In particular, a recent study (Zeighami et al., 2017) calculated knee CP locations of healthy and OA subjects by using bi-planar X-ray images in squat positions, and found medially located CPs in OA subjects, especially on the lateral compartment.

In summary, most studies calculating KCFs and their distribution involve subjects with total knee replacement, there are limited and controversial data on healthy and OA subjects with limited sample sizes, and the few studies analyzing activities different from walking, such as stair ascent and descent, did not include the effect of the anatomical parameters (Meireles et al., 2019; Price et al., 2020). Therefore, it is unclear how variable are KCFs and their distribution when the personalized anatomical parameters are considered during different activities in knee OA subjects, and so is the consequent relationship between KCF distribution and the anatomical parameters.

Therefore, the aim of this study was to analyze the distribution of KCFs during three different motor activities (i.e., walking, stair ascending and stair descending) in a cohort of 51 knee OA patients with varus malalignment, and to evaluate the effects of the anatomical parameters (i.e., TFA and CPs) on the medial and lateral KCFs.

2 Methods

2.1 Patients and radiographic measurements

A total of 51 patients (42 males, 9 females, mean age 53 ± 8.6 years, mean BMI 26.5 ± 3.9 kg/m^2) with medial knee OA (graded ≤3 Kellgren-Lawrence), varus malalignment >4°, and no lateral knee OA nor patellofemoral compartment symptoms, participated in this study (Table 1). Long-leg full weight-bearing radiographs and Rosenberg 45° knee flexion radiographs were

TABLE 1 Characteristics of the 51 knee OA patients with varus malalignment (mean (std)).

Age [yrs]	Gender [F/M]	BMI [kg/m^2]	Tibiofemoral angle [deg]	Contact point locations		Tibial width [mm]	Contact point locations normalized to tibial width	
				Medial [mm]	Lateral [mm]		Medial [%]	Lateral [%]
53 (8.6)	42 M/9 F	26.5 (3.9)	7.8 (3.5)	34.2 (4.7)	11.7 (1.3)	87.9 (7.6)	39 (5)	13 (2)

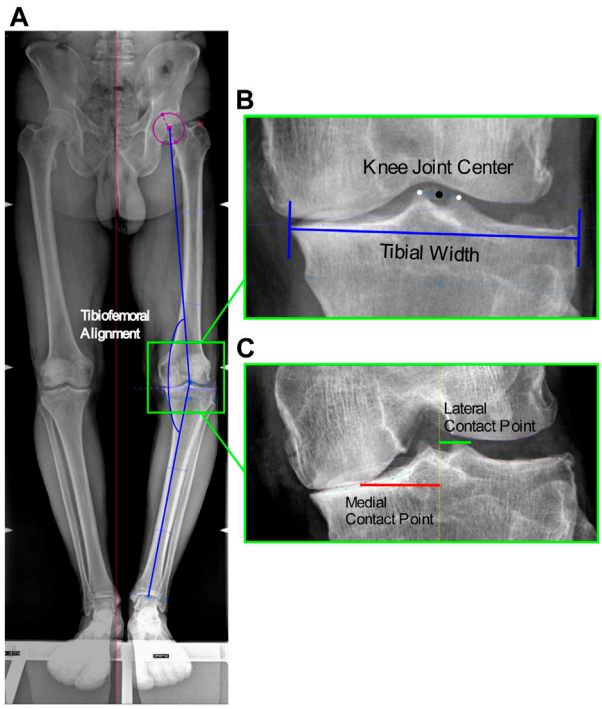

FIGURE 1
Image-based measurements of the anatomical parameters. **(A)** Tibiofemoral angle from antero-posterior RX: angle between the femoral mechanical axis connecting the hip and knee joint centers, and the tibial mechanical axis connecting the knee and ankle joint centers; **(B)** Knee joint center: midpoint of the centers of the tibial spines, and Tibial width from antero-posterior RX; **(C)** Location of the medial and lateral contact points from Rosenberg RX at the minimum joint space width calculated as the minimum Euclidian distance between the two splines defined on the femoral condyle and tibial plateau, among the interpolated point along the two splines.

acquired to measure TFA and CP locations, respectively; in addition, tibial widths were measured on the long-leg radiographs to normalize CP locations (Figure 1).

TFA was measured as the hip-knee-ankle axis, i.e., the angle between the femoral mechanical axis connecting the hip and knee joint centers, and the tibial mechanical axis connecting the knee and ankle joint centers. The hip center was defined as the center of the circle that best fitted the femoral head; the knee joint center as the midpoint of the centers of the tibial spines; and the ankle center as the mid-width of the tibia and fibula at the level of the plafond (Paley, 2002) (Figure 1). The measured mean TFA was 7.8° ± 3.5°. In addition, the mean tibial widths measured on the radiographs were 87.9 ± 7.6 mm.

Medial and lateral CP locations were identified as the points at the minimum joint space width on the medial and lateral knee compartments. The minimum joint space width was calculated as the minimum Euclidian distance between the two splines defined on the femoral condyle and tibial plateau, among the interpolated point along the two splines (Marsh et al., 2013), implemented in in-house software (Figure 1). The measured mean CP locations medial and lateral of the knee joint center were respectively 34.3 ± 4.7 mm and 11.7 ± 1.3 mm, which corresponded to 39% ± 5% and 13% ± 2% normalized to the tibial widths.

2.2 Motion capture data

Motion capture data including 3D marker trajectories, ground reaction forces and EMG activities, were acquired during walking, stair ascent and stair descent for five repetitions each. Walking was performed at self-selected speed; stair ascent and descent was performed step-over-step on a staircase with four steps, each 16 cm high, 28 cm deep and 86 cm wide, with no railings nor banisters, and with two force plates under the second and third step. The patients were first instrumented with 22 reflective markers on pelvis and lower limbs according to the established IORgait marker set and protocol (Leardini et al., 2007). Then motion capture data were simultaneously collected using an 8-camera motion capture system (100 Hz, Vicon 612 Motion System, Oxford, United Kingdom), two embedded force plates (2000 Hz, Kistler, Winterthur, Switzerland), and surface EMG (2000 Hz, Wave Wireless, COMETA, Milan, Italy) through adhesive disposable electrodes placed according to the SENIAM recommendations, from the following muscles: gluteus medius, erector spinae, rectus femoris, vastus medialis, biceps femoris, semitendinosus, medial gastrocnemius and tibialis anterior.

EMG signals were first detrended, band-pass filtered (40–200 Hz), full wave rectified and low-pass filtered at 6 Hz with a 6th order Butterworth filter to obtain envelopes (Winter, 2009). Then, to account for physiological electromechanical delay (Corcos et al., 1992), time-shifting in a range of 10–100 ms was applied to the EMG envelopes corresponding to the highest cross-correlation coefficient of two time sequences (Żuk et al., 2018).

2.3 Musculoskeletal modeling and simulations of motor activities

A freely-available and validated full-body musculoskeletal model including 18 body segments and 92 musculotendon actuators (Lerner et al., 2015) was used for this study, in

conjunction with experimental 3D marker trajectories and ground reaction forces to ultimately calculate joint reaction forces during the different motor activities, by implementing an optimization-based inverse-dynamics workflow in OpenSim (Delp et al., 2007). The musculoskeletal model includes the possibility to personalize the TFA based on the image measurements, and an augmented mechanism in the tibiofemoral joint model (i.e., additional bodies and joints) to solve for medial and lateral knee contact forces, allowing personalization of medial and lateral CP locations (Lerner et al., 2015).

To evaluate the effect of TFA and CPs, we created a set of musculoskeletal models for each patient and performed simulations with the following four conditions of personalization.

- Uninformed model (UI): This model included the baseline values of 0° TFA and CP locations of 20 mm medial and lateral of the knee joint center (Lerner et al., 2015), with no personalization of the knee anatomical parameters.
- TFA-informed model (TFAI): This model included the personalization of the TFA of both limbs for each patient, according to the radiographic measurements.
- CP-informed model (CPI): This model included the personalization of the medial and lateral CP locations of both limbs for each patient, according to the radiographic measurements.
- Fully-informed model (FI): This model included the full personalization of TFA and CP locations.

First, the models were scaled to each subject by scaling the dimensions of each body segment, mass and inertial properties, and the elements attached to the body segments, based on (i) the distances between the experimental markers from the static trial and the corresponding virtual markers on the model, and (ii) body mass. Joint angles during the motor activities were then calculated through Inverse Kinematics, by minimizing the errors between experimental and virtual markers. Then, muscle forces were calculated by decomposing the joint moments among the musculotendon actuators through Static Optimization, by minimizing the sum of muscle activations squared and accounting for the force–length–velocity relationship (Anderson and Pandy, 2001). Finally, the medial, lateral and total knee contact forces were calculated from the instantaneous force equilibrium through Joint Reaction Analysis (Steele et al., 2012). When the models predicted physiologically impossible tensile LCFs, the LCF was constrained to zero (i.e., unloaded), and a tensile force representing the collateral ligament was recruited to maintain equilibrium (Brandon et al., 2014). In addition, the muscle activations predicted by the models were used in a quantitative comparison with the corresponding processed EMG data to indirectly validate the modeling outputs of KCFs. This indirect validation is presented in the Supplementary Material S1.

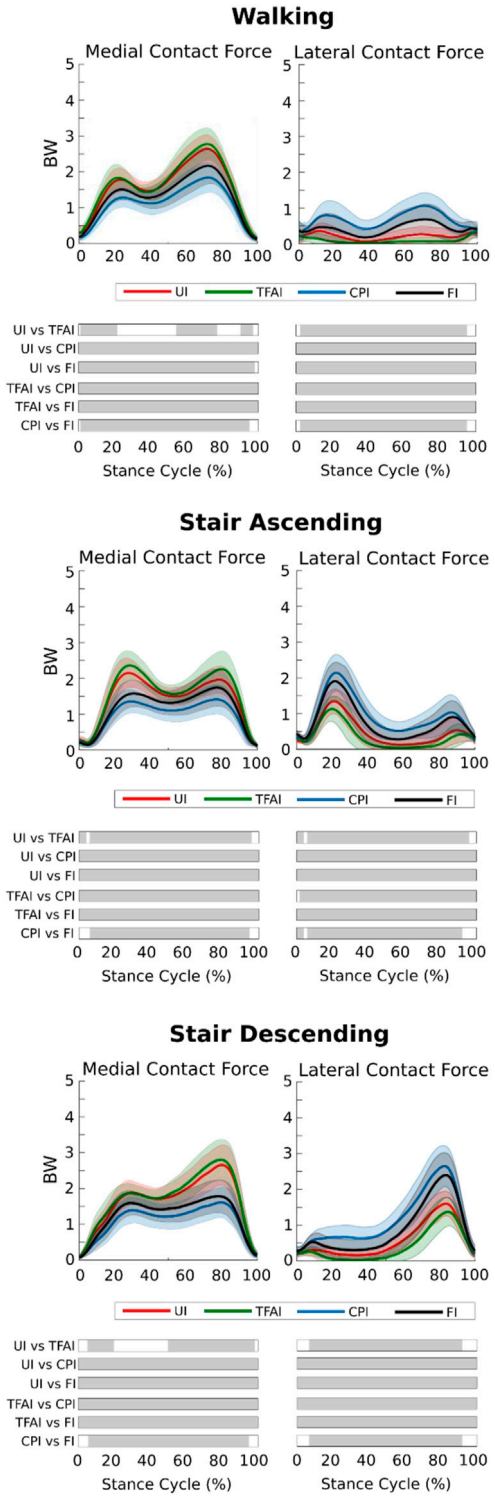

FIGURE 2
Medial and lateral knee contact forces from the four models with different levels of personalization during the three motor activities (mean ± std). Time intervals during stance with statistically significant differences (*post hoc* SPM t-tests) are reported as Gy bars below each subplot.

2.4 Data analysis

First, all KCFs were normalized to the percentage of stance phase of motor activity cycle and to each subject body-weight (BW). To evaluate the effect of TFA and CP on MCF and LCF, the forces from all models were first expressed as mean and standard deviation among the patients, and plotted. Then statistical parametric mapping (Nichols and Holmes, 2002) was used to evaluate

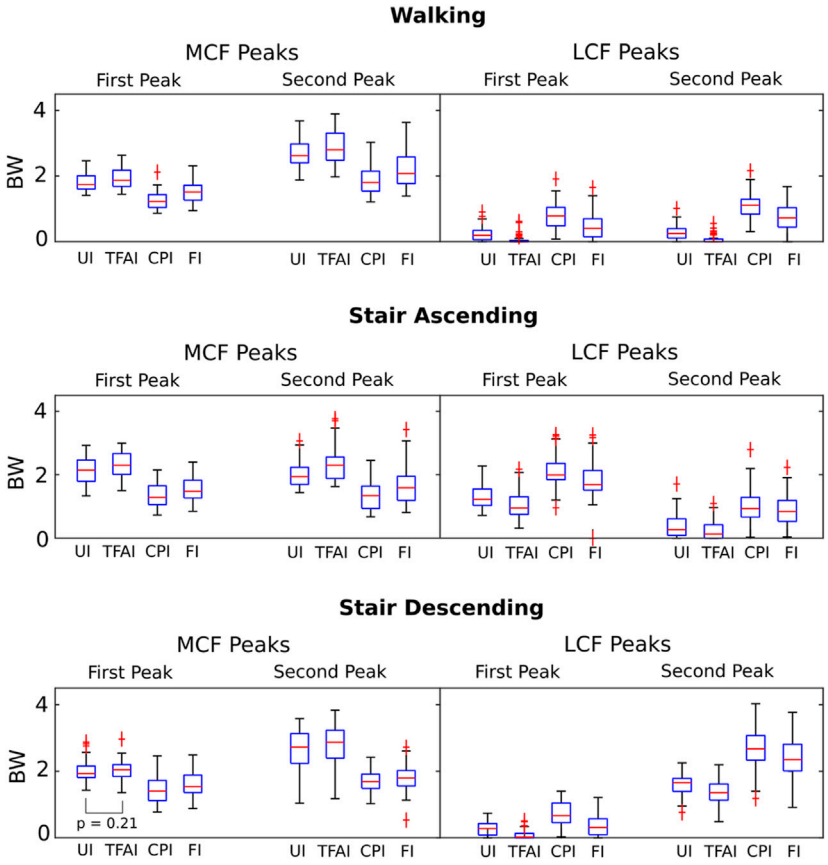

FIGURE 3
Boxplot distributions of the medial and lateral knee contact forces from the four models with different levels of personalization at the 1st and 2nd force peaks during the three different motor activities. All distributions are significantly different (Wilcoxon signed-rank tests) among the four models, except the one indicated.

statistically significant differences in KCFs among the models across the motor activity cycles. Specifically, non-parametric repeated measures ANOVA and associated *post hoc* analysis, i.e., non-parametric two-tailed paired t-tests, were conducted among the forces obtained from the four models, by using the SPM1D package (SPM, www.spm1d.org, v0.4 (Pataky et al., 2013)) implemented in MATLAB. The differences were considered clinically relevant if significant differences occurred for at least a consecutive 4% of the motor activity cycle (Wesseling et al., 2018; Valente et al., 2021).

To analyze the effect on the distribution of the KCF peaks, the two force peaks corresponding to the typical double-bump force pattern across the motor activity cycles were calculated and presented as boxplot distribution with quartiles. Then Wilcoxon signed-rank tests ($\alpha = 0.05$) were applied to evaluate statistically significant differences between each pair of models.

In addition, to analyze how KCFs were distributed during the three motor activities, the medial-to-total contact force ratios (MFRatio) were calculated from the FI model outputs across the stance phase of walking, stair ascending and stair descending, and averaged among the patients. In addition, the MFRatio at the two force peaks were calculated and presented as boxplot distribution with quartiles.

Finally, to evaluate the relationship between the anatomical parameters and KCFs, a multiple regression analysis was performed. The independent variables were TFA, normalized medial CP and normalized lateral CP, and the dependent variables were MCF, LCF and MFRatio at the two force peaks from the FI model outputs. The coefficients of determination R^2 and the coefficient estimates of each independent variable with the corresponding *p*-values were calculated in the linear regression model (i.e., $y = c_0 + c_1x_1 + c_2x_2 + c_3x_3$). Variance inflation factors were also calculated to measure multicollinearity among the independent variables in the multiple regression model.

3 Results

3.1 Effect of the anatomical parameters on KCFs

We found that TFA and CP locations significantly affected the predicted KCFs during all three motor activities. SPM non-parametric ANOVA among models showed significance for the whole stance phase of the gait cycles, and the *post hoc* comparisons of the forces between models showed significant differences in most of the stance phases in all cases (Figure 2). Focusing on the peaks of KCFs, we found that all distributions were significantly different among the four models, except from the first peak of MCF between

TABLE 2 Medial and lateral knee contact forces from the 4 models with different levels of personalization at the 1st and 2nd force peaks during the three motor activities (Median and Interquartile Range). UI: Uninformed, TFAI: Tibiofemoral-Informed, CPI: Contact-Points-Informed, FI: Fully-Informed models.

	Medial contact force				Lateral contact force			
	1st peak		2nd peak		1st peak		2nd peak	
	Median	IQR	Median	IQR	Median	IQR	Median	IQR
Walking								
UI	1.74	0.40	2.62	0.58	0.20	0.28	0.25	0.29
TFAI	1.87	0.49	2.80	0.83	0.00	0.04	0.00	0.09
CPI	1.22	0.39	1.80	0.61	0.79	0.56	1.11	0.45
FI	1.52	0.45	2.08	0.81	0.41	0.55	0.73	0.59
Stair Ascending								
UI	2.14	0.67	1.94	0.54	1.22	0.52	0.27	0.52
TFAI	2.30	0.66	2.30	0.68	0.95	0.56	0.13	0.42
CPI	1.28	0.59	1.34	0.70	1.99	0.51	0.93	0.62
FI	1.47	0.56	1.59	0.76	1.69	0.62	0.85	0.66
Stair Descending								
UI	1.93	0.35	2.72	0.89	0.28	0.34	1.66	0.39
TFAI	2.05	0.36	2.87	0.84	0.02	0.14	1.36	0.48
CPI	1.40	0.60	1.69	0.42	0.67	0.59	2.67	0.74
FI	1.54	0.53	1.79	0.46	0.31	0.48	2.35	0.80

UI and TFAI (Figure 3; Table 2). The largest force differences always occurred between TFAI and CPI model outputs, whose medians of KCF distributions reached a difference of 1.2 BW in MCF and 1.3 BW in LCF during stair descending (Figure 3; Table 2).

In general, we found that the introduction of TFA in the models led to a systematic increase in MCF and a decrease in LCF, while, on the contrary, the introduction of CPs systematically decreased MCF and increased LCF. Specifically, the introduction of CPs always led to more marked variations in KCFs compared to the introduction of TFA. Indeed, passing from UI to TFAI always led to less variations in KCFs than passing from UI to CPI, and FI model outputs were always closer to CPI than TFAI model outputs (Figures 2, 3; Table 2).

3.2 KCF medial-lateral distribution and relationship with the anatomical parameters

We found that the KCFs had different medial-lateral distributions according to the motor activity analyzed. Indeed, focusing on the FI model outputs, the mean MFRatio was over 50% (i.e., more medially distributed KCFs) for the 90% of the stance phase of walking, which decreased to the 65% of stair ascending and the 64% of stair descending (Figure 4A). Focusing on the KCF peaks, we found a median MFRatio value of 75% (IQR 22%) at the highest force peak during walking, which decreased to 47% (IQR 15%) during stair ascending, and 43% (IQR 14%) during stair descending (Figure 4B).

Regarding the relationship between anatomical parameters and KCFs, we found significant R^2, ranging from 0.3 to 0.67, at both force peaks during all motor activities in the multiple regression analysis (Table 3). Specifically, for the MCF, we found significant coefficients of the anatomical parameters for the medial CP only, except one case for the TFA, while for the LCF and MFRatio, we found significant coefficients for TFA and medial CP; the coefficients of the lateral CP were not significant except two mild cases for the MFRatio (Table 3). The Variance inflation factors were 1.52 for TFA, 1.49 for medial CP and 1.12 for lateral CP, indicating low collinear relationships among anatomical parameters.

4 Discussion

In this study, we analyzed the effect of knee anatomical parameters of TFA and CP locations on the medial and lateral knee contact forces, and how these medial and lateral forces were distributed and related to the anatomical parameters during walking, stair ascending and stair descending in a cohort of 51 knee OA patients with varus malalignment. To achieve our objective, we used musculoskeletal modeling with image-based personalization of the anatomical parameters to calculate medial and lateral knee contact forces during the three motor activities.

Overall, we found that medial and lateral knee contact forces are more affected by the location of knee CPs than TFA in knee OA patients with varus malalignment, and medial-lateral force distribution varies with the motor activity performed by the

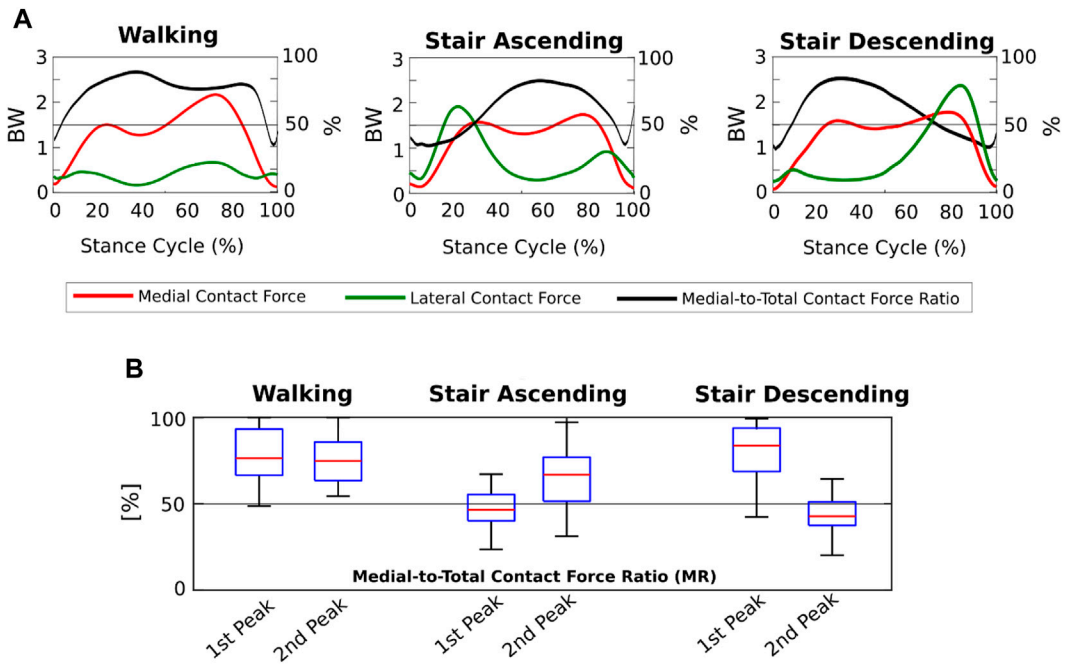

FIGURE 4
Medial-lateral distribution of the knee contact forces from the Fully-Informed model. **(A)** Medial and lateral contact forces (BW), and medial-to-total contact force ratios (MFRatio) (%) across the three motor activity cycles; **(B)** Boxplot distributions of the medial-to-total contact force ratios (MFRatio) (%) at the 1st and 2nd force peaks during the three different motor activities.

patients, where the major responsible is the location of the medial CPs, especially in more demanding motor activities.

Introducing personalized CP locations in our models led to significantly decreased loads on the medial compartment of the knee and significantly increased loads on the lateral compartment, with an effect that was always markedly larger than the opposite effect of introducing personalized TFA in all motor activities (Figures 2, 3; Table 2). Our study is the first one analyzing the effect of TFA and CP locations on KCFs in patients with varus malalignment not only during walking, i.e., also stair ascending and descending, showing a comparable effect and even more marked of what found during walking. For example, at the highest force peak of stair descending, the MCF showed a decrease of 1 BW passing from the uninformed to the contact-point-informed model and an increase of only 0.1 BW passing from the uninformed to the tibiofemoral-alignment-informed model, while the fully-informed model showed a 0.9 BW decrease from the uninformed model (Figure 3; Table 2). Consequently, including personalized locations of CPs is crucial in the analysis of KCFs of patients with varus malalignment. Previous sensitivity studies that used the same baseline model have shown the same trend on the medial compartment of decreased loading when the medial CPs are more medially located and increased loading when the varus TFA increases (Lerner et al., 2015; Saliba et al., 2017). We found good agreement on the effect of CPs from our knee OA cohort with the reported MCF sensitivity of −0.04 BW/mm to medial CPs and 0.008 BW/mm to lateral CPs, but less agreement on the effect of TFA with the reported MCF sensitivity to TFA of 0.06 BW/deg during walking (Saliba et al., 2017), as we found less force variation related to TFA (i.e. 0.02 BW/deg). However (Saliba et al., 2017), performed a sensitivity analysis including a majority of healthy subjects (14 healthy and 9 knee OA subjects), while our study included a larger cohort of 51 knee OA patients with varus malalignment with smaller TFA dynamics, which could explain this difference.

The medial-lateral distribution of the KCFs passed from markedly medial during walking to slightly medial during stair ascending and descending, where the forces were even more laterally distributed at the force peaks. We found that while during walking the 90% of the gait cycle showed KCFs more medially distributed, during stair ascending and descending a markedly different trend occurred (Figure 4). Indeed, on average the LCFs were larger than the MCFs around the force peaks, i.e., MFRatio below 50%, leading to an overall less medially distributed load across the cycles of stair ascending and descending (Figure 4). Previous research on medial-lateral KCF distribution in OA subjects via musculoskeletal modeling showed mean MFRatio ranging from 63% to 87% on the force peak during walking (Kumar et al., 2013; Sritharan et al., 2017; Van Rossom et al., 2018; Zeighami et al., 2021), which is in agreement with our findings (i.e., MFRatio of 75%). In addition, we found agreement on the different medial-lateral KCF distribution during stair ascending with a previous study showing MFRatio slightly below 50% especially on the force peak in 10 symptomatic OA subjects (Price et al., 2020). Conversely, our findings differed from those of the other study analyzing stair negotiation (Meireles et al., 2019), where the authors found MCFs larger than LCFs on the force peak of stair ascending and descending. However, only 5 patients (with bilateral OA) were included, and without personalization of TFA and CP locations in the models, which could have markedly affected how medial-lateral forces were distributed, especially during stair negotiation activities.

TABLE 3 Multiple regression analysis ($y = c_0 + c_1x_1 + c_2x_2 + c_3x_3$) including the anatomical parameters as independent variables (X) and the knee forces as dependent variables (y) at the 1st and 2nd force peaks during the three different motor activities. Y-intercepts and regression coefficients for each anatomical parameter with the corresponding *p*-values, and R^2 with the corresponding *p*-values are reported in the table. Statistically-significant values are highlighted in bold. TFA: Tibiofemoral Angle, nCP med: Normalized Medial Contact Point, nCP lat: Normalized Lateral Contact Point.

Walking												
	Medial contact force				Lateral contact force				Medial-to-total ratio			
	First peak		Second peak		First peak		Second peak		First peak		Second peak	
	Coeff	*p*	Coeff	*p*	Coeff	*p*	Coeff	*p*	Coeff	*p*	Coeff	*p*
Intercept	2.500	**0.000**	4.054	**0.000**	−0.043	**0.000**	0.708	**0.000**	1.091	**0.000**	0.848	**0.000**
TFA	0.016	0.170	0.034	0.087	−0.040	**0.031**	−0.069	**0.000**	0.017	**0.009**	0.022	**0.000**
nCPmed	−3.769	**0.000**	−6.310	**0.000**	2.760	**0.014**	3.228	**0.002**	−1.499	**0.000**	−1.232	**0.000**
nCPLat	2.920	0.180	2.707	0.461	−2.157	0.525	−5.384	0.081	1.156	0.335	1.694	0.048
R^2	0.55	**0.000**	0.57	**0.000**	0.35	**0.000**	0.57	**0.000**	0.51	**0.000**	0.67	**0.000**
Stair Ascending												
	Medial Contact Force				Lateral Contact Force				Medial-to-Total Ratio			
	First Peak		Second Peak		First Peak		Second Peak		First Peak		Second Peak	
	Coeff	*p*	Coeff	*p*	Coeff	*p*	Coeff	*p*	Coeff	*p*	Coeff	*p*
Intercept	2.535	**0.000**	2.404	**0.000**	2.736	**0.000**	1.168	**0.000**	0.560	**0.000**	0.722	**0.000**
TFA	−0.001	0.956	0.078	**0.001**	−0.063	**0.029**	−0.076	**0.002**	0.009	**0.026**	0.028	**0.000**
nCPmed	−4.072	**0.000**	−4.187	**0.002**	3.211	0.062	2.064	0.146	−1.051	**0.000**	−1.053	**0.010**
nCPLat	4.109	0.174	2.480	0.546	−11.905	0.300	−3.966	0.374	1.757	**0.020**	1.087	0.381
R^2	0.37	**0.000**	0.55	**0.000**	0.30	**0.002**	0.37	**0.000**	0.54	**0.000**	0.56	**0.000**
Stair Descending												
	Medial Contact Force				Lateral Contact Force				Medial-to-Total Ratio			
	First Peak		Second Peak		First Peak		Second Peak		First Peak		Second Peak	
	Coeff	*p*	Coeff	*p*	Coeff	*p*	Coeff	*p*	Coeff	*p*	Coeff	*p*
Intercept	2.781	**0.000**	3.055	**0.000**	−0.283	**0.000**	2.884	**0.000**	1.227	**0.000**	0.566	**0.000**
TFA	0.018	0.239	−0.014	0.503	−0.016	0.298	−0.080	**0.011**	0.006	0.351	0.008	**0.031**
nCPmed	−4.773	**0.000**	−4.773	**0.000**	3.676	**0.000**	3.952	**0.027**	−1.867	**0.000**	−1.098	**0.000**
nCPLat	4.255	0.147	5.221	0.203	−4.060	0.162	−10.172	0.082	1.667	0.195	1.788	**0.010**
R^2	0.56	**0.000**	0.30	**0.002**	0.44	**0.000**	0.38	**0.000**	0.49	**0.000**	0.61	**0.000**

We found that the anatomical parameters explain approximately the 30%–67% of the variability in the knee forces analyzed, as suggested by the R^2 found in the multiple regression analysis (Table 3). The location of the medial CPs was the anatomical parameter that best predicted medial contact forces, showing significant coefficients at both force peaks during all motor activities. TFA and medial CPs have a comparable effect on lateral contact forces and medial-to-total force ratio, while lateral CPs have a negligible effect on all knee forces (Table 3). In agreement with our findings, a recent study on a smaller cohort of OA subjects during walking showed that the medial CP locations have larger effect than TFA on KCFs, although they found no significant correlation between TFA and KCFs, likely due to the lower TFA variability of their smaller cohort (Zeighami et al., 2021).

The locations of knee CPs that we identified in our patients via radiographic measurements (Table 1) were in good agreement with those found in recent research using biplanar radiographic images in different squat positions and including 9 OA patients (Zeighami et al., 2017). Indeed, the authors found medial and lateral CPs of 36% and 12% normalized to the tibial width medial and lateral of the knee

center at 45° knee flexion squat, very close to 39% and 13% of our subjects from the Rosenberg 45° knee flexion position. In fact, although our absolute CP locations were larger than those from the previous study, we found bigger tibial widths in our cohort, likely due to the large majority of males compared to the large majority of females included in (Zeighami et al., 2017).

Our predictions of medial and lateral contact forces have some limitations. First, our knee models did not include CP locations varying with the knee flexion angle. Although a recent study found that CP trajectory can lead to a few significant differences in MCF peaks in healthy subjects (Zeighami et al., 2018), the same authors found no significant differences in medial CPs among different squat positions in OA subjects and a significant difference in lateral CPs between 70° and 0° knee flexion, confirming a good identification of our CPs included in the models. In addition, we identified CPs on 2D radiographic measurements, which were not validated against more accurate 3D measurements, although the above-discussed comparison with CP locations from more accurate measurements (Zeighami et al., 2017) showed very close values.

In conclusion, in this study we found that in knee OA subjects with varus malalignment, the location of knee contact points, especially on the medial compartment, has a major effect on medial and lateral knee contact forces rather than tibiofemoral alignment, and the medial-lateral force distribution depends on the motor activity, where stair ascending and descending show increased lateral forces that lead to less medially-distributed loads compared to walking. Further analyses including the relationship with kinematics and kinetics parameters will help explain this mechanism. We found that including personalized locations of CPs is crucial in the analysis of knee forces in patients with varus malalignment, and evaluating the accuracy of image-based identification of CP locations will consequently help improving the accuracy of force predictions.

Data availability statement

The raw data supporting the conclusion of this article will be made available by the authors, without undue reservation.

Ethics statement

The studies involving humans were approved by Ethics Committee Area Vasta Emilia Centro (CE-AVEC). The studies were conducted in accordance with the local legislation and institutional requirements. The participants provided their written informed consent to participate in this study.

Author contributions

GV: Conceptualization, Data curation, Formal Analysis, Investigation, Methodology, Supervision, Visualization, Writing–original draft, Writing–review and editing. GG: Data curation, Methodology, Software, Writing–review and editing. GD: Data curation, Project administration, Writing–review and editing. SZ: Data curation, Funding acquisition, Project administration, Resources, Writing–review and editing. FT: Conceptualization, Funding acquisition, Project administration, Supervision, Writing–review and editing.

Funding

This study was funded by the Italian Ministry of Health with the project code RF-2018-12368274.

Conflict of interest

The authors declare that the research was conducted in the absence of any commercial or financial relationships that could be construed as a potential conflict of interest.

Publisher's note

Supplementary material

The Supplementary Material for this article can be found online at: https://www.frontiersin.org/articles/10.3389/fbioe.2023.1254661/full#supplementary-material

References

Anderson, F. C., and Pandy, M. G. (2001). Static and dynamic optimization solutions for gait are practically equivalent. *J. Biomech.* 34, 153–161. doi:10.1016/s0021-9290(00)00155-x

Andriacchi, T. P., and Mündermann, A. (2006). The role of ambulatory mechanics in the initiation and progression of knee osteoarthritis. *Curr. Opin. Rheumatol.* 18, 514–518. doi:10.1097/01.bor.0000240365.16842.4e

Brandon, S. C. E., Miller, R. H., Thelen, D. G., and DeLuzio, K. J. (2014). Selective lateral muscle activation in moderate medial knee osteoarthritis subjects does not unload medial knee condyle. *J. Biomech.* 47, 1409–1415.

Corcos, D. M., Gottlieb, G. L., Latash, M. L., Almeida, G. L., and Agarwal, G. C. (1992). Electromechanical delay: an experimental artifact. *J. Electromyogr. Kinesiol.* 2, 59–68. doi:10.1016/1050-6411(92)90017-D

De Pieri, E., Nüesch, C., Pagenstert, G., Viehweger, E., Egloff, C., and Mündermann, A. (2022). High tibial osteotomy effectively redistributes compressive knee loads during walking. *J. Orthop. Res. Jor.* 41, 591–600. doi:10.1002/jor.25403

Dell'Isola, A., Smith, S. L., Andersen, M. S., and Steultjens, M. (2017). Knee internal contact force in a varus malaligned phenotype in knee osteoarthritis (KOA). *Osteoarthr. Cartil.* 25, 2007–2013. doi:10.1016/j.joca.2017.08.010

Delp, S. L., Anderson, F. C., Arnold, A. S., Loan, P., Habib, A., John, C. T., et al. (2007). OpenSim: open-source software to create and analyze dynamic simulations of movement. *IEEE Trans. Biomed. Eng.* 54, 1940–1950. doi:10.1109/TBME.2007.901024

Felson, D. T. (2013). Osteoarthritis as a disease of mechanics. *Osteoarthr. Cartil.* 21, 10–15. doi:10.1016/j.joca.2012.09.012

Fregly, B. J., Besier, T. F., Lloyd, D. G., Delp, S. L., Banks, S. A., Pandy, M. G., et al. (2012). Grand challenge competition to predict *in vivo* knee loads: grand challenge competition. *J. Orthop. Res.* 30, 503–513. doi:10.1002/jor.22023

Fregly, B. J., D'Lima, D. D., and Colwell, C. W. (2009). Effective gait patterns for offloading the medial compartment of the knee. *J. Orthop. Res.* 27, 1016–1021. doi:10.1002/jor.20843

Gerus, P., Sartori, M., Besier, T. F., Fregly, B. J., Delp, S. L., Banks, S. A., et al. (2013). Subject-specific knee joint geometry improves predictions of medial tibiofemoral contact forces. *J. Biomech.* 46, 2778–2786. doi:10.1016/j.jbiomech.2013.09.005

Halder, A., Kutzner, I., Graichen, F., Heinlein, B., Beier, A., and Bergmann, G. (2012). Influence of limb alignment on mediolateral loading in total knee replacement: *in vivo* measurements in five patients. *J. Bone Jt. Surg.* 94, 1023–1029. doi:10.2106/JBJS.K.00927

Imani Nejad, Z., Khalili, K., Hosseini Nasab, S. H., Schütz, P., Damm, P., Trepczynski, A., et al. (2020). The capacity of generic musculoskeletal simulations to predict knee joint loading using the CAMS-knee datasets. *Ann. Biomed. Eng.* 48, 1430–1440. doi:10.1007/s10439-020-02465-5

Kumar, D., Manal, K. T., and Rudolph, K. S. (2013). Knee joint loading during gait in healthy controls and individuals with knee osteoarthritis. *Osteoarthr. Cartil.* 21, 298–305. doi:10.1016/j.joca.2012.11.008

Kutzner, I., Bender, A., Dymke, J., Duda, G., von Roth, P., and Bergmann, G. (2017). Mediolateral force distribution at the knee joint shifts across activities and is driven by tibiofemoral alignment. *Bone Jt. J.* 99-B, 779–787. doi:10.1302/0301-620X.99B6.BJJ-2016-0713.R1

Kutzner, I., Trepczynski, A., Heller, M. O., and Bergmann, G. (2013). Knee adduction moment and medial contact force – facts about their correlation during gait. *PLoS ONE* 8, e81036. doi:10.1371/journal.pone.0081036

Leardini, A., Sawacha, Z., Paolini, G., Ingrosso, S., Nativo, R., and Benedetti, M. G. (2007). A new anatomically based protocol for gait analysis in children. *Gait Posture* 26, 560–571. doi:10.1016/j.gaitpost.2006.12.018

Lerner, Z. F., DeMers, M. S., Delp, S. L., and Browning, R. C. (2015). How tibiofemoral alignment and contact locations affect predictions of medial and lateral tibiofemoral contact forces. *J. Biomech.* 48, 644–650. doi:10.1016/j.jbiomech.2014.12.049

Marsh, M., Souza, R. B., Wyman, B. T., Hellio Le Graverand, M.-P., Subburaj, K., Link, T. M., et al. (2013). Differences between X-ray and MRI-determined knee cartilage thickness in weight-bearing and non-weight-bearing conditions. *Osteoarthr. Cartil.* 21, 1876–1885. doi:10.1016/j.joca.2013.09.006

Meireles, S., Reeves, N. D., Jones, R. K., Smith, C. R., Thelen, D. G., and Jonkers, I. (2019). Patients with medial knee osteoarthritis reduce medial knee contact forces by altering trunk kinematics, progression speed, and stepping strategy during stair ascent and descent: A pilot study. *J. Appl. Biomech.* 35, 280–289. doi:10.1123/jab.2017-0159

Miyazaki, T. (2002). Dynamic load at baseline can predict radiographic disease progression in medial compartment knee osteoarthritis. *Ann. Rheum. Dis.* 61, 617–622. doi:10.1136/ard.61.7.617

Nichols, T. E., and Holmes, A. P. (2002). Nonparametric permutation tests for functional neuroimaging: A primer with examples. *Hum. Brain Mapp.* 15, 1–25. doi:10.1002/hbm.1058

Paley, D. (2002). *Principles of deformity correction*. Berlin, Heidelberg: Springer. doi:10.1007/978-3-642-59373-4

Pataky, T. C., Robinson, M. A., and Vanrenterghem, J. (2013). Vector field statistical analysis of kinematic and force trajectories. *J. Biomech.* 46, 2394–2401. doi:10.1016/j.jbiomech.2013.07.031

Price, P. D. B., Gissane, C., and Cleather, D. J. (2020). The influence of pain on tibiofemoral joint contact force and muscle forces in knee osteoarthritis patients during stair ascent. *Eng. Rep.* 2, e12227. doi:10.1002/eng2.12227

Richards, R. E., Andersen, M. S., Harlaar, J., and van den Noort, J. C. (2018). Relationship between knee joint contact forces and external knee joint moments in patients with medial knee osteoarthritis: effects of gait modifications. *Osteoarthr. Cartil.* 26, 1203–1214. doi:10.1016/j.joca.2018.04.011

Saliba, C. M., Brandon, S. C. E., and Deluzio, K. J. (2017). Sensitivity of medial and lateral knee contact force predictions to frontal plane alignment and contact locations. *J. Biomech.* 57, 125–130. doi:10.1016/j.jbiomech.2017.03.005

Sritharan, P., Lin, Y.-C., Richardson, S. E., Crossley, K. M., Birmingham, T. B., and Pandy, M. G. (2017). Musculoskeletal loading in the symptomatic and asymptomatic knees of middle-aged osteoarthritis patients: force contributions in osteoarthritic knees. *J. Orthop. Res.* 35, 321–330. doi:10.1002/jor.23264

Steele, K. M., DeMers, M. S., Schwartz, M. H., and Delp, S. L. (2012). Compressive tibiofemoral force during crouch gait. *Gait Posture* 35, 556–560. doi:10.1016/j.gaitpost.2011.11.023

Trepczynski, A., Moewis, P., Damm, P., Schütz, P., Dymke, J., Hommel, H., et al. (2021). Dynamic knee joint line orientation is not predictive of tibio-femoral load distribution during walking. *Front. Bioeng. Biotechnol.* 9, 754715. doi:10.3389/fbioe.2021.754715

Valente, G., Taddei, F., Leardini, A., and Benedetti, M. G. (2021). Effects of hip abductor strengthening on musculoskeletal loading in hip dysplasia patients after total hip replacement. *Appl. Sci.* 11, 2123. doi:10.3390/app11052123

Van Rossom, S., Khatib, N., Holt, C., Van Assche, D., and Jonkers, I. (2018). Subjects with medial and lateral tibiofemoral articular cartilage defects do not alter compartmental loading during walking. *Clin. Biomech.* 60, 149–156. doi:10.1016/j.clinbiomech.2018.10.015

Van Rossom, S., Wesseling, M., Smith, C. R., Thelen, D. G., Vanwanseele, B., Dieter, V. A., et al. (2019). The influence of knee joint geometry and alignment on the tibiofemoral load distribution: A computational study. *Knee* 26, 813–823. doi:10.1016/j.knee.2019.06.002

Walter, J. P., Korkmaz, N., Fregly, B. J., and Pandy, M. G. (2015). Contribution of tibiofemoral joint contact to net loads at the knee in gait: contribution of tibiofemoral joint contact. *J. Orthop. Res.* 33, 1054–1060. doi:10.1002/jor.22845

Wesseling, M., Meyer, C., Corten, K., Desloovere, K., and Jonkers, I. (2018). Longitudinal joint loading in patients before and up to one year after unilateral total hip arthroplasty. *Gait Posture* 61, 117–124. doi:10.1016/j.gaitpost.2018.01.002

Whatling, G. M., Biggs, P. R., Elson, D. W., Metcalfe, A., Wilson, C., and Holt, C. (2020). High tibial osteotomy results in improved frontal plane knee moments, gait patterns and patient-reported outcomes. *Knee Surg. Sports Traumatol. Arthrosc.* 28, 2872–2882. doi:10.1007/s00167-019-05644-7

Winter, D. A. (2009). *Biomechanics and motor control of human movement*. 4th ed. Hoboken, N.J: Wiley.

Yamagata, M., Taniguchi, M., Tateuchi, H., Kobayashi, M., and Ichihashi, N. (2021). The effects of knee pain on knee contact force and external knee adduction moment in patients with knee osteoarthritis. *J. Biomech.* 123, 110538. doi:10.1016/j.jbiomech.2021.110538

Zeighami, A., Aissaoui, R., and Dumas, R. (2018). Knee medial and lateral contact forces in a musculoskeletal model with subject-specific contact point trajectories. *J. Biomech.* 69, 138–145. doi:10.1016/j.jbiomech.2018.01.021

Zeighami, A., Dumas, R., and Aissaoui, R. (2021). Knee loading in OA subjects is correlated to flexion and adduction moments and to contact point locations. *Sci. Rep.* 11, 8594. doi:10.1038/s41598-021-87978-2

Zeighami, A., Dumas, R., Kanhonou, M., Hagemeister, N., Lavoie, F., de Guise, J. A., et al. (2017). Tibio-femoral joint contact in healthy and osteoarthritic knees during quasi-static squat: A bi-planar X-ray analysis. *J. Biomech.* 53, 178–184. doi:10.1016/j.jbiomech.2017.01.015

Żuk, M., Syczewska, M., and Pezowicz, C. (2018). Use of the surface electromyography for a quantitative trend validation of estimated muscle forces. *Biocybern. Biomed. Eng.* 38, 243–250. doi:10.1016/j.bbe.2018.02.001

frontiers | Frontiers in Bioengineering and Biotechnology

TYPE Original Research
PUBLISHED 07 December 2023
DOI 10.3389/fbioe.2023.1286993

OPEN ACCESS

EDITED BY
João Manuel R. S. Tavares,
University of Porto, Portugal

REVIEWED BY
Francesco Travascio,
University of Miami, United States
Lei Zhang,
Southwest Medical University, China

*CORRESPONDENCE
Wen Zhang,
wenzhang@suda.edu.cn
Wei Xu,
13962157016@139.com
Liubing Li,
lbli@suda.edu.cn

†These authors have contributed equally to this work and share first authorship

RECEIVED 01 September 2023
ACCEPTED 27 November 2023
PUBLISHED 07 December 2023

CITATION
Hu Z, Ren W, Peng J, Gu Z, Wu C, Wu W, Zhang W, Xu W and Li L (2023), Biomechanics and finite element analysis comparing posterior T-plates with LCP for fixation of posterolateral tibial plate fractures.
Front. Bioeng. Biotechnol. 11:1286993.
doi: 10.3389/fbioe.2023.1286993

Biomechanics and finite element analysis comparing posterior T-plates with LCP for fixation of posterolateral tibial plate fractures

Zhenghui Hu[1†], Weizhi Ren[1†], Jian Peng[1], Zenghui Gu[1], Chenying Wu[1], Weicheng Wu[1], Wen Zhang[2*], Wei Xu[1*] and Liubing Li[1*]

[1]Department of Orthopedics, The Second Affiliated Hospital of Soochow University, Suzhou, China, [2]Orthopedic Institute of Soochow University, Suzhou, China

Objective: The treatment for posterolateral tibial plateau fractures (PTPF) have been subjects of controversy. We conducted a study to improve the fixation of PTPF through a lateral approach.

Methods: We utilized 40 synthetic tibias and categorized the fracture models into five groups based on the locking compression plate (LCP) and T-distal radius plate (TPP) via various forms of fixation with screws through the posterolateral (PL) fracture fragments. I: Two-screw fixation using two locking screws (LPTL). II: Two-screw fixation with both variable angle locking screws (LPTV). III: One-screw fixation with one locking screw (LPOL). IV: One-screw fixation with one locking screw and two anteroposterior lag screws (LPOLTL). V: a distal radius plate with three locking screws (TPP). Biomechanical tests were conducted to observe the axial compression displacement of the PL fracture fragments at force levels of 250 N, 500 N, and 750 N, as well as to determine the failure load and the axial stiffness for each respective group.

Results: Under a 750 N load condition, the displacements within the five experimental groups exhibited the following trend: V < II < I< IV < III. However, there were no significant differences between Group V and Group II, Group I and Group IV ($p > 0.05$), and only Group III demonstrated a displacement exceeding 3 mm. The failure load and the axial stiffness exhibited the same trend. Conversely, statistical significance was identified among the remaining group compared with Group III ($p < 0.05$). Regarding the finite element analysis, the maximum displacements for the five models under the load of 750 N exhibited the following trend: V < II < I< IV < III. The following trends were observed in maximum von Mises stresses for these models under the load of 750 N: V < II < IV< I < III.

Conclusion: It is crucial to address the inadequate mechanical strength associated with single screw fixation of LCP for fixing PL fractures in a clinical setting. The biomechanical strength of two-screw fixation surpasses that of single-screw fixation. Introducing variable-angle screws can further enhance the fixation range. Furthermore, the addition of two lag screws threaded from anterior to posterior can compensate the mechanical stability, when PL fracture is fixed with single screw in clinic.

KEYWORDS

posterolateral tibial plateau fracture, biomechanical research, retention strength, finite element analysis, lateral approach

1 Introduction

The tibial plateau confers essential stability to the knee joint while also functioning as a pivotal weight-bearing interface (Schatzker and Kfuri, 2022). Given the widespread adoption of computed tomography (CT), posterolateral tibial plateau fractures (PTPF), either in isolation or concomitant with other columnar fractures, have emerged as more prevalent than previously documented in the literature (Shen et al., 2019; Chen et al., 2020; Cai et al., 2021). It is worth noting that articular surfaces >2 mm and inversion deformities >4° contribute to an elevated risk of osteoarthritis (Honkonen, 1994; Rademakers et al., 2007; Parkkinen et al., 2014; Shen et al., 2019). Hence, it is imperative to underscore the significance of proper treatment of PTPF.

PTPF constitute 8%–15% of all plateau fractures, resulting from a combination of valgus and axial stresses during knee flexion (Higgins et al., 2009). The unique injury mechanism often leads to predominantly posterior and lateral displacement in terms of fracture displacement trends (Zhang et al., 2020). As a result, surgical access has primarily been explored through lateral or posterior approaches. Although the posterior approach and implant fixation offers biomechanical benefits, it comes with a heightened risk of iatrogenic injury and limited exposure of the fracture site (Kim et al., 2018; Cai et al., 2021; Durigan et al., 2023). On the other hand, the lateral approach stands as one of the most prevalent surgical options embraced by a majority of surgeons, given its lower risk of vascular and nerve injuries (Cho et al., 2017; Sun et al., 2018; Hu et al., 2020).

Given these considerations, the question arises: Can the lateral approach be a viable option for achieving satisfactory fixation strength in cases of PTPF?

It was established that the biomechanical strength conferred by a solitary screw for posterolateral (PL) fracture fragment fixation with locking compression plate (LCP) does not align with the physiological demands of the human body (Zhang et al., 2012). Building upon previous work (Hu et al., 2020; Zhang et al., 2020) in biomechanical assessment of LCP-immobilized PL fractures, our study delved into the disparities in mechanical strength stemming from differences in the number of screws fixation in LCP transverse-arm to stabilize the PL fracture fragment through the lateral approach.

2 Materials and methods

The current fracture model was established upon the work of Sohn et al. (Sohn et al., 2015). Our synthetic bone model (Synbone, type 1110. SYNBONE AG, Kulai, Johor, Malaysia) was composed of rigid foam, infused with cancellous bone material to replicate the properties of a normal tibia. The procurement was carried out from a manufacturer that ensured uniformity in terms of material composition, structure, and attributes. Following the axial compression of the PL fracture fragment using a custom-designed T-shaped applicator, the artificial tibia was securely positioned within an embedding container containing custom self-coagulating dentine powder and dentine water. To attain satisfactory solidification of the dentine powder, the cooling period was limited to 60 min. Subsequent to fixation, specialized biomechanical testing was conducted employing dedicated equipment.

In our experiment, a total of 40 synthetic tibiae were utilized, distributed across five groups with an average of eight specimens per group. These tibiae were employed to simulate a posterior lateral split fracture model. For lateral fixation, a 3.5-mm LCP was employed, while posterior fixation was achieved using a distal radius support plate. To secure the fracture fragment, a combination of locking screws with varying lengths, variable-angle locking screws, and lag screws were utilized.

2.1 Posterolateral fracture model Construction

The PL fracture model is established with the details of the model outlined in Figure 1. The LAPD is the vertical distance from the lateral exit point of the PTPF to the anterior cortex of the fibular head. The anterior edge of the fibular head was designated as point b with an Line ab dimension of 10 mm to ascertain the exit position of the lateral margin of the fracture line, identified as point a. Subsequently, an osteotomy was executed with a lateral margin fracture angle (LMFA) of 13°. The PHD is the horizontal distance between the medial cortex of the fibular head and the posterior exit point of the posterolateral column fracture. Posteriorly, the medial margin of the fibular head was utilized as point c, with a Line cd measure of 23 mm to determine the exit location of the posterior medial margin, denoted as point d, along the fracture line. The osteotomy was carried out with a posterior margin fracture angle (PMFA) of 20°. The exit point e of the lower fracture line was established based on the coordinates of point a, point d, a sagittal fracture angle (SFA) of 78°, and a posterior coronal height (PCH) value of 31 mm. Subsequently, an osteotomy was executed. Our modeling referenced previous studies (Sun et al., 2018; Zhang et al., 2020; Ren et al., 2022).

Osteotomies were executed using a thin-knife chainsaw, and geometric measurements were conducted utilizing AutoCAD software (AutoCAD, 2020; Autodesk, San Rafael, CA, United States). All geometric measurements and preparations were carried out under the supervision of an experienced surgeon. To enhance uniformity, a skilled swing saw operator was chosen after undergoing training on 30 artificial tibiae. This approach aimed to ensure consistent size and shape of the fracture fragment in each instance.

2.2 Grouping of fixation models of PL fracture

The created split fracture model was meticulously repositioned and subsequently secured with two Kirschner pins, extending from the posterior-lateral to posterior-medial aspect, to ensure precise anatomical realignment. The plate was affixed to the tibial cortex, aligning the upper margin of the plate with the articular surface of the tibia, while the longitudinal arm of the plate maintained a parallel orientation to the tibia's longitudinal axis. Five groups of plate fixation strategies were employed in constructing the fracture model, as delineated below. Group Ⅰ: the LCP was postposition and

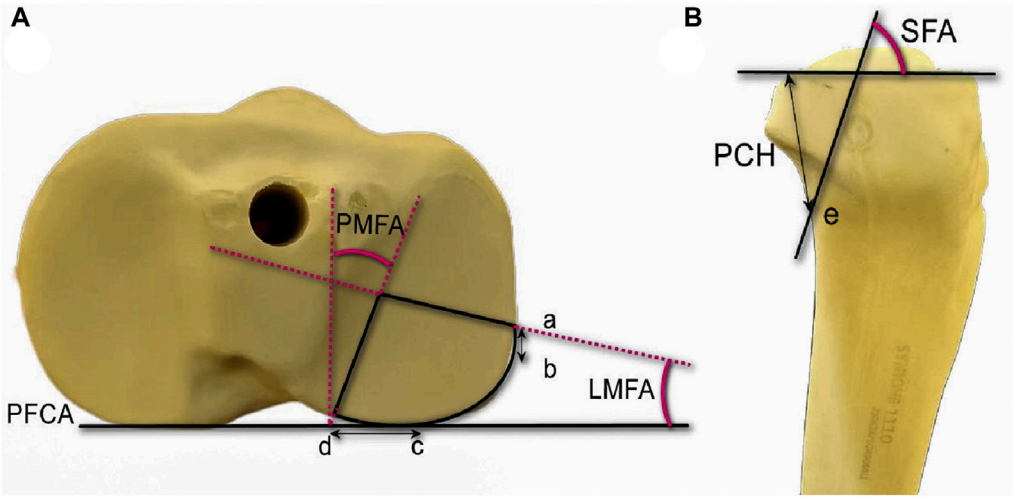

FIGURE 1
Cranial and lateral views of the posterolateral (PL) split fracture model of tibial plateau. **(A)** Cranial view. PFCA, posterior femoral condyle axis; point a, lateral exit point of the PL fracture; point b, anterior edge of the articular facet of fibular head; point c, medial edge of the articular facet of fibular head; point d, posterior exit point of the PL fracture; angle LMFA, angle between the lateral fracture line of the PL fragment and the PFCA; angle PMFA, angle between the medial l fracture line of the PL fragment and the line perpendicular to the PFCA. **(B)** Lateral view. angle SFA, angle between the joint line of the PL fragment with the coronal fracture line; point e, exit point below PL fracture.

the anterior edge of the penultimate locking screw of the plate was positioned lateral exit point of the PL fracture, thereby permitting PL fracture fragment fixation with two conventional locking screws (LPTL). Group II: the plate position was similar to Group I. Differently, the last two locking screws were substituted with variable angle locking screws (10° posterior offset, LPTV). Group III: the LCP was not postposition and PL fracture fragment was fixed with only one locking screws (LPOL). Group IV: the plate position was similar to Group III, PL fracture allowing for the secure passage of a complete screw. Additionally, two lag screws were introduced from the anterior to posterior direction, fixing PL fracture beneath the locking screw (LPOLTL). Group V: the T-type distal radius plate was situated to rear of the PL fracture, ensuring two screws of the transverse arm plus one screw of the longitudinal arm effectively fixing the fracture fragment (TPP) (Shen et al., 2019) (Figures 2A–E).

All the materials mentioned above were sourced from the same manufacturer to ensure uniform material properties. The creation of fracture models was carried out consistently by a single experienced surgeon to replicate fracture reduction and fixation. It is important to note that factors influencing knee joint pressure, such as ligaments, muscles, and surrounding soft tissues, were not taken into account in this study.

2.3 Biomechanical testing and finite element analysis

2.3.1 Biomechanical testing

Each model was positioned on a material testing machine (E10000 Linear-Torsion All-Electric Dynamic Test Instrument, InstronE10000, Instron Corporation Norwood, MA, United States) for testing (Figure 3). To account for the femur's compression against the plateau during body flexion, a T-shaped applicator (designed to mimic shear stress) was customized to apply compression to the posterolateral fracture fragment (Feng et al., 2021).

Considering that the biomechanical load experienced by a normal adult knee is approximately 2–3 times the body weight, with the lateral plateau bearing 45% of this load (Ogaya et al., 2014), we aimed to replicate the load in our experiments. For instance, with a 60 kg adult body weight, the pressure on the lateral platform approximates 250, 500, and 750 N for 1–3 times the body weight. Therefore, axial loads of 250, 500, and 750 N were selected to simulate the lateral platform loads in our experiments. These loads were applied at a rate of 10N/s to each fracture model after mounting.

During testing, axial displacement was continuously monitored from the initial position to peak load using axial displacement software, integrated with Bluehill software (Instron, Norwood, MA, United States). Load-displacement curves were generated for each fracture model. Failure load was defined as the vertical displacement of the posterior lateral fracture fragments up to 3 mm. The maximum peak load was limited to 750 N or the load corresponding to a deformation of 3 mm. As a result, we evaluated biomechanical stability using displacements at 250, 500, 750 N, and failure load levels.

2.4 Statistical analysis

We employed IBM SPSS Statistics 27 for statistical analysis to assess the vertical displacements of the five fracture models under distinct loading conditions, along with the failure loads, treated as measures conforming to a normal distribution. To conduct comparisons, we utilized one-way ANOVA, with a significance level set at $p < 0.05$ to establish statistical significance.

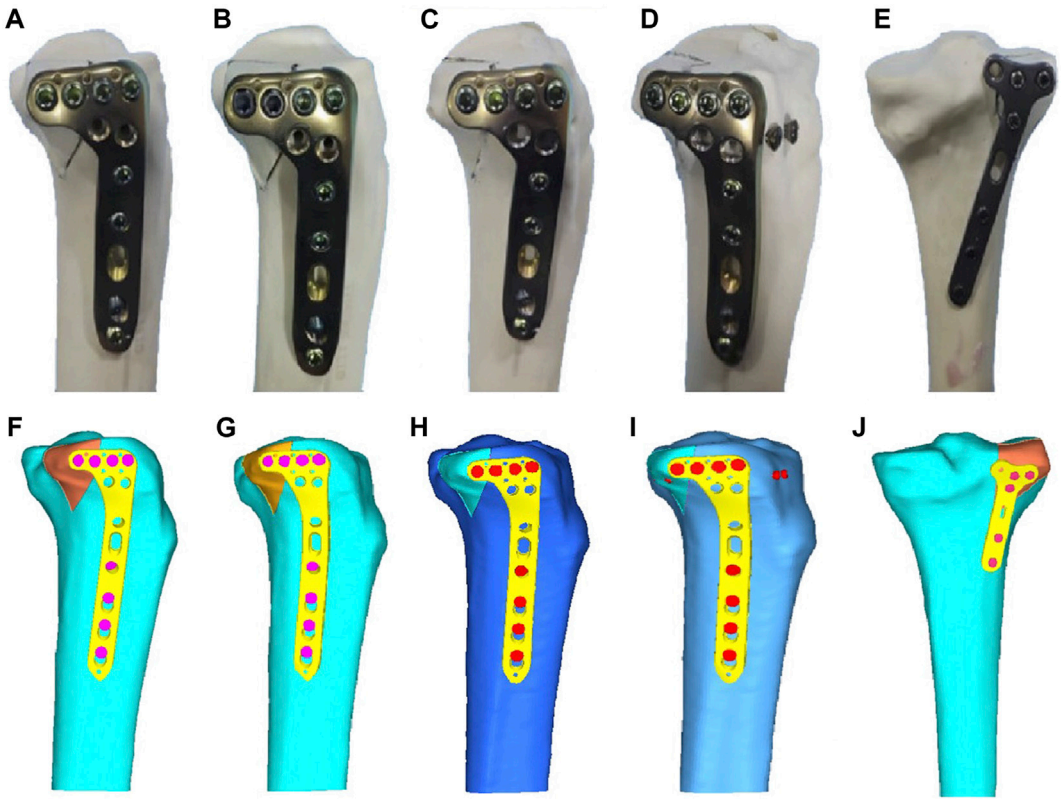

FIGURE 2
Five different internal fixation models of the posterolateral (PL) fracture. **(A)** Fixation with two conventional locking screws in the transverse arm of the LCP. **(B)** Fixation with two variable-angle locking screws in the transverse arm of the LCP. **(C)** Fixation with one locking screw in the transverse arm of the LCP. **(D)** Fixation with one locking screw in the transverse arm of the LCP plus two anterior and posterior lag screws. **(E)** Posterior support with a T-shaped distal radius plate fixation. **(F)** Fixed by two locking screws of the LCP of the finite element model. **(G)** Fixed by two variable angle locking screws of the LCP of the finite element model. **(H)** Fixed by one locking screw of the LCP of the finite element model. **(I)** Fixed by one locking screw with two-antero-posterior lag screws of the LCP of the finite element model. **(J)** Fixed by posteriorly supported T-shaped distal radius plate of the finite element model.

2.5 Finite element analysis

With the informed consent obtained, we enrolled a healthy adult male volunteer, aged 30, devoid of knee ailments and major systemic health conditions, to participate in the study. Employing a 64-row multislice spiral CT scanner, scans were conducted from the knee to the ankle, maintaining a slice spacing of 0.625 mm. The acquired CT images were stored in DICOM format within Mimics software (version 19.0, Materialise, Leuven, Belgium). Subsequently, a three-dimensional model of the tibia was formulated, leveraging the tissue's grayscale values and region segmentation. This preliminary model underwent refinement in Geomagic Studio (version 12, Geomagic, NC State, United States) through a smoothing process, rectifying the three-dimensional model's surface. The various segments of the finite element model were then imported into Hypermesh software (version 2017, Altair, Inc., United States), a meshing tool for finite element analysis. Meshing was performed employing quadratic tetrahedral elements (Solid187) to ensure optimal discretization. The tibia was characterized as isotropic, linear elastic, and homogeneous. Each model was constructed using quadratic tetrahedron elements ranging in size from 0.5 to 1.0 mm. A convergence test was executed across all models, ensuring that the maximum change remained below 1%. The material properties were validated based on the previous work (Huang et al., 2019). The three-dimensional model of the plate and screws was developed in compliance with the manufacturer's specifications using computer-aided design software Creo Parametric (PTC, Inc., United States). All interactions between fracture fragments and implants were modeled as frictional contact, with a coefficient of friction of 0.4 assigned to replicate the conditions (Rancourt et al., 1990). The tibia model was integrated into Geomagic Studio software (3D Systems Inc., Rock Hill, SC, United States).

For the internal fixation models of PL tibial plateau fractures, the tibia model was combined with internal fixations using Creo Parametric software, utilizing relative data. It is worth noting that our finite element analysis models had been validated previously (Ren et al., 2022). Five models of fracture fixation were same with the groups of biomechanical testing. That was Ⅰ: Group LPTL; Ⅱ: Group LPTV; Ⅲ: Group LPOL; Ⅳ: Group LPOLTL; and Ⅴ: Group TPP (Figures 2F–J).

Axial compression of the PL split fracture fragment was executed utilizing three distinct axial loading conditions: 250, 500, and 750 N, with the load applied perpendicular to the tibial plateau. The Young's modulus (MPa) and Poisson's ratio used for the finite element analysis were outlined in Table 1 (Qiu et al., 2011;

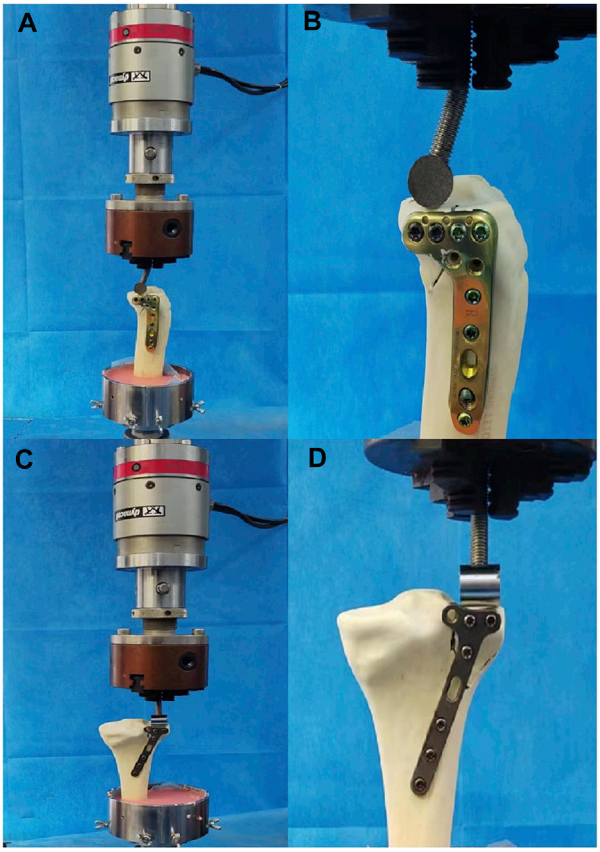

FIGURE 3
Positioning of different fixation model of PL fracture within the machine. **(A)** Fixation of the locking compression plate at the lateral side. **(B)** Local magnification of **(A)** showing biomechanical test. **(C)** Fixation of T-shaped distal radius plate at the posterior side. **(D)** Local magnification of **(C)** showing biomechanical test.

TABLE 1 The Young's modulus (MPa) and Poisson's ratio.

Material	Young's modulus (MPa)	Poisson's ratio
Plate	110000	0.3
Screw	110000	0.3
Cortical bone	14000	0.3
Cancellous bone	700	0.3

TABLE 2 Number of elements in five groups of models.

Model	Nodes	Elements
LPTL	823586	539115
LPTV	813802	531882
LPOL	902541	552457
LPOLTL	863564	562391
TPP	781469	514402

Anwar et al., 2017; Huang et al., 2019). Meanwhile, Table 2 provided insight into the node and element counts for each group of models. The analysis of five fixation models was conducted using ANSYS Mechanical APDL 19.0 software (ANSYS, Inc., United States).

3 Results

3.1 Biomechanical testing of five fixation model for PTPF

Biomechanical Testing of five fixation model was performed including the vertical displacement across three distinct axial loads, failure loads and axial stiffness (Table 3). The trends in displacement were consistent across all five fracture fixation models, ranging from 250 to 750 N. The findings indicate that Group V exhibited the least displacement, while Group III demonstrates the highest degree of displacement. The disparity in displacements between Group V and Group II did not attain statistical significance ($p > 0.05$). The distinction in displacements between Group I and Group IV did not achieve statistical significance ($p > 0.05$). Significant disparities in displacements were identified among the remaining four groups when compared to Group III ($p < 0.05$) (Figure 4A).

The failure load and axial stiffness exhibit a comparable trend to the displacement. Figures 4B, C illustrate the failure loads and axial stiffness values across the five model groups, along with the associated statistical variances. Group V exhibited a maximum failure load and axial stiffness, while Group III the lowest values. The difference in failure load and axial stiffness between Group V and Group II did not attain statistical significance ($p > 0.05$). Likewise, the distinction between Group I and Group IV did not achieve statistical significance ($p > 0.05$). Significant disparities were identified among the remaining four groups compared to Group III ($p < 0.05$).

3.2 Finite element analysis results test

The displacements and stresses observed in the five fixation groups of PL split fractures under loads ranging from 250 to 750 N displayed in Table 4, and the von Mises stress distributions were detailed in Table 5. The finite element analysis showed the displacements at 750 N were approximated from small to large as V < II < I < IV < III and the stresses were approximated from small to large as V < II < IV < I < III. Figure 5 showed the von Mises stress distribution of among five groups of internal fixation devices and both bone and internal fixation. The stresses in the plate of Group I (LPTL) were mainly concentrated at the distal end of the last two screws in the transverse row; the stresses in the plate of Group II (LPTV) were concentrated at the points similar to those of Group I and those of Group III (LPOL) plate stresses were concentrated on the proximal end of the last screw and the corner of the plate; Group IV (LPOLTL) plate stresses were concentrated on the last screw, but the distal end of the two anteroposterior lag screws shared some of the stresses; and Group V (TPP) plate stress concentrations were seen in the transverse arm proximally posteriorly lateral to the two screws and in the first screw below as well as at the plate between the three screw holes.

TABLE 3 Vertical displacement, failure loads and axial stiffnesses of five sets of fracture models under three different loads.

Group	Vertical displacement (mm) (mean ± SD, mm)			Load to failure (mean ± SD, N)	Axial stiffness (mean ± SD, N/mm)
	250N	500N	750N		
LPTL	0.86 ± 0.07	1.70 ± 0.08	2.60 ± 0.18	885.40 ± 27.72	295.10 ± 9.24
LPTV	0.73 ± 0.09	1.50 ± 0.13	2.28 ± 0.06	957.50 ± 16.31	319.20 ± 5.44
LPOL	1.13 ± 0.18	2.06 ± 0.20	3.24 ± 0.22	723.40 ± 20.55	241.10 ± 6.85
LPOLTL	0.89 ± 0.11	1.70 ± 0.09	2.64 ± 0.12	874.50 ± 21.45	291.50 ± 7.15
TPP	0.70 ± 0.07	1.45 ± 0.14	2.24 ± 0.23	994.20 ± 61.41	331.40 ± 20.47

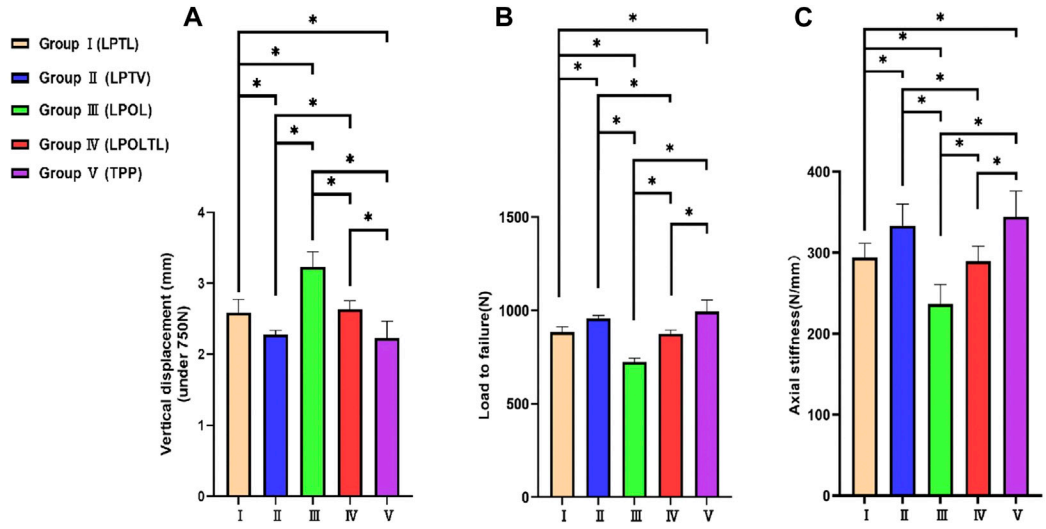

FIGURE 4
Synopsis of statistical analyses across the five model groups. **(A)** The displacement of the posterolateral fracture fragment under 750N axial loads. **(B)** The Load to failure for five groups of models. **(C)** The Axial stiffness for five groups of models. The bars indicated the mean, and the error bars indicated the standard deviation. *$p < 0.05$.

TABLE 4 Axial compression displacement of the internal fixation under three loads in five sets of fracture models.

Group	Displacement (mm)		
	250N	500N	750N
LPTL	0.27	0.54	0.81
LPTV	0.27	0.53	0.79
LPOL	0.37	0.74	1.11
LPOLTL	0.27	0.55	0.83
TPP	0.23	0.46	0.68

TABLE 5 Von Mises stresses of internal fixation under three loads for five sets of fracture models.

Group	Von Mises stress (MPa)		
	250N	500N	750N
LPTL	114.2	228.4	342.6
LPTV	100.44	200.89	301.34
LPOL	138.21	276.42	414.63
LPOLTL	107.22	214.45	321.68
TPP	96.07	192.14	288.21

4 Discussion

The choice of fixation model and surgical approach for the treatment of PTPF remain controversial. Our study evaluated the differences in strength among LCP with different screws fixation through lateral approach and distal radius plate with three screws fixation through posterior approach for the treatment of PTPF. The biomechanical test and finite element analysis showed relatively consistent results. That was PTPF with LCP and single-locking screw fixation exhibited the weakest

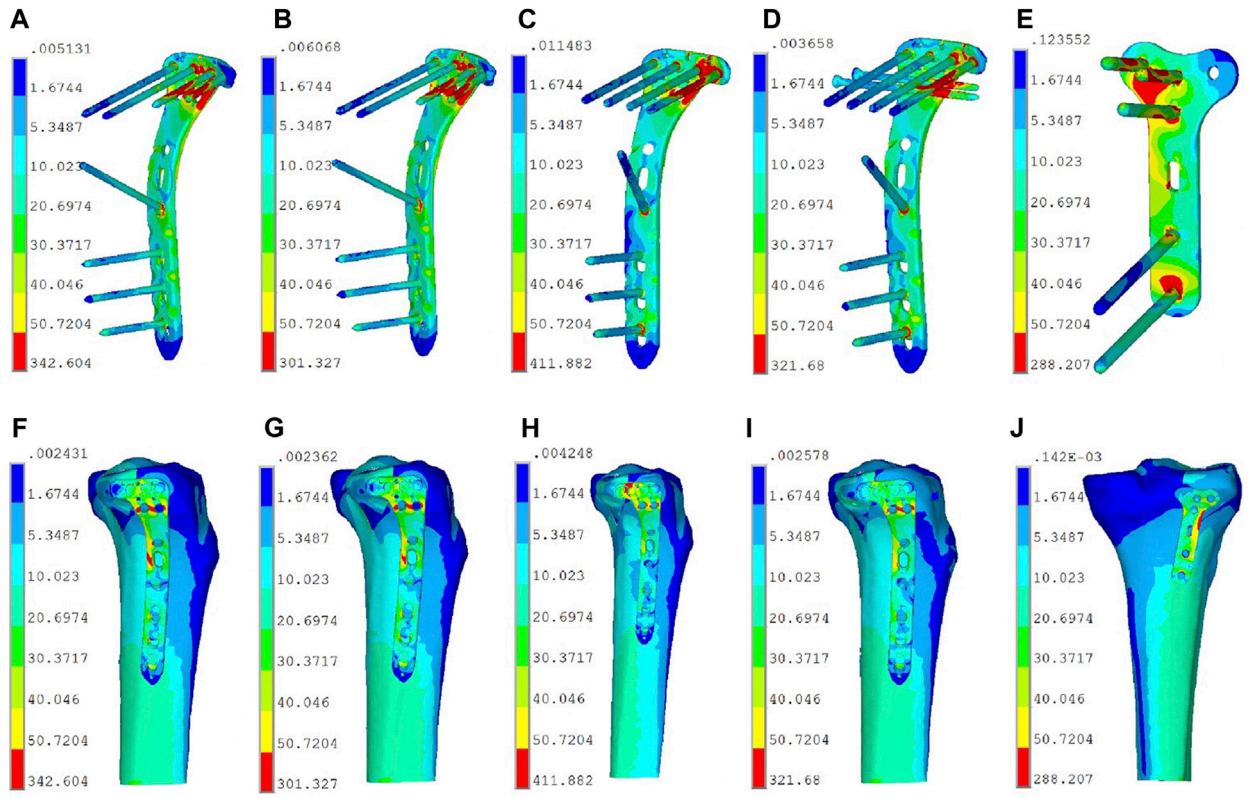

FIGURE 5
The von Mises stress distribution of among five groups of internal fixation devices and both bone and internal fixation. **(A)** Group I (LPTL) internal fixation stresses. **(B)** Group II (LPTV) internal fixation stresses. **(C)** Group III (LPOL) internal fixation stresses. **(D)** Group IV (LPOLTL) internal fixation stresses. **(E)** Group V (TPP) internal fixation stresses. **(F)** Group I (LPTL) both bone and internal fixation stresses. **(G)** Group II (LPTV) both bone and internal fixation stresses. **(H)** Group III (LPOL) both bone and internal fixation stresses. **(I)** Group IV (LPOLTL) both bone and internal fixation stresses. **(J)** Group V (TPP) both bone and internal fixation stresses.

compressive yield strength and the greatest displacement. Other four groups had good stability. The compressive yield strength of LCP with two variable angle locking screws fixation was semblable to that of posterior plate fixation. Similarly, LCP with two conventional locking screws exhibited compressive yield strength similar to that of one locking screws assisted two anteroposterior lag screws.

4.1 Internal fixation for posterolateral tibial plateau fracture

Through posterior approach, distal radius plate can provide multiply screws for the fixation of PL fracture fragments (Shen et al., 2019). In our study, we selected distal radius plate, utilizing two screws in the transverse arm and one in the longitudinal arm of the plate, totaling three screws for the stabilization of the fracture fragment. This fixation model (TPP) exhibited the highest level of mechanical strength for PTPF fixation. Therefore, Wang et al. (Shuaishuai et al., 2023) advocated treating PTPF through posterolateral approach. It was posited that the superior mechanical strength of the posterior plate was primarily attributed to its higher shear resistance in stabilizing fracture fragments (Giordano et al., 2022). Finite element analysis revealed that the stress on the Group TPP was concentrated between the three screws along the plate body, the shear resistance force of the plate and three screws served to distribute stress more evenly, thereby diminishing the overall stress on the internal fixation (Figures 5E, J).

Nevertheless, the posterior approach is accompanied by a potential risk of neurovascular injury, and the presence of obstructing anatomical structures, such as muscular ligaments, renders its execution comparatively more challenging (Tao et al., 2008; Cho et al., 2017; Sun et al., 2017). In contrast, the lateral approach stands out as one of the simpler and more commonly employed surgical routes, characterized by a reduced risk of vascular and nerve injury (Hu et al., 2016; Hu et al., 2020; Mao et al., 2021). In our analysis, we evaluated the number of transverse arms of the LCP utilized in stabilizing fracture fragments across various groups. We observed that with a axial load of 750 N, low support of the single-screw in the transverse arm of the plate caused further displacement exceeding 3 mm of the posterolateral (PL) fragment of fracture. This condition manifested the lowest performance in terms of compressive yield strength across all three applied axial loads, corroborating the findings reported in the existing studies by

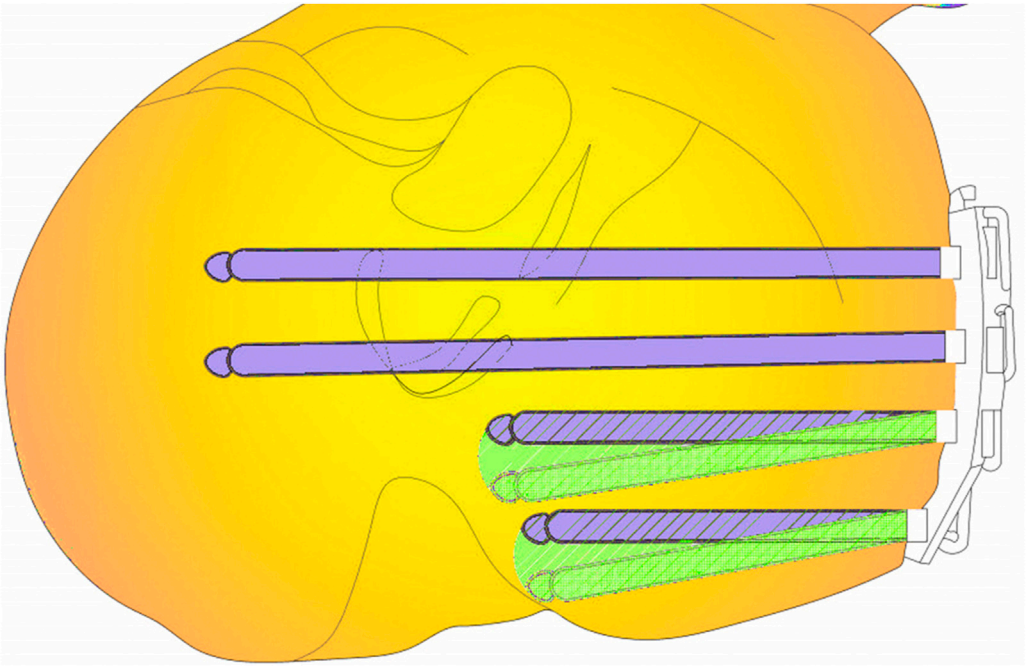

FIGURE 6
The figure **s**hows a cross section of a PL fracture. Violet color indicates conventional locking screws, green screws are variable angle locking screws, and the green range indicates an increase in fixing field.

other researchers in the field (Ren et al., 2018; Sun et al., 2018; Hu et al., 2020). Finite element analysis revealed that one screw fixation led to obvious stress concentration (Figures 5C, H), which might explain fixation failure. Conversely, we observed a diminished von Mises stress of the internal fixation device in Group I and Group II. The dual screws shared stress together (Figures 5A, B, F, G), increasing stress dispersion. Similarly, partial stress concentrations were observed on the anteroposterior lag screws in Group IV (Figure 5D). The stresses in the plate body near the fracture line experienced a significant reduction compared to the Group of one-screw fixation (Figure 5I). This finding was consistent with the results of our biomechanical test, which demonstrated superior compression displacement, failure load, and axial stiffness in Group IV compared to Group III. The biomechanical results showed that the axial stiffness of Group I and Group IV were very close to each other, so we believed that when two screws in the transverse arm cannot be achieved to fix the fracture fragments in clinic, we can choose to add two anterior and posterior lag screws to increase the strength of stable fixation. This fixation method was documented in earlier studies (Gao et al., 2023). Von Mises theory states that ductile materials fail when the so-called "von Mises stress" exceeds the uniaxial yield strength (Velic et al., 2021). At a loading equivalent to 300% of the body weight, the plate material exhibits a yield strength of 800 MPa (Lalwani et al., 2013). We did not find stresses in the internal fixation device that exceeded this range. This suggested that no failure risk of mechanics would be expected in the implants.

We observed similar von Mises stress distributions in both Group I and Group II. However, the internal fixation stresses were lower in Group II compared to Group I. The disparity between the two groups in the mechanical tests also reached statistical significance ($p < 0.05$). Upon analysis, we attributed this observation to the screw offset angle. It caused an increased area of screw fixation on the bone fragment resulting to a reduction in von Mises stresses.

4.2 Variable screw placement angle

In our study, variable angle locking screw fixation, particularly for the two posterior screws, increased the fixation area for PL fractures and concurrently enhanced fixation strength. It is important to note that large offset angles should be avoided. While Tidwell (Tidwell et al., 2016) reported decreasing fixation strength with increasing screw angle, our data contradicts this. Instead, we observed a significant increase in fixation intensity. This discrepancy might stem from the increased fixation area due to the larger offset angle. A key concern was plate screw loosening over time. Hebert-Davies (Hebert-Davies et al., 2013) found no significant reduction in torque force between the plate and screw with a multiaxial screw offset up to 10°, implying stability between the screw and implant plate. Based on these findings, we maintained a 10° offset in our experiments for stability, as illustrated in Figure 6. Consistent with previous studies (Hu et al., 2016; Jiang et al., 2018), we also ensured the length of the last variable angle screw was under 35 mm.

When the final screw was positioned with a rearward offset of 10°, we defined the offset area as a sector, represented by S′, To determine S′, the diameter of this variable angle locking screw was taken as 35 mm. Consequently, the offset area was calculated to be approximately 107 mm^2, using the equation: $S' = 10°/360° \times \pi R^2$.

According to Taylor et al. (Taylor et al., 2004), the load exerted on the knee joint during walking is about double an individual's body weight. Consequently, the primary load-bearing regions of both medial and lateral platforms cover areas of approximately 389 and 363 mm^2, respectively. These values represent 33.2% and 42.9% of the total area of the medial and lateral platforms, respectively. It is clear that the rearward offset introduced by variable angle locking screws significantly expands the PL fracture fixation area, enhancing the overall strength of the fixation.

In clinical settings, constraints such as the presence of the fibular collateral ligament or extreme posterior displacement of the PL fracture fragment can hinder the feasibility of achieving two-locking screw fixation. In such cases, the utilization of variable angle screws can fulfill the requirement for two-screw fixation of the PL fracture fragment. Importantly, our biomechanical testing and finite element analysis validated the biomechanical attributes of variable angle locking screws. When contrasted with the posterior plate, the distinction was found to lack statistical significance, despite the variable angle locking screws exhibiting inadequate mechanical strength in comparison to the posterior support plate. Given these considerations, we are inclined to believe that the use of LCP variable angle locking screws for PL fracture fixation is a viable clinical approach, with low risk of damage to the neurovascular bundle.

4.3 Limitations and prospects

Several limitations were acknowledged in this experiment. The study exclusively focused on the PL split fracture model, as validated models for collapsed fractures were lacking. Future experiments are planned to encompass collapsed fractures and combined cleavage-collapsed fractures. The current experimental model was constructed based on existing literature, yet the clinical spectrum of PL fractures is diverse, thus failing to encompass all fracture types. Additionally, synthetic bones were chosen for their uniformity and resemblance to human tibias in terms of dimensions and properties. This study did not use a cadaveric bone model supported by the fibula. Amirouche and Solitro et al. (Amirouche and Solitro, 2011) posit that, to date, a definitive modeling model for the knee joint has not been established. It is noteworthy that the biomechanical testing employed in this study is static and mimics an individual standing on one leg. Further studies will aim to address these limitations and provide a more comprehensive perspective on PL fracture fixation. The study was also limited by the fact that different coatings were not considered, which Patel et al. proved that there was a contribution of the coating to implant stability (Patel et al., 2015). Our study did not consider the problem of loosening that occurs when screws are inserted into the bone (Mejia et al., 2020). Additionally, the study did not explore the relationship between screw characteristics, insertion torque, and stability (Addevico et al., 2020). Other factors impacting stability such as intrannular materials (Bronsnick et al., 2015), insertion torque (Addevico et al., 2021), porous media for bone (Travascio et al., 2015), bone mechanobiology (Volz et al., 2021) were not conferred in our study.

Our objective was to assess the viability of utilizing a lateral approach for fixation, complemented by the incorporation of tension or variable angle screws, with the aim of enhancing the stability of the fractured fragment. This investigation will be pursued further in our future research endeavors.

5 Conclusion

Introducing variable-angle locking screws can further enhance the fixation range, with the resultant biomechanical stability similar to that of a posteriorly supported plate. It is imperative to make intraoperative adjustments to the screw arrangement to achieve the requisite mechanical strength, avoiding reliance on single screw from the plate fixing PL fracture.

Data availability statement

The original contributions presented in the study are included in the article/supplementary material, further inquiries can be directed to the corresponding authors.

Author contributions

ZH: Writing–original draft. WR: Supervision, Writing–review and editing. JP: Supervision, Writing–review and editing. ZG: Supervision, Writing–review and editing. CW: Supervision, Writing–review and editing. WW: Supervision, Writing–review and editing. WZ: Software, Validation, Writing–review and editing. WX: Conceptualization, Methodology, Supervision, Visualization, Writing–review and editing. LL: Conceptualization, Data curation, Funding acquisition, Methodology, Resources, Writing–review and editing.

Funding

The authors declare financial support was received for the research, authorship, and publication of this article. This research was funded by Gusu Talent Program (2020092), Suzhou Key Disciplines (No. SZXK202104), Open Project of the State Key Laboratory of Radiation Medicine and Radiation Protection Jointly Constructed by the Ministry and the Province (GZK1202215). This research was supported by Suzhou key Disciplines (SZXK202104).

Acknowledgments

The authors would like to thank all the experimenters who participated in this experiment, the imaging physicians for the data measurements, and the finite element laboratory faculty members.

Conflict of interest

The authors declare that the research was conducted in the absence of any commercial or financial relationships that could be construed as a potential conflict of interest.

Publisher's note

References

Addevico, F., Morandi, M., Scaglione, M., and Solitro, G. F. (2020). Screw insertion torque as parameter to judge the fixation. Assessment of torque and pull-out strength in different bone densities and screw-pitches. *Clin. Biomech. (Bristol, Avon)* 72, 130–135. doi:10.1016/j.clinbiomech.2019.12.004

Addevico, F., Solitro, G. F., and Morandi, M. M. (2021). Salvaging pull-out strength in a previously stripped screw site: a comparison of three rescue techniques. *J. Funct. Morphol. Kinesiol* 6 (3), 71. doi:10.3390/jfmk6030071

Amirouche, F., and Solitro, G. F. (2011). Challenges in modeling total knee arthroplasty and total hip replacement. *Procedia IUTAM* 2, 18–25. doi:10.1016/j.piutam.2011.04.003

Anwar, A., Lv, D., Zhao, Z., Zhang, Z., Lu, M., Nazir, M. U., et al. (2017). Finite element analysis of the three different posterior malleolus fixation strategies in relation to different fracture sizes. *Injury* 48 (4), 825–832. doi:10.1016/j.injury.2017.02.012

Bronsnick, D., Harold, R. E., Youderian, A., Solitro, G., Amirouche, F., and Goldberg, B. (2015). Can high-friction intraannular material increase screw pullout strength in osteoporotic bone? *Clin. Orthop. Relat. Res.* 473 (3), 1150–1154. doi:10.1007/s11999-014-3975-1

Cai, P., Yuan, M., Ji, H., Cui, X., Shen, C., Zhou, X., et al. (2021). The treatment of posterolateral tibial plateau fracture with a newly designed anatomical plate via the trans-supra-fibular head approach: preliminary outcomes. *BMC Musculoskelet. Disord.* 22 (1), 804. doi:10.1186/s12891-021-04684-w

Chen, L., Xiong, Y., Yan, C., Zhou, W., Lin, Z., He, Z., et al. (2020). Fibular neck osteotomy approach in treatment of posterolateral tibial plateau fractures: a retrospective case series. *Med. Sci. Monit. Int. Med. J. Exp. Clin. Res.* 26, e927370. doi:10.12659/msm.927370

Cho, J. W., Kim, J., Cho, W. T., Kim, J. K., Samal, P., Gujjar, P. H., et al. (2017). Approaches and fixation of the posterolateral fracture fragment in tibial plateau fractures: a review with an emphasis on rim plating via modified anterolateral approach. *Int. Orthop.* 41 (9), 1887–1897. doi:10.1007/s00264-017-3563-6

Durigan, J. R., Moraes, C. M. S., Hamra, P., Zamboni, C., Mercadante, M. T., Hungria, J. O. S., et al. (2023). TEMPORARY REMOVAL: depression fractures of the posterolateral tibial plateau: treatment by lateral femoral epicondyle osteotomy approach. *Injury* S0020-1383 (23), 00100–00106. doi:10.1016/j.injury.2023.02.003

Feng, J., Gu, Y., You, W., and Rui, G. (2021). A posterolateral sheared fracture of the tibial plateau: a case presentation. *BMC Musculoskelet. Disord.* 22 (1), 488. doi:10.1186/s12891-021-04373-8

Gao, W., Qi, X., Zhao, K., Feng, X., Yang, Y., Liu, P., et al. (2023). Lateral locking plate plus antero-posterior lag screws techniques for the management of posterolateral tibial plateau fracture: preliminary clinical results and biomechanical study. *Archives Orthop. trauma Surg.* 143 (6), 3163–3172. doi:10.1007/s00402-022-04554-7

Giordano, V., Pires, R. E., Pimenta, F. S., Campos, T. V. O., Andrade, M. A. P., and Giannoudis, P. V. (2022). Posterolateral fractures of the tibial plateau revisited: a simplified treatment algorithm. *J. knee Surg.* 35 (9), 959–970. doi:10.1055/s-0040-1721026

Hebert-Davies, J., Laflamme, G. Y., Rouleau, D., Canet, F., Sandman, E., Li, A., et al. (2013). A biomechanical study comparing polyaxial locking screw mechanisms. *Injury* 44 (10), 1358–1362. doi:10.1016/j.injury.2013.06.013

Higgins, T. F., Kemper, D., and Klatt, J. (2009). Incidence and morphology of the posteromedial fragment in bicondylar tibial plateau fractures. *J. Orthop. Trauma* 23 (1), 45–51. doi:10.1097/bot.0b013e31818f8dc1

Honkonen, S. E. (1994). Indications for surgical treatment of tibial condyle fractures. *Clin. Orthop. Relat. Res.* 302 (302), 199–205. doi:10.1097/00003086-199405000-00031

Hu, S., Chen, S., Chang, S., Xiong, W., and Tuladhar, R. (2020). Treatment of isolated posterolateral tibial plateau fracture with a horizontal belt plate through the anterolateral supra-fibular-head approach. *BioMed Res. Int.* 2020, 1–8. doi:10.1155/2020/4186712

Hu, S. J., Chang, S. M., Zhang, Y. Q., Ma, Z., Du, S. C., and Zhang, K. (2016). The anterolateral supra-fibular-head approach for plating posterolateral tibial plateau fractures: a novel surgical technique. *Injury* 47 (2), 502–507. doi:10.1016/j.injury.2015.11.010

Huang, S., Ji, T., and Guo, W. (2019). Biomechanical comparison of a 3D-printed sacrum prosthesis versus rod-screw systems for reconstruction after total sacrectomy: a finite element analysis. *Clin. Biomech. (Bristol, Avon)* 70, 203–208. doi:10.1016/j.clinbiomech.2019.10.019

Jiang, L., Zheng, Q., and Pan, Z. (2018). Comparison of extended anterolateral approach in treatment of simple/complex tibial plateau fracture with posterolateral tibial plateau fracture. *J. Orthop. Surg. Res.* 13 (1), 303. doi:10.1186/s13018-018-1007-7

Kim, Y., Yoon, Y. C., Cho, J. W., Cho, W. T., Jeon, N. H., Oh, C. W., et al. (2018). Rim Plate augmentation of the posterolateral bare area of the tibial plateau using a 3.5-mm precontoured locking compression plate: a cadaveric study. *J. Orthop. trauma* 32 (5), e157–e160. doi:10.1097/bot.0000000000001129

Lalwani, G., Henslee, A. M., Farshid, B., Parmar, P., Lin, L., Qin, Y. X., et al. (2013). Tungsten disulfide nanotubes reinforced biodegradable polymers for bone tissue engineering. *Acta biomater.* 9 (9), 8365–8373. doi:10.1016/j.actbio.2013.05.018

Mao, W., Chen, G., Zhu, Y., Zhang, M., Ru, J., Wang, J., et al. (2021). Treatment of tibial plateau fractures involving the posterolateral column using the extended anterolateral approach. *Medicine* 100 (38), e27316. doi:10.1097/md.0000000000027316

Mejia, A., Solitro, G., Gonzalez, E., Parekh, A., Gonzalez, M., and Amirouche, F. (2020). Pullout strength after multiple reinsertions in radial bone fixation. *Hand (N Y)* 15 (3), 393–398. doi:10.1177/1558944718795510

Ogaya, S., Naito, H., Iwata, A., Higuchi, Y., Fuchioka, S., and Tanaka, M. (2014). Knee adduction moment and medial knee contact force during gait in older people. *Gait Posture* 40 (3), 341–345. doi:10.1016/j.gaitpost.2014.04.205

Parkkinen, M., Madanat, R., Mustonen, A., Koskinen, S. K., Paavola, M., and Lindahl, J. (2014). Factors predicting the development of early osteoarthritis following lateral tibial plateau fractures: mid-term clinical and radiographic outcomes of 73 operatively treated patients. *Scand. J. Surg.* 103 (4), 256–262. doi:10.1177/1457496914520854

Patel, S., Solitro, G. F., Sukotjo, C., Takoudis, C., Mathew, M. T., Amirouche, F., et al. (2015). Nanotopography and surface stress analysis of Ti6Al4V bioimplant: an alternative design for stability. *Jom* 67 (11), 2518–2533. doi:10.1007/s11837-015-1341-8

Qiu, T. X., Teo, E. C., Yan, Y. B., and Lei, W. (2011). Finite element modeling of a 3D coupled foot-boot model. *Med. Eng. Phys.* 33 (10), 1228–1233. doi:10.1016/j.medengphy.2011.05.012

Rademakers, M. V., Kerkhoffs, G. M., Sierevelt, I. N., Raaymakers, E. L., and Marti, R. K. (2007). Operative treatment of 109 tibial plateau fractures: five-to 27-year follow-up results. *J. Orthop. Trauma* 21 (1), 5–10. doi:10.1097/bot.0b013e31802c5b51

Rancourt, D., Shirazi-Adl, A., Drouin, G., and Paiement, G. (1990). Friction properties of the interface between porous-surfaced metals and tibial cancellous bone. *J. Biomed. Mater. Res.* 24 (11), 1503–1519. doi:10.1002/jbm.820241107

Ren, D., Liu, Y., Lu, J., Xu, R., and Wang, P. (2018). A novel design of a plate for posterolateral tibial plateau fractures through traditional anterolateral approach. *Sci. Rep.* 8 (1), 16418. doi:10.1038/s41598-018-34818-5

Ren, W., Zhang, W., Jiang, S., Peng, J., She, C., Li, L., et al. (2022). The study of Biomechanics and clinical anatomy on a novel plate designed for posterolateral tibial plateau fractures via anterolateral approach. *Front. Bioeng. Biotechnol.* 10, 818610. doi:10.3389/fbioe.2022.818610

Schatzker, J., and Kfuri, M. (2022). Revisiting the management of tibial plateau fractures. *Injury* 53 (6), 2207–2218. doi:10.1016/j.injury.2022.04.006

Shen, Q. J., Zhang, J. L., Xing, G. S., Liu, Z. Y., Li, E. Q., Zhao, B. C., et al. (2019). Surgical treatment of lateral tibial plateau fractures involving the posterolateral column. *Orthop. Surg.* 11 (6), 1029–1038. doi:10.1111/os.12544

Shuaishuai, W., Minglei, Z., Yue, Y., Dapeng, W., Tongtong, Z., and Huimin, L. (2023). Clinical application of the modified posterolateral approach for treating posterior tibial plateau fractures. *Front. Bioeng. Biotechnol.* 11, 1150541. doi:10.3389/fbioe.2023.1150541

Sohn, H. S., Yoon, Y. C., Cho, J. W., Cho, W. T., Oh, C. W., and Oh, J. K. (2015). Incidence and fracture morphology of posterolateral fragments in lateral and bicondylar tibial plateau fractures. *J. Orthop. trauma* 29 (2), 91–97. doi:10.1097/bot.0000000000000170

Sun, H., He, Q. F., Zhang, B. B., Zhu, Y., Zhang, W., and Chai, Y. M. (2018). A biomechanical evaluation of different fixation strategies for posterolateral fragments in tibial plateau fractures and introduction of the 'magic screw. *Knee* 25 (3), 417–426. doi:10.1016/j.knee.2018.03.015

Sun, H., Zhu, Y., He, Q. F., Shu, L. Y., Zhang, W., and Chai, Y. M. (2017). Reinforcement strategy for lateral rafting plate fixation in posterolateral column fractures of the tibial plateau: the magic screw technique. *Injury* 48 (12), 2814–2826. doi:10.1016/j.injury.2017.10.033

Tao, J., Hang, D. H., Wang, Q. G., Gao, W., Zhu, L. B., Wu, X. F., et al. (2008). The posterolateral shearing tibial plateau fracture:. *Knee* 15 (6), 473–479. doi:10.1016/j.knee.2008.07.004

Taylor, W. R., Heller, M. O., Bergmann, G., and Duda, G. N. (2004). Tibio-femoral loading during human gait and stair climbing. *J. Orthop. Res. official Publ. Orthop. Res. Soc.* 22 (3), 625–632. doi:10.1016/s0736-0266(03)00240-7

Tidwell, J. E., Roush, E. P., Ondeck, C. L., Kunselman, A. R., Reid, J. S., and Lewis, G. S. (2016). The biomechanical cost of variable angle locking screws. *Injury* 47 (8), 1624–1630. doi:10.1016/j.injury.2016.06.001

Travascio, F., Asfour, S., Serpieri, R., and Rosati, L. (2015). Analysis of the consolidation problem of compressible porous media by a macroscopic variational continuum approach. *Math. Mech. Solids* 22 (5), 952–968. doi:10.1177/1081286515616049

Velic, A., Jaggessar, A., Tesfamichael, T., Li, Z., and Yarlagadda, P. (2021). Effects of nanopillar size and spacing on mechanical perturbation and bactericidal killing efficiency. *Nanomater. (Basel, Switz.* 11 (10), 2472. doi:10.3390/nano11102472

Volz, M., Elmasry, S., Jackson, A. R., and Travascio, F. (2021). Computational modeling intervertebral disc pathophysiology: a review. *Front. physiology* 12, 750668. doi:10.3389/fphys.2021.750668

Zhang, B. B., Hu, H., Zhan, S., Mei, J., Zhu, Y., and Luo, C. F. (2020). Biomechanical analysis of "Barrel hoop plate" technique for the posterolateral fragments of tibial plateau fractures with different displacement tendency. *Injury* 51 (11), 2465–2473. doi:10.1016/j.injury.2020.07.059

Zhang, W., Luo, C. F., Putnis, S., Sun, H., Zeng, Z. M., and Zeng, B. F. (2012). Biomechanical analysis of four different fixations for the posterolateral shearing tibial plateau fracture. *Knee* 19 (2), 94–98. doi:10.1016/j.knee.2011.02.004

frontiers | Frontiers in Bioengineering and Biotechnology

TYPE Original Research
PUBLISHED 13 December 2023
DOI 10.3389/fbioe.2023.1276864

OPEN ACCESS

EDITED BY
Bernardo Innocenti,
Université libre de Bruxelles, Belgium

REVIEWED BY
Ben W. Heller,
Sheffield Hallam University,
United Kingdom
Dusan Radivoje Mitic,
University of Belgrade, Serbia

*CORRESPONDENCE
Wei Liu,
liuwei2@nbu.edu.cn
Yaodong Gu,
guyaodong@nbu.edu.cn

RECEIVED 13 August 2023
ACCEPTED 15 November 2023
PUBLISHED 13 December 2023

CITATION
Shao E, Mei Q, Baker JS, Bíró I, Liu W and Gu Y (2023), The effects of non-Newtonian fluid material midsole footwear on tibial shock acceleration and attenuation.
Front. Bioeng. Biotechnol. 11:1276864.
doi: 10.3389/fbioe.2023.1276864

The effects of non-Newtonian fluid material midsole footwear on tibial shock acceleration and attenuation

Enze Shao[1], Qichang Mei[1,2], Julien S. Baker[3], István Bíró[4], Wei Liu[1]* and Yaodong Gu[1,5]*

[1]Faculty of Sport Science, Ningbo University, Ningbo, China, [2]Auckland Bioengineering Institute, The University of Auckland, Auckland, New Zealand, [3]Centre for Population Health and Medical Informatics, Hong Kong Baptist University, Kowloon, Hong Kong SAR, China, [4]Faculty of Engineering, University of Szeged, Szeged, Hungary, [5]Department of Radiology, Ningbo No. 2 Hospital, Ningbo, China

Introduction: Given the possibility of higher ground temperatures in the future, the pursuit of a cushioning material that can effectively reduce sports injuries during exercise, particularly one that retains its properties at elevated temperatures, has emerged as a serious concern.

Methods: A total of 18 man recreational runners were recruited from Ningbo University and local clubs for participation in this study. Frequency analysis was employed to investigate whether there is a distinction between non-Newtonian (NN) shoes and ethylene vinyl acetate (EVA) shoes.

Results: The outcomes indicated that the utilization of NN shoes furnished participants with superior cushioning when engaging in a 90° cutting maneuver subsequent to an outdoor exercise, as opposed to the EVA material. Specifically, participants wearing NN shoes exhibited significantly lower peak resultant acceleration (p = 0.022) and power spectral density (p = 0.010) values at the distal tibia compared to those wearing EVA shoes. Moreover, shock attenuation was significantly greater in subjects wearing NN shoes (p = 0.023) in comparison to EVA shoes. Performing 90° cutting maneuver in NN shoes resulted in significantly lower peak ground reaction force (p = 0.010), vertical average loading rate (p < 0.010), and vertical instantaneous loading rate (p = 0.030) values compared to performing the same maneuvers in EVA shoes.

Conclusion: The study found that the PRA and PSD of the distal tibia in NN footwear were significantly lower compared to EVA footwear. Additionally, participants exhibited more positive SA while using NN footwear compared to EVA. Furthermore, during the 90° CM, participants wearing NN shoes showed lower PGRF, VAIL, and VILR compared to those in EVA shoes. All these promising results support the capability of NN footwear to offer additional reductions in potential injury risk to runners, especially in high-temperature conditions.

KEYWORDS

non-Newtonian flow, ethylene vinyl acetate, shock acceleration, biomechanics, tibial

1 Introduction

The increased public participation in sports over the last few decades has led to a rise in sport-related pathologies among both recreational and competitive athletes (Knowles et al., 2006; Marconcin et al., 2023). In most sports, athletes commonly employ a heel-toe gait pattern when landing during sports performance (Anderson et al., 2020). In such instances, pronation at the subtalar joint (STJ) occurs from the moment of heel strike to midstance (Leung et al., 1998; Phan et al., 2018). According to Klingman et al. (1997), the pronation of the STJ is correlated with knee flexion and internal tibial rotation. This sequence of movements assumes a pivotal role in dampening the shock when the heel comes into contact with the ground. It is conjectured that the compensatory internal rotation of the femur might aid in preserving alignment during knee extension (Tiberio, 1987; Boutris et al., 2018). Nevertheless, over the long term, athletes and sports performers face an elevated likelihood of encountering discomfort, or worse, injuries to the patellofemoral joint, which has the potential to undermine athletic prowess (Deng et al., 2022). Furthermore, it has been reported that the majority of chronic injuries occurring in the lower limbs are intricately linked to cumulative loading (Van Gent et al., 2007). Particularly pertinent in the realm of athletics, it is noteworthy that between 35% and 49% of fatigue fractures manifest in the tibia (Crossley et al., 1999; Bennell et al., 2004). Numerous variables may indeed exert an impact on bone remodeling, thereby influencing the performance of fatigued bones. What is evident is that biomechanics elucidates the extent of mechanical loading endured by the bone throughout the course of a movement (Levenston and Carter, 1998; Logerstedt et al., 2022). Upon impact with the ground, the velocity of the foot decelerates to zero, leading to the generation of great ground reaction forces (GRF) (Whittle, 1999). This alteration in momentum leads to the compressive loading of lower extremities, resulting in an impact shock delivered via the musculoskeletal system. Consequently, local segment peak accelerations occur at progressively delayed intervals (Derrick, 2004; Reenalda et al., 2019). The correlation between tibial acceleration (TA) and bone strain remains enigmatic and may be intricate due to the influence of localized muscle forces.

It is noteworthy that measuring peak TA using a device directly attached to the tibia proves to be an effective method for revealing plausible correlations with essential GRF parameters (Hennig and Lafortune, 1991). Moreover, due to their convenience, an increasing number of studies are employing wearable inertial measurement units (IMUs) to collect TA data. This approach has provided valuable insights into the mechanisms contributing to the understanding of stress fractures and joint motion injuries (Yong et al., 2018; Milner et al., 2022), utilizing technological approaches such as frequency analysis (Xiang et al., 2022) and machine learning (Tenforde et al., 2020).

When a runner's heel strikes the ground, the rapid deceleration creates a shock wave that travels from the foot to the torso and through the entire skeletal system. The energy of this shockwave is assimilated by various components, encompassing footwear, running surfaces, muscles, bones, and other structural tissues (Derrick et al., 1998). This process of absorbing impact energy, consequently diminishing the amplitude of the shock wave between the foot and the head, is denoted as shock attenuation (SA). In addition to internal forces (Richards et al., 2018), SA and the magnitude of impact acceleration emerge as two pivotal variables scrutinized in running research (Milner et al., 2006), owing to their conjectured correlation with prospective injuries. Researchers believe that in order to minimize damage to proximal structures, SA can be achieved through an interplay of passive and active mechanisms (Derrick et al., 1998; Milner et al., 2006; Zadpoor and Nikooyan, 2012). Based on the above hypotheses, previous studies have explored several factors, such as the performance of eccentric muscle contractions (Mizrahi et al., 2000), running speed (Sheerin et al., 2019), exercise fatigue interventions (Flynn et al., 2004), running surface (Boey et al., 2017), and running shoes (Xiang et al., 2022), while observing and comparing changes in TA. To be definitive, subjects experienced highly significant changes in TA at different running speeds, during different motion interfaces, and under enhanced eccentric muscle contractions. Nevertheless, there is some controversy surrounding the effect of different footwear types on TA (Cheung et al., 2006; Sinclair et al., 2013). These disputes mostly arise due to the variations in footwear conditions and the distinct production process requirements across different footwear companies. Indeed, to ascertain the effect of footwear on tibial impact, more definitive information is required, considering factors such as the exercise environment, movement standards, and other relevant variables. It is worth noting that during exercise, the temperature of the running shoe will naturally increase, which could potentially lead to a deterioration in its cushioning properties (Kinoshita and Bates, 1996).

Indeed, this is often a factor that is overlooked by researchers. Amidst the ongoing escalation of average global temperatures, particularly in the realm of extreme climatic conditions, running footwear may pose an augmented risk of injury to the runner as it experiences heightened temperatures during outdoor exercise engagement (Ebi et al., 2021). This emphasizes the importance of investigating and addressing the impact of temperature changes on running shoe properties for the safety and well-being of athletes. Given the potential for higher ground temperatures in the future, the quest for a cushioning material that can effectively reduce sports injuries during exercise, particularly one that retains its properties at elevated temperatures, has emerged as an urgent necessity. Drawing from the findings of impact dynamics and materials development studies (de Goede et al., 2019), it has been demonstrated that non-Newtonian (NN) fluid materials possess the capability to effectively manage impact force or acceleration decay scenarios. Therefore, in the development of sports protective equipment (Hrysomallis, 2009; Schmitt et al., 2010; La Fauci et al., 2023), designers utilize the viscoelastic and permanent deformation properties of NN fluid to minimize the impact damage of solids on the human body. Undoubtedly, the specific temperature may exert a discernible influence on the functionality of non-Newtonian fluid materials. The effectiveness of these materials in SA and protective equipment largely depends on maintaining the appropriate temperature during their usage. Past investigations have demonstrated that a substantial elevation in the temperature of EVA footwear can lead to a notable surge in the vulnerability to lower limb injuries when individuals partake in physical activities (Shariatmadari et al., 2010). It's worth noting that M. Hojjat et al. observed that the rheological properties of non-Newtonian fluids exhibited shear-thinning behavior following an increase in temperature (Hojjat et al., 2011). Therefore, the incorporation of materials with NN fluid properties into footwear has the potential to provide protection for athletes during outdoor running or sports activities, particularly when the temperature of the footwear rises. By leveraging the unique

characteristics of NN fluid, footwear can better adapt to varying impact conditions, ensuring enhanced SA, and reducing the risk of injuries for athletes.

2 Materials and methods

In this section, we primarily delineate the research hypothesis of this endeavor, elucidate the precise steps undertaken for data acquisition, and expound upon the methodologies employed for data processing throughout the experiment. Subsequently, the statistical analysis approach is detailed. In essence, two IMUs were affixed to the anterolateral distal aspects of the tibia in the subjects. This was carried out to juxtapose the TA and mechanical attributes of the subjects when executing a 90°CM while clad in both EVA and NN footwear.

2.1 Working research hypothesis

The research hypothesis of this study was that there would be significant differences in tibial acceleration and attenuation when participants wore NN shoes during outdoor running sessions for extended periods, as compared to EVA shoes. By examining the impact attenuation and SA of these shoes, this study aims to assess their effectiveness in providing protection and comfort to athletes during outdoor activities in elevated temperatures.

2.2 Participants

Considering the potential differences in TA and impact attenuation due to gender (Sinclair et al., 2012), a total of 18 man recreational runners (age: 24.32 ± 1.20 years, height: 1.78 ± 0.04 m, mass: 64.61 ± 1.22 kg, BMI: 20.22 ± 0.41 kg/m^2) were recruited from Ningbo University and local clubs for participation in this study. A statistical power analysis was performed employing G*Power software, employing a moderate effect size to mitigate the risk of a type II error and ascertain the minimum number of participants requisite for this inquiry (Erdfelder et al., 1996). The input parameters for this experiment were tailored as follows: the effect size was set at 0.4, the significance level (Alpha) at 0.05, the test efficacy (Power) at 0.8, the number of measurements at 3, and the Nonsphericity at 0.5. The sample size employed in this study was adequate to yield statistical power exceeding 80%. The inclusion criteria for participants consisted of recreational level runners, right leg-dominant, and habitual rearfoot strikers. Recreational runners are defined as individuals who engage in running activities 2–4 times per week and cover a distance of at least 20 kilometers per week (Liu et al., 2020). To be eligible for the experiment, the recruited runners had to exhibit no lower limbs injuries or foot deformities in the 6 months preceding the testing Before data collection, all subjects were fully familiarized with testing procedures and different running shoes. All data collection was obtained at the same time of day to minimize the effects of diurnal variation on experimental results. Additionally, all participants were provided with the option to withdraw from the experiment at any stage of testing, and written informed consent was obtained from each participant before commencement of the study. The Ethics Committee of the Ningbo University Research Institute granted approval for this study (RAGH202208193312), which was conducted in adherence to the principles of the Declaration of Helsinki.

2.3 Experiment protocol

The test was divided into three parts, with the first part aimed at determining whether all subjects met the inclusion criteria. In accordance with a previous study, the dominant foot was determined to be the right foot based on the single-legged hop for distance test. The rearfoot strike pattern was characterized by employing the strike index, denoting the center of pressure within the initial 0%–33% of the foot length at contact, as measured by the Footscan® pressure plate (Rsscan International, Olen, Belgium).

The second part of the test consisted of an outdoor five-kilometer even-paced running session in EVA and NN shoes. Participants engaged in a standardized warm-up routine, comprising a 5-min jog at a self-selected pace on a motorized treadmill, along with several stretching exercises. The participants were blinded to the type of shoe used during testing, and shoes were assigned to participants in a random sequence. Afterwards, the participants wore EVA or NN footwear for a 5-kilometer outdoor run, with 18 participants trained in an average outdoor temperature of 38.12 ± 1.20 degrees Celsius. The run was completed at an average pace of 10.8 ± 0.5 km/h. Following 3 days of rest, the subjects once again engaged in a five-kilometer outdoor run, this time wearing EVA or NN shoes, under similar temperature conditions.

The third part of the test involved subjects wearing EVA and NN shoes and collecting the surface temperature of the running shoes immediately after completing a 5-kilometer outdoor run. Immediately after the outdoor run, tibial impact testing was conducted in the laboratory. This involved the simultaneous collection of the subject's vertical ground reaction force and accelerometer data. Indeed, the frequent requirement to perform unexpected or anticipated cutting maneuver (CM) while running or engaging in outdoor activities poses a significant risk of injury (Nagano et al., 2016). Previous studies have confirmed that there is a greater risk during 90° CM. Therefore, in this study, 90° CM was chosen as the impact test action. This was used to assess the effects of footwear and other variables on tibial impact during lateral movements, which were common in various sports and outdoor activities.

The IMUs (IMeasureU V1, Auckland, New Zealand; dimensions: 40 mm × 28 mm × 15 mm, weight: 12 g, resolution: 16 bit) were affixed to the proximal and distal anteromedial regions of the tibia on the dominant leg of each participant using straps. Precisely, two Inertial Measurement Units (IMUs) were situated on the anterior medial aspect of the tibia, exactly 2 centimeters proximal to the ankle and 3 centimeters from the tibia's proximal end (Laughton et al., 2003), and securely fastened with athletic tape up to an acceptable tension level. The vertical axis of the accelerometer was aligned with the tibia (as depicted in Figure 1) (Tenforde et al., 2020). The tension of the belt was carefully adjusted to a level where the acceleration traces for a given impact force remained insensitive to the accelerometer attachment force. This

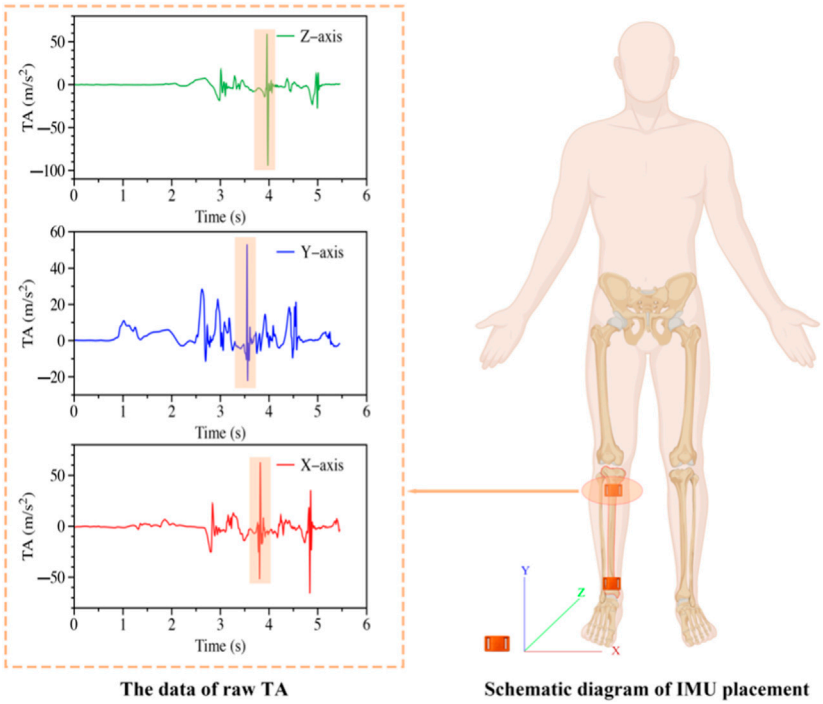

FIGURE 1
Data of raw TA (left) and the IMU fixed position (right). The orange shaded portion of the TA raw data represents the acceleration data recorded during the CMs.

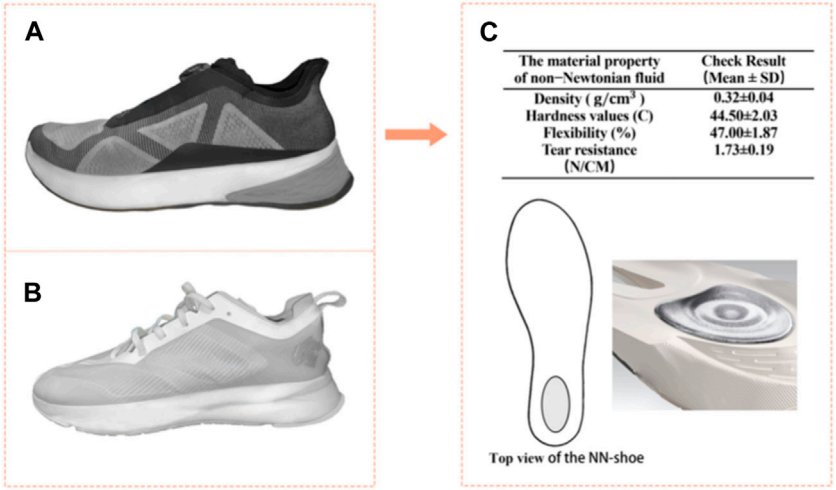

FIGURE 2
Experimental shoes were used by the participants. **(A)** indicate the non-Newtonian fluid (NN) shoe; **(B)** indicate the EVA shoe; **(C)** indicate the material property of non-Newtonian fluid as well as the location of cushion materials within the midsole.

measure was taken to ensure the reproducibility of the data collected during the study (Mizrahi and Susak, 1982). Subsequently, participants performed 90° CM at the corner of the laboratory's six-meter track, maintaining a running speed consistent with outdoor conditions. IMUs were synchronized with an embedded AMTI force platform (AMTI, Watertown, MA, United States), which was placed in the center of the pathway.

A single-beam electronic timing gate (Brower Timing Systems, Draper, UT, United States) was employed to record and control the subject's running speed. During the experiment, each participant performed 90° CM 10 times, and after completing each set of CM, the subject was given a 1-min rest period before the next set. This approach ensures sufficient recovery time between trials to minimize fatigue and maintain the consistency of data collection.

2.4 Footwear characteristics

NN shoes (as shown in Figure 2A) were developed and manufactured by the Japanese manufacturer (Descente Ltd., Kabushiki–gaisha Desanto, Osaka, Japan). The same manufacturer, Descente Ltd., also produced the EVA shoes utilized in this investigate (as shown in Figure 2B). In the NN shoes, the NN material was placed in a triangular area on the heel of the midsole (as shown in Figure 2C). The NN materials and preparation methods used in the footwear have been disclosed in a patent of invention (patent publication No: CN116285389A), and the material properties comply with the national requirements for the production of the footwear in question (Figure 2C).

2.5 Data collection and processing

AMTI was utilized to collect GRF data during the CM at a frequency of 1,000 Hz. As for the GRF of CM, a vertical threshold of 20N was utilized to detect foot strike and toe-off events, thus delineating the stance phase (Yu et al., 2021). To reduce the influence of random noise, the GRF data were filtered using a low-pass, second-order Butterworth filter with a cut-off frequency set at 20 Hz (David et al., 2018). All of the GRF magnitudes were scaled to body mass. This study addresses the vertical GRF associated with the 90° CM performed by the subjects. The key parameters to be compared and analyzed are the peak ground reaction force (PGRF), vertical average loading rate (VALR), and vertical instantaneous loading rate (VILR) (Jiang et al., 2021). These parameters are essential in understanding the impact forces experienced during the CM and their potential implications for injury risk and performance.

The IMUs collected TA data at a frequency of 500 Hz while the subjects were wearing both types of footwear.

To eliminate a linear trend, the raw data signal underwent a process of subtraction, wherein a least-squares best-fit line was deducted from it (Shorten and Winslow, 1992). Subsequently, the collected data was filtered using a second-order Butterworth low-pass filter with a cutoff frequency set at 60 Hz (Hennig and Lafortune, 1991). While axial acceleration is commonly reported, recent recommendations suggest evaluating resultant acceleration (RA) (Sheerin et al., 2019; Milner et al., 2020). Calculated RA was completed using the following formula:

$$\mathbf{RA} = \sqrt{x^2 + y^2 + z^2}$$

x, y, and z represent the acceleration variations in the coronal, sagittal, and transverse planes of the IMU, respectively (shown in Figure 1, right).

Peak resultant acceleration (PRA) was identified as the peak occurring between 50% and 60% of stance. Time-domain and frequency parameters from the accelerometers at both ends of the tibia were computed using a custom MATLAB R2018b program (The MathWorks, Natick, MA, United States). Time-domain parameters were determined based on the last stance phase performed by each participant. To achieve this, the power spectrum was analyzed by converting the time-domain signal to frequency using a discrete fast Fourier transform (FFT). The unfiltered TA data from each stance stage underwent detrending and were subsequently extended with zeros to achieve a total of 2048 data points, ensuring periodicity. To determine the power of the standing-phase TA in the frequency domain, the power spectral density (PSD) was calculated using a square window (Shorten and Winslow, 1992). The PSD analysis was conducted within the frequency range from 0 to the Nyquist frequency (FN) and then normalized into 1 Hz bins (Gillespie and Dickey, 2003). A transfer function has been previously used to determine the degree of SA in human running by calculating the ratio of each frequency bin the distal and proximal tibia signal (i.e., the transmissibility of each frequency component) (Hamill et al., 1995). The transfer function was computed across all frequencies ranging from 0 to FN, aiming to ascertain the extent of SA taking place between the distal and proximal tibia. This calculation was achieved by:

$$\textbf{Shock attenuation} = 10 \times log_{10}\left(PSD_{p\_tibia} / PSD_{d\_tibia}\right)$$

At each of the frequencies, the transfer function determined the gain or attenuation, measured in decibels, between the distal and proximal tibia signals. Positive values signified a gain, indicating an increase in signal strength, while negative values denoted attenuation, representing a reduction in signal strength.

2.6 Statistical analysis

All discrete feature data, including PGRF, VALR, VILR, and PRA, are presented as mean ± standard deviation. A one-way repeated measures analysis of variance (ANOVA) was conducted to assess the impact of shoe condition (differentiating between NN and EVA footwear) on the discrete data. A significance level of $p < 0.05$ was considered acceptable. The *post hoc* pairwise comparison was conducted using the Bonferroni correction, which adjusted the significance level to $p < 0.033$. The Shapiro-Wilk test was utilized to evaluate the normal distribution of RA, PSD, and SA during the 90° CM. Following the results of the normality test (Pataky et al., 2015), SPM1D or SNPM1D analysis was conducted to examine the differences in RA, PSD, and SA when wearing different footwear, respectively. For this analysis, MATLAB R2018b (The MathWorks, Natick, MA, United States) was used to perform all the statistical calculations.

3 Results

Following the completion of the 5-kilometer run, the midsole temperature of the NN footwear escalated from 22.53°C ± 0.43°C to 54.84°C, while the midsole temperature of the EVA footwear rose from 22.46°C ± 0.52°C to 50.87°C. As indicated in Table 1, there was no statistically significant difference in the PRA of the proximal tibia between the two types of footwear ($p = 0.270$). Additionally, the time of foot contact with the ground during the 90° CM was nearly similar for both footwear conditions ($p = 0.550$). The ANOVA revealed a statistical difference in the PRA of the distal tibia between the two shoe conditions ($p = 0.022$). In comparison to EVA shoes, subjects exhibited significantly lower values for PGRF ($p = 0.020$), VALR ($p <$

TABLE 1 The ANOVA results in the discrete characteristics of the two types of shoes {data were presented in mean [standard deviation (SD)]}.

Discrete characteristics	NN	EVA	F–Value	*p*–Value
PRA at distal tibia (g)	14.21 (1.17)	15.37 (2.28)	1.423	**p = 0.022**
PRA at proximal tibia (g)	7.99 (3.61)	10.45 (1.94)	2.367	*p* = 0.270
PGRF (N/kg)	2.43 (0.19)	2.61 (0.30)	5.662	**p = 0.010**
VALR (N/kg/s)	85.23 (23.14)	95.16 (28.02)	12.511	**p < 0.010**
VILR (N/kg/s)	154.27 (28.33)	160.24 (37.22)	17.312	**p = 0.030**
Contact Time (s)	0.24 (0.03)	0.23 (0.02)	0.932	*p* = 0.550

The bold values are meant to indicate that there is statistical significance in the group.

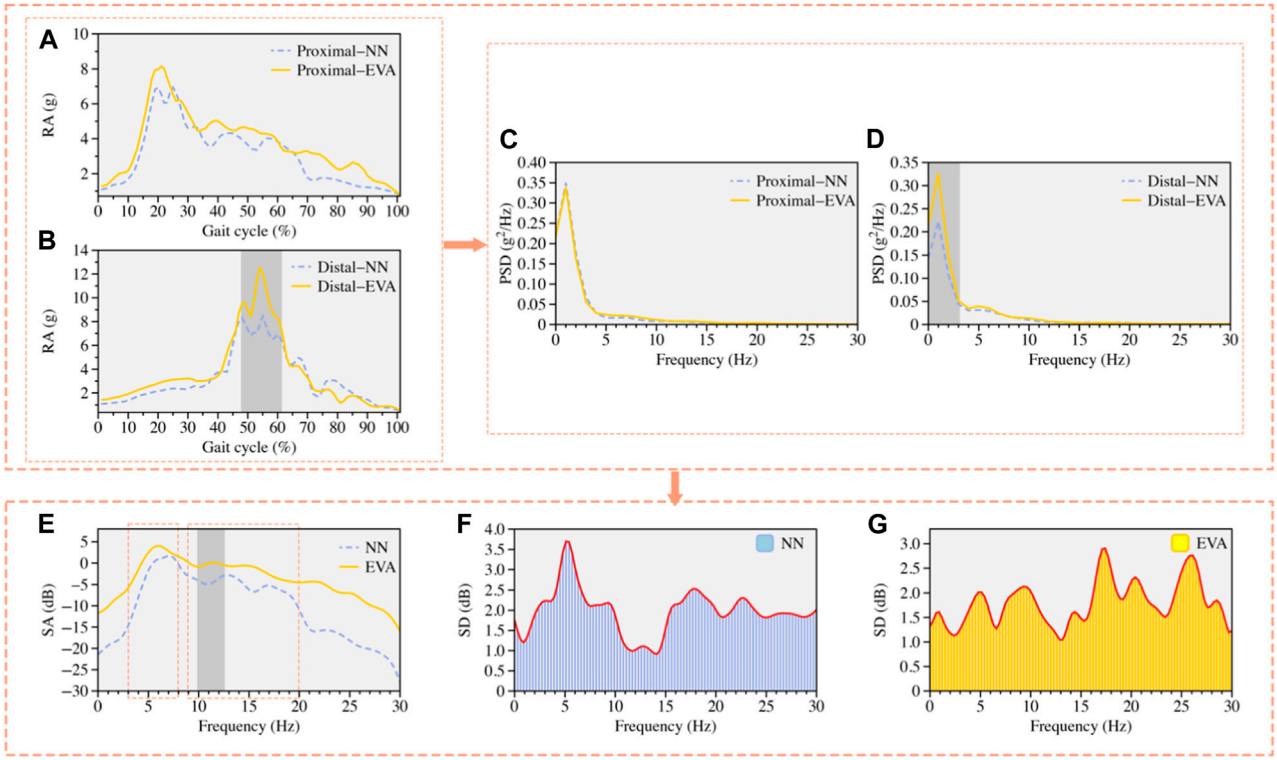

FIGURE 3
The results of the TA processing in the time and frequency domains for the two types of footwear (NN and EVA) were plotted. These encompass the following variables: RA of the proximal tibia **(A)**, RA of the distal tibia **(B)**; PSD of the proximal **(C)** and distal **(D)** tibia; SA from the distal tibia to the proximal tibia **(E)**, and changes in SD of SA in the tibia for non-Newtonian **(F)** and EVA **(G)** footwear. **(A) (B) (C) (D) (E)** The curves depicted in the figures represent the mean changes for the corresponding variables. The deeply shaded areas correspond to the station phases or frequency bands wherein a significant main effect was detected based on the SNPM1D test.

0.010), and VILR (p = 0.030) when performing 90° CM while wearing the NN footwear.

Based on the results of the Shapiro-Wilk test, it was determined that RA, PSD, and SA did not follow a normal distribution (p < 0.05). As a result, these non-normally distributed data were analyzed using the SNPM1D method. As depicted in Figure 3, when comparing the changes in RA with different footwear (Figures 3A, B), it was observed that RA in the distal tibia was significantly higher in the peak region when wearing EVA footwear compared to NN footwear (p = 0.011, 47%–61 stage). As depicted in Figures 3B, C, the PSD in the lower frequency range of the distal tibia exhibited a statistically significant difference between the NN and EVA footwear (p = 0.010). The EVA footwear exhibited significantly greater PSD power at low frequencies compared to the NN footwear. As shown in Figures E, F, the NN footwear demonstrated significantly greater SA at higher frequencies (10–13 Hz) compared to the EVA footwear (p = 0.023). However, there was no significant variation in SA at lower frequencies (3–8 Hz) between the two types of footwear (as shown in Figures E, G).

4 Discussion

The primary objective of this study was to examine the alterations in time and frequency domain attributes of TA in subjects wearing different types of footwear after completing a 5-kilometer run in higher temperature conditions. The research focused on comparing the impact and SA performance of running shoes embedded with NN footwear and EVA running shoes. Through the analysis of TA in both time and frequency domains, the study aimed to elucidate the potential advantages of using NN footwear in offering functional cushioning and decreasing sports-related injuries during exercise in hot environments.

These findings indicate that both types of footwear experienced significant temperature increases during the running activity in higher temperature conditions, with the NN footwear showing a slightly higher temperature rise compared to the EVA footwear. Based on the 90° CM test conducted after the temperature change of the footwear, the study found that the PRA at the distal tibia was significantly lower in NN shoes compared to EVA shoes. Additionally, the PGRF, VALR, and VILR were also significantly lower in NN shoes than in EVA shoes, as indicated in Table 1.

An ideal approach for precisely assessing injury risk in runners would involve direct in-vivo measurement of bone strain. Nevertheless, this approach is invasive and impractical for routine use, as it necessitates surgical implantation of strain gauges or other invasive methods (Liu et al., 2009). Consequently, it has become a widely employed approach to attach accelerometers to the body segments of interest to calculate the corresponding impact forces (Gruber et al., 2014). Previous studies have aimed to observe the protective impact of running shoes on the human body during exercise. This has been achieved by investigating the effect of various footwear conditions, such as traditional footwear (Sinclair and Sant, 2017), minimalist footwear (Sinclair et al., 2013), and customized footwear (Laughton et al., 2003) on alterations in TA. This study builds on previous research and contributes to the understanding of how global temperature changes may impact the performance and function of footwear.

It was readily evident from the time and frequency domain results for TA that distinct footwear conditions led to alterations in distal TA. In the time-domain analysis, the waveforms of TA exhibited differences in their shape and amplitude, indicating variations in impact forces and loading patterns on the tibia between the two types of shoes. These changes are crucial indicators of how the footwear's cushioning and SA properties influenced the tibial response to impact forces during the CM. Previous studies have established that RA effectively mitigated the impact of accelerometer misalignment and accounted for loading forces across all three axes (Norris et al., 2014). The joint kinematics observed at impact, including greater heel vertical velocity, increased lower leg angle, reduced knee flexion angle, and an extended stride length, contribute to higher TA levels upon impact (Potthast et al., 2010). However, throughout the experimental process, we maintained consistency requirements for all factors except the footwear condition. Thus, it is highly plausible that the decreased PRA of the distal tibia in heel strike mode could suggest that the NN footwear might have offered superior mechanical cushioning during braking, in conjunction with the active mechanism of the body's muscular contraction. Compared to NN shoes, EVA shoes resulted in greater TA power magnitude in the lower range. This aligns with previous studies indicating that employing heel strikes leads to increased power amplitude at lower frequencies (Oakley and Pratt, 1988). As the heel strike mode of running involves reduced knee flexion and velocity, it induces an elevation in the power amplitude of the tibial signal below 10 Hz. In other words, engaging in running with NN shoes may lead to an increase in a specific knee flexion angle, where a compliant knee assumes a more significant role in active shock attenuation during rearfoot running compared to the ankle. No significant alteration in impact force and impact attenuation was observed in the proximal tibia when wearing different footwear, which could be attributed to the mechanical cushioning function of the footwear predominantly acting from the ankle to the distal tibia (Schütte et al., 2018). The mechanical cushioning function of footwear, typically concentrated in the midsole area, proves particularly effective in mitigating impact forces transmitted to the distal tibia. When the foot contacts the ground during running, the cushioning materials in the midsole efficiently absorb and disperse impact energy, thereby reducing the forces exerted on the distal tibia and safeguarding the lower limb against excessive loading.

Consequently, for knee injury prevention, it becomes crucial to consider additional measures that focus on mechanical cushioning or training tools that enhance active cushioning. This is especially important as the knee plays a more substantial role in shock absorption of external forces compared to the ankle (Hamill et al., 2014). Furthermore, NN footwear exhibited a greater SA effect in the higher frequency domain when compared to EVA footwear. This indicates that the tibia is able to dissipate a higher amount of shock load with NN footwear (Gruber et al., 2014). SA can be considered an accelerometry variable that may offer a more precise reflection of impact severity, particularly when the effective mass is not constant. The extent of required attenuation can modify the runner's kinematics and performance, making it a critical factor to consider (Derrick, 2004). Prior research has validated that higher PGRF, VAIL, and VILR may elevate the risk of injury in runners (Logan et al., 2010). Conversely, higher impact and loading rates could suggest that the footwear provides insufficient cushioning, thereby increasing the risk of lower extremity injuries. The findings presented in Table 1 demonstrated that, with no alteration to other footwear properties, the footwear with only the addition of NN material exhibited substantial changes in PGRF, VAIL, and VILR. Indeed, the significant changes in PGRF, VAIL, and VILR illustrated the positive impact of NN material on the footwear's shock-absorbing capabilities. The study emphasizes the potential of employing advanced materials in sports footwear design to enhance athlete performance and reduce the risk of injury, particularly in situations where elevated temperatures may affect the cushioning properties of the footwear.

In the process of interpreting the results, it is crucial to acknowledge several limitations inherent in the current study. Specifically, only male runners who habitually employ a rearfoot strike pattern were recruited as participants. Hence, it is important to note that these findings are not applicable to habitual mid- and forefoot strike runners. Ultimately, it's imperative to note that this study was conducted within a controlled laboratory setting and the impact of similar training in runners' more natural environment

remains unknown. In addition, future studies should also consider the biomechanical effects associated with gender differences.

5 Conclusion

The study found that the PRA and PSD of the distal tibia in NN footwear were significantly lower compared to EVA footwear. Additionally, participants exhibited more positive SA while using NN footwear compared to EVA. Furthermore, during the 90° CM, participants wearing NN shoes showed lower PGRF, VAIL, and VILR compared to those in EVA shoes. All these promising results support the capability of NN footwear to offer additional reductions in potential injury risk to runners, especially in high-temperature conditions.

Data availability statement

The original contributions presented in the study are included in the article/Supplementary Material, further inquiries can be directed to the corresponding authors.

Ethics statement

The studies involving humans were approved by the ethics committee of ningbo university. The studies were conducted in accordance with the local legislation and institutional requirements. The participants provided their written informed consent to participate in this study.

Author contributions

ES: Conceptualization, Data curation, Formal Analysis, Investigation, Methodology, Writing–original draft. QM: Data curation, Formal Analysis, Writing–original draft. JB: Methodology, Supervision, Writing–review and editing. IB: Data curation, Methodology, Writing–original draft. WL: Conceptualization, Formal Analysis, Investigation, Methodology, Writing–original draft. YG: Conceptualization, Formal Analysis, Funding acquisition, Investigation, Methodology, Writing–review and editing.

Funding

The author(s) declare financial support was received for the research, authorship, and/or publication of this article. This study was sponsored by the Zhejiang Provincial Natural Science Foundation of China for Distinguished Young Scholars (LR22A020002), Zhejiang Provincial Key Research and Development Program of China (2021C03130), Zhejiang Provincial Natural Science Foundation (LTGY23H040003), Ningbo key R&D Program (2022Z196), the Project of NINGBO Leading Medical & Health Discipline (Nos 2022-F15 and Nos 2022-F22), Ningbo Natural Science Foundation (20221JCGY010532 and 20221JCGY010607), Public Welfare Science & Technology Project of Ningbo, China (2021S134), and Zhejiang Rehabilitation Medical Association Scientific Research Special Fund (ZKKY2023001).

Conflict of interest

The authors declare that the research was conducted in the absence of any commercial or financial relationships that could be construed as a potential conflict of interest.

The author(s) declared that they were an editorial board member of Frontiers, at the time of submission. This had no impact on the peer review process and the final decision.

Publisher's note

References

Anderson, L. M., Bonanno, D. R., Hart, H. F., and Barton, C. J. (2020). What are the benefits and risks associated with changing foot strike pattern during running? A systematic review and meta-analysis of injury, running economy, and biomechanics. *Sports Med.* 50, 885–917. doi:10.1007/s40279-019-01238-y

Bennell, K., Crossley, K., Jayarajan, J., Walton, E., Warden, S., Kiss, Z. S., et al. (2004). Ground reaction forces and bone parameters in females with tibial stress fracture. *Med. Sci. Sports Exerc.* 36, 397–404. doi:10.1249/01.mss.0000117116.90297.e1

Boey, H., Aeles, J., Schütte, K., and Vanwanseele, B. (2017). The effect of three surface conditions, speed and running experience on vertical acceleration of the tibia during running. *Sports Biomech.* 16, 166–176. doi:10.1080/14763141.2016.1212918

Boutris, N., Byrne, R. A., Delgado, D. A., Hewett, T. E., Mcculloch, P. C., Lintner, D. M., et al. (2018). Is there an association between noncontact anterior cruciate ligament injuries and decreased hip internal rotation or radiographic femoroacetabular impingement? A systematic review. *Arthrosc. J. Arthrosc. Relat. Surg.* 34, 943–950. doi:10.1016/j.arthro.2017.08.302

Cheung, R. T., Ng, G. Y., and Chen, B. F. (2006). Association of footwear with patellofemoral pain syndrome in runners. *Sports Med.* 36, 199–205. doi:10.2165/00007256-200636030-00002

Crossley, K., Bennell, K., Wrigley, T., and Oakes, B. W. (1999). Ground reaction forces, bone characteristics, and tibial stress fracture in male runners. *Med. Sci. Sports Exerc.* 31, 1088–1093. doi:10.1097/00005768-199908000-00002

David, S., Mundt, M., Komnik, I., and Potthast, W. (2018). Understanding cutting maneuvers–The mechanical consequence of preparatory strategies and foot strike pattern. *Hum. Mov. Sci.* 62, 202–210. doi:10.1016/j.humov.2018.10.005

De Goede, T. C., De Bruin, K. G., and Bonn, D. (2019). High-velocity impact of solid objects on Non-Newtonian Fluids. *Sci. Rep.* 9, 1250. doi:10.1038/s41598-018-37543-1

Deng, F., Adams, R., Pranata, A., Cui, F., and Han, J. (2022). Tibial internal and external rotation taping for improving pain in patients with patellofemoral pain syndrome. *J. Sci. Med. Sport* 25, 644–648. doi:10.1016/j.jsams.2022.04.003

Derrick, T. R. (2004). The effects of knee contact angle on impact forces and accelerations. *Med. Sci. Sports Exerc.* 36, 832–837. doi:10.1249/01.mss.0000126779.65353.cb

Derrick, T. R., Hamill, J., and Caldwell, G. E. (1998). Energy absorption of impacts during running at various stride lengths. *Med. Sci. Sports Exerc.* 30, 128–135. doi:10.1097/00005768-199801000-00018

Ebi, K. L., Capon, A., Berry, P., Broderick, C., De Dear, R., Havenith, G., et al. (2021). Hot weather and heat extremes: health risks. *Lancet* 398, 698–708. doi:10.1016/s0140-6736(21)01208-3

Erdfelder, E., Faul, F., and Buchner, A. (1996). GPOWER: a general power analysis program. *Behav. Res. Methods, Instrum. Comput.* 28, 1–11. doi:10.3758/bf03203630

Flynn, J. M., Holmes, J. D., and Andrews, D. M. (2004). The effect of localized leg muscle fatigue on tibial impact acceleration. *Clin. Biomech.* 19, 726–732. doi:10.1016/j.clinbiomech.2004.04.015

Gillespie, K. A., and Dickey, J. P. (2003). Determination of the effectiveness of materials in attenuating high frequency shock during gait using filterbank analysis. *Clin. Biomech.* 18, 50–59. doi:10.1016/s0268-0033(02)00171-7

Gruber, A. H., Boyer, K. A., Derrick, T. R., and Hamill, J. (2014). Impact shock frequency components and attenuation in rearfoot and forefoot running. *J. Sport health Sci.* 3, 113–121. doi:10.1016/j.jshs.2014.03.004

Hamill, J., Derrick, T. R., and Holt, K. G. (1995). Shock attenuation and stride frequency during running. *Hum. Mov. Sci.* 14, 45–60. doi:10.1016/0167-9457(95)00004-c

Hamill, J., Gruber, A. H., and Derrick, T. R. (2014). Lower extremity joint stiffness characteristics during running with different footfall patterns. *Eur. J. Sport Sci.* 14, 130–136. doi:10.1080/17461391.2012.728249

Hennig, E. M., and Lafortune, M. A. (1991). Relationships between ground reaction force and tibial bone acceleration parameters. *J. Appl. Biomechanics* 7, 303–309. doi:10.1123/ijsb.7.3.303

Hojjat, M., Etemad, S. G., Bagheri, R., and Thibault, J. (2011). Rheological characteristics of non-Newtonian nanofluids: experimental investigation. *Int. Commun. Heat Mass Transf.* 38, 144–148. doi:10.1016/j.icheatmasstransfer.2010.11.019

Hrysomallis, C. (2009). Surrogate thigh model for assessing impact force attenuation of protective pads. *J. Sci. Med. Sport* 12, 35–41. doi:10.1016/j.jsams.2007.07.013

Jiang, X., Zhou, H., Quan, W., Hu, Q., Baker, J. S., and Gu, Y. (2021). Ground reaction force differences between bionic shoes and neutral running shoes in recreational male runners before and after a 5 km run. *Int. J. Environ. Res. Public Health* 18, 9787. doi:10.3390/ijerph18189787

Kinoshita, H., and Bates, B. T. (1996). The effect of environmental temperature on the properties of running shoes. *J. Appl. Biomechanics* 12, 258–268. doi:10.1123/jab.12.2.258

Klingman, R. E., Liaos, S. M., and Hardin, K. M. (1997). The effect of subtalar joint posting on patellar glide position in subjects with excessive rearfoot pronation. *J. Orthop. Sports Phys. Ther.* 25, 185–191. doi:10.2519/jospt.1997.25.3.185

Knowles, S. B., Marshall, S. W., and Guskiewicz, K. M. (2006). Issues in estimating risks and rates in sports injury research. *J. Athl. Train.* 41, 207–215. doi:10.17615/texn-bm57

La Fauci, G., Parisi, M., Nanni, A., Crosetta, L., Pugno, N. M., and Colonna, M. (2023). Design and proof-of-concept of an advanced protective system for the dissipation of tangential impact energy in helmets, based on non-Newtonian fluids. *Smart Mater. Struct.* 32, 044004. doi:10.1088/1361-665x/acc148

Laughton, C. A., Davis, I. M., and Hamill, J. (2003). Effect of strike pattern and orthotic intervention on tibial shock during running. *J. Appl. Biomechanics* 19, 153–168. doi:10.1123/jab.19.2.153

Leung, A., Mak, A., and Evans, J. (1998). Biomechanical gait evaluation of the immediate effect of orthotic treatment for flexible flat foot. *Prosthetics Orthot. Int.* 22, 25–34. doi:10.3109/03093649809164454

Levenston, M. E., and Carter, D. R. (1998). An energy dissipation-based model for damage stimulated bone adaptation. *J. Biomechanics* 31, 579–586. doi:10.1016/s0021-9290(98)00039-6

Liu, Q., Mo, S., Cheung, V. C., Cheung, B. M., Wang, S., Chan, P. P., et al. (2020). Classification of runners' performance levels with concurrent prediction of biomechanical parameters using data from inertial measurement units. *J. Biomechanics* 112, 110072. doi:10.1016/j.jbiomech.2020.110072

Liu, T., Inoue, Y., and Shibata, K. (2009). Development of a wearable sensor system for quantitative gait analysis. *Measurement* 42, 978–988. doi:10.1016/j.measurement.2009.02.002

Logan, S., Hunter, I., Hopkins, J. T., Feland, J. B., and Parcell, A. C. (2010). Ground reaction force differences between running shoes, racing flats, and distance spikes in runners. *J. Sports Sci. Med.* 9, 147–153.

Logerstedt, D. S., Ebert, J. R., Macleod, T. D., Heiderscheit, B. C., Gabbett, T. J., and Eckenrode, B. J. (2022). Effects of and response to mechanical loading on the knee. *Sports Med.* 52, 201–235. doi:10.1007/s40279-021-01579-7

Marconcin, P., Silva, A. L., Flôres, F., Nunes, A., Lourenço, J. F., Peralta, M., et al. (2023). Association between musculoskeletal injuries and depressive symptoms among athletes: a systematic review. *Int. J. Environ. Res. Public Health* 20, 6130. doi:10.3390/ijerph20126130

Milner, C. E., Ferber, R., Pollard, C. D., Hamill, J., and Davis, I. S. (2006). Biomechanical factors associated with tibial stress fracture in female runners. *Med. Sci. Sports Exerc.* 38, 323–328. doi:10.1249/01.mss.0000183477.75808.92

Milner, C. E., Foch, E., Gonzales, J. M., and Petersen, D. (2022). Biomechanics associated with tibial stress fracture in runners: a systematic review and meta-analysis. *J. Sport Health Sci.* 12, 333–342. doi:10.1016/j.jshs.2022.12.002

Milner, C. E., Hawkins, J. L., and Aubol, K. G. (2020). Tibial acceleration during running is higher in field testing than indoor testing. *Med. Sci. Sports Exerc.* 52, 1361–1366. doi:10.1249/mss.0000000000002261

Mizrahi, J., and Susak, Z. (1982). *In-vivo elastic and damping response of the human leg to impact forces.*

Mizrahi, J., Verbitsky, O., and Isakov, E. (2000). Shock accelerations and attenuation in downhill and level running. *Clin. Biomech.* 15, 15–20. doi:10.1016/s0268-0033(99)00033-9

Nagano, Y., Sasaki, S., Higashihara, A., and Ishii, H. (2016). Gender differences in trunk acceleration and related posture during shuttle run cutting. *Int. Biomech.* 3, 33–39. doi:10.1080/23335432.2016.1191372

Norris, M., Anderson, R., and Kenny, I. C. (2014). Method analysis of accelerometers and gyroscopes in running gait: a systematic review. *Proc. Institution Mech. Eng. Part P J. Sports Eng. Technol.* 228, 3–15. doi:10.1177/1754337113502472

Oakley, T., and Pratt, D. (1988). Skeletal transients during heel and toe strike running and the effectiveness of some materials in their attenuation. *Clin. Biomech.* 3, 159–165. doi:10.1016/0268-0033(88)90062-9

Pataky, T. C., Vanrenterghem, J., and Robinson, M. A. (2015). Zero-vs. one-dimensional, parametric vs. non-parametric, and confidence interval vs. hypothesis testing procedures in one-dimensional biomechanical trajectory analysis. *J. Biomechanics* 48, 1277–1285. doi:10.1016/j.jbiomech.2015.02.051

Phan, C.-B., Nguyen, D.-P., Lee, K.-M., and Koo, S. (2018). Relative movement on the articular surfaces of the tibiotalar and subtalar joints during walking. *Bone & Jt. Res.* 7, 501–507. doi:10.1302/2046-3758.78.bjr-2018-0014.r1

Potthast, W., Brüggemann, G.-P., Lundberg, A., and Arndt, A. (2010). The influences of impact interface, muscle activity, and knee angle on impact forces and tibial and femoral accelerations occurring after external impacts. *J. Appl. Biomechanics* 26, 1–9. doi:10.1123/jab.26.1.1

Reenalda, J., Maartens, E., Buurke, J. H., and Gruber, A. H. (2019). Kinematics and shock attenuation during a prolonged run on the athletic track as measured with inertial magnetic measurement units. *Gait Posture* 68, 155–160. doi:10.1016/j.gaitpost.2018.11.020

Richards, R. E., Andersen, M. S., Harlaar, J., and Van Den Noort, J. (2018). Relationship between knee joint contact forces and external knee joint moments in patients with medial knee osteoarthritis: effects of gait modifications. *Osteoarthr. Cartil.* 26, 1203–1214. doi:10.1016/j.joca.2018.04.011

Schmitt, K.-U., Liechti, B., Michel, F. I., Stämpfli, R., and Brühwiler, P. A. (2010). Are current back protectors suitable to prevent spinal injury in recreational snowboarders? *Br. J. Sports Med.* 44, 822–826. doi:10.1136/bjsm.2010.072728

Schütte, K. H., Seerden, S., Venter, R., and Vanwanseele, B. (2018). Influence of outdoor running fatigue and medial tibial stress syndrome on accelerometer-based loading and stability. *Gait Posture* 59, 222–228. doi:10.1016/j.gaitpost.2017.10.021

Shariatmadari, M., English, R., and Rothwell, G. (2010). "Effects of temperature on the performance of footwear foams: review of developments," in Proceedings of the 26th Southern Biomedical Engineering Conference SBEC 2010, College Park, Maryland, USA, April 2010 (Springer), 409–413.

Sheerin, K. R., Reid, D., and Besier, T. F. (2019). The measurement of tibial acceleration in runners—a review of the factors that can affect tibial acceleration during running and evidence-based guidelines for its use. *Gait Posture* 67, 12–24. doi:10.1016/j.gaitpost.2018.09.017

Shorten, M. R., and Winslow, D. S. (1992). Spectral analysis of impact shock during running. *J. Appl. Biomechanics* 8, 288–304. doi:10.1123/ijsb.8.4.288

Sinclair, J., Greenhalgh, A., Brooks, D., Edmundson, C. J., and Hobbs, S. J. (2013). The influence of barefoot and barefoot-inspired footwear on the kinetics and kinematics of running in comparison to conventional running shoes. *Footwear Sci.* 5, 45–53. doi:10.1080/19424280.2012.693543

Sinclair, J., Greenhalgh, A., Edmundson, C. J., Brooks, D., and Hobbs, S. J. (2012). Gender differences in the kinetics and kinematics of distance running: implications for footwear design. *Int. J. Sports Sci. Eng.* 6, 118–128.

Sinclair, J., and Sant, B. (2017). The effects of cross-fit footwear on the kinetics and kinematics of running. *Footwear Sci.* 9, 41–48. doi:10.1080/19424280.2016.1268212

Tenforde, A. S., Hayano, T., Jamison, S. T., Outerleys, J., and Davis, I. S. (2020). Tibial acceleration measured from wearable sensors is associated with loading rates in injured runners. *PM&R* 12, 679–684. doi:10.1002/pmrj.12275

Tiberio, D. (1987). The effect of excessive subtalar joint pronation on patellofemoral mechanics: a theoretical model. *J. Orthop. Sports Phys. Ther.* 9, 160–165. doi:10.2519/jospt.1987.9.4.160

Van Gent, R., Siem, D., Van Middelkoop, M., Van Os, A., Bierma-Zeinstra, S., Koes, B., et al. (2007). Incidence and determinants of lower extremity running injuries in long

distance runners: a systematic review * COMMENTARY. *Br. J. Sports Med.* 41, 469–480. doi:10.1136/bjsm.2006.033548

Whittle, M. W. (1999). Generation and attenuation of transient impulsive forces beneath the foot: a review. *Gait Posture* 10, 264–275. doi:10.1016/s0966-6362(99)00041-7

Xiang, L., Gu, Y., Rong, M., Gao, Z., Yang, T., Wang, A., et al. (2022). Shock acceleration and attenuation during running with minimalist and maximalist shoes: a time-and frequency-domain analysis of tibial acceleration. *Bioengineering* 9, 322. doi:10.3390/bioengineering9070322

Yong, J. R., Silder, A., Montgomery, K. L., Fredericson, M., and Delp, S. L. (2018). Acute changes in foot strike pattern and cadence affect running parameters associated with tibial stress fractures. *J. Biomechanics* 76, 1–7. doi:10.1016/j.jbiomech.2018.05.017

Yu, L., Mei, Q., Xiang, L., Liu, W., Mohamad, N. I., István, B., et al. (2021). Principal component analysis of the running ground reaction forces with different speeds. *Front. Bioeng. Biotechnol.* 9, 629809. doi:10.3389/fbioe.2021.629809

Zadpoor, A. A., and Nikooyan, A. A. (2012). The effects of lower-extremity muscle fatigue on the vertical ground reaction force: a meta-analysis. *Proc. Institution Mech. Eng. Part H J. Eng. Med.* 226, 579–588. doi:10.1177/0954411912447021

frontiers | Frontiers in Bioengineering and Biotechnology

TYPE Original Research
PUBLISHED 21 December 2023
DOI 10.3389/fbioe.2023.1320404

OPEN ACCESS

EDITED BY
Bernardo Innocenti,
Université libre de Bruxelles, Belgium

REVIEWED BY
Silvio Rene Lorenzetti,
Swiss Federal Institute of Sport Magglingen, Switzerland
Yang Song,
Óbuda University, Hungary

*CORRESPONDENCE
Shengnian Zhang,
zhangsnx@163.com

RECEIVED 12 October 2023
ACCEPTED 27 November 2023
PUBLISHED 21 December 2023

CITATION
Peng D, Mao Z, Zhang W, Yu J and Zhang S (2023), *In vivo* knee biomechanics during badminton lunges at different distances and different foot positions by using the dual fluoroscopic imaging system.
Front. Bioeng. Biotechnol. 11:1320404.
doi: 10.3389/fbioe.2023.1320404

In vivo knee biomechanics during badminton lunges at different distances and different foot positions by using the dual fluoroscopic imaging system

Di Peng, Zheng Mao, Wang Zhang, Jinglun Yu and Shengnian Zhang*

Key Laboratory of Exercise and Health Sciences of Ministry of Education, School of Exercise and Health, Shanghai University of Sport, Shanghai, China

Background: Lunges are common in badminton. Distance and foot position affect knee joint loadings under lunges, which are closely related to knee injury incidence. Investigations involving dynamic knee motion *in vivo*, kinetics, and muscle activation in lunges, especially during lunges of different distances and foot positions, are instrumental for understanding knee performance and injury risks of players.

Methods: A total of 10 experienced badminton athletes (10 females; height, 164.5 ± 5.0 cm; weight, 59.3 ± 6.0 kg; and age, 22 ± 1.0 years) were recruited. By using a high-speed dual fluoroscopic imaging system, Qualisys motion capture system, Kistler force plate, and Delsys electromyography simultaneously, data were collected during players' 1.5 times leg length lunge, the maximum lunge, and the maximum lunge while the foot rotated externally. Magnetic resonance and dual fluoroscopic imaging techniques were used to analyze the *in vivo* knee kinematics.

Results: Compared with the 1.5 times leg length lunge, knee flexion for the maximum lunge increased significantly ($p < 0.05$). The anterior–posterior ground reaction force (GRF) and vertical GRF of the maximum lunge were significantly higher than those of the 1.5 times leg length lunge. During the two different foot position lunges with the maximum distance, the posterior translation of knee joint was larger ($p < 0.05$) when the foot rotated externally than the normal maximum lunge. Moreover, the anterior–posterior GRF and vertical GRF increased significantly when the foot rotated externally. Significant differences were observed in valgus–varus rotation torque and internal–external rotation torque of the knee joint under the two distance lunges and two foot position lunges ($p < 0.05$). No significant difference was found in knee muscle activation during the two distance lunges and during the two foot position lunges.

Conclusion: High knee torque and compressive loadings with increasing lunge distance may cause knee injuries in badminton. When lunging in the external foot rotation under the maximum distance, high quadriceps force and posterior tibia translation force could result in knee injuries among badminton players.

KEYWORDS

fluoroscopy, knee kinematics, badminton, lunges, sports injury

1 Introduction

Badminton is a highly demanding game characterized by high-intensity, intermittent actions (Phomsoupha and Laffaye, 2015). The lunge is one of the most frequently used movements in badminton (Shariff et al., 2009). The sudden and repeated lunge is relevant to badminton injuries, and it is especially common in overuse injuries. The prevalence of overuse injuries in badminton matches is about 36%, and the majority of injuries occur in the lower extremities (Jacobson et al., 2005). The knee joint is a highly documented injured site in the lower extremities of badminton players (Jørgensen and Winge, 1990).

The incidence of knee injuries is closely associated with strenuous impact force (Dos'Santos et al., 2018). Large vertical and horizontal loadings at the heel contact phase under lunges generate a high joint torque on the knee joint, contributing to anterior cruciate ligament (ACL) injuries (Abián-Vicén et al., 2012; Lam et al., 2017). In addition, repeated and accumulated loadings can cause overuse knee injuries (Shariff et al., 2009; Boesen et al., 2011), such as patellar tendinosis or patellofemoral joint pain syndrome (Jørgensen and Winge, 1990; Kimura et al., 2010; Lam et al., 2017).

High loadings influence the dynamic knee motion during lunges, resulting in large anterior tibia translation (ATT) and large varus rotation (Hewett et al., 2005). Notably, large tibia internal rotation can significantly strain the ACL (Markolf et al., 1995) and increase the potential risk of the knees. Abnormal movements of the knee joint can also lead to meniscus tear and cartilage degeneration (Riemann and Lephart, 2002). Abnormal kinematics and consequent abnormal cartilage deformation within the joints initiate knee osteoarthritis (Felson et al., 2000; Sharma et al., 2001).

The left-forward lunge is considered a critical maneuver for badminton biomechanics because of its significantly higher external and insole loadings than other lunge directions (Dos'Santos et al., 2018; Hong et al., 2014). Besides lunges of different directions, players also perform lunges of various distances to move into the best position for varying offensive and defensive shots in a match. The lunge distance is the distance from which the player begins to lunge until the last footstep before hitting the shuttlecock, which indirectly reflects the players' lunging performance. Lunge distances have been linked with the leg length of badminton players, such as 1.5 times leg length (Kuntze et al., 2010) and 2.5 times leg length (Hong et al., 2014; Huang et al., 2014). The maximum lunging distance is also analyzed to assess the players' maximal lunge capabilities (Hu et al., 2015). Thus, increased attention to impact loading characteristics during the left-forward lunge of different distances is warranted. Players show different foot positions frequently during lunges in competition, especially when the lunge distance increases to the maximum. No clear indication is given concerning the optimal angle of foot placement in badminton lunges. However, foot placement and body alignment play a significant role in balance and mobility (Paillard et al., 2006). Furthermore, foot position affects the muscle activation level of the lower limbs, especially affecting the activation of quadriceps and hamstrings of knee joints (Wang et al., 1990). Thus, lunge distance and foot position are suggested to be essential for lunge performances and badminton injuries.

Accurate quantification of six degrees of freedom (DOF) knee kinematics during lunges is critical to promote sports performances and recognize abnormal motion relevant to injury mechanisms of badminton players. In general, the external joint moments and 3D motion of players were previously used as surrogate variables to analyze lunge characteristics (Huang et al., 2014; Hu et al., 2015). How precisely the femur and the tibia translate or rotate under left-forward lunges in badminton has been scarcely reported *in vivo*, as well as under left-forward lunges of different distances and different foot positions. The dual fluoroscopy imaging system (DFIS) enables the accurate monitoring of *in vivo* bone motion without soft tissue artifacts (Li et al., 2013). DFIS is a new non-invasive bone movement tracking system that has been used for 3D kinematic measurement. It has been validated with submillimeter and sub-degree accuracy in translation and rotation (Yack et al., 1994).

The current study used DFIS to measure *in vivo* knee translations and rotations of badminton players during left-forward lunges of two distances and two foot positions, as well as to investigate the kinetics and knee muscle activation of players performing lunges. The primary objective of this study was to investigate the *in vivo* knee performance in left-forward lunges and examine the knee biomechanics and potential knee injury risks in badminton lunges. The second objective was to explore the effects of distance and foot position on the knee performance of badminton players in left-forward lunges. We hypothesized that femoral valgus rotation, posterior translation, and distal translation may increase in the maximum lunge. We observed distinct knee performances of kinetics and muscle activation in players doing left-forward lunges under two distances and two foot positions.

2 Materials and methods

2.1 Study protocol

Ten experienced badminton athletes were recruited in this study (10 females; height, 164.5 ± 5.0 cm; weight 59.3 ± 6.0 kg; and age, 22 ± 1.0 years) according to experience. The players were all active participants in singles badminton competitions at the university level and had at least 5 years of badminton experience. All participants had no history of injuries or surgeries in their lower limbs. The right leg must be their dominant leg, and we verified this information by observing which leg the subjects used when they were asked to kick a football. All players were free from any lower extremity injuries for at least 6 months prior to the experiment. The task encompassed three components: the left-forward lunge at a distance of 1.5 times the individual's leg length, the individual's maximum left-forward distance, and the maximum left-forward lunge with foot external rotation. This study was approved by the local ethics committee, and all participants signed an informed consent form.

High-speed dual-plane fluoroscopic imaging system, force plate (60 cm × 50 cm × 10 cm, Kistler Corporation, Winterthur, Switzerland) with 1,000 Hz, motion analysis system of eight cameras (Oqus700+, Qualisys, Switzerland) with 200 Hz, and Delsys wireless surface electromyography with 2000 Hz were used simultaneously in the study (Figure 1). DFIS images were acquired using two commercially available BV Pulsera C-arms and 40 cm

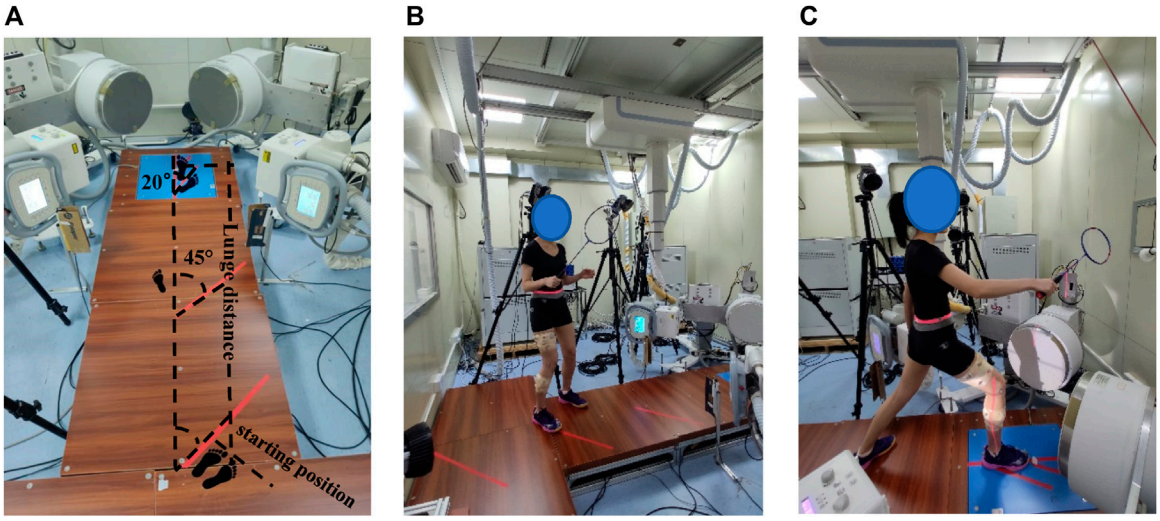

FIGURE 1
(A) Experimental set-up. **(B)** Subject prepared a standardized initial position at the starting position. **(C)** Subject performed the 1.5 times *leg length left-forward lunge.

image intensifiers with a sampling frequency of 100 Hz, 60–70 kVp, 60–70 mA, and 1 ms pulsed exposure during lunging.

2.2 Data collection

The subjects' right knee was scanned by a 3-T magnetic resonance imaging (MRI) scanner before the trial (voxel size: 0.3 mm × 0.3 mm × 1.0 mm, FOV read: 180 mm, and slice thickness: 1 mm). Bone contours from MRI images were extracted to reconstruct the 3D geometry of the femur and tibia in Avizon 2019.1 (Thermo Fisher Scientific) software. These high-resolution images were manually segmented to create a finite element mesh of the bones of the femur and tibia.

The basic data of the participants (i.e., age, gender, body weight, and height) were collected. The leg length (vertical distance from the anterior superior iliac spine to the ground) was also measured. One experimenter explained the procedure to subjects, instructed them to perform warm-up exercises for 10 min, including stretching and jogging, and familiarized them with left-forward lunges.

Eight surface electrodes were set to the right lower limb's rectus femoris, vastus lateral, vastus medial, biceps femoris, semitendinosus, lateral gastrocnemius, medial gastrocnemius, and tibialis anterior. Subsequently, we tested the maximum voluntary contraction (MVC) of the muscles when subjects were asked to resist to complete isometric contraction for 5–8 s, to normalize the EMG data of each muscle. Reflective markers were placed over the participants' right legs according to a previous segment model (Lam WK et al., 2017).

All participants were asked to wear Decathlon BS 530 badminton shoes during lunge trials, and this shoe is often used in badminton training and competitions. Lunge tasks included a lunge distance equal to 1.5 times the length of an individual's leg, individual's maximum distance, and maximum lunge with foot external rotation. The interval between groups was 30 s. Compared with the maximum lunge, the femur rotated externally, the right toe was far from the body, and the foot deviation angle increased by 20° in the maximum lunge with foot external rotation (Figure 1). Both tasks were required to lunge with the maximum distance. That 20° deviation angle was based on the angle of players' foot external rotation in training and matches, as well as the suggestions from coaches.

Before the actual trial, each participant familiarized themselves with the left-forward lunge. Nine successful lunges (one block of three trials) should be collected successfully. The participants prepared a standardized initial position at the starting point holding the badminton racket, extended their dominant leg as far as possible, and landed on the force platform while hitting the shuttlecock. After hitting, participants were required to return to the starting position quickly. A successful lunge trial consisted of maximum effort, correct foot placement at the starting and ending line, contact of the dominant leg with the center of the force plate, the hit of the shuttlecock, and rapid recovery. Participants performed each lunge in one step. Lunge start and finish points were marked out as visual references. The start point was 45° with respect to the longitudinal axis of the force platform (Figure 1).

2.3 Data reduction

2.3.1 3D kinematic and kinetic data

Raw kinematic and kinetic data were exported to Visual3D software (C-Motion Inc., Rockville, MD, United States) and filtered using low-pass Butterworth filters with cutoff frequencies of 10 and 50 Hz, respectively. The ground reaction forces were normalized by body weight (BW). The contact phase of the lunge was identified as the period from initial heel contact of the landing foot to toe off,

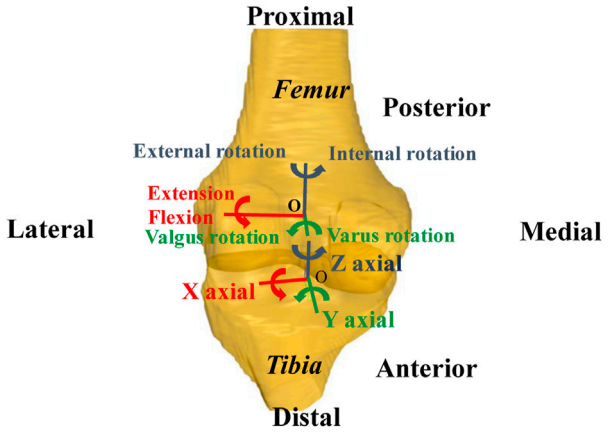

FIGURE 2
Coordinate systems of femur and tibia.

starting with vertical ground reaction force (VGRF) excessed to 10N until the right toe off the ground as determined by the force plate.

2.3.2 6DOF characteristics of the tibiofemoral joint

Coordinate systems were established to investigate 6DOF kinematics of the tibiofemoral joint (Most et al., 2004; Kai et al., 2014). The *X*-axis of the femoral coordinate system was constructed by connecting circle centers of medial and lateral condyles with a line (Figure 2). The *Z*-axis was drawn parallel to the posterior wall of the femoral shaft in the sagittal plane. The *Y*-axis was perpendicular to the *X*-axis and long axes. The middle point of the *X*-axis was defined as the origin of the femoral coordinate system. For that tibia coordinate system, the *X*-axis was drawn parallel to the posterior edge of the tibial plateau. The *Z*-axis was the long axis of the tibial shaft through the middle of tibial spines. The *Y*-axis was perpendicular to the *X*-axis and *Z*-axis. The midpoint of the connecting line of the tibial plateaus was defined as the origin of the tibial coordinate system. Using Rhino 6.0 SR5 software (Robert McNeel and Associates, United States), the virtual DFIS setup environment was established and bony landmarks were sketched. The 3D bone model was optimally positioned to match the projection contour of the DFIS image, and we calculated the 6DOF kinematics of the tibiofemoral joint with the tibial and femoral coordinate systems established (Figure 3). The *in vivo* knee motion was described as the relative motion of the tibial coordinate system with respect to the femoral coordinate system.

2.3.3 Electromyography data

The electromyography (EMG) data were processed in Delsys EMGworks Analysis 4.2.0.0 software (Calculation Toolkit 1.5.2.0). Raw EMG signals were filtered and smoothed using a Butterworth filter at the band-pass frequency (10–400 Hz) to attenuate artefacts. After adjusting baseline and full-wave rectification, the root mean square (RMS) and integrated electromyography (IEMG) amplitude of each signal were calculated. The RMS and IEMG data were normalized to the MVC of each muscle. The muscle pre-activation and post-activation were defined as the muscle activity level of 50 ms before and after touchdown, and the co-activation was the ratio of agonist muscles against antagonistic muscles.

2.4 Statistical analysis

The normality of the variables was tested with a Shapiro–Wilk test, and we found that all variables were normally distributed. Repeated-measures ANOVA ($\alpha = 0.05$) and Turkey's post-test were used to compare differences in 6DOF knee kinematics among the three left-forward lunges. The paired-T test was used to compare the differences *in vivo* knee 6DOF kinematics (antero–posterior tibial translation, mediolateral tibial translation, internal–external tibial rotation, and varus–valgus tibial rotation), kinetics, and muscle activities between the two distance lunges and two foot position lunges. Parameters are shown by mean ± standard deviation. Significance analysis was performed by IBM SPSS statistics 26.0 (IBM Inc., Chicago, IL, United States) software, and the significance α level was set at $p < 0.05$.

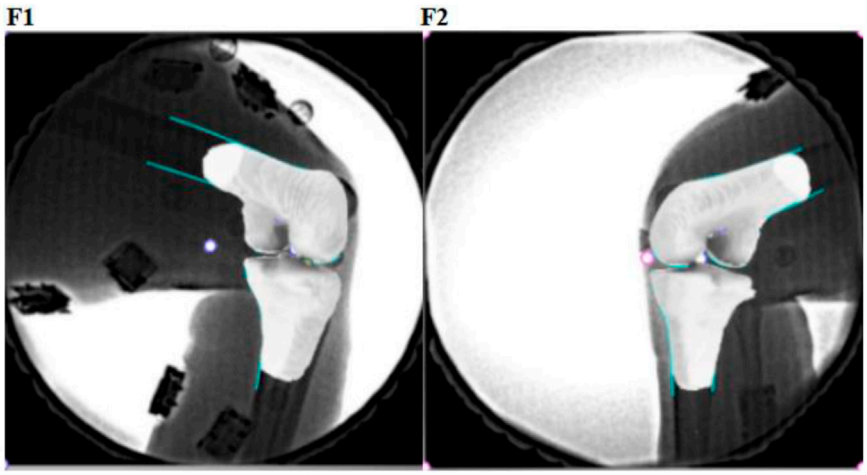

FIGURE 3
Dual-plane fluoroscopic images (F1 and F2) with 3D knee models were combined to reproduce the knee position.

TABLE 1 Six degrees of freedom of the tibiofemoral joint in the phases of three lunges.

6 degrees of freedom	1.5 times leg length lunge		The maximum lunge		The maximum lunge with foot external rotation	
	Braking	Recovery	Braking	Recovery	Braking	Recovery
Flexion (+)Extension (−) (deg)	57.3 ± 7.8	46.6 ± 6.3	61.8 ± 9.6	51.1 ± 7.8*	64.3 ± 8.9	52.2 ± 7.0
Valgus (+)Varus (−) rotation (deg)	−7.2 ± 1.9	−8.5 ± 2.9	−8.6 ± 2.8*	−10.3 ± 3.4*	−7.8 ± 2.8	−8.2 ± 4.0
External (+)Internal (−) rotation (deg)	3.2 ± 2.0	3.1 ± 1.8	2.8 ± 1.6	2.6 ± 1.5	3.9 ± 1.2	3.9 ± 2.7
Lateral (+)Medial (−) translation (mm)	−2.1 ± 0.6	1.30 ± 1.2	−1.9 ± 1.2	1.2 ± 0.9	−1.4 ± 0.4	0.7 ± 0.3
Anterior (+)Posterior (−) translation (mm)	−7.0 ± 3.6	−7.6 ± 4.0	−7.1 ± 3.4	−7.9 ± 4.1	−6.0 ± 2.9	−7.0 ± 3.9
Proximal (+)Distal (−) translation (mm)	26.4 ± 2.4	26.8 ± 2.8	26.1 ± 3.0	26.4 ± 3.0	26.0 ± 3.2	26.2 ± 3.1

Denotes the variable that was significantly different under lunges at two distance and two foot position, significant p values ($p < 0.05$); SD, standard deviation. The braking phase was from the initial contact to the maximum knee flexion, and the recovery phase was from the maximum knee flexion time to the right toe off the ground.

3 Results

3.1 6DOF kinematics of tibiofemoral joint

For the two distance lunges, compared with the 1.5 times leg length lunge, the flexion and varus rotation of the tibiofemoral joint increased significantly by 4.5° ($p = 0.014$) and 1.6° ($p = 0.033$) during the maximum left-forward lunge. In particular, the varus rotation significantly increased by 1.4° ($p = 0.048$) in the braking phase of the maximum lunge compared with that of the 1.5 times leg length lunge. The flexion and varus rotation increased by 4.5° ($p = 0.033$) and 1.9° ($p = 0.048$), respectively, in the recovery phase under the maximum distance (Table 1).

In terms of the characteristic points during the two distance lunges, compared with the 1.5 times leg length lunge, the flexion increased significantly by 4.0° ($p = 0.014$) at the initial contact moment in the maximum lunge (Figure 4), and the flexion increased significantly at the point of initial GRF peak by 5.2° ($p = 0.01$). The varus rotation of the knee joint increased significantly both from 0.03 s before the maximum knee flexion to 0.01 s before the maximum knee flexion ($p < 0.05$). The varus rotation increased significantly from 0.03 s after the maximum knee flexion to 0.05 s after the maximum knee flexion ($p < 0.05$). The posterior translation of the femur relative to tibia significantly increased at 0.04 and 0.05 s after maximum knee flexion ($p < 0.05$).

During the two foot position lunges, the posterior translation of the femur relative to the tibia decreased significantly ($p < 0.05$) in the maximum lunge with foot external rotation, especially at 0.02 s, 0.01 s before the maximum knee flexion and 0.01 s after the maximum knee flexion (Figure 4). When the foot position changed, the lateral translation of the femur relative to the tibia decreased significantly to 1.09 mm ($p = 0.034$) at 0.04 s after the maximum knee flexion.

3.2 Kinetics

During the two distance lunges, for the maximum lunge, the VGRF significantly increased 0.02BW ($p = 0.013$; Figure 5), the anterior-posterior GRF significantly increased 0.05BW ($p = 0.001$), and the medial-lateral GRF significantly decreased 0.01BW ($p = 0.001$). During the two foot position lunges, when the landing foot rotated externally, the vertical GRF decreased significantly ($p = 0.023$), the anterior–posterior GRF significantly decreased by 0.07BW ($p = 0.022$), and the medial–lateral GRF increased by 0.01BW significantly ($p = 0.002$).

We noted significant differences in valgus–varus rotation torque and internal–external rotation torque of the knee joint under the two distance lunges and two foot position lunges ($p < 0.05$). The lunge distance and foot position had no significant effect on knee power in the left-forward lunge.

3.3 Muscle activation

Under the two distance lunges, the muscle activities of the knees in pre-activation and post-activation were higher in the maximum lunge than in the 1.5 times leg length lunge. Under the two foot position lunges, the activity level of thigh and calf muscles in the pre-activation and post-activation of the maximum distance with foot rotated externally were higher than those of the maximum lunge. Under the two distance and two foot position left-forward lunges, no significant difference was observed in knee muscle co-activation, pre-activation, and post-activation (Figure 6).

4 Discussion

Compared with the 1.5 times leg length lunge, the flexion and varus rotation of the knee joint significantly increased under the maximum lunge. The posterior tibia translation and the knee muscle co-activation increased under the maximum distance with the foot external rotation than the maximum lunge. This result supported our hypothesis that the increased lunge distance and the increased foot external rotation would increase the flexion and varus rotation of the knee joint.

Previous studies showed that the flexion of the knee increases and the tibia moves anteriorly during static lunges (Komistek et al., 2003). The internal tibial rotation increases sharply during low knee flexion tasks (Qi et al., 2013). When the knee flexion was at 30°–120°, the tibia rotated internally constantly (Moro-oka et al., 2008), the posterior translation of the femur related to the tibia moved to 13.3 ±

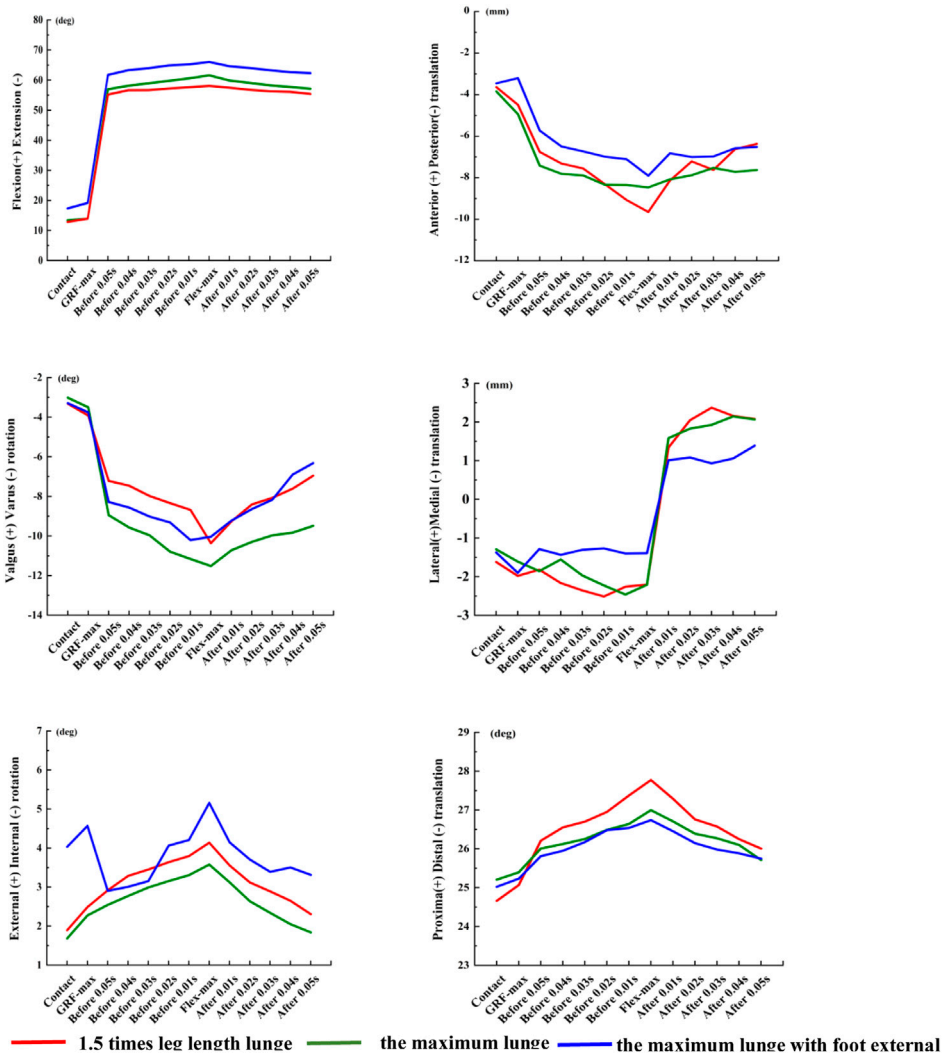

FIGURE 4
Six degrees of freedom of the knee joint in the characteristic points of three left-forward lunges. Contact, the initial moment of foot contact force plate; GRF-max, the point of peak vertical reaction force; Flex-max, the moment of the knee maximum flexion; Before/After 0.05 s, Before/After the maximum knee flexion 0.05 s; Before/After 0.04 s, Before/After the maximum knee flexion 0.04 s; Before/After 0.03 s, Before/After the maximum knee flexion 0.03 s; Before/After 0.02 s, Before/After the maximum knee flexion 0.02 s; Before/After 0.01 s, and Before/After the maximum knee flexion 0.01 s.

3.2 mm, and the tibia rotated in varus by 4.1° ± 3.6° (Qi et al., 2013). However, the anterior–posterior translation of the femur was larger than the results of this study, and the varus–valgus rotation was small, which was relevant to the static one-leg squat trial *versus* the dynamic left-forward lunges.

The kinematics of the knee during functional tasks could be influenced by external forces, joint position, and the balance of active and passive contributory forces across the knee (Myers et al., 2012). The 6DOF knee motion varied during functional activities to fulfill the tasks or to optimize the motor output efficiency. Studies confirmed that ATT significantly increases as demand on the quadriceps increases, and landing produces significantly greater peak ATT than walking and unweighted full extension (Myers et al., 2012). ATT increases with knee flexion during a lunge activity (Defrate et al., 2006). With the lunge distance increasing in this experiment, the flexion and varus rotation of the knee joint significantly increased during the maximum lunge than those during the 1.5 times leg length lunge. Thus, the knee regulated stability mechanically by the inherent geometry of bones and soft tissue stiffness among tasks.

Persistent abnormal knee kinematics could be a putative factor in the degeneration of cartilage (Gill et al., 2009). The increased varus shear force and the anterior tibia drawer force during the maximum lunge may lead to the excessive tension of ACL of badminton players. We knew that ACL plays an important role in maintaining knee joint stability as the main passive restraint of the knees during activities (Ahmed et al., 1992). However, women have lower torsional knee joint stiffness than men in response to combined rotational loads (Hsu et al., 2006). With the increasing demands on the thigh musculature in activities, women cannot

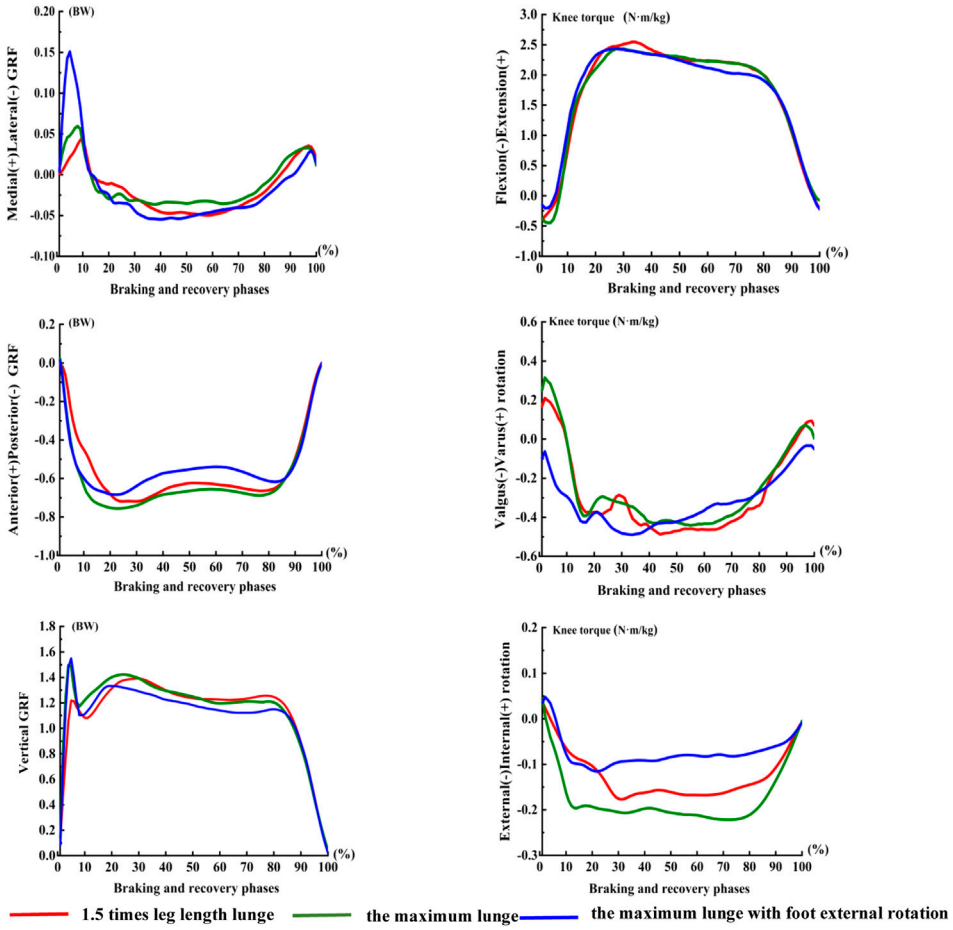

FIGURE 5
Torque of knee in the phases of three left-forward lunges. The braking and recovery phase of the lunge was defined as the period from initial heel contact of the landing foot to toe off, starting with VGRF excessed to 10N until the right toe off the ground determined by the force plate.

generate a sufficient reaction moment against the externally applied internal rotation moment of the shank relative to the femur (Kiriyama et al., 2009). These findings illustrated that the potential risk of knee injury among female players is high when lunging in foot external rotation with multiple loadings.

When the foot rotated externally under the maximum distance, the posterior movement of the femur relative to the tibia significantly decreased at 0.02 s before, 0.01 s before, and 0.01 s after the maximum knee flexion than the maximum lunge. Posterior cruciate ligament (PCL) played a key role in limiting tibia posterior translation. The strong external load exerted on the proximal tibia under knee flexion resulted in excessive posterior movement of the tibia, which may eventually lead to PCL injuries. When the tibia moved posteriorly at knee 90° flexion, the internal torque and varus rotation moment simultaneously acted on the knee joint, which may result in non-contact PCL rupture (Markolf et al., 1996). In addition, with the increased foot external rotation during the maximum lunge, the lateral translation of the femur relative to the tibia decreased significantly at 0.04 s after the maximum knee flexion. The rotation of lower limbs could change the force line of the ankle joint, making it move medially during external rotation (Riemann et al., 2011).

The first valley and the second peak of the sagittal plane knee moment in the maximum lunge were larger than those of 1.5 times leg length lunge, which may be due to the increased knee work with large lunge distance. The knee did negative work in the sagittal plane during the braking phase and then began to do positive work after the maximum knee flexion. The muscle completed eccentric contraction when braking and performed negative work to absorb human energy. In the recovery phase, the muscle performed concentric contraction to complete the lower limb push and extend for the next hit. In addition, VGRF at the maximum distance increased significantly than that at the 1.5 times leg length lunge, especially at the first peak of VGRF. Strenuous impact forces in badminton lunges are closely related to knee injury incidence, especially ACL injuries (Abián-Vicén et al., 2012; Dos'Santos et al., 2018; Lam et al., 2017).

In terms of muscle activation, the pre-activation levels of the quadriceps and hamstrings increased as the lunge distance increased. This result may be related to the large VGRF under the maximum lunge distance. High muscle pre-activation modulated the 6DOF knee kinematics mechanically to maintain stability. Thus, the thigh muscles could regulate the translation and rotation of the tibia within a limited range under different functional

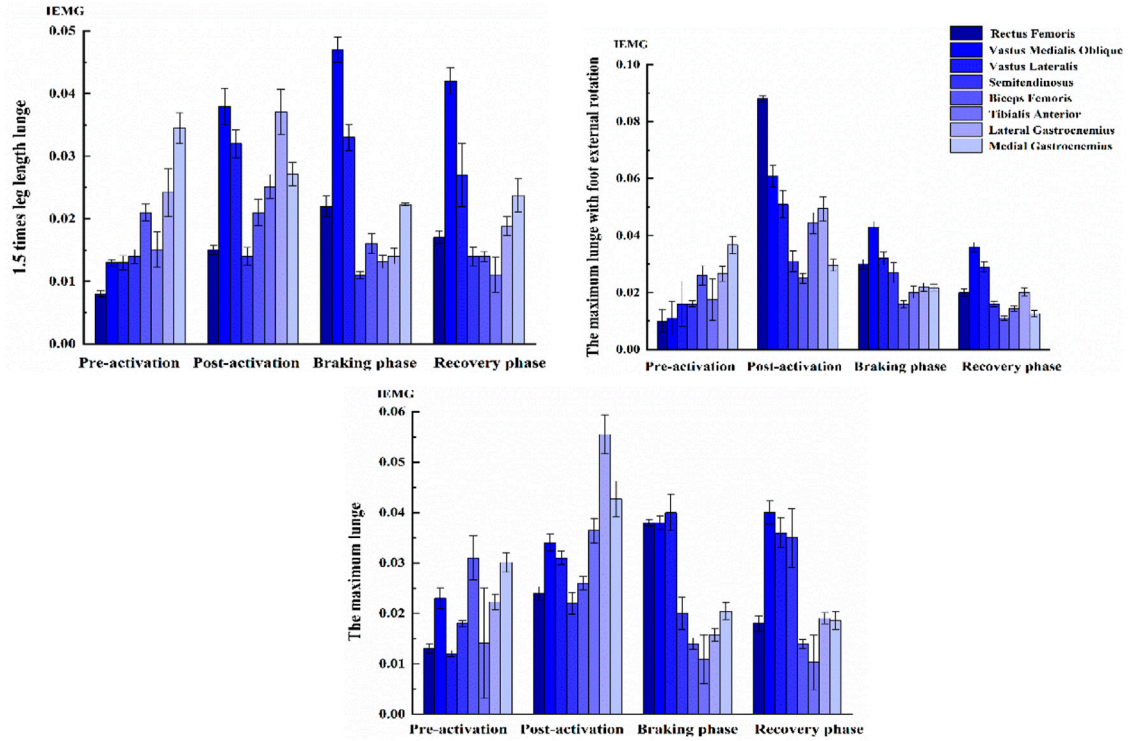

FIGURE 6
Muscle activation level of knee in left-forward lunges. The time of muscle pre-activation was defined as 50 ms before touchdown, the time of muscle post-activation was defined as 50 ms after the maximum knee flexion, the braking phase was from the initial contact to the maximum knee flexion, and the recovery phase was from the maximum knee flexion time to the right toe off the ground.

activities. The preparatory and reflexive muscle activations of the quadriceps and hamstrings were integral during activities, such as walking and landing, in providing knee joint stability to control translations and rotations (Riemann and Lephart, 2002). This phenomenon may also help explain why the ATT and internal tibia rotation increased in previous studies where efforts had been made to minimize thigh musculature pre-activation and hamstring co-activation during trials (Shariff et al., 2009).

However, co-activation in the thigh and calf increased during the maximum distance. The knee muscles maintained strong activities during the maximum distance to strengthen joint stability. Studies have reported that quadriceps contraction applies an anterior shear force on the proximal end of the tibia through the patellar tendon (Wall et al., 2012). As the quadriceps force increases, so does the anterior shear force, ATT, and ACL force (DeMorat et al., 2004). A modeling study of ACL function suggested that quadriceps force and compressive force acting at the tibiofemoral joint contribute greatly to the total load on the ACL (Pflum et al., 2004).

When the knee is in an extended position, and in the absence of hamstring co-activation, the quadriceps reportedly produce sufficient ATT to tear the ACL (DeMorat et al., 2004). Combined with quadriceps muscle force or anterior shear force, the increased ACL load is higher under the knee internal rotation torque than under the external rotation torque (Markolf et al., 2004). In competitive sports, eccentric quadriceps contraction during landing and the resulting shear force on the proximal end of the tibia have been reported to be risk factors for ACL injury (Hewett et al., 2006). Compared with the maximum distance, the pre-activation of the thigh and calf muscles increased under foot external rotation. The abnormal muscle force of the knee could contribute greatly to the total load on the ACL. The foot position affected the activity level of the quadriceps, and the hamstrings were also activated differently when changing foot position (Wang et al., 1990). Moreover, the activation of the medial hamstring muscle was observed to increase significantly during landing in tibia internal rotation than in external rotation (Mohamed et al., 2003). The lateral translation of the tibiofemoral joint decreased significantly under the maximum lunge with foot external rotation, which may induce abnormal medial translation of the tibia. The internal structures of the knee that constrained this translation were biceps femoris muscle contraction or ligaments in tension. Thus, in this study, we observed an increase in activation of biceps femoris when lunging in foot external rotation.

In this study, a small sample size was used. Two-step or three-step lunges were excluded from this study because of the limited space of the laboratory. Given the limitation of the shooting perspective of DFIS, the initial contact and the maximum flexion of the knee cannot be captured at the same time, so these data were collected separately to analyze the full motion phase. This study focused on *in vivo* knee bone movement by DFIS, so further investigations on the mechanical characteristics of the internal tissues of the knee joint are necessary through modeling and finite element analysis (Sun et al., 2022; Cen et al., 2023; Song et al., 2023).

5 Conclusion

This study described the 6DOF knee motion characteristics. It also revealed the kinematics and knee muscle activation during badminton lunges at different distances and different foot positions. This study revealed two key findings: 1) the higher vertical GRF, the larger varus rotation and flexion of the knee joint during the maximum lunge; thus, high knee torque and load may cause a potential risk injury with the increased distance; 2) during the two foot position lunges, the increased posterior tibia translation may increase the risk of knee injury with the foot external rotation. These data may provide theoretical guidance for lunge biomechanics to promote sports performance and prevent injury among badminton athletes.

Data availability statement

The original contributions presented in the study are included in the article/Supplementary Material, further inquiries can be directed to the corresponding author.

Ethics statement

The studies involving humans were approved by The Ethics Committee of Shanghai University of Sport. The studies were conducted in accordance with the local legislation and institutional requirements. The participants provided their written informed consent to participate in this study.

Author contributions

DP: Conceptualization, Data curation, Project administration, Supervision, Writing–original draft, Writing–review and editing. ZM: Formal Analysis, Methodology, Software, Validation, Visualization, Writing–review and editing. WZ: Conceptualization, Methodology, Project administration, Software, Validation, Visualization, Writing–review and editing. JLY: Formal Analysis, Project administration, Resources, Software, Supervision, Validation, Writing–review and editing. SNZ: Conceptualization, Funding acquisition, Methodology, Project administration, Resources, Supervision, Validation, Visualization, Writing–review and editing.

Funding

The author(s) declare that financial support was received for the research, authorship, and/or publication of this article. This work was supported by the key R&D plan of China for Winter Olympics (Ministry of Science and Technology of the People's Republic of China, Grant No. 2020YFF0303800).

Conflict of interest

The authors declare that the research was conducted in the absence of any commercial or financial relationships that could be construed as a potential conflict of interest.

Publisher's note

Supplementary material

The Supplementary Material for this article can be found online at: https://www.frontiersin.org/articles/10.3389/fbioe.2023.1320404/full#supplementary-material

References

Abián-Vicén, J., Del Coso, J., González-Millán, C., Salinero, J. J., and Abián, P. (2012). Analysis of dehydration and strength in elite badminton players. *PLoS One* 7 (5), e37821. doi:10.1371/journal.pone.0037821

Ahmed, A. M., Burke, D. L., Duncan, N. A., and Chan, K. H. (1992). Ligament tension pattern in the flexed knee in combined passive anterior translation and axial rotation. *J. Orthop. Res.* 10 (6), 854–867. doi:10.1002/jor.1100100615

Boesen, A. P., Boesen, M. I., Koenig, M. J., Bliddal, H., Torp-Pedersen, S., and Langberg, H. (2011). Evidence of accumulated stress in Achilles and anterior knee tendons in elite badminton players. *Knee Surg. sports Traumatol. Arthrosc.* 19 (1), 30–37. doi:10.1007/s00167-010-1208-z

Cen, X., Song, Y., Yu, P., Sun, D., Simon, J., Bíró, I., et al. (2023). Effects of plantar fascia stiffness on the internal mechanics of idiopathic pes cavus by finite element analysis: implications for metatarsalgia. *Comput. Methods Biomech. Biomed. Engin.*, 1–9. doi:10.1080/10255842.2023.2268231

Defrate, L. E., Papannagari, R., Gill, T. J., Moses, J. M., Pathare, N. P., and Li, G. (2006). The 6 degrees of freedom kinematics of the knee after anterior cruciate ligament deficiency: an *in vivo* imaging analysis. *Am. J. Sports Med.* 34 (8), 1240–1246. doi:10.1177/0363546506287299

DeMorat, G., Weinhold, P., Blackburn, T., Chudik, S., and Garrett, W. (2004). Aggressive quadriceps loading can induce noncontact anterior cruciate ligament injury. *Am. J. Sports Med.* 32 (2), 477–483. doi:10.1177/0363546503258928

Dos'Santos, T., Thomas, C., Comfort, P., and Jones, P. A. (2018). The effect of angle and velocity on change of direction biomechanics: an angle-velocity trade-off. *Sports Med.* 48 (10), 2235–2253. doi:10.1007/s40279-018-0968-3

Felson, D. T., Lawrence, R. C., Dieppe, P. A., Hirsch, R., Helmick, C. G., Jordan, J. M., et al. (2000). Osteoarthritis: new insights. Part 1: the disease and its risk factors. *Ann. Intern Med.* 133 (8), 635–646. doi:10.7326/0003-4819-133-8-200010170-00016

Gill, T. J., Van de Velde, S. K., Wing, D. W., Oh, L. S., Hosseini, A., and Li, G. (2009). Tibiofemoral and patellofemoral kinematics after reconstruction of an isolated posterior cruciate ligament injury: *in vivo* analysis during lunge. *Am. J. Sports Med.* 37 (12), 2377–2385. doi:10.1177/0363546509341829

Hewett, T. E., Myer, G. D., and Ford, K. R. (2006). Anterior cruciate ligament injuries in female athletes: Part 1, mechanisms and risk factors. *Am. J. Sports Med.* 34 (2), 299–311. doi:10.1177/0363546505284183

Hewett, T. E., Myer, G. D., Ford, K. R., Heidt, R. S., Jr, Colosimo, A. J., McLean, S. G., et al. (2005). Biomechanical measures of neuromuscular control and valgus loading of the knee predict anterior cruciate ligament injury risk in female athletes: a prospective study. *Am. J. Sports Med.* 33 (4), 492–501. doi:10.1177/0363546504269591

Hong, Y., Wang, S. J., Lam, W. K., and Cheung, J. T. (2014). Kinetics of badminton lunges in four directions. *J. Appl. Biomech.* 30 (1), 113–118. doi:10.1123/jab.2012-0151

Hsu, W. H., Fisk, J. A., Yamamoto, Y., Debski, R. E., and Woo, S. L. (2006). Differences in torsional joint stiffness of the knee between genders: a human cadaveric study. *Am. J. Sports Med.* 34 (5), 765–770. doi:10.1177/0363546505282623

Hu, X., Li, J. X., Hong, Y., and Wang, L. (2015). Characteristics of plantar loads in maximum forward lunge tasks in badminton. *PLoS One* 10 (9), e0137558. doi:10.1371/journal.pone.0137558

Huang, M. T., Lee, H. H., Lin, C. F., Tsai, Y. J., and Liao, J. C. (2014). How does knee pain affect trunk and knee motion during badminton forehand lunges? *J. Sports Sci.* 32 (7), 690–700. doi:10.1080/02640414.2013.848998

Jacobson, J. A., Miller, B. S., and Morag, Y. (2005). Golf and racquet sports injuries. *Semin. Musculoskelet. Radiol.* 9 (4), 346–359. doi:10.1055/s-2005-923379

Jørgensen, U., and Winge, S. (1990). Injuries in badminton. *Sports Med.* 10 (1), 59–64. doi:10.2165/00007256-199010010-00006

Kai, S., Sato, T., Koga, Y., Omori, G., Kobayashi, K., Sakamoto, M., et al. (2014). Automatic construction of an anatomical coordinate system for three-dimensional bone models of the lower extremities--pelvis, femur, and tibia. *J. Biomech.* 47 (5), 1229–1233. doi:10.1016/j.jbiomech.2013.12.013

Kimura, Y., Ishibashi, Y., Tsuda, E., Yamamoto, Y., Tsukada, H., and Toh, S. (2010). Mechanisms for anterior cruciate ligament injuries in badminton. *Br. J. Sports Med.* 44 (15), 1124–1127. doi:10.1136/bjsm.2010.074153

Kiriyama, S., Sato, H., and Takahira, N. (2009). Gender differences in rotation of the shank during single-legged drop landing and its relation to rotational muscle strength of the knee. *Am. J. Sports Med.* 37 (1), 168–174. doi:10.1177/0363546508324692

Komistek, R. D., Dennis, D. A., and Mahfouz, M. (2003). *In vivo* fluoroscopic analysis of the normal human knee. *Clin. Orthop. Relat. Res.* 410, 69–81. doi:10.1097/01.blo.0000062384.79828.3b

Kuntze, G., Mansfield, N., and Sellers, W. (2010). A biomechanical analysis of common lunge tasks in badminton. *J. Sports Sci.* 28 (2), 183–191. doi:10.1080/02640410903428533

Lam, W. K., Ding, R., and Qu, Y. (2017). Ground reaction forces and knee kinetics during single and repeated badminton lunges. *J. Sports Sci.* 35 (6), 587–592. doi:10.1080/02640414.2016.1180420

Li, J. S., Hosseini, A., Cancre, L., Ryan, N., Rubash, H. E., and Li, G. (2013). Kinematic characteristics of the tibiofemoral joint during a step-up activity. *Gait Posture* 38 (4), 712–716. doi:10.1016/j.gaitpost.2013.03.004

Markolf, K. L., Burchfield, D. M., Shapiro, M. M., Shepard, M. F., Finerman, G. A., and Slauterbeck, J. L. (1995). Combined knee loading states that generate high anterior cruciate ligament forces. *J. Orthop. Res.* 13 (6), 930–935. doi:10.1002/jor.1100130618

Markolf, K. L., O'Neill, G., Jackson, S. R., and McAllister, D. R. (2004). Effects of applied quadriceps and hamstrings muscle loads on forces in the anterior and posterior cruciate ligaments. *Am. J. Sports Med.* 32 (5), 1144–1149. doi:10.1177/0363546503262198

Markolf, K. L., Slauterbeck, J. L., Armstrong, K. L., Shapiro, M. M., and Finerman, G. A. (1996). Effects of combined knee loadings on posterior cruciate ligament force generation. *J. Orthop. Res.* 14 (4), 633–638. doi:10.1002/jor.1100140419

Mohamed, O., Perry, J., and Hislop, H. (2003). Synergy of medial and lateral hamstrings at three positions of tibial rotation during maximum isometric knee flexion. *Knee* 10 (3), 277–281. doi:10.1016/s0968-0160(02)00140-0

Moro-oka, T. A., Hamai, S., Miura, H., Shimoto, T., Higaki, H., Fregly, B. J., et al. (2008). Dynamic activity dependence of *in vivo* normal knee kinematics. *J. Orthop. Res.* 26 (4), 428–434. doi:10.1002/jor.20488

Most, E., Axe, J., Rubash, H., and Li, G. (2004). Sensitivity of the knee joint kinematics calculation to selection of flexion axes. *J. Biomech.* 37 (11), 1743–1748. doi:10.1016/j.jbiomech.2004.01.025

Myers, C. A., Torry, M. R., Shelburne, K. B., Giphart, J. E., LaPrade, R. F., Woo, S. L., et al. (2012). *In vivo* tibiofemoral kinematics during 4 functional tasks of increasing demand using biplane fluoroscopy. *Am. J. Sports Med.* 40 (1), 170–178. doi:10.1177/0363546511423746

Paillard, T., Noé, F., Rivière, T., Marion, V., Montoya, R., and Dupui, P. (2006). Postural performance and strategy in the unipedal stance of soccer players at different levels of competition. *J. Athl. Train.* 41 (2), 172–176. PMID: 16791302; PMCID: PMC1472651.

Pflum, M. A., Shelburne, K. B., Torry, M. R., Decker, M. J., and Pandy, M. G. (2004). Model prediction of anterior cruciate ligament force during drop-landings. *Med. Sci. Sports Exerc* 36 (11), 1949–1958. doi:10.1249/01.mss.0000145467.79916.46

Phomsoupha, M., and Laffaye, G. (2015). The science of badminton: game characteristics, anthropometry, physiology, visual fitness and biomechanics. *Sports Med.* 45 (4), 473–495. doi:10.1007/s40279-014-0287-2

Qi, W., Hosseini, A., Tsai, T. Y., Li, J. S., Rubash, H. E., and Li, G. (2013). *In vivo* kinematics of the knee during weight bearing high flexion. *J. Biomech.* 46 (9), 1576–1582. doi:10.1016/j.jbiomech.2013.03.014

Riemann, B. L., and Lephart, S. M. (2002). The sensorimotor system, part I: the physiologic basis of functional joint stability. *J. Athl. Train.* 37 (1), 71–79.

Riemann, B. L., Limbaugh, G. K., Eitner, J. D., and LeFavi, R. G. (2011). Medial and lateral gastrocnemius activation differences during heel-raise exercise with three different foot positions. *J. Strength Cond. Res.* 25 (3), 634–639. doi:10.1519/JSC.0b013e3181cc22b8

Shariff, A. H., George, J., and Ramlan, A. A. (2009). Musculoskeletal injuries among Malaysian badminton players. *Singap. Med. J.* 50 (11), 1095–1097.

Sharma, L., Song, J., Felson, D. T., Cahue, S., Shamiyeh, E., and Dunlop, D. D. (2001). The role of knee alignment in disease progression and functional decline in knee osteoarthritis. *JAMA* 286 (2), 188–195. doi:10.1001/jama.286.2.188

Song, Y., Cen, X., Chen, H., Sun, D., Munivrana, G., Bálint, K., et al. (2023). The influence of running shoe with different carbon-fiber plate designs on internal foot mechanics: a pilot computational analysis. *J. Biomech.* 153, 111597. doi:10.1016/j.jbiomech.2023.111597

Sun, D., Song, Y., Cen, X., Wang, M., Baker, J. S., and Gu, Y. (2022). Workflow assessing the effect of Achilles tendon rupture on gait function and metatarsal stress: combined musculoskeletal modeling and finite element analysis. *Proc. Inst. Mech. Eng. H.* 236 (5), 676–685. doi:10.1177/09544119221085795

Wall, S. J., Rose, D. M., Sutter, E. G., Belkoff, S. M., and Boden, B. P. (2012). The role of axial compressive and quadriceps forces in noncontact anterior cruciate ligament injury: a cadaveric study. *Am. J. Sports Med.* 40 (3), 568–573. doi:10.1177/0363546511430204

Wang, J. W., Kuo, K. N., Andriacchi, T. P., and Galante, J. O. (1990). The influence of walking mechanics and time on the results of proximal tibial osteotomy. *J. Bone Jt. Surg. Am.* 72 (6), 905–909. doi:10.2106/00004623-199072060-00017

Yack, H. J., Riley, L. M., and Whieldon, T. R. (1994). Anterior tibial translation during progressive loading of the ACL-deficient knee during weight-bearing and nonweight-bearing isometric exercise. *J. Orthop. Sports Phys. Ther.* 20 (5), 247–253. doi:10.2519/jospt.1994.20.5.247

frontiers | Frontiers in Bioengineering and Biotechnology

TYPE Brief Research Report
PUBLISHED 22 December 2023
DOI 10.3389/fbioe.2023.1298402

OPEN ACCESS

EDITED BY
Bernardo Innocenti,
Université Libre de Bruxelles, Belgium

REVIEWED BY
Francesco Travascio,
University of Miami, United States
Yun Peng,
NuVasive, United States

*CORRESPONDENCE
Weidong Xu,
xuwdshanghai@126.com
Shaobai Wang,
wangs@innomotion.biz

†These authors have contributed equally to this work and share first authorship

RECEIVED 21 September 2023
ACCEPTED 13 December 2023
PUBLISHED 22 December 2023

CITATION
Wu D, Zhao X, Wu B, Zhou L, Luo Y, Huang X, Xu W and Wang S (2023), Subregional analysis of joint stiffness facilitates insight into ligamentous laxity after ACL injury.
Front. Bioeng. Biotechnol. 11:1298402.
doi: 10.3389/fbioe.2023.1298402

Subregional analysis of joint stiffness facilitates insight into ligamentous laxity after ACL injury

Danni Wu[1†], Xuan Zhao[1†], Bin Wu[2†], Lan Zhou[1], Ye Luo[1], Xiaofan Huang[1], Weidong Xu[2*] and Shaobai Wang[1*]

[1]Key Laboratory of Exercise and Health Sciences of Ministry of Education, Shanghai University of Sport, Shanghai, China, [2]Department of Orthopedics, Changhai Hospital, The Navy Medical University, Shanghai, China

Purpose: Increased incidence of anterior cruciate ligament injuries has amplified the need for quantitative research in clinical and academic settings. We used a novel digital arthrometer to measure knee laxity in healthy people and patients with anterior cruciate ligament injuries. Changes in stiffness were also assessed to develop new indicators for detecting anterior cruciate ligament injury. The purpose of this study was to use arthrometer to measure the quantitative indicator of knee laxity, bringing clinicians a new perspective on how to identify injury to the ACL.

Methods: In this cross-sectional study, anterior tibial displacement under continuous loading was measured using a novel digital arthrometer in 30 patients with unilateral anterior cruciate ligament injury and 30 healthy controls. Load-displacement curves were plotted, using real-time load and displacement changes. Stiffness was defined by the slope of the applied load to tibial displacement. Anterior tibial displacement and instantaneous stiffness values under different loads were compared. The restricting contribution of the anterior cruciate ligament transformed the displacement-stiffness curve from a sharp decrease to a stable increase, resulting in a minimum stiffness value. Using the minimum stiffness as the turning point, the load-displacement curve was divided into regions 1 and 2. The two regions' stiffness changes were compared. Based on the findings, receiver operating characteristic curves were plotted and the area under the curve was calculated to estimate the diagnostic accuracy.

Results: Anterior tibial displacement was significantly greater in the anterior cruciate ligament injury group than in the controls under each 10-N increase load ($p < 0.05$). In the anterior cruciate ligament injury group, instantaneous stiffness was significantly lower on the injured side than on the healthy side ($p < 0.05$). In the two regions of the load-displacement curve, stiffness was significantly lower in the anterior cruciate ligament injury group than in the control group (all, $p < 0.05$). Receiver operating characteristic curves were plotted, using changes in stiffness under the two regions in both groups. Stiffness in region 2 had the largest area under the curve (0.94; 95% CI, 0.88–0.99). Using the cut-off value of 9.62 N/mm to detect ACL injury, the sensitivity and specificity were 93% and 82%, respectively.

Conclusion: Our investigation of ligament stiffness provides novel insights into the properties of knee laxity. Stiffness in the later stages of increased loading <9.62 N/mm could be a valid indicator for identifying knee laxity.

KEYWORDS

anterior cruciate ligament, knee laxity, stiffness, regional analysis, load-displacement curve

Introduction

An accurate assessment of knee laxity is essential for the treatment and rehabilitation evaluation of anterior cruciate ligament (ACL) injuries. Physical examination is a convenient and rapid diagnostic tool frequently used to achieve this assessment in clinical practice (IW et al., 1989; Benjaminse et al., 2006). The Lachman test is an effective tool for examining anterior tibial translation, with studies indicating a sensitivity of 81%–94% and a specificity of 81%–98% (van Eck et al., 2013b; Rohman and Macalena, 2016). However, this test is influenced by a clinician's experience and a patient's muscle tone (IW et al., 1989; Benjaminse et al., 2006). Arthrometers are devices that apply a repeatable load to the knee joint and mechanically measure the resulting displacement (IW et al., 1989; Benjaminse et al., 2006). Measurement with these devices, compared to a physical examination, provides more objective, quantitative, and accurate information. An arthrometer is a commonly used clinical instrument for the objective assessment of ACL injuries (Pugh et al., 2009; Rohman and Macalena, 2016).

Several types of arthrometers exist. For example, the KT1000 (MED Metric Corp., San Diego, CA, United States) has commonly been used to evaluate ACL injuries (Küpper et al., 2007). In 1985, the KT2000 arthrometer was first used by researchers to visualize load-displacement curves to reflect the differences in relaxation with increasing load (Daniel et al., 1985b). Stiffness is defined by the slope of the applied load to the tibial displacement (Markolf et al., 1976). It is often used to reflect the biomechanical properties of ligaments (Woo et al., 1991). As the load increases, the stiffness changes, thereby representing a different condition of the ligament. However, previous studies that used the KT1000 or KT2000 have demonstrated that the application of load was typically discontinuous during the test. By contrast, (IW et al., 1989) suggested that discrepancies exist in the retest results of this device. For knee laxity measurements, the KiRA (I+, Italy) and the GNRB (Genourob, Laval, France) have recently been certified to be comparable to the KT-1000. The KiRA is a device that measures knee rotational and translational laxity using triaxial accelerometers and gyroscopes (Raggi et al., 2019). In a study of reliability, Runer et al. (2021) evaluated the measurements of four arthrometers (KT-1000, Rolimeter, KLT and Kira). The results showed that the KiRA device measured higher values than the other devices and had a 34% false positive rate. The GNRB is a computerized device that uses pressure and motion sensors to evaluate knee laxity automatically in a consistent direction and speed (Smith et al., 2022). However, Mouarbes et al. (2018) discovered poor retesting consistency while investigating the reliability of the GNRB for testing knee relaxation in healthy adults. Therefore, the problem of how to improve the accuracy of arthrometer measurements remains to be resolved.

A recent novel arthrometer (Ligs, Innomotion, Shanghai, China), has built-in load and displacement sensors to continuously record real-time load and displacement with an accuracy of 1 N and 0.1 mm. Ligs is optimized in terms of structure and measurement methodology. The interrater reliability and the intrarater reliability were considered excellent with ICC score of 0.91 and 0.94. The sensitivity and specificity of Ligs for the identification of ACL injuries were 87% and 73% at a load of 150N (Wu et al., 2023). In the present study, we compared differences in knee laxity between healthy individuals and patients with ACL injuries by using this novel digital arthrometer. We hypothesized that a significant difference would exist in knee laxity between healthy individuals and patients with ACL injuries. When arthrometer is used to measure knee laxity, a gradual increasing load is accompanied by an initial directional compression of the knee joint. Subsequently the ACL acts to initiate a restrictive effect on the tibia (Maitland et al., 1995). We divide the load-displacement curves into different regions based on the above two phases and then analyze the stiffness changes in these two regions. Therefore, we propose a novel objective indicator to identify knee laxity by analyzing stiffness changes in different regions. We hypothesized that these two regions of stiffness variation would show different characteristics between healthy individuals and patients with ACL injuries.

Materials and methods

Participants

Thirty patients with unilateral ACL injuries were enrolled as the study group. Participants in the ACL injury group were identified by sports medicine specialists based on clinical symptoms and magnetic resonance imaging (MRI) results. MRI images demonstrated increased T2 signal, diffuse thickening, and structural disturbances in the ACL. In addition, the Lachman test results were positive. Furthermore, 30 healthy participants were included as a control group. All healthy participants were subjected to a physical examination to ensure that their knee joints were in good functioning condition. The study was conducted in accordance with the Declaration of Helsinki and was approved by the ethics committee of our institution (approval no. 1XXXXXXXXXX0). All participants signed an informed consent form before participation in the trial.

Data acquisition

The Ligs arthrometer was used to assess knee laxity under continuous loads. Load and displacement were input into the Ligs storage unit by using digital sensor with a sampling rate of 30Hz. Displacement recording was initiated when the load exceeded 20 N to attenuate the impact of muscle tissue (Wu et al., 2023). The load is accurate to 1 N, and the displacement is accurate to 0.1 mm. Patients were required to maintain continuous muscle relaxation throughout the duration of the test. After fixing the lower leg, the tibia was displaced anteriorly by pushing the thruster that was located behind the lower leg (Figure 1).

Continuous loads were applied up to 150 N, and the displacement corresponding to each 10N increase load was recorded. A load-displacement curve was plotted to observe the change in stiffness (Figure 2A). The stiffness value of the ACL was minimal when it functioned as a tibial restraint, and gradually increased thereafter (Figure 2B). Taking the minimum stiffness as the turning point, the load-displacement curve was divided into two regions (Figure 2A). The stiffness of region 1 was estimated as follows: 52 N divided by the corresponding anterior tibial displacement (ATD). The stiffness in region 2 was estimated as

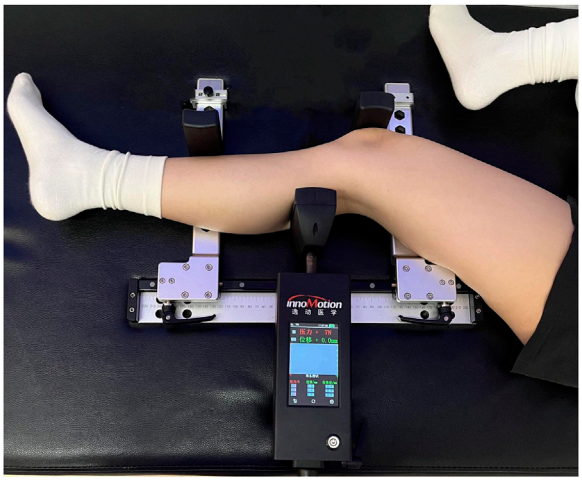

FIGURE 1
Measurement of anterior tibial displacement (ATD), using the Ligs (Innomotion, Shanghai, China). The lower leg is fixed by the patella and the distal tibial component. The tibia is displaced anteriorly by pushing on the thruster located at the posterior lower leg.

follows: 98 N (calculated as 150 N–52 N) divided by the difference in the ATD between 150 N and 52 N.

Statistical analysis

The Kolmogorov–Smirnov test was used to verify the normality of all variables. The Wilcoxon test was used for variables that did not conform to normality. Effect sizes were calculated. Cohen's d effect size classification was defined as 0.2 for a small effect, 0.5 for a medium effect, and 0.8 for a large effect (1990). The independent *t*-test was used to compare the displacement and instantaneous stiffness corresponding to each 10N increase load. In addition, the minimum stiffness, corresponding load, and stiffnesses in the two regions were also compared between the control and ACL injury groups. A paired sample *t*-test was used to compare the minimum stiffness, corresponding load, and stiffnesses in the two regions on the injured and healthy sides in the ACL injury group. Appropriate variables to construct the receiver operating characteristic (ROC) curve were selected, based on the group comparison results. The area under the curve (AUC) was calculated to determine the appropriate diagnostic criteria for detecting ACL injury. The sensitivity and specificity were further calculated. Statistical analyses were conducted using SPSS software (version 23.0; IBM, Armonk, NY, United States). The significance level was set at $p < 0.05$.

Results

The 30 patients included 13 patients had left-sided ACL injuries and 17 patients had right-sided ACL injuries, comprised 22 men and 8 women, aged 23 ± 3.3 years, with a mean body mass index of 21.1 kg/m2. The control group comprised 17 men and 13 women, aged 22 ± 3.0 years, with a mean body mass index of 20.9 kg/m2. There were no statistical differences in gender ($p = 0.18$), age ($p = 0.19$), or body mass index ($p = 0.79$) between the two groups of participants.

The mean ± standard deviation of displacements, corresponding to each 10N increase in load between the ACL injury group and the control group, are shown in Table 1. The displacement was significantly greater in the ACL injury group (all $p < 0.001$), with the largest effect size observed at the load of 150 N (effect size = 2.2).

The comparison results of instantaneous stiffness on the injured and healthy sides in the ACL injury group are shown in Figure 3. The stiffness was significantly lower on the injured side (all, $p < 0.001$), with the largest effect size at the load of 150 N (effect size = 1.5).

The comparison results of the minimum stiffness, corresponding load, and stiffnesses in the two regions in the

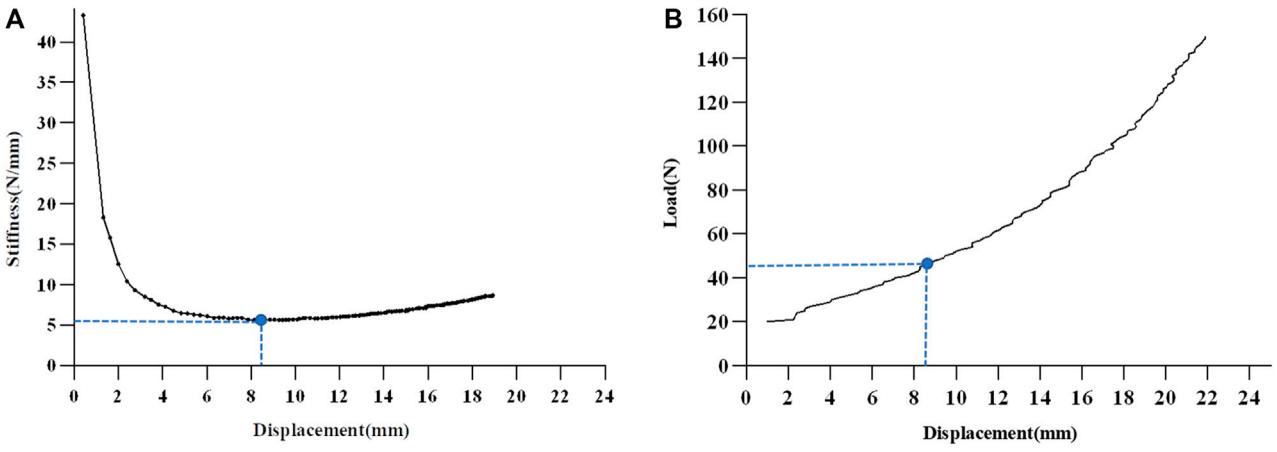

FIGURE 2
The Schematic diagram of load-displacement curve division. **(A)** The load-displacement curve is divided into two regions, using the group mean minimum value of stiffness as the turning point. **(B)** The restricting contribution of the anterior cruciate ligament transforms the displacement-stiffness curve from a sharp decrease to a stable increase, resulting in a minimum stiffness value. *ACL* anterior cruciate ligament.

TABLE 1 Comparison of ATD in the ACL injury group and the control group.

Loads (N)	ACL injury group (mm)	Control group (mm)	*p*-Value	Effect size
30	4.5 ± 1.1	3.8 ± 0.5	0.001**	0.8
40	7.4 ± 1.8	6.3 ± 0.7	0.001**	1.2
50	9.7 ± 2.1	8.2 ± 0.9	0.000***	1.4
60	11.1 ± 2.2	9.8 ± 1.1	0.000***	1.6
70	13.5 ± 2.3	11.0 ± 1.2	0.000***	1.7
80	14.9 ± 2.2	12.1 ± 1.3	0.000***	1.7
90	16.3 ± 2.3	13.0 ± 1.4	0.000***	1.8
100	17.7 ± 2.3	13.9 ± 1.5	0.000***	1.8
110	18.7 ± 2.4	14.7 ± 1.6	0.000***	1.9
120	19.8 ± 2.5	15.4 ± 1.7	0.000***	2.0
130	20.8 ± 2.4	16.0 ± 1.7	0.000***	2.1
140	21.8 ± 2.6	16.6 ± 1.8	0.000***	2.1
150	22.6 ± 2.6	17.2 ± 1.9	0.000***	2.2

ATD: anterior tibial displacement.
Data are reported as M ± SD; the level of significance was established *a priori* at $p < 0.05$.
**$p < 0.01$.
***$p < 0.001$.

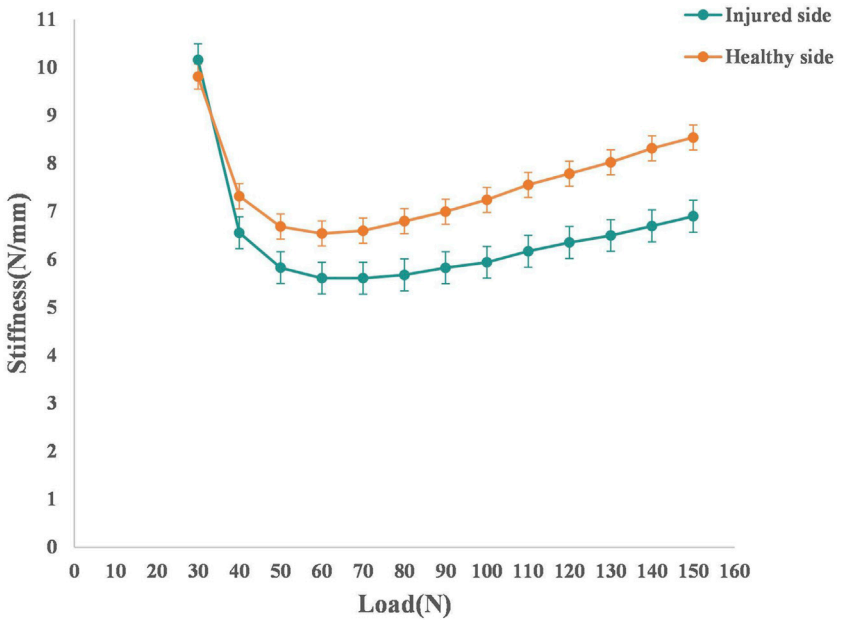

FIGURE 3
The average load-stiffness curves of the injured and healthy sides in the ACL injury group. Both groups have 30 knees *ACL* anterior cruciate ligament.

control and ACL injury groups are shown in Table 2. We observed no significant difference in the corresponding load at the minimum stiffness between the control and ACL injury groups ($p = 0.62$). The minimum stiffness of the injured side in the ACL injury group was significantly lower than that of the healthy side and the control group (all $p < 0.05$). The load-displacement curve was divided into two regions, using the minimum stiffness mean value of the two groups as the turning point. The stiffness in the two regions of the injured side in the ACL injury group was significantly lower than that of the healthy side and the control group (all $p < 0.05$). The stiffness in region 2 of the healthy side in the ACL injury group was significantly lower than that of the control group ($p < 0.05$).

ROC curves were plotted, based on changes in stiffness in the two regions in the control and ACL injury groups. The ROC curves

TABLE 2 Comparison of the minimum stiffness, corresponding load, and stiffness in region 1 and region 2 between the control and ACL injury groups.

Variable	Control group	ACL injury group	
		Injured side (N/mm)	Healthy side (N/mm)
Load (N)	50.1 ± 5.2	53.0 ± 5.7	50.7 ± 6.0
Minimum stiffness (N/mm)	6.0 ± 0.7	4.9 ± 0.8*	5.8 ± 0.9**
Stiffness in region 1 (N/mm)	6.2 ± 0.7	5.4 ± 1.6*	6.2 ± 1.3**
Stiffness in region 2 (N/mm)	11.5 ± 1.6	8.1 ± 1.5*	10.4 ± 1.9*, **

Data are reported as the mean ± standard deviation. The level of significance is established *a priori* at $p < 0.05$.
*Statistically significant difference, compared with the control group ($p < 0.05$).
**Statistically significant difference, compared with the injured side ($p < 0.05$).
ACL, anterior cruciate ligament.

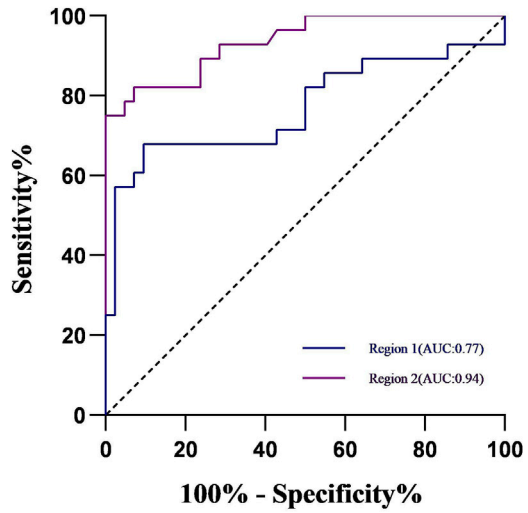

FIGURE 4
The ROC curve of stiffness in the two regions. *ROC* receiver operating curve.

of stiffness in the two regions are shown in Figure 4. The stiffness in region 2 had the largest AUC [0.94 (95% CI 0.88–0.99)]. The point near the upper left corner was defined as the best diagnostic criterion for detecting ACL injury, with a critical value of 9.62 N/mm. The sensitivity and specificity were 93% and 82%, respectively.

Discussion

In this study, we used a novel digital arthrometer to measure knee laxity in patients after ACL injury. The most important finding of this study was the discovery of sensitive indicators to identify ACL injuries by conducting subregional analysis of load-displacement curves. We believe that these results will help clinicians fully understand the biomechanical properties of the ligament after injury and will provide a reference for the grading and diagnosis of ligament injuries. Our results demonstrated that stiffness in the ACL injury group was significantly lower than that of the control group in both defined regions. After ACL injury, Paterno et al. (2012) observed a 15- to 25-fold increase in the risk of contralateral ACL injury. In our study, the ACL injury group, compared to the control group, had significantly lower stiffness on the healthy side in region 2. This finding indicated an earlier onset of mechanical changes in ligament properties among patients with ACL injuries, compared to these changes in healthy individuals. We plotted ROC curves to reflect the change in stiffness under different subregions. Region 2 had the largest AUC (0.94) at a cut-off value of 9.62 N/mm, and a sensitivity and specificity of 93% and 82%, respectively. The observed changes in ACL stiffness within region 2 may reflect preinjury mechanical properties. Therefore, the findings of this study support our initial hypothesis that alterations in stiffness at various regions along the load-displacement curve could serve as a clinical indicator for identifying ACL injuries.

KT1000 and KT2000 are widely used arthrometers. A meta-analysis by van Eck et al. (2013a) showed that, the higher the applied load, the higher was the diagnostic power. In this aforementioned study, the average sensitivity increased by 39% (54%–93%) from 69N to 89N to the manual maximum load. KT1000 and KT2000 arthrometers have been used to establish widely accepted diagnostic criteria; for example, a side-to-side difference greater than 3 mm at 134 N was considered a good diagnostic value (Daniel et al., 1985b; Rangger et al., 1993). However, side-to-side differences usually use the uninjured knee as the reference, which makes accurately assessing knee laxity in patients with bilateral knee injuries difficult. In addition, in a study of knee laxity among healthy individuals, a side-to-side difference of greater than 3 mm was found in 2% of healthy individuals (Daniel et al., 1985a). Markolf et al. (1976); Markolf et al. (1984) previously suggested that stiffness could be an important indicator for assessing ligament injury. They used the KT2000 arthrometer to obtain ATD data from controls ($n = 21$) and ACL-injured patients ($n = 6$) to assess stiffness changes. Their results were that patients with ACL injuries (3.8 N/mm) had significantly lower stiffness values than did healthy individuals (23.2 N/mm) at a load of 134 N, which is in accordance with the results of our study. Instantaneous stiffness was lower in ACL patients than in healthy participants ($p < 0.05$). Therefore, the stiffness characteristics can objectively reflect the biomechanical properties of the ACL and can be used to differentiate the injured knee from the healthy knee.

In a study by Eagar et al. (2001), which used the KT2000 quantitative Lachman's ACL injury test, the authors found that the minimum stiffness value corresponded to a mean load of 49 N at different knee flexion angles. This finding was similar

to the results of our study wherein the mean load at the turning point between the two regions of the two groups was 52 N. Before the turning point, the applied load causes directional compression of the soft tissues of the lower leg to overcome the weight of the lower leg (Minns et al., 1973; Maitland et al., 1995). After the turning point, the stiffness curve tended to flatten in response to the restraining effect of the ACL on the tibia (Figure 2B). We plotted ROC curves reflecting the change in stiffness under different subregions. Region 2 had the largest AUC (0.94), with a cut-off value of 9.62 N/mm and sensitivity and specificity of 93% and 82%, respectively. Therefore, we suggest that the stiffness characteristics after the turning point (region 2) can objectively reflect the biomechanical properties of the ACL and can be used to differentiate the ACL-injured knee from the healthy knee.

In the present study, we compared the ATD 10-N interval between the injured and healthy knee in the ACL injury group. The ATD of the healthy knee was significantly lower than that of the injured knee. In the case of ACL injury, ATD exhibits a significant increase due to loss of restraint, thereby resulting in an alteration in the slope of the stiffness-displacement curve. Typical curves have an initial low stiffness linear region and an end high stiffness linear region with transitional nonlinear regions in between (Markolf et al., 1976). With increasing load, the load-displacement curve inflects because of the limiting effect of the ACL on ATD, at which point the minimum value of stiffness occurs (Figure 2A). In the present study, the mean load at the turning point between the two regions of the two groups was 52 N. In addition, the minimum stiffness of the ACL injury group was significantly lower than that of the control group. The mean displacement of the control group under the 52N load was interestingly 8.6 mm, whereas the displacement on the healthy side in the ACL injury group was 8.7 mm. However, in region 2, the stiffness of the healthy knee in the ACL group was significantly lower than that of the control group ($p < 0.05$). The decrease in stiffness indicated a change in the ACL constraint of the ACL on the tibia (Liu et al., 2002). These features can provide a reference point for the differentiation between normal and ACL-injured knees. We hypothesized that alterations in the stiffness of region 2 may serve as a significant predictor for ACL injury and offer novel insights into the clinical grading of such injuries.

When it comes to clinical utility, the Ligs device offers several benefits. First of all, for the user, Ligs device is simple and convenient to operate. The straightforward and adaptable operation minimizes measurement inaccuracies that the examiner may have caused. Previous studies have confirmed the excellent intra- and inter-rater reliability (intraclass correlation, >0.9) of the Ligs arthrometer (Chen et al., 2022; Wu et al., 2023). Second, for the patient, the operation is more flexible because the rocker at the end of the main unit controls the load application. The loading can be customized for each participant during the test based on their acceptable range. Above all, Ligs comes equipped with integrated load and displacement sensors that have a 30Hz sampling frequency. As a result, frame by frame recording of real-time changes in load and displacement is possible. Furthermore, there are no scenario limitations when using the device due to its portable size and the short time required for testing.

This study has limitations which should be considered. First of all, in our study, the participants were patients who were prepared to undergo ACL reconstruction surgery, so the mechanical properties of each part of the structure were not studied in depth enough and were limited to the macroscopic stiffness changes of the knee joint. However, the knee joint has a complex structural composition, including tissues with different biomechanical properties such as the joint capsule, ligaments, and menisci. The tensile energy dissipation and mechanical properties of the meniscus are highly dependent on the direction of loading, as demonstrated in the study of the mechanical properties of the meniscus by Morejon et al. (2023). In addition, the water content of the meniscus is inversely related to its energy dissipation. Accordingly, the effects of ACL injury on the mechanical properties of different knee joint structures should be analyzed in depth in future studies. Secondly, in our study, only patients with isolated ACL injuries were included. For patients with combined meniscal injuries of different types and levels, the loading settings of the Ligs device and the effect on outcomes are not clear. Zhang et al. (2016) confirmed in a study that the location of the meniscal rupture modifies knee kinematics in patients with ACL combined with meniscal injuries. Musahl et al. (2016) found that a concomitant injury to the anterolateral capsule, medial meniscus, or lateral meniscus is associated with increased knee rotatory laxity in patients with an ACL injury. In a study by Massey et al. (2019) on the failure loads of different suture repair techniques after meniscal tears, the results showed that the failure loads of the parallel technique, cross-stitch technique and rebar repair of radial meniscal tears were 85.5 N ± 22.0, 76.2 N ± 28.8, and 124.1 N ± 27.1, respectively. Therefore, individuals should be more accurately categorized according to the type of injury in future studies to further investigate the mechanisms by which meniscal injuries alter joint biomechanics. In addition, future studies should evaluate patients undergoing different reconstructive procedures. And then, we only included patients with a complete ACL injury. Patients with different ACL injury classifications were therefore not studied in detail. Further research is needed to investigate whether load-displacement curves can be used to classify ACL injuries. In addition, our study was limited to healthy college students and adults. The results of the study are not applicable to adolescent and child patients. Future studies should fully consider the ligament laxity characteristics of different age groups to expand the applicability of the findings.

Conclusion

In the present study, we used a novel digital arthrometer to investigate the ligament stiffness characteristics after ACL injury. This study demonstrated that the two regions of the load-displacement curve following ACL injury have significantly different biomechanical characteristics. These results provide new insights into the laxity characteristics of the knee after ACL injury. Based on the results of the present study, we propose that a stiffness value less than 9.62 N/mm is a new diagnostic reference. We believe that this indicator may be a useful for identifying knee laxity in the later stages of increased loading.

Data availability statement

The raw data supporting the conclusions of this article will be made available by the authors, without undue reservation.

Ethics statement

The studies involving humans were approved by Institutional Review Board of Shanghai University of Sports. The studies were conducted in accordance with the local legislation and institutional requirements. The participants provided their written informed consent to participate in this study.

Author contributions

DW: Data curation, Formal Analysis, Methodology, Writing–original draft, Writing–review and editing. XZ: Methodology, Writing–original draft. BW: Formal Analysis, Methodology, Writing–original draft. LZ: Formal Analysis, Methodology, Writing–original draft. YL: Formal Analysis, Methodology, Writing–original draft. XH: Methodology, Writing–original draft. WX: Conceptualization, Resources, Supervision, Writing–review and editing. SW: Conceptualization, Funding acquisition, Resources, Supervision, Writing–review and editing.

Funding

The author(s) declare financial support was received for the research, authorship, and/or publication of this article. This work was supported by the Basic research projects of basic strengthening program (Grant No. 2020-JCJQ-ZD-264); and Sponsored by Program of Shanghai Academic/Technology Research Leader (Grant No. 21XD1434800).

Acknowledgments

The authors would like to thank the editors from Editage for their language services.

Conflict of interest

The authors declare that the research was conducted in the absence of any commercial or financial relationships that could be construed as a potential conflict of interest.

Publisher's note

References

Benjaminse, A., Gokeler, A., and Van Der Schans, C. P. (2006). Clinical diagnosis of an anterior cruciate ligament rupture: a meta-analysis. *J. Orthop. Sports Phys. Ther.* 36, 267–288. doi:10.2519/jospt.2006.2011

Chen, Y., Cao, S., Wang, C., Ma, X., and Wang, X. (2022). Quantitative analysis with load-displacement ratio measured via digital arthrometer in the diagnostic evaluation of chronic ankle instability: a cross-sectional study. *J. Orthop. Surg. Res.* 17, 287. doi:10.1186/s13018-022-03177-3

Cohen, J. (1988). *Statistical power analysis for the behavioral sciences*. 2nd ed. Hillsdale, NJ: Lawrence Erlbaum Associates, Publishers, 567. Computers, Environment and Urban Systems, 14, 71.

Daniel, D. M., Malcom, L. L., Losse, G., Stone, M. L., Sachs, R., and Burks, R. (1985a). Instrumented measurement of anterior laxity of the knee. *J. Bone Jt. Surg. Am.* 67, 720–726. doi:10.2106/00004623-198567050-00006

Daniel, D. M., Stone, M. L., Sachs, R., and Malcom, L. (1985b). Instrumented measurement of anterior knee laxity in patients with acute anterior cruciate ligament disruption. *Am. J. Sports Med.* 13, 401–407. doi:10.1177/036354658501300607

Eagar, P., Hull, M. L., and Howell, S. M. (2001). A method for quantifying the anterior load-displacement behavior of the human knee in both the low and high stiffness regions. *J. Biomech.* 34, 1655–1660. doi:10.1016/s0021-9290(01)00142-7

Iw, F., and Cd, W.-S. (1989). Is the KT1000 knee ligament arthrometer reliable? *J. Bone Jt. Surg. Br.* 71, 843–847. doi:10.1302/0301-620x.71b5.2584257

KüPPER, J. C., Loitz-Ramage, B., Corr, D. T., Hart, D. A., and Ronsky, J. L. (2007). Measuring knee joint laxity: a review of applicable models and the need for new approaches to minimize variability. *Clin. Biomech. (Bristol, Avon)* 22, 1–13. doi:10.1016/j.clinbiomech.2006.08.003

Liu, W., Maitland, M. E., and Bell, G. D. (2002). A modeling study of partial ACL injury: simulated KT-2000 arthrometer tests. *J. Biomech. Eng.* 124, 294–301. doi:10.1115/1.1468636

Maitland, M. E., Bell, G. D., Mohtadi, N. G., and Herzog, W. (1995). Quantitative analysis of anterior cruciate ligament instability. *Clin. Biomech. (Bristol, Avon)* 10, 93–97. doi:10.1016/0268-0033(95)92045-n

Markolf, K. L., Kochan, A., and Amstutz, H. C. (1984). Measurement of knee stiffness and laxity in patients with documented absence of the anterior cruciate ligament. *J. Bone Jt. Surg. Am.* 66, 242–252. doi:10.2106/00004623-198466020-00011

Markolf, K. L., Mensch, J. S., and Amstutz, H. C. (1976). Stiffness and laxity of the knee--the contributions of the supporting structures. A quantitative *in vitro* study. *J. Bone Jt. Surg. Am.* 58, 583–594. doi:10.2106/00004623-197658050-00001

Massey, P., Mcclary, K., Parker, D., Barton, R. S., and Solitro, G. (2019). The rebar repair for radial meniscus tears: a biomechanical comparison of a reinforced suture repair versus parallel and cross-stitch techniques. *J. Exp. Orthop.* 6, 38. doi:10.1186/s40634-019-0206-4

Minns, R. J., Soden, P. D., and Jackson, D. S. (1973). The role of the fibrous components and ground substance in the mechanical properties of biological tissues: a preliminary investigation. *J. Biomech.* 6, 153–165. doi:10.1016/0021-9290(73)90084-5

Morejon, A., Dalbo, P. L., Best, T. M., Jackson, A. R., and Travascio, F. (2023). Tensile energy dissipation and mechanical properties of the knee meniscus: relationship with fiber orientation, tissue layer, and water content. *Front. Bioeng. Biotechnol.* 11, 1205512. doi:10.3389/fbioe.2023.1205512

Mouarbes, D., Cavaignac, E., Chiron, P., BéRARD, E., and Murgier, J. (2018). Evaluation of reproducibility of robotic knee testing device (GNRB) on 60 healthy knees. *J. Orthop.* 15, 94–98. doi:10.1016/j.jor.2018.01.031

Musahl, V., Rahnemai-Azar, A. A., Costello, J., Arner, J. W., Fu, F. H., Hoshino, Y., et al. (2016). The influence of meniscal and anterolateral capsular injury on knee laxity in patients with anterior cruciate ligament injuries. *Am. J. Sports Med.* 44, 3126–3131. doi:10.1177/0363546516659649

Paterno, M. V., Rauh, M. J., Schmitt, L. C., Ford, K. R., and Hewett, T. E. (2012). Incidence of contralateral and ipsilateral anterior cruciate ligament (ACL) injury after primary ACL reconstruction and return to sport. *Clin. J. Sport Med.* 22, 116–121. doi:10.1097/jsm.0b013e318246ef9e

Pugh, L., Mascarenhas, R., Arneja, S., Chin, P. Y., and Leith, J. M. (2009). Current concepts in instrumented knee-laxity testing. *Am. J. Sports Med.* 37, 199–210. doi:10.1177/0363546508323746

Raggi, F., Roberti Di Sarsina, T., Signorelli, C., Marcheggiani Muccioli, G. M., Macchiarola, L., Cucurnia, I., et al. (2019). Triaxial accelerometer can quantify the Lachman test similarly to standard arthrometers. *Knee Surg. Sports Traumatol. Arthrosc.* 27, 2698–2703. doi:10.1007/s00167-018-5306-7

Rangger, C., Daniel, D. M., Stone, M. L., and Kaufman, K. (1993). Diagnosis of an ACL disruption with KT-1000 arthrometer measurements. *Knee Surg. Sports Traumatol. Arthrosc.* 1, 60–66. doi:10.1007/bf01552161

Rohman, E. M., and Macalena, J. A. (2016). Anterior cruciate ligament assessment using arthrometry and stress imaging. *Curr. Rev. Musculoskelet. Med.* 9, 130–138. doi:10.1007/s12178-016-9331-1

Runer, A., Roberti Di Sarsina, T., Starke, V., Iltchev, A., Felmet, G., Braun, S., et al. (2021). The evaluation of Rolimeter, KLT, KiRA and KT-1000 arthrometer in healthy

individuals shows acceptable intra-rater but poor inter-rater reliability in the measurement of anterior tibial knee translation. *Knee Surg. Sports Traumatol. Arthrosc.* 29, 2717–2726. doi:10.1007/s00167-021-06540-9

Smith, K., Miller, N., and Laslovich, S. (2022). The reliability of the GNRB® knee arthrometer in measuring ACL stiffness and laxity: implications for clinical use and clinical trial design. *Int. J. Sports Phys. Ther.* 17, 1016–1025. doi:10.26603/001c.38252

Van Eck, C. F., Loopik, M., Van Den Bekerom, Fu, F. H., and Kerkhoffs, G. M. (2013a). Methods to diagnose acute anterior cruciate ligament rupture: a meta-analysis of instrumented knee laxity tests. *Knee Surg. Sports Traumatol. Arthrosc.* 21, 1989–1997. doi:10.1007/s00167-012-2246-5

Van Eck, C. F., Van Den Bekerom, Fu, F. H., Poolman, R. W., and Kerkhoffs, G. M. (2013b). Methods to diagnose acute anterior cruciate ligament rupture: a meta-analysis of physical examinations with and without anaesthesia. *Knee Surg. Sports Traumatol. Arthrosc.* 21, 1895–1903. doi:10.1007/s00167-012-2250-9

Woo, S. L., Hollis, J. M., Adams, D. J., Lyon, R. M., and Takai, S. (1991). Tensile properties of the human femur-anterior cruciate ligament-tibia complex. The effects of specimen age and orientation. *Am. J. Sports Med.* 19, 217–225. doi:10.1177/036354659101900303

Wu, D., Wang, D., Han, Y., Guo, L., and Wang, S. (2023). A novel digital arthrometer to measure anterior tibial translation. *J. Orthop. Surg. Res.* 18, 101. doi:10.1186/s13018-022-03497-4

Zhang, Y., Huang, W., Yao, Z., Ma, L., Lin, Z., Wang, S., et al. (2016). Anterior cruciate ligament injuries alter the kinematics of knees with or without meniscal deficiency. *Am. J. Sports Med.* 44, 3132–3139. doi:10.1177/0363546516658026

frontiers | Frontiers in Bioengineering and Biotechnology

TYPE Original Research
PUBLISHED 08 January 2024
DOI 10.3389/fbioe.2023.1255625

OPEN ACCESS

EDITED BY
João Manuel R. S. Tavares,
University of Porto, Portugal

REVIEWED BY
Xiaogang Wu,
Taiyuan University of Technology, China
Anthony J. Petrella,
Colorado School of Mines, United States

*CORRESPONDENCE
Qida Zhang,
zhangqida621@163.com

RECEIVED 09 July 2023
ACCEPTED 21 December 2023
PUBLISHED 08 January 2024

CITATION
Zhang Q, Li Z, Chen Z, Peng Y, Jin Z and Qin L (2024), Prediction of knee biomechanics with different tibial component malrotations after total knee arthroplasty: conventional machine learning vs. deep learning.
Front. Bioeng. Biotechnol. 11:1255625.
doi: 10.3389/fbioe.2023.1255625

Prediction of knee biomechanics with different tibial component malrotations after total knee arthroplasty: conventional machine learning vs. deep learning

Qida Zhang[1]*, Zhuhuan Li[2], Zhenxian Chen[3], Yinghu Peng[4], Zhongmin Jin[5,6] and Ling Qin[1]

[1]Musculoskeletal Research Laboratory, Department of Orthopaedics and Traumatology, The Chinese University of Hong Kong, Hong Kong, Hong Kong SAR, China, [2]State Key Laboratory for Manufacturing System Engineering, School of Mechanical Engineering, Xi'an Jiaotong University, Xi'an, China, [3]Key Laboratory of Road Construction Technology and Equipment (Ministry of Education), School of Mechanical Engineering, Chang'an University, Xi'an, China, [4]CAS Key Laboratory of Human-Machine Intelligence-Synergy Systems, Shenzhen Institutes of Advanced Technology Chinese Academy of Sciences, Shenzhen, China, [5]Tribology Research Institute, School of Mechanical Engineering, Southwest Jiaotong University, Chengdu, China, [6]Institute of Medical and Biological Engineering, School of Mechanical Engineering, University of Leeds, Leeds, United Kingdom

The precise alignment of tibiofemoral components in total knee arthroplasty is a crucial factor in enhancing the longevity and functionality of the knee. However, it is a substantial challenge to quickly predict the biomechanical response to malrotation of tibiofemoral components after total knee arthroplasty using musculoskeletal multibody dynamics models. The objective of the present study was to conduct a comparative analysis between a deep learning method and four conventional machine learning methods for predicting knee biomechanics with different tibial component malrotation during a walking gait after total knee arthroplasty. First, the knee contact forces and kinematics with different tibial component malrotation in the range of $\pm 5^{\circ}$ in the three directions of anterior/posterior slope, internal/external rotation, and varus/valgus rotation during a walking gait after total knee arthroplasty were calculated based on the developed musculoskeletal multibody dynamics model. Subsequently, deep learning and four conventional machine learning methods were developed using the above 343 sets of biomechanical data as the dataset. Finally, the results predicted by the deep learning method were compared to the results predicted by four conventional machine learning methods. The findings indicated that the deep learning method was more accurate than four conventional machine learning methods in predicting knee contact forces and kinematics with different tibial component malrotation during a walking gait after total knee arthroplasty. The deep learning method developed in this study enabled quickly determine the biomechanical response with different tibial component malrotation during a walking gait after total knee arthroplasty. The proposed method offered surgeons and surgical robots the ability to establish a calibration

safety zone, which was essential for achieving precise alignment in both preoperative surgical planning and intraoperative robotic-assisted surgical navigation.

KEYWORDS

total knee arthroplasty, accurate rotational alignment, musculoskeletal multibody dynamics model, deep learning, machine learning, biomechanics

1 Introduction

Accurate alignment of tibiofemoral components is a critical element in obtaining favorable clinical outcomes for patients after total knee arthroplasty (TKA). Poor rotational alignment of tibiofemoral components can result in knee stiffness (Bedard et al., 2011; Kim et al., 2014), evaluated joint contact stress (Chen et al., 2015; Ueyama et al., 2020; Tang et al., 2022), and a high prevalence of TKA revisions (Dalury et al., 2013; Panni et al., 2018; Rajgopal et al., 2022). Moreover, over 50% of patients who experienced joint pain after TKA had mal-rotational alignment of the knee components, which is a substantial contributor to joint pain and functional deficit (Hofmann et al., 2003; Bell et al., 2014; Abdelnasser et al., 2019b; Rajgopal et al., 2022). The focus of most clinical studies has been on assessing the impact of component malrotation on knee function through postoperative evaluations. Notwithstanding, these assessments fail to provide surgeons accurately and quickly with the necessary biomechanical performance data for preoperative surgical planning or intraoperative surgical guidance. This lack of information may result in unsatisfactory recovery of patient knee function after TKA caused by component malrotation. Barrack et al. evaluated the relationship between anterior knee pain and component rotation after TKA, discovering that patients with anterior knee pain had an average of 6.2° of internal rotation compared to a mere 0.4° of external rotation in pain-free patients (Barrack et al., 2001). Similarly, Abdelnasser et al. investigated the effects of intra-operative intentional malrotation of the tibial component on vivo kinematics, revealing that internal rotation of the tibial component in TKA can result in postoperative extension deficits, potentially causing pain and knee stiffness (Abdelnasser et al., 2019a). These clinical findings underscored the importance of accurate component alignment in determining the knee function of TKA patients. Therefore, developing effective and quick methods to correct component malrotation during preoperative planning and intraoperative surgical guidance to prevent unsatisfactory functional recovery after surgery remains a pressing clinical challenge.

Numerous computational studies have explored the impact of component malrotation on knee biomechanics during a walking gait after TKA using musculoskeletal multibody dynamics and finite element methods (Kuriyama et al., 2014; Smith et al., 2016; Vanheule et al., 2017; Fang et al., 2022; Tang et al., 2022). Chen et al. found that varus-valgus malrotation of the tibial/femoral component and internal-external malrotation of the femoral component with a 5° variation impacted peak medial contact force by 17.8%–53.1%, peak lateral contact force by 35.0%–88.4%, and peak total contact force by 5.2%–18.7% using a multibody dynamics model (Chen et al., 2015). Likewise, Kang et al. demonstrated that external malrotation of the femoral component increased the lateral contact stress of the tibial component, whereas internal malrotation increased the medial contact stress using a finite element method (Kang et al., 2016). Nonetheless, these computational models have a significant limitation in that they are typically time-consuming and computationally demanding. As a result, accurately and quickly predicting the biomechanical response to component malrotation during preoperative surgical planning or intraoperative surgical guidance using computational models remains a considerable challenge.

Recently, artificial intelligence (AI) techniques have emerged as a promising alternative for quickly and accurately predicting human biomechanics. Numerous studies have employed machine learning methods to forecast ground reaction forces from patient gaits (Oh et al., 2013; Guo et al., 2017; Wouda et al., 2018; Johnson et al., 2019; Komaris et al., 2019), computer vision methods to estimate patient poses (Mehrizi et al., 2019; Tamura et al., 2020), and wearable sensors to assess patient kinematics (Stetter et al., 2019; Gholami et al., 2020; Mundt et al., 2020). Stetter et al. demonstrated that combining wearable sensors and artificial neural networks accurately estimated knee joint forces across various movements, including linear motions, changes of direction, and jumps (Stetter et al., 2019). Zhu et al. proposed a knee contact force prediction method that integrated artificial fish swarm and random forest algorithms, with experiments verified that the proposed method outperformed classical multibody dynamics analysis and artificial neural network models (Zhu et al., 2020). Moreover, Rane et al. trained a deep neural network using a set of kinematic, kinetic, and electromyographic measurements from 156 subjects during gaits and showed that the magnitudes of the medial knee joint force and muscle forces predicted by the proposed method were in good agreement with those derived from musculoskeletal modeling. (Rane et al., 2019). However, there is a paucity of literature on the development of machine/deep learning methods for accurately predicting knee biomechanics with different tibial component malrotation in TKA. Additionally, it remains uncertain whether a noteworthy distinction exists between the deep learning method and conventional machine learning methods in predicting knee biomechanics under different tibial component malrotations during a walking gait in TKA. Therefore, the development of machine/deep learning methods for accurate and rapid prediction of knee biomechanics with different tibial component malrotations during a walking gait in TKA is essential for preoperative surgical planning and intraoperative robotic-assisted surgical navigation.

The objective of the present study was to: 1) develop deep learning method and conventional machine learning methods to predict knee biomechanics with different tibial component malrotation during a walking gait after TKA using the dataset

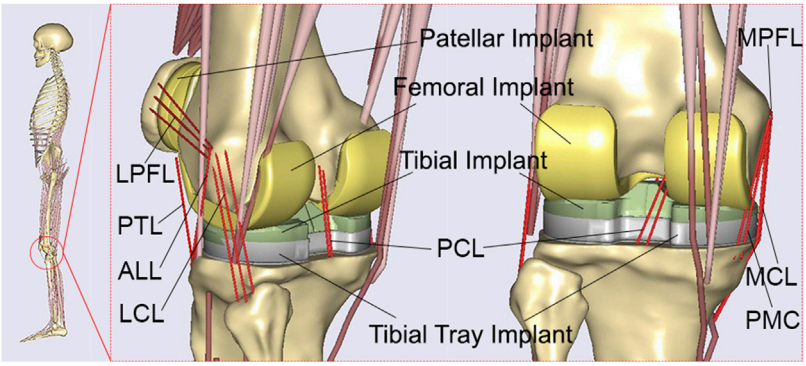

FIGURE 1
The developed patient-specific musculoskeletal multibody dynamics model of total knee arthroplasty.

derived from the developed musculoskeletal multibody dynamics model; 2) conduct a comparative analysis between the deep learning method and conventional machine learning methods for predicting knee contact forces and kinematics with different tibial component malrotation during a walking gait after TKA.

2 Materials and methods

2.1 Musculoskeletal multibody dynamics model

A patient-specific musculoskeletal multibody dynamics model of TKA (Chen et al., 2016; Zhang et al., 2019; Zhang et al., 2020) was developed using Anybody modeling system (version 6.0; AnyBody Technology, Aalborg, Denmark), based on an advanced bone morphing technique utilizing the patient's preoperative and postoperative computed tomography (CT) scans (Damsgaard et al., 2006; Pellikaan et al., 2014) (Figure 1). Data from a TKA patient (gender: male; mass: 75 kg; height: 180 cm; surgery: left knee), obtained from the publicly SimTK website (https://simtk.org/home/kneeloads), was employed to develop the patient-specific musculoskeletal model (Fregly et al., 2012). The patient's database included the geometries of knee implants and the lower limb bones derived from patient CT scans. In addition, marker trajectories and ground reaction forces obtained from motion capture experiments were included in the database. The segments and each muscle's isometric strength were scaled according to the patient's weight and height utilizing a length-mass-fat scaling approach (Rasmussen et al., 2005; Lund et al., 2015; Marra et al., 2015; Chen et al., 2016; Hu et al., 2019). An innovative knee joint model consisting of 11 degrees of freedom was established via the force-dependent kinematics method, including deformable contact models of the artificial knee joint (Andersen and Rasmussen, 2011; Marra et al., 2015; Chen et al., 2016). The tibiofemoral joint had 6° of freedom, and the patellofemoral joint had 5° of freedom, assuming a rigid patellar tendon ligament (PTL) (Chen et al., 2016). Three deformable contact models were defined between the femoral component and the medial/lateral tibial components, as well as between the femoral component and the patellar component, based on the elastic foundation theory (Fregly et al., 2003). The knee joint model was enveloped by ligaments including the medial collateral ligament (MCL), lateral collateral ligament (LCL), posterior cruciate ligament (PCL), posterior-medial capsule (PMC), anterior-lateral ligament (ALL), medial patellofemoral ligament (MPFL), and lateral patellofemoral ligament (LPFL) (Chen et al., 2016; Zhang et al., 2020). These ligaments were modeled as nonlinear spring elements with a piecewise force-displacement relationship (Blankevoort et al., 1991). An inverse kinematics method (Andersen et al., 2010) was conducted to determine the pelvic motion, hip angles, and foot locations based on the walking gait data, the scaled musculoskeletal model, and the optimized marker locations (Marra et al., 2015; Chen et al., 2016). These kinematics and ground reaction forces were subsequently input into the inverse dynamics analysis, which incorporated the force-dependent kinematics method (Andersen and Rasmussen, 2011; Marra et al., 2015; Chen et al., 2016), to calculate tibiofemoral contact forces and kinematics. In the inverse dynamics analysis, a cubic polynomial muscle recruitment criterion was also adopted to determine which set of muscles will balance a given external load. Additional information regarding the development of the musculoskeletal multibody dynamics model of TKA can be found in our previous studies (Chen et al., 2016; Zhang et al., 2019; Zhang et al., 2020).

As per the patient's surgical report (Fregly et al., 2012; Chen et al., 2015; Chen et al., 2016), two 90° cuts were made on the proximal tibia in the coronal and sagittal planes with respect to the long axis. The distal femur was cut at 6° valgus from the anatomical axis. A 3° external rotation cut was made on the posterior femur with respect to the posterior condyles. These cuts were defined as the neutral position of the femoral and tibial components in the developed patient-specific musculoskeletal multibody dynamics model of TKA. To investigate the effect of tibial component malrotation, the rotational positions of the tibial component were modified from the neutral position in 343 cases: neutral, ±1°, ±3°, and ±5° of anterior-posterior slope, ±1°, ±3° and ±5° of internal-external rotation, and ±1°, ±3° and ±5° of varus-valgus rotation (Figure 2). Each tibial component with the same femoral component was separately imported into the developed patient-specific musculoskeletal multibody dynamics model of TKA. The knee contact forces and kinematics during a walking gait under different tibial component malrotation in the range of ±5° in the three directions of anterior/posterior slope, internal/external rotation, and varus/valgus rotation were calculated. These results will serve as a dataset to develop deep learning and machine learning methods (Table 1).

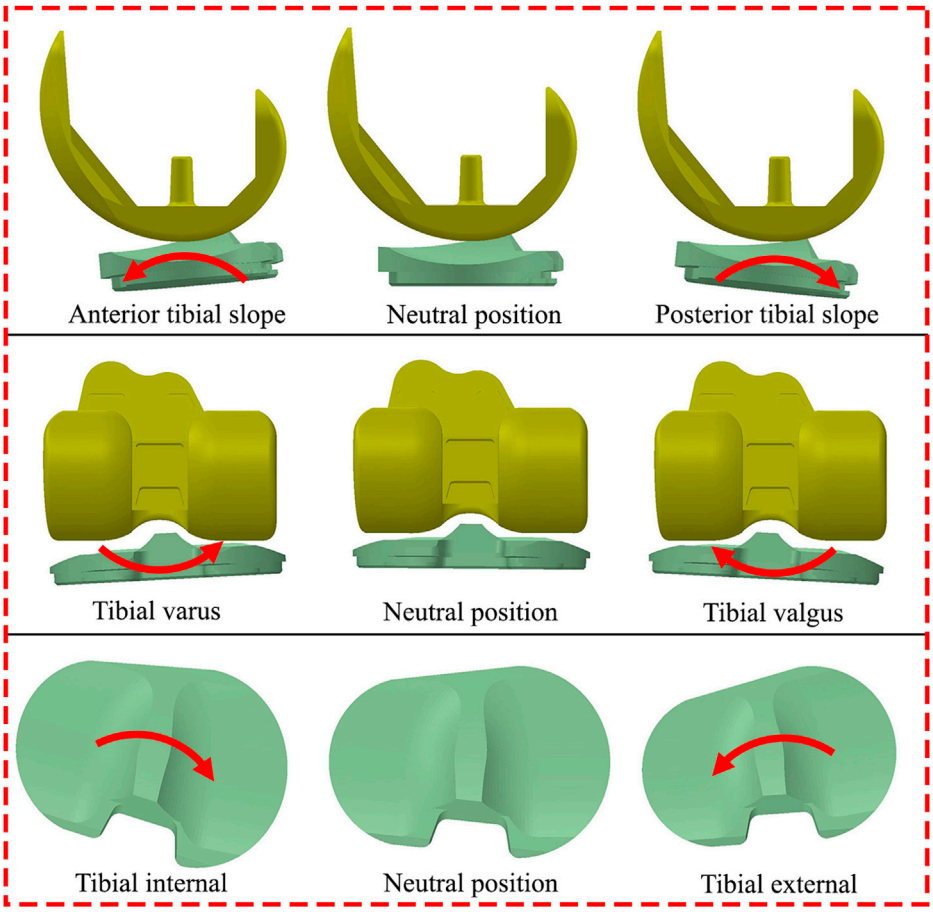

FIGURE 2
Schematic diagram for different tibial component malrotation.

TABLE 1 Predictor and predicted features used in deep learning and machine learning methods.

Predictor features		Predicted features	
Tibial Component Malrotation	Anterior-Posterior Slope	Contact Forces	Total Contact Force
			Medial Contact Force
			Lateral Contact Force
	Internal-External Rotation		Flexion-Extension Rotation
		Kinematics	Internal-External Rotation
			Varus-Valgus Rotation
	Varus-Valgus Rotation		Anterior-Posterior Translation
			Proximal-Distal Translation
			Medial-Lateral Translation

2.2 Deep learning model

A deep learning model using recurrent neural networks (RNNs) was developed to predict knee contact forces and kinematics with different tibial component malrotations over a walking gait cycle. The model utilized predictor features of tibial component malrotation, including anterior-posterior slope, internal-external rotation, and varus-valgus rotation (Figure 2; Table 1). The predicted features included knee contact forces and kinematics (Table 1). The RNN architecture consisted of two bi-directional long short-term memory (LSTM) cells (Hochreiter and Schmidhuber, 1997) and three fully-connected layers. Different

tibial component malrotation were represented by $x^i \in R^{A\times T}$ with A tibial component malrotation variables over T time steps. The knee biomechanics over a walking gait cycle were obtained using the musculoskeletal multibody dynamics model and stored in $y^i \in R^{B\times T}$ with B output variables. RNNs were trained to with the aim of minimizing the objective function:

$$J(X,Y,\theta) = \frac{1}{N}\sum_{i=1}^{N}\left\|y^i - \hat{y}^i\right\|^2 + \lambda\|\theta\|^2$$

The training set, $X = \{x^1, x^2, \ldots, x^N\}$ and $Y = \{y^1, y^2, \ldots, y^N\}$, comprised different tibial component malrotation and corresponding knee biomechanics derived from the musculoskeletal model. RNNs predicted knee biomechanics time series trends ($\hat{y}^i$) based on the corresponding predictor features (different tibial component malrotation). Here, λ is the regularization parameter, which controls the trade-off between fitting the training data and keeping the parameter values small. θ is the parameter vector that the model aims to learn. It contains the weights associated with each feature in the input matrix X.

RNNs were trained for 10,000 iterations using Adam optimization with a learning rate of 0.0001 (Kingma and Ba, 2014). The weights of the RNNs were randomly initialized from a Gaussian distribution ($\mu = 0$, $\sigma = 0.01$). An L2 regularization ($\lambda = 0.001$) and batch size of 2 were employed. These hyperparameters were fine-tuned based on our dataset and experimental setup, aiming to optimize the training process and enhance the model's performance. PyTorch served as the implementation framework for the deep learning model in this study (Paszke et al., 2017).

2.3 Machine learning model

Similarly, four ensemble learning methods were developed to predict knee contact forces and kinematics with different component malrotation over a walking gait cycle. These models utilized predictor features of tibial component malrotation, including anterior-posterior slope, internal-external rotation, and varus-valgus rotation (Figure 2; Table 1). The predicted features included knee contact forces and kinematics (Table 1). Four ensemble learning methods were developed using Scikit-learn in Python (Pedregosa et al., 2012; Buitinck et al., 2013): Random Forest regression, AdaBoost regression, Gradient Boosting regression, Voting regression. Ensemble methods aimed to enhance the generalizability and robustness of a single estimator by combining the predictions of multiple base estimators built using a given learning algorithm (Pedregosa et al., 2012).

The Random Forest algorithm (Breiman, 2001; Pedregosa et al., 2012) was applied in this study, which involved merging k base learned models (M_1, M_2, …, M_K) to construct an enhanced composite prediction model, denoted as M^*. To generate base model M_i, k training sets [D_1, D_2, …, D_K, where D_i ($1 \le i \le k$)] were derived from a given dataset D. The given dataset in this study referred to the original dataset that contained the input features (e.g., tibial component malrotation features like anterior-posterior slope, internal-external rotation, varus-valgus rotation) and corresponding output variables (knee contact forces and kinematics). The given dataset was used to generate k training datasets through a technique called bootstrap aggregating or "bagging." Bagging involved random sampling with replacement from the given dataset, resulting in k unique training datasets (D_1, D_2, …, D_K). Each training dataset was used to train a separate base model (M_1, M_2, …, M_K) within the Random Forest ensemble. The purpose of creating multiple training datasets was to introduce diversity among the base models, as each base model was trained on a different subset of the original dataset. When a new data tuple was presented to the ensemble model, each base model returned a predicted result, and the ensemble model produced the final prediction by averaging or taking the mode of the predicted results from the base models (Pedregosa et al., 2012; Zhu et al., 2020).

The AdaBoost algorithm (Freund and Schapire, 1997; Pedregosa et al., 2012) was employed in this study, utilizing sequential weak learners, which were models that only marginally outperform random guessing, such as small decision trees, to repeatedly modified versions of the data. These weak learners were iteratively applied to modified versions of the data. The final prediction was obtained by combining the predictions of all weak learners through a weighted majority vote or sum. During each boosting iteration, the weights w_1, w_2, …, w_N assigned to each training sample were adjusted. Initially, all weights were set to $w_i = 1/N$, enabling the first iteration to train a weak learner on the original data (Pedregosa et al., 2012). Subsequently, at each iteration, the weights of the training samples were individually modified, and the learning algorithm was reapplied to the reweighted data. Specifically, for a given iteration, the weights of training examples incorrectly predicted by the previous boosted model were increased, while the weights of correctly predicted examples were decreased (Pedregosa et al., 2012). As the iterations progressed, examples that were challenging to predict received progressively greater influence. This iterative adjustment of weights compelled each subsequent weak learner to focus on the examples that were previously missed by the preceding weak learners in the sequence (Drucker, 1997; Hastie et al., 2009; Pedregosa et al., 2012). By iteratively adjusting the weights and training weak learners, AdaBoost constructed a strong ensemble model that combines the predictions of the individual weak learners to improve overall regression prediction performance.

The Gradient Boosting algorithm, as proposed by Friedman and refined by Pedregosa et al., leveraged the combination of multiple weak learners to construct robust ensemble models (Friedman, 2001; Pedregosa et al., 2012). By employing gradient descent optimization, each subsequent model was trained to minimize the loss function, such as mean squared error, of the previous model. During each iteration, the algorithm calculated the gradient of the loss function with respect to the predictions of the current ensemble and utilized this gradient to train a new weak model. The objective was to minimize the gradient, thereby improved the overall performance of the ensemble. The predictions of the newly trained model were then integrated into the ensemble, reinforcing the collective predictive capability. This iterative process continued until a predefined stopping criterion was satisfied (Pedregosa et al., 2012).

The voting regression algorithm combined different machine learning regression algorithms and returned the average predicted values (Pedregosa et al., 2012). In this approach, multiple regression models were trained using various algorithms, including Random Forest, AdaBoost and Gradient Boosting. Each individual model

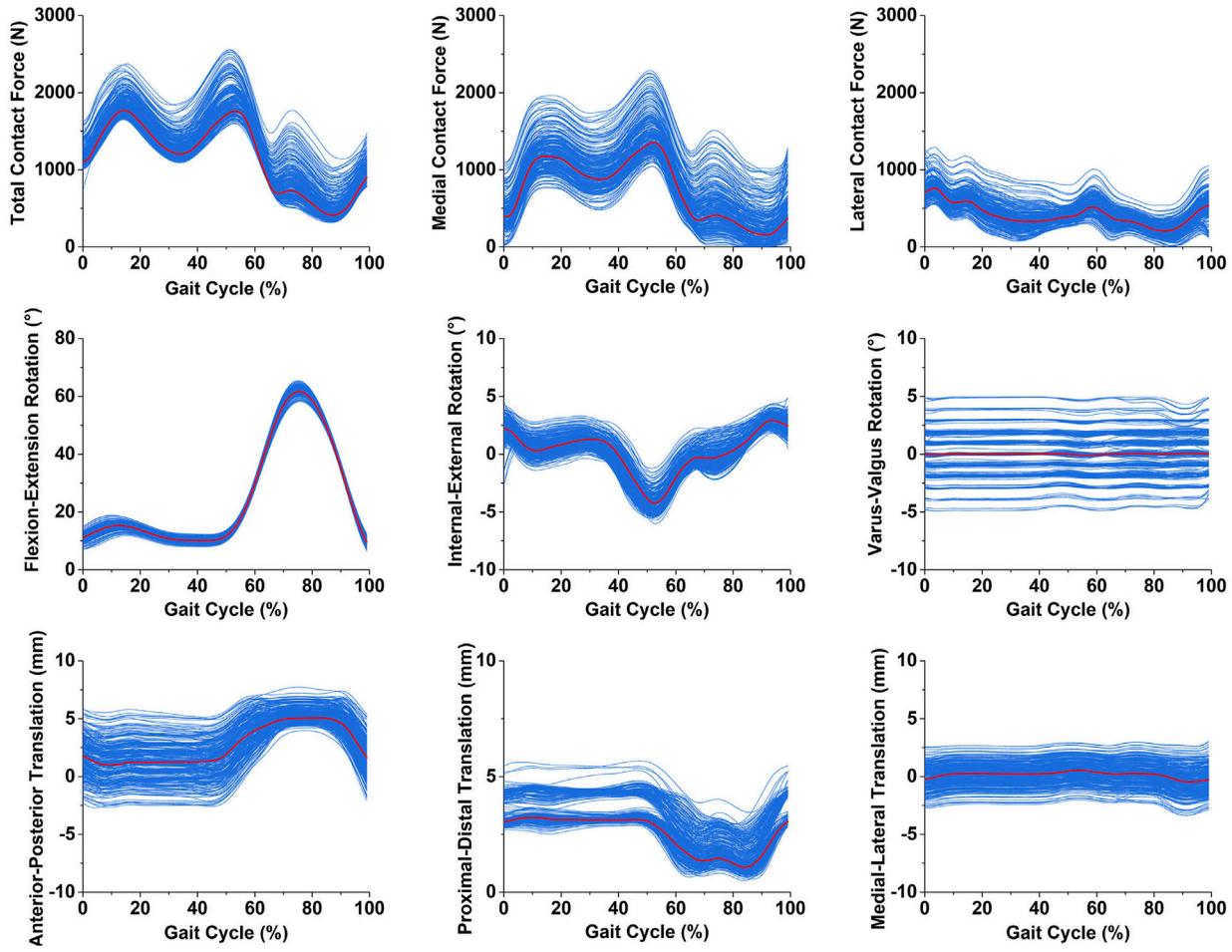

FIGURE 3
The knee biomechanics under different tibial component malrotation during a walking gait after total knee arthroplasty (the red line represent knee biomechanics under tibial component neutral position during a walking gait; the blue line represent knee biomechanics under different tibial component malrotation during a walking gait).

generated its prediction for a given input, and the final prediction was obtained by averaging the predicted values of all models. The voting algorithm allowed for a more robust prediction by considering the collective knowledge of multiple models and balancing out their individual weaknesses. The voting regression approach was particularly useful when the individual models had similar performance levels, as it leveraged their combined strengths to improve overall prediction accuracy (Pedregosa et al., 2012).

2.4 Performance analyses

The deep learning and learning models developed in this study were evaluated for accuracy using 5-fold cross-validation, where the dataset was divided into 5 equal subgroups used for the training and validation (Burton et al., 2021). An additional test dataset withheld from the cross-validation was used to confirm the performance of the models. To ensure consistency across all deep learning and machine learning algorithms, the same cross-validation splits were used for all models. To evaluate the models, each subgroup was held out for evaluation once, and all models were trained five times. The performance of the developed deep learning and machine learning models was assessed against musculoskeletal multibody dynamics model outputs, which were considered the ground truth. The evaluation was conducted using two metrics: Root mean square error (RMSE) and Pearson correlation coefficient. The Pearson correlation coefficient ρ was classified as weak ($\rho \leq 0.35$), moderate ($0.35 < \rho \leq 0.67$), strong ($0.67 < \rho \leq 0.9$), and excellent ($0.9 < \rho$) according to the obtained values.

3 Results

The knee total contact forces, medial contact forces, lateral contact forces, flexion-extension rotation, internal-external rotation, varus-valgus rotation, anterior-posterior translation, proximal-distal translation, and medial-lateral translation during a walking gait under different tibial component malrotation in the range of ±5° in the three directions were presented in Figure 3.

The comparison of ground truth values and deep learning prediction for knee contact forces under different tibial component malrotation during walking gait after TKA was

TABLE 2 The comparison of ground truth values and deep learning prediction for knee contact forces under different tibial component malrotation during a walking gait after total knee arthroplasty.

Predicted Feature	Training set		Validation set		Test set	
	RMSE (N)	ρ	RMSE (N)	ρ	RMSE (N)	ρ
Total contact forces	7.77	0.999	32.54	0.995	38.44	0.995
Medial contact forces	33.90	0.995	37.41	0.995	51.78	0.993
Lateral contact forces	11.68	0.999	15.47	0.999	19.74	0.999

TABLE 3 The comparison of ground truth values and machine learning prediction for knee contact forces under different tibial component malrotation during a walking gait after total knee arthroplasty.

Regression Models	Total contact forces		Medial contact forces		Lateral contact forces	
	RMSE(N)	ρ	RMSE(N)	ρ	RMSE(N)	ρ
Random Forest	63.15	0.987	58.51	0.992	23.93	0.998
AdaBoost	75.15	0.983	81.94	0.982	34.84	0.994
Gradient Boosting	65.98	0.986	58.33	0.992	30.22	0.994
Voting	62.32	0.987	70.55	0.984	24.85	0.998

presented in Table 2. For the training set, the RMSE for total contact force, medial contact force, and lateral contact force were 7.77, 33.90, and 11.17 N, respectively, as predicted by the deep learning model. The Pearson correlation coefficient for total contact force, medial contact force, and lateral contact force were 0.999, 0.995, and 0.999, respectively, as predicted by the deep learning model. For the validation set, the RMSE for total contact force, medial contact force, and lateral contact force were 32.54, 37.41, and 15.47 N, respectively, as predicted by the deep learning model. The Pearson correlation coefficient for total contact force, medial contact force, and lateral contact force were 0.995, 0.995, and 0.999, respectively, as predicted by the deep learning model. For the test set, the RMSE for total contact force, medial contact force, and lateral contact force were 38.44, 51.78, and 19.74 N, respectively, as predicted by the deep learning model. The Pearson correlation coefficient for total contact force, medial contact force, and lateral contact force were 0.995, 0.993, and 0.999, respectively, as predicted by the deep learning model.

The comparison of ground truth values and four machine learning predictions for knee contact forces under different tibial component malrotation during a walking gait after TKA was presented in Table 3. For the Random Forest regression model (test set), the RMSE and Pearson correlation coefficient for total contact force, medial contact force, and lateral contact force were 63.15, 58.51, and 23.93 N, respectively, and 0.987, 0.992, and 0.998, respectively. For the AdaBoost regression model (test set), the RMSE and Pearson correlation coefficient for total contact force, medial contact force, and lateral contact force were 75.15, 81.94, and 34.84 N, respectively, and 0.983, 0.982, and 0.994, respectively. For the Gradient Boosting regression model (test set), the RMSE and Pearson correlation coefficient for total contact force, medial contact force, and lateral contact force were 65.98, 58.33, and 30.22 N, respectively, and 0.986, 0.992, and 0.994, respectively. For the Voting regression model (test set), the RMSE and Pearson correlation coefficient for total contact force, medial contact force, and lateral contact force were 62.32, 70.55, and 24.85 N, respectively, and 0.987, 0.984, and 0.998, respectively.

The comparison of ground truth values and deep learning prediction for knee kinematics under different tibial component malrotation during a walking gait after TKA was presented in Table 4. For the training set, the RMSE for flexion-extension rotation, internal-external rotation, varus-valgus rotation, anterior-posterior translation, proximal-distal translation, and medial-lateral translation were 0.07°, 0.04°, 0.11°, 0.04 mm, 0.03, and 0.05 mm, respectively, as predicted by the deep learning model. The Pearson correlation coefficient for flexion-extension rotation, internal-external rotation, varus-valgus rotation, anterior-posterior translation, proximal-distal translation, and medial-lateral translation were 0.999, 0.999, 0.998, 0.999, 0.999, and 0.998, respectively, as predicted by the deep learning model. For the validation set, the RMSE for flexion-extension rotation, internal-external rotation, varus-valgus rotation, anterior-posterior translation, proximal-distal translation, and medial-lateral translation were 0.12°, 0.20°, 0.10°, 0.20, 0.29, and 0.07 mm, respectively, as predicted by the deep learning model. The Pearson correlation coefficient for flexion-extension rotation, internal-external rotation, varus-valgus rotation, anterior-posterior translation, proximal-distal translation, and medial-lateral translation were 0.998, 0.996, 0.998, 0.997, 0.997, and 0.999, respectively, as predicted by the deep learning model. For the test set, the RMSE for flexion-extension rotation, internal-external rotation, varus-valgus rotation, anterior-posterior translation, proximal-distal translation, and medial-lateral translation were 0.19°, 0.18°, 0.11°, 0.16, 0.35, and 0.06 mm, respectively, as predicted by the deep learning model. The

TABLE 4 The comparison of ground truth values and deep learning prediction for knee kinematics under different tibial component malrotation during a walking gait after total knee arthroplasty.

Predicted Features	Training set		Validation set		Test set	
	RMSE	ρ	RMSE	ρ	RMSE	ρ
Flexion-Extension Rotation (°)	0.07	0.999	0.12	0.998	0.19	0.998
Internal-External Rotation (°)	0.04	0.999	0.20	0.996	0.18	0.998
Varus-Valgus Rotation (°)	0.11	0.998	0.10	0.998	0.11	0.998
Anterior-Posterior Translation (mm)	0.04	0.999	0.20	0.997	0.16	0.998
Proximal-Distal Translation (mm)	0.03	0.999	0.29	0.997	0.35	0.997
Medial-Lateral Translation (mm)	0.05	0.998	0.07	0.999	0.06	0.999

TABLE 5 The comparison of ground truth values and machine learning prediction for knee kinematics (rotation) under different tibial component malrotation during a walking gait after total knee arthroplasty.

Regression Models	Flexion-extension rotation (°)		Internal-external rotation (°)		Varus-valgus rotation (°)	
	RMSE	ρ	RMSE	ρ	RMSE	ρ
Random Forest	0.13	0.999	0.28	0.996	0.22	0.996
AdaBoost	0.23	0.998	0.29	0.995	0.24	0.996
Gradient Boosting	0.14	0.999	0.25	0.996	0.25	0.996
Voting	0.16	0.999	0.31	0.995	0.24	0.996

Pearson correlation coefficient for flexion-extension rotation, internal-external rotation, varus-valgus rotation, anterior-posterior translation, proximal-distal translation, and medial-lateral translation were 0.998, 0.998, 0.998, 0.998, 0.997, and 0.999, respectively, as predicted by the deep learning model.

The comparison of ground truth values and machine learning prediction for knee kinematics (rotation) under different tibial component malrotation during a walking gait after TKA was presented in Table 5. For the Random Forest regression model (test set), the RMSE and Pearson correlation coefficient for flexion-extension rotation, internal-external rotation, and varus-valgus rotation were 0.13°, 0.28°, and 0.22°, respectively, and 0.999, 0.996, and 0.996, respectively. For the AdaBoost regression model (test set), the RMSE and Pearson correlation coefficient for flexion-extension rotation, internal-external rotation, and varus-valgus rotation were 0.23°, 0.29°, and 0.24°, respectively, and 0.998, 0.995, and 0.996, respectively. For the Gradient Boosting regression model (test set), the RMSE and Pearson correlation coefficient for flexion-extension rotation, internal-external rotation, and varus-valgus rotation were 0.14°, 0.25°, and 0.25°, respectively, and 0.999, 0.996, and 0.996, respectively. For the Voting regression model (test set), the RMSE and Pearson correlation coefficient for flexion-extension rotation, internal-external rotation, and varus-valgus rotation were 0.16°, 0.31°, and 0.24°, respectively, and 0.999, 0.995, and 0.996, respectively.

The comparison of ground truth values and machine learning prediction for knee kinematics (translation) under different tibial component malrotation during a walking gait after TKA was presented in Table 6. For the Random Forest regression model (test set), the RMSE and Pearson correlation coefficient for anterior-posterior translation, proximal-distal translation, and medial-lateral translation were 0.30, 0.29, and 0.15 mm, respectively, and 0.995, 0.995, and 0.998, respectively. For the AdaBoost regression model (test set), the RMSE and Pearson correlation coefficient for anterior-posterior translation, proximal-distal translation, and medial-lateral translation were 0.31 mm, 0.47, and 0.22 mm, respectively, and 0.995, 0.994, and 0.997, respectively. For the Gradient Boosting regression model (test set), the RMSE and Pearson correlation coefficient for anterior-posterior translation, proximal-distal translation, and medial-lateral translation were 0.29, 0.56, and 0.18 mm, respectively, and 0.996, 0.992, and 0.998, respectively. For the Voting regression model (test set), the RMSE and Pearson correlation coefficient for anterior-posterior translation, proximal-distal translation, and medial-lateral translation were 0.34, 0.60, and 0.15 mm, respectively, and 0.995, 0.992, and 0.998, respectively.

4 Discussion

The most important findings of the present study were that the deep learning method were capable of accurately and reliability predicting knee contact forces (total contact force, medical contact force, and lateral contact force) and kinematics (flexion-extension rotation, internal-external rotation, varus-valgus rotation, anterior-posterior translation, proximal-distal translation, and medial-lateral

TABLE 6 The comparison of ground truth values and machine learning prediction for knee kinematics (translation) under different tibial component malrotation during a walking gait after total knee arthroplasty.

Regression Models	Anterior-posterior translation (mm)		Proximal-distal translation (mm)		Medial-lateral translation (mm)	
	RMSE	ρ	RMSE	ρ	RMSE	ρ
Random Forest	0.30	0.995	0.29	0.995	0.15	0.998
AdaBoost	0.31	0.995	0.47	0.994	0.22	0.997
Gradient Boosting	0.29	0.996	0.56	0.992	0.18	0.998
Voting	0.34	0.995	0.60	0.992	0.15	0.998

translation) with different tibial component malrotation during a walking gait after TKA, compared to four conventional machine learning methods.

The dataset of knee contact forces and kinematics with different tibial component malrotation during a walking gait after TKA (Figure 3) was based on our developed and validated musculoskeletal multibody dynamics model (Chen et al., 2015; Chen et al., 2016; Zhang et al., 2023). Our previous studies have shown that the musculoskeletal multibody dynamics model could accurately predict knee contact forces and kinematics during a walking gait after TKA (Zhang et al., 2019; Zhang et al., 2020), which were generally in excellent agreement with the experimental data previously measured in the patients via instrumented prosthesis. Nonetheless, the musculoskeletal multibody dynamics model is subject to time-intensive procedures and limited in its capacity to promptly generate the biomechanical response of the patient's knee joint after TKA. During the preoperative planning phase of a patient's knee arthroplasty, the musculoskeletal multibody dynamics model may not be able to quickly offer the surgeon precise information regarding the biomechanical relationship between the prosthesis position and the knee biomechanics in TKA because of the time-consuming of computational models. The deep/machine learning models that were developed in this paper to predict the knee contact forces and kinematics with different tibial component malrotation during a walking gait after TKA effectively overcomes the limitations of musculoskeletal multibody dynamics models in clinical applications. These models could quickly and accurately predict knee biomechanics for different component malrotation to facilitate optimal preoperative planning and intraoperative guidance for TKA procedures.

The RMSE (38.44 N) (testing set) of the deep learning method in predicting the total contact force under different tibial component malrotation during a walking gait after TKA was significantly lower than the RMSE (62.32–75.15 N) (testing set) of four machine learning methods in predicting the total contact force under different tibial component malrotation after TKA. Similarly, the RMSE (51.78 N) (testing set) of the deep learning method in predicting the medial contact force under different tibial component malrotation during a walking gait after TKA was lower than the RMSE (58.33–81.94 N) (testing set) of four machine learning methods in predicting the medial contact force under different tibial component malrotation after TKA. The RMSE (19.74 N) (testing set) of the deep learning method in predicting the lateral contact force under different tibial component malrotation during a walking gait after TKA was lower than the RMSE (23.93–34.84 N) (testing set) of four machine learning methods in predicting the lateral contact force under different tibial component malrotation after TKA. These results revealed that compared to four conventional machine learning methods, the developed deep learning method had higher accuracy in predicting total contact force, medial contact force, and lateral contact force under different tibial component malrotation during a walking gait after TKA, as evidenced by the relatively low RMSE values and high Pearson correlation coefficients (Tables 2, 3).

Furthermore, the RMSE (0.18°) (testing set) of the deep learning method in predicting the internal-external rotation under different tibial component malrotation during a walking gait after TKA was significantly lower than the RMSE (0.25°–0.31°) (testing set) of four machine learning methods in predicting the internal-external rotation under different tibial component malrotation after TKA. Similarly, the RMSE (0.11°) (testing set) of the deep learning method in predicting the varus-valgus rotation under different tibial component malrotation during a walking gait after TKA was significantly lower than the RMSE (0.22°–0.25°) (testing set) of four machine learning methods in predicting the varus-valgus rotation under different tibial component malrotation after TKA. The RMSE (0.16 mm) (testing set) of the deep learning method in predicting the anterior-posterior translation under different tibial component malrotation during a walking gait after TKA was significantly lower than the RMSE (0.29–0.34 mm) (testing set) of four machine learning methods in predicting the anterior-posterior translation under different tibial component malrotation after TKA. The RMSE (0.06 mm) (testing set) of the deep learning method in predicting the medial-lateral translation under different tibial component malrotation during a walking gait after TKA was significantly lower than the RMSE (0.15–0.22 mm) (testing set) of four machine learning methods in predicting the medial-lateral translation under different tibial component malrotation after TKA. These results indicated that compared to four machine learning methods, the developed deep learning model had higher accuracy in predicting internal-external rotation, varus-valgus rotation, anterior-posterior translation, and medial-lateral translation under different tibial component malrotation during a walking gait after TKA, as

evidenced by the relatively low RMSE values and high Pearson correlation coefficients (Tables 4–6).

However, the RMSE (0.19°) (testing set) of the deep learning method in predicting the flexion-extension rotation under different tibial component malrotation during a walking gait after TKA (Table 4) was marginally higher than the RMSE (testing set) of the Random Forest regression model (0.13°), Gradient Boosting regression model (0.14°), and Voting regression model (0.16°), but was lower than the AdaBoost regression model (0.23°) in predicting the flexion-extension rotation under different tibial component malrotation after TKA (Table 5). The RMSE (0.35 mm) (testing set) of the deep learning method in predicting the proximal-distal translation under different tibial component malrotation during a walking gait after TKA (Table 4) was marginally higher than the RMSE (testing set) of the random forest regression model (0.29 mm), but was still lower than the RMSE (testing set) of AdaBoost regression model (0.47 mm), Gradient Boosting regression model (0.56 mm), and Voting regression model (0.60 mm) in predicting the proximal-distal translation under different tibial component malrotation after TKA (Table 6). Nevertheless, the deep learning model demonstrated higher accuracy in predicting the flexion-extension rotation and the proximal-distal translation under different tibial component malrotation during a walking gait after TKA, compared to other machine learning methods.

Several limitations of this study should be discussed. Firstly, the dataset of knee contact forces and kinematics with different tibial component malrotation during a walking gait after TKA was established using our developed musculoskeletal multibody dynamics model based on a patient's experimental data. The objective of this study was to develop deep/machine learning methods to predict knee biomechanics for different tibial component malrotation during a walking gait in TKA. The focus was on establishing the relationship between different tibial component malrotation and the knee biomechanics specifically within TKA. The main intention of this study was not to predict knee biomechanics from different gaits across patients. Therefore, this study conclusively demonstrated that the deep learning method was able to predict the knee contact forces and kinematics accurately and quickly under different tibial component malrotation in TKA, which provides surgeons and surgical robots with a calibration safety zone for the preoperative planning and intraoperative guidance in TKA. Because of the limited number of patients, it was recommended that the reader construes the current study as a case series. This could potentially serve as a significant initial step for forthcoming extensive investigations, especially in large-scale research studies leveraging computer vision, deep learning and musculoskeletal simulation. The effect of different patients and prosthesis designs on knee biomechanics for different component malrotation will continue to be explored in future work. Secondly, the use of mechanical alignment, anatomical alignment, and kinematic alignment in TKA remains controversial. The alignment of the prosthesis in this study was based on the principle of mechanical alignment, and the biomechanical effects of different tibiofemoral component malrotation under different alignment principles will also be further investigated in future work. Thirdly, the objective of this study was to utilize the developed deep/machine learning methods to predict knee biomechanics during a walking gait in TKA for different tibial component malrotation. However, it is important to note that the biomechanical effects of different femoral component malrotation should be investigated in future work. Fourthly, walking gait was taken into consideration in this study since it is the activity that occurs the most frequently in day-to-day life, and direct *in vivo* measurements of joint contact forces derived from instrumented TKA prostheses are available for use in model validation. Deep learning models of knee biomechanics under different tibiofemoral component malrotation after TKA with various gait patterns, such as squatting, stair climbing, and jumping, will be investigated comprehensively in future work. Finally, in this study, four conventional machine learning methods and a deep learning method were employed to predict knee contact forces and kinematics with different tibial component malrotation during a walking gait in TKA. A larger dataset should be involved in future studies. Additional investigation is necessary to explore the optimization of both the sample size and algorithm.

5 Conclusion

The deep learning method developed in the present study was able to accurately and rapidly predict knee contact forces and kinematics with different tibial component malrotation during a walking gait after TKA, outperforming four conventional machine learning methods. The proposed method provided surgeons and surgical robots with the capability to establish a calibration safety zone, a critical aspect in ensuring precise alignment for both preoperative surgical planning and intraoperative robotic-assisted surgical navigation.

Data availability statement

The raw data supporting the conclusion of this article will be made available by the authors, without undue reservation.

Author contributions

QZ: Conceptualization, Methodology, Writing–original draft, Writing–review and editing. ZL: Formal Analysis, Visualization, Writing–original draft. ZC: Conceptualization, Methodology, Writing–review and editing. YP: Methodology, Writing–review and editing. ZJ: Conceptualization, Writing–review and editing. LQ: Writing–review and editing.

Funding

The author(s) declare financial support was received for the research, authorship, and/or publication of this article. This study was supported by "National Natural Science Foundation of China" [Grants numbers: 11902048, 52035012].

Conflict of interest

The authors declare that the research was conducted in the absence of any commercial or financial relationships that could be construed as a potential conflict of interest.

Publisher's note

All claims expressed in this article are solely those of the authors and do not necessarily represent those of their affiliated organizations, or those of the publisher, the editors and the reviewers. Any product that may be evaluated in this article, or claim that may be made by its manufacturer, is not guaranteed or endorsed by the publisher.

Supplementary material

The Supplementary Material for this article can be found online at: https://www.frontiersin.org/articles/10.3389/fbioe.2023.1255625/full#supplementary-material

References

Abdelnasser, M. K., Adi, M. M., Elnaggar, A. A., and Tarabichi, S. (2019a). Internal rotation of the tibial component in total knee arthroplasty can lead to extension deficit. *Knee Surg. Sports Traumatol. Arthrosc.* 28 (9), 2948–2952. doi:10.1007/s00167-019-05695-w

Abdelnasser, M. K., Elsherif, M. E., Bakr, H., Mahran, M., Othman, M. H. M., and Khalifa, Y. (2019b). All types of component malrotation affect the early patient-reported outcome measures after total knee arthroplasty. *Knee Surg. Relat. Res.* 31 (1), 5. doi:10.1186/s43019-019-0006-2

Andersen, M., and Rasmussen, J. (2011). "Total knee replacement musculoskeletal model using a novel simulation method for non-conforming joints," in Proceedings of the International Society of Biomechanics Conference International Society of Biomechanics.

Andersen, M. S., Damsgaard, M., MacWilliams, B., and Rasmussen, J. (2010). A computationally efficient optimisation-based method for parameter identification of kinematically determinate and over-determinate biomechanical systems. *Comput. Methods Biomech. Biomed. Engin.* 13 (2), 171–183. doi:10.1080/10255840903067080

Barrack, R. L., Schrader, T., Bertot, A. J., Wolfe, M. W., and Myers, L. (2001). Component rotation and anterior knee pain after total knee arthroplasty. *Clin. Orthop. Relat. Res.* 392, 46–55. doi:10.1097/00003086-200111000-00006

Bedard, M., Vince, K. G., Redfern, J., and Collen, S. R. (2011). Internal rotation of the tibial component is frequent in stiff total knee arthroplasty. *Clin. Orthop. Relat. Res.* 469 (8), 2346–2355. doi:10.1007/s11999-011-1889-8

Bell, S. W., Young, P., Drury, C., Smith, J., Anthony, I., Jones, B., et al. (2014). Component rotational alignment in unexplained painful primary total knee arthroplasty. *Knee* 21 (1), 272–277. doi:10.1016/j.knee.2012.09.011

Blankevoort, L., Kuiper, J. H., Huiskes, R., and Grootenboer, H. J. (1991). Articular contact in a three-dimensional model of the knee. *J. Biomech.* 24 (11), 1019–1031. doi:10.1016/0021-9290(91)90019-j

Breiman, L. (2001). Random forests. *Mach. Learn.* 45 (1), 5–32. doi:10.1023/A:1010933404324

Buitinck, L., Louppe, G., Blondel, M., Pedregosa, F., Mueller, A., Grisel, O., et al. (2013). *API design for machine learning software: experiences from the scikit-learn project*. arXiv preprint arXiv:1309.0238. Available at: https://doi.org/10.48550/arXiv.1309.0238.

Burton, W. S., 2nd, Myers, C. A., and Rullkoetter, P. J. (2021). Machine learning for rapid estimation of lower extremity muscle and joint loading during activities of daily living. *J. Biomech.* 123, 110439. doi:10.1016/j.jbiomech.2021.110439

Chen, Z., Wang, L., Liu, Y., He, J., Lian, Q., Li, D., et al. (2015). Effect of component malrotation on knee loading in total knee arthroplasty using multi-body dynamics modeling under a simulated walking gait. *J. Orthop. Res.* 33 (9), 1287–1296. doi:10.1002/jor.22908

Chen, Z., Zhang, Z., Wang, L., Li, D., Zhang, Y., and Jin, Z. (2016). Evaluation of a subject-specific musculoskeletal modelling framework for load prediction in total knee arthroplasty. *Med. Eng. Phys.* 38 (8), 708–716. doi:10.1016/j.medengphy.2016.04.010

Dalury, D. F., Pomeroy, D. L., Gorab, R. S., and Adams, M. J. (2013). Why are total knee arthroplasties being revised? *J. Arthroplasty* 28 (8), 120–121. doi:10.1016/j.arth.2013.04.051

Damsgaard, M., Rasmussen, J., Christensen, S. T., Surma, E., and de Zee, M. (2006). Analysis of musculoskeletal systems in the AnyBody modeling system. *Simul. Model. Pract. Theory* 14 (8), 1100–1111. doi:10.1016/j.simpat.2006.09.001

Drucker, H. (1997). Improving regressors using boosting techniques. *ICML* 97, 107–115.

Fang, C., Luan, Y., Wang, Z., Shao, L., Qu, T., and Cheng, C. K. (2022). Moderate external rotation of tibial component generates more natural kinematics than internal rotation after total knee arthroplasty. *Front. Bioeng. Biotechnol.* 10, 910311. doi:10.3389/fbioe.2022.910311

Fregly, B. J., Bei, Y., and Sylvester, M. E. (2003). Experimental evaluation of an elastic foundation model to predict contact pressures in knee replacements. *J. Biomech.* 36 (11), 1659–1668. doi:10.1016/s0021-9290(03)00176-3

Fregly, B. J., Besier, T. F., Lloyd, D. G., Delp, S. L., Banks, S. A., Pandy, M. G., et al. (2012). Grand challenge competition to predict *in vivo* knee loads. *J. Orthop. Res.* 30 (4), 503–513. doi:10.1002/jor.22023

Freund, Y., and Schapire, R. E. (1997). A decision-theoretic generalization of on-line learning and an application to boosting. *J. Comput. Syst. Sci.* 55 (1), 119–139. doi:10.1006/jcss.1997.1504

Friedman, J. H. (2001). Greedy function approximation: a gradient boosting machine. *Ann. Stat.* 29 (5), 1189–1232. doi:10.1214/aos/1013203451

Gholami, M., Napier, C., and Menon, C. (2020). Estimating lower extremity running gait kinematics with a single accelerometer: a deep learning approach. *Sensors (Basel)* 20 (10), 2939. doi:10.3390/s20102939

Guo, Y., Storm, F., Zhao, Y., Billings, S. A., Pavic, A., Mazzà, C., et al. (2017). A new proxy measurement algorithm with application to the estimation of vertical ground reaction forces using wearable sensors. *Sensors (Basel)* 17 (10), 2181. doi:10.3390/s17102181

Hastie, T., Tibshirani, R., Friedman, J. H., and Friedman, J. H. (2009). *The elements of statistical learning: data mining, inference, and prediction*. New York: Springer.

Hochreiter, S., and Schmidhuber, J. (1997). Long short-term memory. *Neural comput.* 9 (8), 1735–1780. doi:10.1162/neco.1997.9.8.1735

Hofmann, S., Romero, J., Roth-Schiffl, E., and Albrecht, T. (2003). Rotational malalignment of the components may cause chronic pain or early failure in total knee arthroplasty. *Orthopade* 32 (6), 469–476. doi:10.1007/s00132-003-0503-5

Hu, J., Xin, H., Chen, Z., Zhang, Q., Peng, Y., and Jin, Z. (2019). The role of menisci in knee contact mechanics and secondary kinematics during human walking. *Clin. Biomech. (Bristol, Avon)* 61, 58–63. doi:10.1016/j.clinbiomech.2018.11.009

Johnson, W. R., Alderson, J., Lloyd, D., and Mian, A. (2019). Predicting athlete ground reaction forces and moments from spatio-temporal driven CNN models. *IEEE Trans. Biomed. Eng.* 66 (3), 689–694. doi:10.1109/tbme.2018.2854632

Kang, K. T., Koh, Y. G., Son, J., Kwon, O. R., Baek, C., Jung, S. H., et al. (2016). Measuring the effect of femoral malrotation on knee joint biomechanics for total knee arthroplasty using computational simulation. *Bone Jt. Res.* 5 (11), 552–559. doi:10.1302/2046-3758.511.bjr-2016-0107.r1

Kim, Y. H., Park, J. W., Kim, J. S., and Park, S. D. (2014). The relationship between the survival of total knee arthroplasty and postoperative coronal, sagittal and rotational alignment of knee prosthesis. *Int. Orthop.* 38 (2), 379–385. doi:10.1007/s00264-013-2097-9

Kingma, D., and Ba, J. (2014). *Adam: a method for stochastic optimization*. arXiv preprint arXiv:1412.6980, Available at: https://doi.org/10.48550/arXiv.1412.6980.

Komaris, D.-S., Pérez-Valero, E., Jordan, L., Barton, J., Hennessy, L., O'Flynn, B., et al. (2019). Predicting three-dimensional ground reaction forces in running by using artificial neural networks and lower body kinematics. *IEEE Access* 7, 156779–156786. doi:10.1109/ACCESS.2019.2949699

Kuriyama, S., Ishikawa, M., Furu, M., Ito, H., and Matsuda, S. (2014). Malrotated tibial component increases medial collateral ligament tension in total knee arthroplasty. *J. Orthop. Res.* 32 (12), 1658–1666. doi:10.1002/jor.22711

Lund, M. E., Andersen, M. S., de Zee, M., and Rasmussen, J. (2015). Scaling of musculoskeletal models from static and dynamic trials. *Int. Biomech.* 2 (1), 1–11. doi:10.1080/23335432.2014.993706

Marra, M. A., Vanheule, V., Fluit, R., Koopman, B. H., Rasmussen, J., Verdonschot, N., et al. (2015). A subject-specific musculoskeletal modeling framework to predict *in vivo* mechanics of total knee arthroplasty. *J. Biomech. Eng.* 137 (2), 020904. doi:10.1115/1.4029258

Mehrizi, R., Peng, X., Xu, X., Zhang, S., and Li, K. (2019). A deep neural network-based method for estimation of 3D lifting motions. *J. Biomech.* 84, 87–93. doi:10.1016/j.jbiomech.2018.12.022

Mundt, M., Thomsen, W., Witter, T., Koeppe, A., David, S., Bamer, F., et al. (2020). Prediction of lower limb joint angles and moments during gait using artificial neural networks. *Med. Biol. Eng. Comput.* 58 (1), 211–225. doi:10.1007/s11517-019-02061-3

Oh, S. E., Choi, A., and Mun, J. H. (2013). Prediction of ground reaction forces during gait based on kinematics and a neural network model. *J. Biomech.* 46 (14), 2372–2380. doi:10.1016/j.jbiomech.2013.07.036

Panni, A. S., Ascione, F., Rossini, M., Braile, A., Corona, K., Vasso, M., et al. (2018). Tibial internal rotation negatively affects clinical outcomes in total knee arthroplasty: a systematic review. *Knee Surg. Sports Traumatol. Arthrosc.* 26 (6), 1636–1644. doi:10.1007/s00167-017-4823-0

Paszke, A., Gross, S., Chintala, S., Chanan, G., Yang, E., DeVito, Z., et al. (2017). "Automatic differentiation in pytorch," in 31st Conference on Neural Information Processing Systems (NIPS 2017), Long Beach, CA.

Pedregosa, F., Varoquaux, G., Gramfort, A., Michel, V., Thirion, B., Grisel, O., et al. (2012). Scikit-learn: machine learning in Python. *J. Mach. Learn. Res.* 12, 2825–2830. doi:10.48550/arXiv.1201.0490

Pellikaan, P., van der Krogt, M. M., Carbone, V., Fluit, R., Vigneron, L. M., Van Deun, J., et al. (2014). Evaluation of a morphing based method to estimate muscle attachment sites of the lower extremity. *J. Biomech.* 47 (5), 1144–1150. doi:10.1016/j.jbiomech.2013.12.010

Rajgopal, A., Sudarshan, P., Kumar, S., and Aggarwal, K. (2022). Failure modes in malrotated total knee replacement. *Arch. Orthop. Trauma Surg.* 143 (5), 2713–2720. doi:10.1007/s00402-022-04569-0

Rane, L., Ding, Z., McGregor, A. H., and Bull, A. M. J. (2019). Deep learning for musculoskeletal force prediction. *Ann. Biomed. Eng.* 47 (3), 778–789. doi:10.1007/s10439-018-02190-0

Rasmussen, J., de Zee, M., Damsgaard, M., Christensen, S. T., Marek, C., and Siebertz, K. (2005). "A general method for scaling musculo-skeletal models," in 2005 International Symposium on Computer Simulation in Biomechanics.

Smith, C. R., Vignos, M. F., Lenhart, R. L., Kaiser, J., and Thelen, D. G. (2016). The influence of component alignment and ligament properties on tibiofemoral contact forces in total knee replacement. *J. Biomech. Eng.* 138 (2), 021017. doi:10.1115/1.4032464

Stetter, B. J., Ringhof, S., Krafft, F. C., Sell, S., and Stein, T. (2019). Estimation of knee joint forces in sport movements using wearable sensors and machine learning. *Sensors (Basel).* 19 (17), 3690. doi:10.3390/s19173690

Tamura, H., Tanaka, R., and Kawanishi, H. (2020). Reliability of a markerless motion capture system to measure the trunk, hip and knee angle during walking on a flatland and a treadmill. *J. Biomech.* 109, 109929. doi:10.1016/j.jbiomech.2020.109929

Tang, J., Wu, T., Shao, H., and Zhou, Y. (2022). Malposition of components and femorotibial mechanical axis changes on pressure distribution in total knee arthroplasty. *Clin. Biomech. (Bristol, Avon)* 96, 105659. doi:10.1016/j.clinbiomech.2022.105659

Ueyama, H., Minoda, Y., Sugama, R., Ohta, Y., Yamamura, K., Nakamura, S., et al. (2020). Malrotation of the fixed-bearing posterior stabilized total knee prosthesis causes a postoperative rotational mismatch between the femur and tibia. *Knee Surg. Sports Traumatol. Arthrosc.* 28 (12), 3810–3820. doi:10.1007/s00167-020-05864-2

Vanheule, V., Delport, H. P., Andersen, M. S., Scheys, L., Wirix-Speetjens, R., Jonkers, I., et al. (2017). Evaluation of predicted knee function for component malrotation in total knee arthroplasty. *Med. Eng. Phys.* 40, 56–64. doi:10.1016/j.medengphy.2016.12.001

Wouda, F., Giuberti, M., Bellusci, G., Maartens, E., Reenalda, J., Beijnum, B.-J., et al. (2018). Estimation of vertical ground reaction forces and sagittal knee kinematics during running using three inertial sensors. *Front. Physiol.* 9, 218. doi:10.3389/fphys.2018.00218

Zhang, Q., Chen, Z., Zhang, J., Hu, J., Peng, Y., Fan, X., et al. (2019). Insert conformity variation affects kinematics and wear performance of total knee replacements. *Clin. Biomech. (Bristol, Avon)* 65, 19–25. doi:10.1016/j.clinbiomech.2019.03.016

Zhang, Q., Chen, Z., Zhang, Z., Jin, Z., Muratoglu, O. K., and Varadarajan, K. M. (2020). Leveraging subject-specific musculoskeletal modeling to assess effect of anterior cruciate ligament retaining total knee arthroplasty during walking gait. *Proc. Inst. Mech. Eng. H.* 234 (12), 1445–1456. doi:10.1177/0954411920947204

Zhang, Q., Peng, Y., Chen, Z., Jin, Z., and Qin, L. (2023). Conformity design can change the effect of tibial component malrotation on knee biomechanics after total knee arthroplasty. *Clin. Biomech. (Bristol, Avon)* 105, 105985. doi:10.1016/j.clinbiomech.2023.105985

Zhu, Y., Xu, W., Luo, G., Wang, H., Yang, J., and Lu, W. (2020). Random forest enhancement using improved artificial fish swarm for the medial knee contact force prediction. *Artif. Intell. Med.* 103, 101811. doi:10.1016/j.artmed.2020.101811

frontiers | Frontiers in Bioengineering and Biotechnology

TYPE Original Research
PUBLISHED 05 February 2024
DOI 10.3389/fbioe.2024.1325339

OPEN ACCESS

EDITED BY
Bernardo Innocenti,
Université libre de Bruxelles, Belgium

REVIEWED BY
Tai-Hua Yang,
National Cheng Kung University, Taiwan
Alicia Fernandez-Fernandez,
Nova Southeastern University, United States

*CORRESPONDENCE
Jianyi Li,
lijianyi@outlook.com
Hongtao Zhang,
femur@163.com

†These authors share first authorship

RECEIVED 21 October 2023
ACCEPTED 23 January 2024
PUBLISHED 05 February 2024

CITATION
Wang F, Jia R, He X, Wang J, Zeng P, Hong H, Jiang J, Zhang H and Li J (2024), Detection of kinematic abnormalities in persons with knee osteoarthritis using markerless motion capture during functional movement screen and daily activities.
Front. Bioeng. Biotechnol. 12:1325339.
doi: 10.3389/fbioe.2024.1325339

Detection of kinematic abnormalities in persons with knee osteoarthritis using markerless motion capture during functional movement screen and daily activities

Fei Wang[1,2†], Rui Jia[3,1†], Xiuming He[4†], Jing Wang[4], Peng Zeng[4], Hong Hong[1], Jiang Jiang[1], Hongtao Zhang[4*] and Jianyi Li[1*]

[1]Department of Anatomy, Guangdong Provincial Key Laboratory of Digital Medicine and Biomechanics, Guangdong Engineering Research Center for Translation of Medical 3D Printing Application, School of Basic Medical Sciences, Southern Medical University, Guangzhou, China, [2]Nanchang Medical College, Nanchang, China, [3]Department of Rehabilitation Medicine, Guangdong Provincial People's Hospital (Guangdong Academy of Medical Sciences), Southern Medical University, Guangzhou, China, [4]Zhongshan Torch Development Zone People's Hospital, Zhongshan, China

Background: The functional movement screen (FMS) has been used to identify deficiencies in neuromuscular capabilities and balance among athletes. However, its effectiveness in detecting movement anomalies within the population afflicted by knee osteoarthritis (KOA), particularly through the application of a family-oriented objective assessment technique, remains unexplored. The objective of this study is to investigate the sensitivity of the FMS and daily activities in identifying kinematic abnormalities in KOA people employing a markerless motion capture system.

Methods: A total of 45 persons, presenting various Kellgren–Lawrence grades of KOA, along with 15 healthy controls, completed five tasks of the FMS (deep squat, hurdle step, and in-line lunge) and daily activities (walking and sit-to-stand), which were recorded using the markerless motion capture system. The kinematic waveforms and discrete parameters were subjected to comparative analysis.

Results: Notably, the FMS exhibited greater sensitivity compared to daily activities, with knee flexion, trunk sagittal, and trunk frontal angles during in-line lunge emerging as the most responsive indicators.

Abbreviations: FMS, functional movement screen; KOA, knee osteoarthritis; PwKOA, persons with KOA; K–L, Kellgren–Lawrence; HC, healthy controls; BMI, body mass index; WOMAC, Western Ontario and McMaster University Osteoarthritis Index; COM ML displacement, medial-lateral displacement of the center of mass; SPM, statistical parametric mapping; SnPM, statistical nonparametric mapping.

Conclusion: The knee flexion, trunk sagittal, and trunk frontal angles during in-line lunge assessed via the markerless motion capture technique hold promise as potential indicators for the objective assessment of KOA.

KEYWORDS

knee osteoarthritis, kinematic abnormalities, functional movement screen, markerless motion capture, objective evaluation

1 Introduction

Objective evaluations play a pivotal role in assessing the therapeutic effectiveness of knee osteoarthritis (KOA) treatments and in monitoring disease progression for precise adjustments in treatment strategies (Bellamy et al., 2009). However, the existing methods of KOA assessment exhibit certain limitations. Radiography lacks the required sensitivity to discern short-term knee alterations (Hayashi et al., 2016). Magnetic resonance imaging is expensive and thus impractical for daily monitoring of persons with KOA (PwKOA) (van Helvoort et al., 2021). Patient-reported outcome measures, when utilized outside clinical settings, tend to be highly subjective and can exhibit a ceiling effect (van der Straaten et al., 2020). Therefore, a need persists for a simple and dependable measurement technique to evaluate KOA objectively.

Recent studies have highlighted the decline in motor and balance capabilities experienced by PwKOA, thereby amplifying the research emphasis on quantitatively assessing exercise and balance functions associated with KOA (Lee et al., 2019; Zeng et al., 2022). Gait analysis has emerged as the most widely used approach for this purpose (Mills et al., 2013). Additionally, some researchers have explored the potential utility of the timed up-and-go test, which involves multiple tasks representative of daily activities, for KOA evaluation (Hsieh et al., 2020). However, PwKOA are more prone to exhibiting compensatory movement strategies when confronted with challenging functional tasks (van der Straaten et al., 2018).

The functional movement screen (FMS) is a systematic screening tool capable of identifying asymmetries or compensatory strategies within the movement patterns of an individual (Smith and Hanlon, 2017; Lee et al., 2019). Although the FMS has been successfully employed to detect deficits in neuromuscular capacity and balance among athletes (Moran et al., 2017; Lee et al., 2018; Suzuki et al., 2022), its potential in identifying movement anomalies within PwKOA remains unexplored. Furthermore, it remains uncertain whether the FMS exhibits greater sensitivity compared to routine daily activities.

Quantitative motion evaluations of KOA have traditionally relied on marker-based motion capture systems, which are not only expensive and time-consuming, but also demand specialized expertise (Topley and Richards, 2020; Vitali and Perkins, 2020). Given that conservative KOA treatment is often administered within the community or at home, a timely and family-oriented objective monitoring technique is required. Owing to its cost-effectiveness and unobtrusive motion assessment capabilities (Takeda et al., 2021), markerless motion capture technology has emerged as a promising alternative. Nonetheless, its potential to detect abnormal motor performance in PwKOA remains largely unexplored.

Therefore, the primary objective of this study is to determine the kinematic parameters that most accurately distinguish between persons with varying Kellgren–Lawrence (K–L) grades of KOA and healthy controls (HC) during FMS (deep squat, hurdle step, and in-line lunge) and daily activities (walking and sit-to-stand) when employing a markerless motion capture system.

2 Methods

2.1 Participants

Fifteen HC from local communities and 45 PwKOA from a local hospital were recruited for the study. The PwKOA were divided into three groups: mild (K–L grade 1), moderate (K–L grade 2), and severe (K–L grade 3/4). Each group contained 15 people. For the purposes of this study, K–L grades 3 and 4 were considered as a single group (Fukaya et al., 2019; Ismailidis et al., 2020). The selected patients had confirmed imaging findings indicative of primary KOA. The HC group exhibited a balanced gender distribution and ages ranging between 45 and 75 years. Exclusion criteria included the existence of a history of knee surgery, unresolved lower extremity joint injury, body mass index >30 kg/m^2, walker use, and inability to adhere to the test protocol.

Ethical approval for this study was obtained from the ethics committee of Zhongshan Torch Development Zone People's Hospital (2022-0001). All participants provided written informed consent.

2.2 Data collection

First, all participants completed the Western Ontario and McMaster University Osteoarthritis Index (WOMAC) questionnaire and then completed five tasks of the FMS (deep squat, hurdle step, and in-line lunge) and daily activities (walking and sit-to-stand). Before the formal test, the participants were trained to ensure that their actions were conducted in accordance with the standard. The instructions provided to the participants are listed in Table 1. All tasks were recorded using a markerless motion capture system. Each participant performed three times for each task, and the average of the three tests was analyzed. The parameters of interest were obtained from the dominant and affected sides of the participants. In cases of bilateral PwKOA, the affected side was defined as the more painful one; in cases of equal pain, the dominant

TABLE 1 Instructions given to the participants.

Task	Instructions to participant
Deep squat	1) Stand with your feet shoulder-width apart and your toes facing forward in line with the mark. Hold the pole above your head with both hands. 2) Keep your trunk upright and your feet and pole in position, squat as deep as you can, then move at your preferred speed back to the starting position
Hurdle step	1) Stand with your feet together and your toes facing forward in line with the mark. Hold the pole behind your neck with both hands. 2) With your trunk upright, bend your dominant (or affected) lower limb over the rail so that the heel touches the floor (without force) and return to the starting position, maintaining alignment between the foot, knee, and hip as much as possible
In-line lunge	1) Position your dominant (affected) heel at the intended mark line, align the other toe with the initial mark line, and extend both knees. 2) Keep your trunk upright and stretch your arms horizontally. 3) Lower your back knee to the heel of your front foot, and then return to the standing position
Sit-to-stand	1) Sit in the chair and lean back with your hands on the armrests. 2) When you hear the "stand up" command, stand up as you would normally do
Walking	1) Stand with your toes facing forward in line with the mark. 2) When you hear the "go" command, walk at a comfortable speed, as you would normally do, until you have passed the stopping line

TABLE 2 Parameters measured for each of the five tasks performed.

	Deep squat	Hurdle step	In-line lunge	Sit-to-stand	Walking
Knee sagittal angel waveform	√	√	√		√
Peak knee flexion angle	√	√	√		√
Hip sagittal angel waveform	√	√	√		√
Peak hip flexion or extension angle	√	√	√		√
Trunk sagittal angle waveform	√	√	√		√
Peak trunk sagittal angle	√	√	√	√	√
Trunk frontal angle waveform	√	√	√		√
Peak trunk frontal angle	√	√	√	√	√
COM ML displacement waveform	√	√	√		
Peak COM ML displacement	√	√	√	√	
Gait phase					√
Stride frequency					√
Step length					√

side was chosen. The parameters of interest encompassed the trunk frontal angle, trunk, hip, and knee sagittal angles, and medial-lateral displacement of the center of mass (COM ML displacement). Balance control proficiency was primarily indicated by the trunk frontal angle, trunk sagittal angle, and COM ML displacement, whereas movement performance was mainly reflected by the hip and knee sagittal angles. Table 2 presents a comprehensive list of the parameters of interest.

Image data were acquired using a markerless motion capture system (Fast-Move Ltd., China) equipped with four standard video cameras with a resolution of 1,624 × 1,240, which were positioned around the testing area with an angle of approximately 90° between the main optical axes of every pair of adjacent cameras. The sampling rate was 30 Hz. Fast-Move 3D Motion software (version 1.2, Fast-Move Ltd., China) was employed for data processing. An artificial intelligence-based joint-point recognition function automatically analyzed the video images using a 21-point body model (Hay, 1993). The 21 key points included the head, chin, neck, bilateral shoulder, elbow, wrist, hand, hip, knee, ankle, heel and big toe. The sagittal joint angle of the lower limbs, trunk tilt angle, and three-dimensional coordinates of the center of mass were calculated based on the three-dimensional coordinates of the aforementioned 21 points.

Pictures related to data collection and processing are provided in the Supplementary Material.

2.3 Data normalization

The kinematic parameters were normalized in terms of time, ranging from 0% to 100%. In the cases of the deep squat, hurdle step, and in-line lunge, normalization occurred between two consecutive points at which the knee reached full extension, using the rate of change of the knee sagittal angle. The sit-to-stand was normalized from the time the trunk started to lean forward to the time the subject stood up straight using the rate of change of the trunk sagittal angle and the up-and-down displacement of the center of mass. For

TABLE 3 Characterization of the participants.

	HC (n = 15)	Mild (n = 15)	Moderate (n = 15)	Severe (n = 15)
Male/female	3/12	3/12	3/12	4/11
Age (years)	52.67 ± 4.65	57.00 ± 6.87[a]	60.80 ± 5.43[a]	64.87 ± 5.67[a, b]
Height (m)	1.56 ± 0.06	1.51 (1.49–1.62)	1.54 ± 0.07	1.57 ± 0.09
Weight (kg)	54.50 (50.40–60.90)	56.32 ± 11.06	59.93 ± 5.23	61.25 ± 12.95
BMI (kg/m^2)	23.07 ± 3.19	23.40 ± 3.06	25.35 ± 2.03	24.67 ± 3.58
Unilateral/Bilateral	-	13/2	11/4	8/7
WOMAC Total	0.00 (0.00–2.00)	9.00 (6.00–16.00)[a]	26.53 ± 13.85[a]	40.80 ± 28.99[a]
WOMAC Pain	0.00 (0.00–0.00)	3.00 (2.00–9.00)[a]	6.13 ± 3.48[a]	9.60 ± 6.01[a]
WOMAC Stiffness	0.00 (0.00–0.00)	0.00 (0.00–0.00)	0.00 (0.00–4.00)	2.00 (0.00–4.00)[a]
WOMAC Function	0.00 (0.00–0.00)	4.00 (3.00–12.00)	18.27 ± 10.53[a]	29.00 ± 25.02[a]

Values other than gender are expressed as mean ± SD, except where the data are non-normally distributed, in which case they are presented as median (IQR).
[a]Significant difference between this and the HC, groups.
[b]Significant difference between this and the mild groups.

the walking stride, normalization spanned from one heel strike to the next.

2.4 Statistical analysis

Statistical analyses were conducted using PASS (version 15.0, NCSS, United States), MATLAB (version 2021a, MathWorks, Inc., United States), and SPSS (version 22.0, IBM Corporation, United States).

The required sample size was calculated based on the group differences observed in the discrete parameters reported by Nüesch *et al.* (2021). To detect an expected difference in knee angle with an effect size of at least 1.12% and 80% power at a significance level of 5%, a minimum of 14 participants was deemed necessary for each group.

One-dimensional statistical parametric or nonparametric mapping (SPM or SnPM) was used to compare the kinematic waveforms of HC and PwKOA in different groups (Pataky et al., 2013; Papi et al., 2020). Depending on the adherence of the data to normality, either a parametric or nonparametric one-way ANOVA was used to compare the time-varying kinematic parameters. To test the null hypothesis stating that no differences exist between the groups, a critical threshold that only 5% of the smooth random curves would be expected to intersect was calculated. In instances of observed significant differences, *post hoc* analyses encompassing parametric or nonparametric two-tailed two-sample t-tests were conducted on HC and PwKOA across various groups. Statistical significance materialized when the SPM curves (SPM{X2}, SnPM{X2}, SPM{t}, or SnPM{t}) intersected the critical threshold at any given node. In all SnPM tests, the iteration count was set at 10,000.

Discrete kinematic parameters were compared between HC and PwKOA across distinct groups through either one-way ANOVA or Wilcoxon's nonparametric test, contingent upon the adherence of the data to normality. Subsequent *post hoc* analyses were conducted for identified significant differences. The significance level was set at $p < 0.05$.

3 Results

3.1 Participants

Table 3 presents the characteristics of the participants, all of whom were right-handed. Notably, the PwKOA were significantly older than the HC group ($p < 0.01$). The substantially lower WOMAC scores among the HC confirmed the absence of knee-related pain or disability.

3.2 SPM analysis

Discernible disparities were observed in specific angular waveforms during the FMS, yet no such disparities emerged during daily activities. Results are shown in Figure 1, Figure 2, Figure 3, Figure 4. The SnPM{t} curves are displayed on the left of the subfigures, and the shaded areas indicate SnPM{t} exceeding the critical threshold (i.e., where statistical differences existed). The discriminant angular waveforms (mean) are displayed on the right of the subfigures. Detailed results are described below.

Regarding the deep squat:

- Participants within the severe group exhibited reduced knee flexion (36%–44%, $P = 0.014$) and increased knee flexion (97%–100%, $P = 0.008$) compared to the HC (Figure 1).

Regarding the hurdle step:

- Participants within the mild (61%–68%, $P = 0.008$) and severe (57%–76%, $P < 0.001$) groups exhibited reduced knee flexion compared to that of HC (Figures 2A,B).

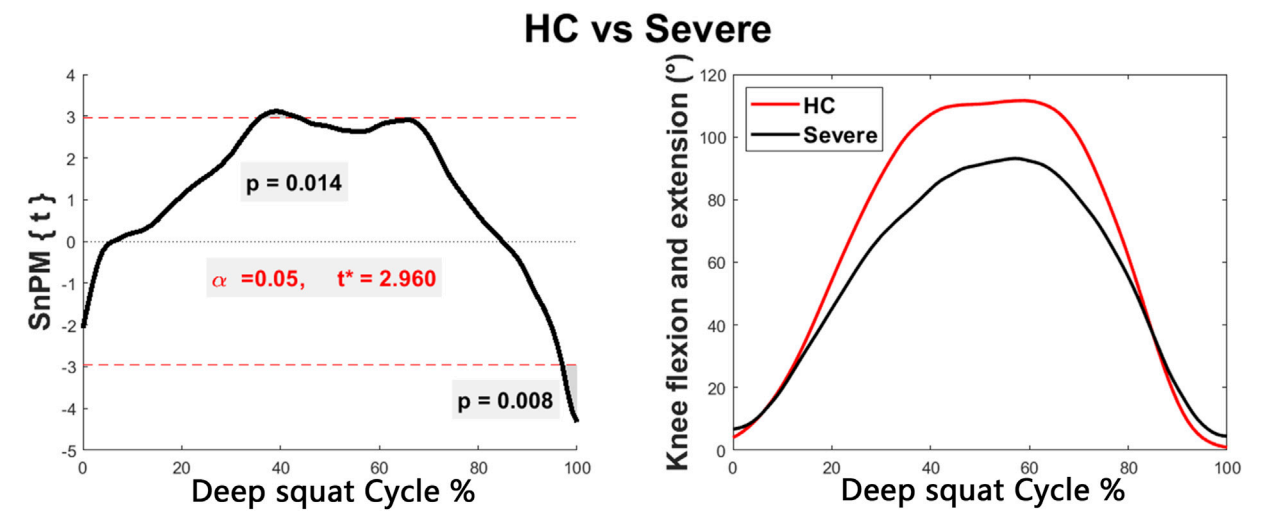

FIGURE 1
Intergroup disparities of the knee sagittal angle during the deep squat. The curve on the left represents the SnPM{t} curve, and the shaded areas indicate SnPM{t} exceeding the critical threshold (i.e., where statistical differences existed). The curves on the right represent the discriminant angular waveforms (mean) between HC and persons in the severe group.

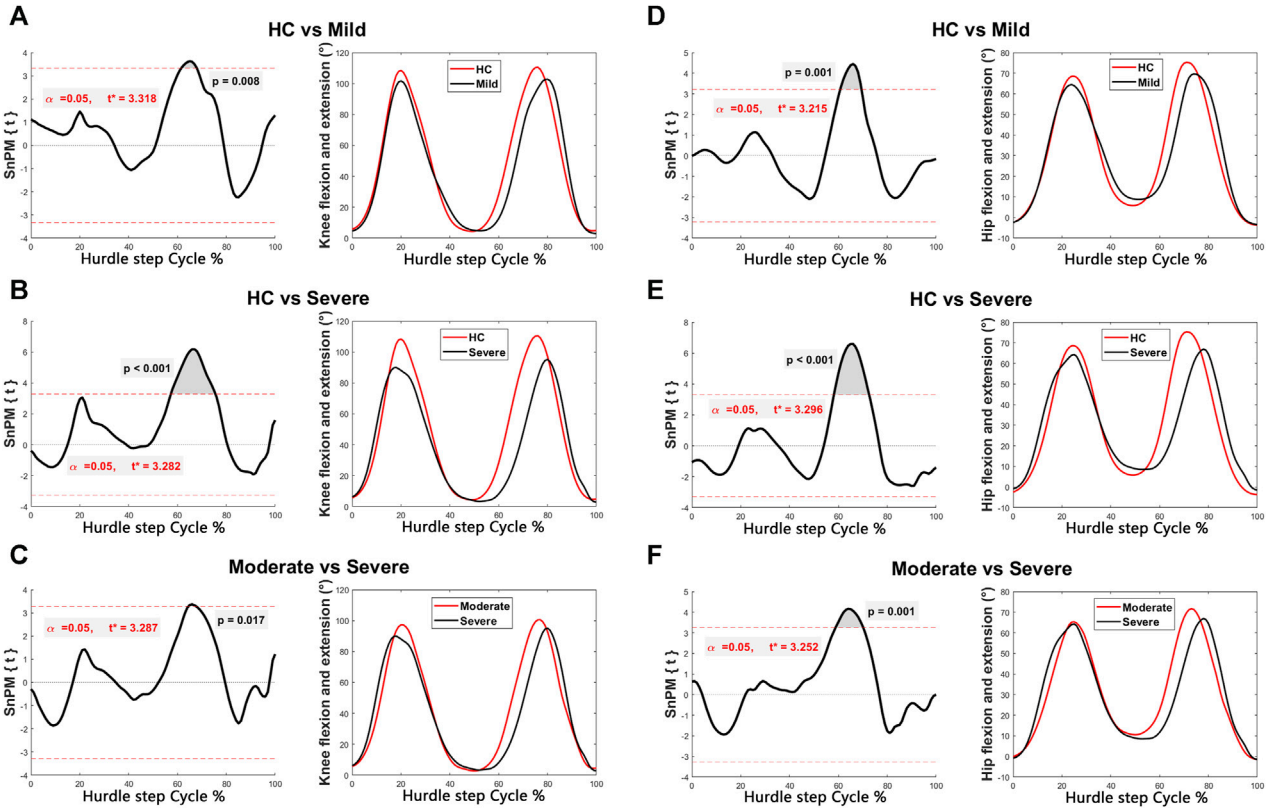

FIGURE 2
Intergroup disparities of the knee and hip sagittal angles during the hurdle step. The SnPM{t} curves are displayed on the left of the subfigures, and the shaded areas indicate SnPM{t} exceeding the critical threshold (i.e., where statistical differences existed). The discriminant angular waveforms (mean) during the hurdle step are displayed on the right of the subfigures. Difference in knee flexion and extension between **(A)** HC and persons in the mild group; **(B)** HC and persons in the severe group; and **(C)** persons in the moderate and severe groups. Differences in hip flexion and extension between **(D)** HC and persons in the mild group; **(E)** HC and persons in the severe group; and **(F)** persons in the moderate and severe groups.

10.3389/fbioe.2024.1325339

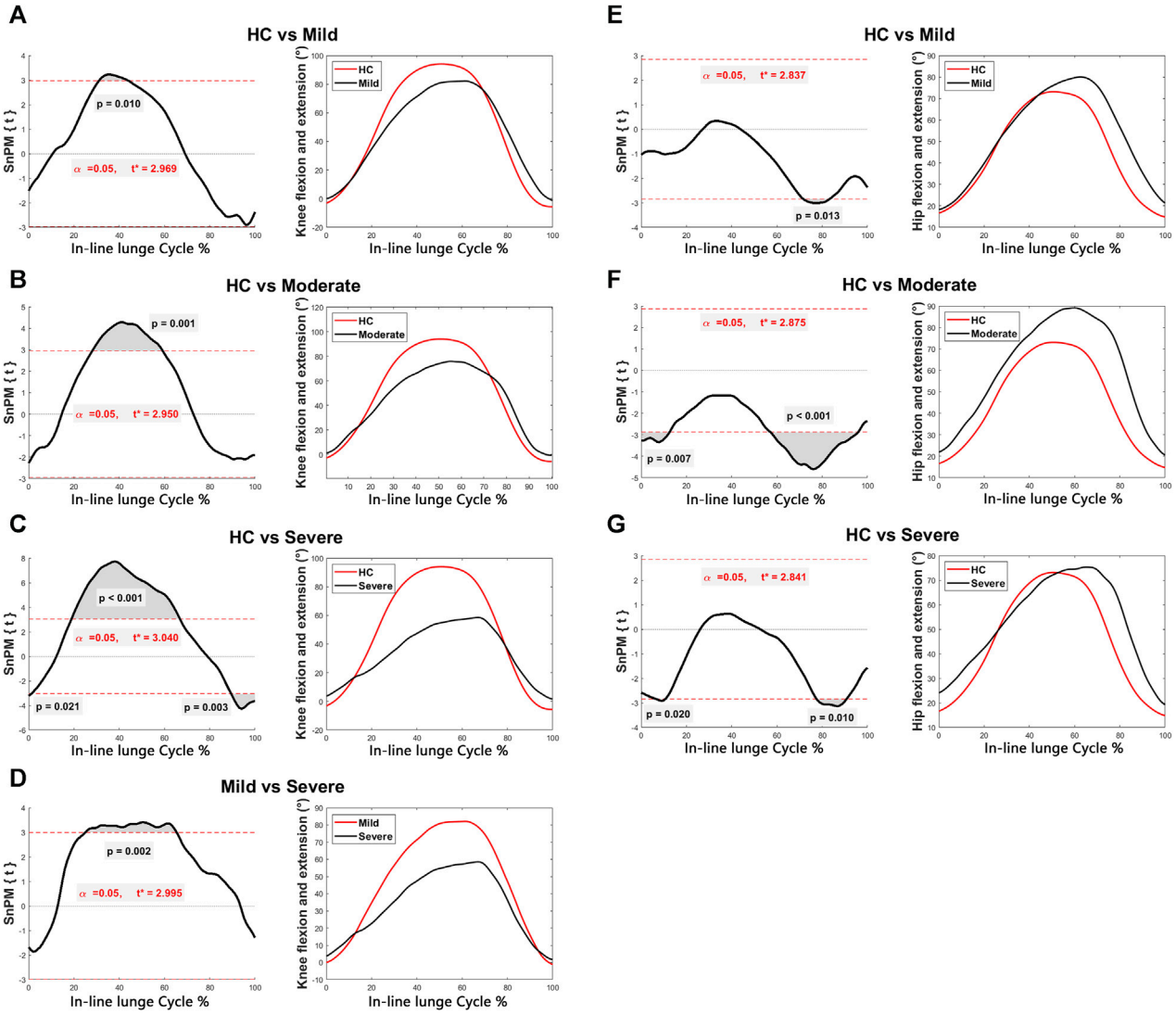

FIGURE 3
Intergroup disparities of the knee and hip sagittal angles during the in-line lunge. The SnPM{t} curves are displayed on the left of the subfigures, and the shaded areas indicate SnPM{t} exceeding the critical threshold (i.e., where statistical differences existed). The discriminant angular waveforms (mean) during the in-line lunge are displayed on the right of the subfigures. Difference in knee flexion and extension between **(A)** HC and persons in the mild group; **(B)** HC and persons in the moderate group; **(C)** HC and persons in the severe group; and **(D)** persons in the mild and severe groups. Difference in hip flexion and extension between **(E)** HC and persons in the mild group; **(F)** HC and persons in the moderate group; and **(G)** HC and persons in the severe group.

- Participants within the severe group exhibited less knee flexion compared to those in the moderate group (65%–68%, $P = 0.017$) (Figure 2C).
- Participants within the mild (61%–69%, $P = 0.001$) and severe (58%–73%, $P < 0.001$) groups exhibited less hip flexion than that of the HC (Figures 2D,E).
- Participants within the severe group exhibited less hip flexion compared to those in the moderate group (59%–70%, $P = 0.001$) (Figure 2F).

Regarding the in-line lunge:

- Participants within the mild (31%–44%, $P = 0.010$), moderate (28%–59%, $P = 0.001$), and severe (19%–67%, $P < 0.001$) groups exhibited reduced knee flexion relative to that of the HC (Figures 3A–C).
- Subjects within the severe group displayed increased knee flexion compared to that of the HC (0%–1%, $P = 0.021$; 89%–100%, $P = 0.003$) (Figure 3C).
- Participants within the severe group demonstrated decreased knee flexion compared to those in the mild group (25%–65%, $P = 0.002$) (Figure 3D).
- The mild (72%–83%, $P = 0.013$), moderate (0%–13%, $P = 0.007$; 57%–96%, $P < 0.001$), and severe (6%–11%, $P = 0.020$; 78%–91%, $P = 0.010$) groups exhibited enhanced hip flexion relative to that of the HC (Figures 3E–G).
- Participants within the mild (53%–86%, $P = 0.002$), moderate (4%–97%, $P < 0.001$), and severe (0%–95%, $P < 0.001$) groups

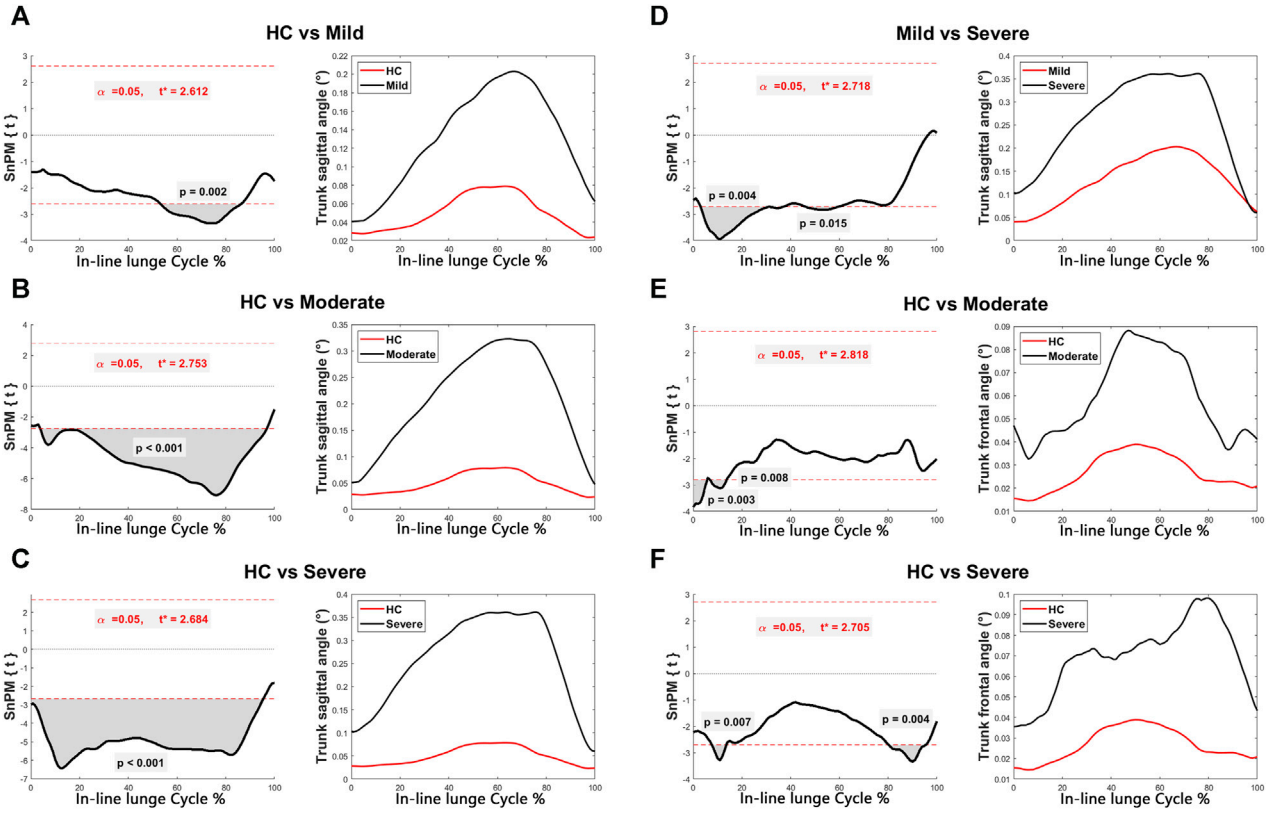

FIGURE 4
Intergroup disparities of the trunk sagittal and frontal angles during the in-line lunge. The SnPM{t} curves are displayed on the left of the subfigures, and the shaded areas indicate SnPM{t} exceeding the critical threshold (i.e., where statistical differences existed). The discriminant angular waveforms (mean) during the in-line lunge are displayed on the right of the subfigures. Difference in trunk sagittal angle between **(A)** HC and persons in the mild group; **(B)** HC and persons in the moderate group; **(C)** HC and persons in the severe group; and **(D)** persons in the mild and severe groups. Difference in trunk frontal angle between **(E)** HC and persons in the moderate group; and **(F)** HC and persons in the severe group.

manifested heightened trunk sagittal angles relative to HC (Figures 4A–C).

- Participants within the severe group displayed increased trunk sagittal angles compared to those in the mild group (3%–37%, P = 0.004; 46%–60%, P = 0.015) (Figure 4D).
- Participants within the moderate (0%–6%, P = 0.003; 7%–14%, P = 0.008) and severe (8%–14%, P = 0.007; 80%–95%, P = 0.004) groups demonstrated elevated trunk frontal angles compared to those of the HC (Figures 4E,F).

3.3 Discrete kinematic parameter analysis

Regarding the deep squat:

- The severe group exhibited a lower peak knee flexion angle compared to that of the HC (P = 0.001).

Regarding the hurdle step:

- No significant differences were observed among the parameters of the four groups (P > 0.05).

Regarding the in-line lunge:

- Participants within the moderate (P = 0.023) and severe (P < 0.001) groups displayed a diminished peak knee flexion angle compared to that of the HC.
- The severe group exhibited a lower peak knee flexion angle compared to the mild group (P = 0.018).
- The mild (P = 0.008), moderate (P < 0.001), and severe groups (P < 0.001) demonstrated an elevated peak trunk sagittal angle relative to that of the HC.
- Participants in the moderate (P = 0.023) and severe groups (P = 0.002) exhibited a heightened peak trunk sagittal angle compared to those in the mild group.
- Participants within the moderate (P = 0.011) and severe groups (P < 0.001) displayed an increased peak trunk frontal angle relative to that of the HC.
- The severe group exhibited a greater peak trunk frontal angle compared to the mild group (P = 0.028).
- Subjects within the severe group showcased a higher peak COM ML displacement than that of the HC (P = 0.010).

Regarding walking:

- Participants within the moderate (P = 0.037) and severe (P = 0.009) groups exhibited reduced peak hip extension angles in comparison to those of the HC.

TABLE 4 Descriptive statistics for the discrete kinematic parameters in four groups.

Parameter	HC	Mild	Moderate	Severe	P
Deep squat					
Peak knee flexion angle (°)	119.16 ± 7.11	110.17 ± 12.84	110.87 (103.96–121.15)	98.54 (83.56–109.41)[a]	0.004[b]
Peak hip flexion angle (°)	111.04 ± 13.64	112.70 ± 13.47	113.84 ± 9.61	111.30 ± 16.60	0.941
Peak trunk sagittal angle (°)	28.33 ± 10.80	34.04 ± 8.96	34.24 ± 9.84	38.90 ± 11.52	0.059
Peak trunk frontal angle (°)	2.89 ± 1.43	3.08 ± 1.20	4.03 ± 1.85	3.88 ± 1.83	0.138
Peak COM ML displacement (mm)	18.74 ± 8.78	18.96 ± 8.14	20.27 ± 5.81	23.16 ± 11.61	0.500
Hurdle step					
Peak knee flexion angle (°)	119.61 ± 9.73	116.91 ± 14.89	115.70 ± 8.80	107.65 ± 14.07	0.055
Peak hip flexion angle (°)	78.10 ± 9.30	76.91 ± 11.00	78.52 ± 7.95	75.50 ± 7.83	0.802
Peak trunk sagittal angle (°)	9.18 ± 2.92	9.50 ± 2.99	8.25 ± 2.48	8.56 ± 1.98	0.549
Peak trunk frontal angle (°)	6.52 ± 2.19	6.95 ± 2.69	8.05 ± 2.97	9.30 ± 4.57	0.096
Peak COM ML displacement (mm)	34.25 ± 16.80	35.04 ± 11.88	32.10 ± 12.89	40.01 ± 20.45	0.600
In-line lunge					
Peak knee flexion angle (°)	95.62 ± 6.80	87.00 ± 14.55	82.53 ± 13.96[a]	64.30 ± 22.28[a,c]	0.000[b]
Peak hip flexion angle (°)	74.55 ± 11.05	85.70 ± 10.21	94.73 ± 19.54	81.28 ± 33.33	0.076
Peak trunk sagittal angle (°)	0.09 ± 0.04	0.20 ± 0.10[a]	0.33 ± 0.12[a,c]	0.42 ± 0.18[a,c]	0.000[b]
Peak trunk frontal angle (°)	0.05 ± 0.03	0.06 (0.03–0.08)	0.10 (0.07–0.14)[a]	0.11 (0.09–0.15)[a,c]	0.000[b]
Peak COM ML displacement (mm)	0.22 ± 0.10	0.27 ± 0.14	0.34 (0.18–0.42)	0.39 (0.28–0.48)[a]	0.012[b]
Sit-to-stand					
Peak trunk sagittal angle (°)	25.41 ± 10.40	26.03 ± 8.47	25.17 ± 6.51	24.14 ± 8.24	0.943
Peak trunk frontal angle (°)	3.81 ± 1.30	4.50 ± 1.53	4.80 ± 1.24	5.90 ± 1.88[a,c]	0.004[b]
Peak COM ML displacement (mm)	42.08 ± 27.70	47.22 ± 18.20	53.65 ± 25.19	54.85 ± 31.22	0.508
Walking					
Peak knee flexion angle (°)	51.32 ± 6.29	50.25 ± 4.47	51.96 ± 6.38	44.87 ± 8.91	0.025[b]
Peak hip extension angle (°)	13.30 ± 5.97	11.91 ± 3.97	9.88 ± 2.80[a]	8.96 ± 4.25[a]	0.039[b]
Peak trunk sagittal angle (°)	3.94 ± 1.02	3.81 ± 1.45	3.57 ± 1.39	3.98 ± 1.42	0.832
Peak trunk frontal angle (°)	1.97 ± 0.83	1.69 ± 0.57	2.45 ± 0.86	2.36 ± 1.11	0.072
Gait phase (stance phase)	62.93 ± 2.23	61.93 ± 3.71	61.09 ± 2.79	60.16 ± 3.07	0.084
Stride frequency (steps/min)	117.87 ± 6.53	112.34 ± 9.89	111.33 ± 9.92	111.94 ± 10.92	0.214
Step length (m)	0.37 ± 0.04	0.34 (0.34–0.39)	0.36 ± 0.03	0.31 ± 0.07[a]	0.033[b]

Values are expressed as mean ± SD, except where the data are non-normally distributed, where these data are presented as median (IQR).
[a]Significant difference between this and the HC, groups.
[c]Significant difference between this and the mild groups.
[b]*p*-value <0.05.

- Subjects in the severe group demonstrated shorter step lengths than those of the HC (P = 0.023).

Regarding sit-to-stand:

- Participants within the severe group exhibited a higher peak trunk frontal angle than participants in the mild group (P = 0.014) and HC (P < 0.001).

A comprehensive presentation of these outcomes is available in Table 4.

4 Discussion

This study explored the sensitivity of FMS (deep squat, hurdle step, and in-line lunge) and daily activities (walking

and sit-to-stand) for identifying kinematic abnormalities in PwKOA through markerless motion capture. Our findings underscore the higher sensitivity of the FMS over daily activities, with the knee flexion, trunk sagittal angle, and trunk frontal angle during the in-line lunge emerging as the most responsive parameters.

Strategic selection of movements is critical in detecting atypical functional performance in PwKOA. In this study, we chose daily activities (walking and sit-to-stand) and FMS (deep squat, hurdle step, and in-line lunge). FMS comprises seven fundamental movement tests, which were screened using human movement patterns during growth and physical activity (Cook et al., 2014a; Cook et al., 2014b). Given that functional anomalies in PwKOA primarily manifest in the lower limbs, FMS actions such as the deep squat, hurdle step, and in-line lunge, which are inherently linked to lower extremity function and holistic balance control, were deemed suitable for analysis. Concurrently, typical routine activities, such as walking and sit-to-stand, were also considered.

KOA motion tests are subjected to an array of data analysis methodologies. Although discrete parameters, encompassing range of motion and specific point values, have been frequently compared (Nüesch et al., 2021), such a limitation to zero-dimensional scalar parameters disregards an entire measurement domain, potentially obscuring disparities occurring at other instances of the task (Pataky et al., 2016). Consequently, the adoption of SPM to compare kinematic waveforms has gained prominence in motion analysis (Malfait et al., 2016; Sole et al., 2017; Goudriaan et al., 2018). Nevertheless, SPM might inadvertently suppress differences in discrete parameters, given that peaks and troughs may occur at disparate temporal points across individuals (Sole et al., 2017). A prior study underscored the complementary nature of these two statistical methodologies in detecting kinematic deviations (Papi et al., 2020). Accordingly, we combined these two methods to probe abnormal motor balance function in PwKOA comprehensively.

In this study, the application of SPM analysis revealed significant intergroup disparities during the FMS, which accentuated as the K-L grade increased, whereas no such disparities surfaced during walking. During the deep squat and in-line lunge, a reduction in knee flexion was evident in PwKOA, which is consistent with prior research (van der Straaten et al., 2020). Furthermore, we found reductions in the knee and hip flexion during the hurdle step in PwKOA, which have not been previously explored. Reduced knee and hip flexion potentially relate to pain and stiffness; however, further exploration is imperative. Additionally, during the in-line lunge, both the trunk sagittal and frontal angles increased with the occurrence and progression of KOA, which may be attributed to heightened trunk oscillation resulting from compromised balance control (Duffell et al., 2014). In contrast to knee flexion observations, PwKOA demonstrated an augmented hip flexion compared to the HC during the in-line lunge, which can be attributed to increased forward trunk inclination. As the markerless system defined the hip sagittal angle in relation to the sagittal plane formed by the trunk axis and the line connecting the hip and knee, greater trunk inclination leads to an increase in the calculated hip flexion. Prior studies (Ismailidis et al., 2020; Nüesch et al., 2021) revealed that PwKOA exhibited less knee flexion and hip extension than HC during walking, a discrepancy not detected by our markerless motion capture system, indicating the need for improved pose estimation algorithms and data labeling (Wade et al., 2022).

Examination of discrete kinematic parameters unveiled significant intergroup differences during both the FMS and daily activities. Consistent with the SPM analysis outcomes, the knee flexion during the deep squat and the trunk sagittal angle, trunk frontal angle, and knee flexion during the in-line lunge exhibited marked variations. Additionally, during the in-line lunge, discrete parameter analysis detected a significant variance in the peak COM ML displacement between the severe PwKOA group and HC, which was not apparent in the SPM analysis. The increase in peak COM ML displacement further underscored the compromised balance of the PwKOA. During walking, PwKOA evidenced diminished step length and peak hip extension angle relative to the HC, a pattern congruent with extant research findings (Mills et al., 2013; Ismailidis et al., 2021). During the sit-to-stand, the peak trunk frontal angle increased as KOA occurred and progressed, which agrees with the findings of earlier investigations (Sonoo et al., 2019). Although previous investigations have highlighted distinctions in the trunk frontal angle and stride frequency during walking and in the trunk sagittal angle during sit-to-stand using marker-based systems (Sonoo et al., 2019; Ismailidis et al., 2021; Waiteman et al., 2022), these differences were not evident in our study, suggesting the potential of markerless motion capture systems for providing improved detection capability.

Several limitations of this study merit consideration. First, during participant recruitment, the age range of the HC was controlled; however, the HC skewed younger than the PwKOA, potentially introducing a source of bias. Furthermore, gender and the affected side could influence the functional performance of PwKOA. Nonetheless, our analysis did not segregate participants based on these variables, primarily due to insufficient statistical power for sample stratification. Third, SPM analysis was not performed for the sit-to-stand measurements. Although we provided standardized instructions, the participants applied various movement strategies during sit-to-stand. Therefore, the difference in the kinematic waveform did not reflect the difference in KOA movement performance.

5 Conclusion

By incorporating the markerless motion capture technique, our study underscored the heightened sensitivity of the FMS over daily activities, with the knee flexion, trunk sagittal angle, and trunk frontal angle during the in-line lunge emerging as promising indicators for objective KOA assessment. The potential effectiveness of these indicators for early KOA screening and their evolution as the disease progresses deserve further exploration within comprehensive cohort studies.

Data availability statement

The raw data supporting the conclusions of this article will be made available by the authors, without undue reservation.

Ethics statement

The studies involving humans were approved by Ethics Committee of Zhongshan Torch Development Zone People's Hospital (2022-0001). The studies were conducted in accordance with the local legislation and institutional requirements. The participants provided their written informed consent to participate in this study. Written informed consent was obtained from the individual(s) for the publication of any potentially identifiable images or data included in this article.

Author contributions

FW: Conceptualization, Data curation, Formal Analysis, Methodology, Writing–original draft, Writing–review and editing. RJ: Data curation, Formal Analysis, Methodology, Writing–review and editing. XH: Data curation, Project administration, Resources, Writing–review and editing. JiW: Resources, Writing–review and editing. PZ: Resources, Writing–review and editing. HH: Formal Analysis, Writing–review and editing. JJ: Formal Analysis, Writing–review and editing. HZ: Conceptualization, Project administration, Resources, Writing–review and editing. JL: Conceptualization, Data curation, Methodology, Project administration, Writing–original draft, Writing–review and editing.

Funding

The author(s) declare financial support was received for the research, authorship, and/or publication of this article. This study was supported by the Natural Science Foundation of Guangdong Province, China (No. 2022A1515011604) and National Key R&D Program of China (No. 2022YFF1202600).

Acknowledgments

We would like to thank the staff of the Zhongshan Torch Development Zone People's Hospital for their help and every volunteer who participated in the experiment.

Conflict of interest

The authors declare that the research was conducted in the absence of any commercial or financial relationships that could be construed as a potential conflict of interest.

Publisher's note

All claims expressed in this article are solely those of the authors and do not necessarily represent those of their affiliated organizations, or those of the publisher, the editors and the reviewers. Any product that may be evaluated in this article, or claim that may be made by its manufacturer, is not guaranteed or endorsed by the publisher.

Supplementary material

The Supplementary Material for this article can be found online at: https://www.frontiersin.org/articles/10.3389/fbioe.2024.1325339/full#supplementary-material

References

Bellamy, E., Wilson, C., and Bellamy, N. (2009). Osteoarthritis Measurement in Routine Rheumatology Outpatient Practice (OMIRROP) in Australia: a survey of practice style, instrument use, responder criteria, and state-attainment criteria. *J. rheumatology* 36 (5), 1049–1055. doi:10.3899/jrheum.080695

Cook, G., Burton, L., Hoogenboom, B. J., and Voight, M. (2014a). Functional movement screening: the use of fundamental movements as an assessment of function-part 2. *Int. J. sports Phys. Ther.* 9 (4), 549–563.

Cook, G., Burton, L., Hoogenboom, B. J., and Voight, M. (2014b). Functional movement screening: the use of fundamental movements as an assessment of function - part 1. *Int. J. sports Phys. Ther.* 9 (3), 396–409.

Duffell, L. D., Southgate, D. F. L., Gulati, V., and McGregor, A. H. (2014). Balance and gait adaptations in patients with early knee osteoarthritis. *Gait posture* 39 (4), 1057–1061. doi:10.1016/j.gaitpost.2014.01.005

Fukaya, T., Mutsuzaki, H., Nakano, W., and Mori, K. (2019). Characteristics of frontal plane lower limb movement during walking in patients with knee osteoarthritis of varying severity. *J. Orthop. Surg. (Hong Kong)* 27 (2), 230949901984808. doi:10.1177/2309499019848085

Goudriaan, M., Van den Hauwe, M., Simon-Martinez, C., Huenaerts, C., Molenaers, G., Goemans, N., et al. (2018). Gait deviations in Duchenne muscular dystrophy-Part 2. Statistical non-parametric mapping to analyze gait deviations in children with Duchenne muscular dystrophy. *Gait posture* 63, 63159–63164. doi:10.1016/j.gaitpost.2018.04.038

Hay, J. G. (1993). *The Biomechanics of sports techniques*. San Francisco: Benjamin-Cummings Publishing Company.

Hayashi, D., Roemer, F. W., and Guermazi, A. (2016). Imaging for osteoarthritis. *Ann. Phys. rehabilitation Med.* 59 (3), 161–169. doi:10.1016/j.rehab.2015.12.003

Hsieh, C., Huang, H., Liu, K., Chen, K., Hsu, S. J., and Chan, C. (2020). Subtask segmentation of timed up and go test for mobility assessment of perioperative total knee arthroplasty. *Sensors (Basel, Switz.* 20, 6302. doi:10.3390/s20216302

Ismailidis, P., Egloff, C., Hegglin, L., Pagenstert, G., Kernen, R., Eckardt, A., et al. (2020). Kinematic changes in patients with severe knee osteoarthritis are a result of reduced walking speed rather than disease severity. *Gait posture* 79, 79256–79261. doi:10.1016/j.gaitpost.2020.05.008

Ismailidis, P., Hegglin, L., Egloff, C., Pagenstert, G., Kernen, R., Eckardt, A., et al. (2021). Side to side kinematic gait differences within patients and spatiotemporal and kinematic gait differences between patients with severe knee osteoarthritis and controls measured with inertial sensors. *Gait posture* 84, 24–30. doi:10.1016/j.gaitpost.2020.11.015

Lee, C., Hsu, M., Chang, W., Wang, S., Chen, C., Chou, P., et al. (2018). Functional movement screen comparison between the preparative period and competitive period in high school baseball players. *J. Exerc. Sci. Fit.* 16 (2), 68–72. doi:10.1016/j.jesf.2018.06.004

Lee, S., Kim, H., and Kim, J. (2019). The Functional Movement Screen total score and physical performance in elite male collegiate soccer players. *J. Exerc. rehabilitation* 15 (5), 657–662. doi:10.12965/jer.1938422.211

Malfait, B., Dingenen, B., Smeets, A., Staes, F., Pataky, T., Robinson, M. A., et al. (2016). Knee and hip joint kinematics predict quadriceps and hamstrings neuromuscular activation patterns in drop jump landings. *PloS one* 11 (4), e0153737. doi:10.1371/journal.pone.0153737

Mills, K., Hunt, M. A., and Ferber, R. (2013). Biomechanical deviations during level walking associated with knee osteoarthritis: a systematic review and meta-analysis. *Arthritis care and Res.* 65 (10), 1643–1665. doi:10.1002/acr.22015

Moran, R. W., Schneiders, A. G., Mason, J., and Sullivan, S. J. (2017). Do Functional Movement Screen (FMS) composite scores predict subsequent injury? A systematic review with meta-analysis. *Br. J. sports Med.* 51 (23), 1661–1669. doi:10.1136/bjsports-2016-096938

Nüesch, C., Ismailidis, P., Koch, D., Pagenstert, G., Ilchmann, T., Eckardt, A., et al. (2021). Assessing site specificity of osteoarthritic gait kinematics with wearable sensors

and their association with patient reported outcome measures (PROMs): knee versus hip osteoarthritis. *Sensors (Basel, Switz.* 21, 5363. doi:10.3390/s21165363

Papi, E., Bull, A. M. J., and McGregor, A. H. (2020). Alteration of movement patterns in low back pain assessed by Statistical Parametric Mapping. *J. biomechanics* 100, 109597. doi:10.1016/j.jbiomech.2019.109597

Pataky, T. C., Robinson, M. A., and Vanrenterghem, J. (2013). Vector field statistical analysis of kinematic and force trajectories. *J. biomechanics* 46 (14), 2394–2401. doi:10.1016/j.jbiomech.2013.07.031

Pataky, T. C., Vanrenterghem, J., and Robinson, M. A. (2016). The probability of false positives in zero-dimensional analyses of one-dimensional kinematic, force and EMG trajectories. *J. biomechanics* 49 (9), 1468–1476. doi:10.1016/j.jbiomech.2016.03.032

Smith, P. D., and Hanlon, M. P. (2017). Assessing the effectiveness of the functional movement screen in predicting noncontact injury rates in soccer players. *J. strength Cond. Res.* 31 (12), 3327–3332. doi:10.1519/JSC.0000000000001757

Sole, G., Pataky, T., Tengman, E., and Häger, C. (2017). Analysis of three-dimensional knee kinematics during stair descent two decades post-ACL rupture - data revisited using statistical parametric mapping. *J. Electromyogr. Kinesiol.* 32, 44–50. doi:10.1016/j.jelekin.2016.12.005

Sonoo, M., Iijima, H., and Kanemura, N. (2019). Altered sagittal plane kinematics and kinetics during sit-to-stand in individuals with knee osteoarthritis: a systematic review and meta-analysis. *J. biomechanics* 96, 109331. doi:10.1016/j.jbiomech.2019.109331

Suzuki, K., Mizoguchi, Y., Kimura, F., Sawada, Y., and Akasaka, K. (2022). Efficacy of injury prevention using functional movement screen training in high-school baseball players: secondary outcomes of a randomized controlled trial. *Healthc. (Basel, Switz.* 10 (12), 2409. doi:10.3390/healthcare10122409

Takeda, I., Yamada, A., and Onodera, H. (2021). Artificial Intelligence-Assisted motion capture for medical applications: a comparative study between markerless and passive marker motion capture. *Comput. methods biomechanics Biomed. Eng.* 24 (8), 864–873. doi:10.1080/10255842.2020.1856372

Topley, M., and Richards, J. G. (2020). A comparison of currently available optoelectronic motion capture systems. *J. biomechanics* 106, 109820. doi:10.1016/j.jbiomech.2020.109820

van der Straaten, R., De Baets, L., Jonkers, I., and Timmermans, A. (2018). Mobile assessment of the lower limb kinematics in healthy persons and in persons with degenerative knee disorders: a systematic review. *Gait posture* 59, 229–241. doi:10.1016/j.gaitpost.2017.10.005

van der Straaten, R., Wesseling, M., Jonkers, I., Vanwanseele, B., Bruijnes, A. K. B. D., Malcorps, J., et al. (2020). Functional movement assessment by means of inertial sensor technology to discriminate between movement behaviour of healthy controls and persons with knee osteoarthritis. *J. neuroengineering rehabilitation* 17 (1), 65. doi:10.1186/s12984-020-00694-2

van Helvoort, E. M., Hodgins, D., Mastbergen, S. C., Marijnissen, A. K., Guehring, H., Loef, M., et al. (2021). Relationship between motion, using the GaitSmartTM system, and radiographic knee osteoarthritis: an explorative analysis in the IMI-APPROACH cohort. *Rheumatol. Oxf. Engl.* 60 (8), 3588–3597. doi:10.1093/rheumatology/keaa809

Vitali, R. V., and Perkins, N. C. (2020). Determining anatomical frames via inertial motion capture: a survey of methods. *J. biomechanics* 106, 109832. doi:10.1016/j.jbiomech.2020.109832

Wade, L., Needham, L., McGuigan, P., and Bilzon, J. (2022). Applications and limitations of current markerless motion capture methods for clinical gait biomechanics. *PeerJ* 10, e12995. doi:10.7717/peerj.12995

Waiteman, M. C., Chia, L., Ducatti, M. H. M., Bazett-Jones, D. M., Pappas, E., de Azevedo, F. M., et al. (2022). Trunk biomechanics in individuals with knee disorders: a systematic review with evidence gap map and meta-analysis. *Sports Med. - open* 8 (1), 145. doi:10.1186/s40798-022-00536-6

Zeng, Z., Shan, J., Zhang, Y., Wang, Y., Li, C., Li, J., et al. (2022). Asymmetries and relationships between muscle strength, proprioception, biomechanics, and postural stability in patients with unilateral knee osteoarthritis. *Front. Bioeng. Biotechnol* 10, 10922832. doi:10.3389/fbioe.2022.922832

frontiers | Frontiers in Bioengineering and Biotechnology

TYPE Original Research
PUBLISHED 08 March 2024
DOI 10.3389/fbioe.2024.1274496

OPEN ACCESS

EDITED BY
Bernardo Innocenti,
Université libre de Bruxelles, Belgium

REVIEWED BY
Silvia Piangiani,
Independent Researcher, Milano, Italy
Qida Zhang,
The Chinese University of Hong Kong, China

*CORRESPONDENCE
Richard J. van Arkel,
r.vanarkel@imperial.ac.uk

RECEIVED 08 August 2023
ACCEPTED 24 January 2024
PUBLISHED 08 March 2024

CITATION
Stoddart JC, Garner A, Tuncer M, Amis AA, Cobb J and van Arkel RJ (2024), Load transfer in bone after partial, multi-compartmental, and total knee arthroplasty.
Front. Bioeng. Biotechnol. 12:1274496.
doi: 10.3389/fbioe.2024.1274496

Load transfer in bone after partial, multi-compartmental, and total knee arthroplasty

Jennifer C. Stoddart[1], Amy Garner[2,3,4], Mahmut Tuncer[5], Andrew A. Amis[1], Justin Cobb[2] and Richard J. van Arkel[1]*

[1]Biomechanics Group, Department of Mechanical Engineering, Imperial College London, London, United Kingdom, [2]Msk Lab, Department of Surgery and Cancer, Imperial College London, London, United Kingdom, [3]Dunhill Medical Trust and Royal College of Surgeons of England Joint Research Fellowship, London, United Kingdom, [4]Nuffield Orthopaedic Centre, Oxford Universities NHS Trust, Oxford, United Kingdom, [5]Meshworks, Alloyed Ltd., Oxford, United Kingdom

Introduction: Arthroplasty-associated bone loss remains a clinical problem: stiff metallic implants disrupt load transfer to bone and, hence, its remodeling stimulus. The aim of this research was to analyze how load transfer to bone is affected by different forms of knee arthroplasty: isolated partial knee arthroplasty (PKA), compartmental arthroplasty [combined partial knee arthroplasty (CPKA), two or more PKAs in the same knee], and total knee arthroplasty (TKA).

Methods: An experimentally validated subject-specific finite element model was analyzed native and with medial unicondylar, lateral unicondylar, patellofemoral, bi-unicondylar, medial bicompartmental, lateral bicompartmental, tricompartmental, and total knee arthroplasty. Three load cases were simulated for each: gait, stair ascent, and sit-to-stand. Strain shielding and overstraining were calculated from the differences between the native and implanted states.

Results: For gait, the TKA femoral component led to mean strain shielding (30%) more than three times higher than that of PKA (4%–7%) and CPKA (5%–8%). Overstraining was predicted in the proximal tibia (TKA 21%; PKA/CPKA 0%–6%). The variance in the distribution for TKA was an order of magnitude greater than for PKA/CPKA, indicating less physiological load transfer. Only the TKA-implanted femur was sensitive to the load case: for stair ascent and gait, almost the entire distal femur was strain-shielded, whereas during sit-to-stand, the posterior femoral condyles were overstrained.

Discussion: TKA requires more bone resection than PKA and CPKA. These finite element analyses suggest that a longer-term benefit for bone is probable as partial and multi-compartmental knee procedures lead to more natural load transfer compared to TKA. High-flexion activity following TKA may be protective of posterior condyle bone resorption, which may help explain why bone loss affects some patients more than others. The male and female bone models used for this research are provided open access to facilitate future research elsewhere.

KEYWORDS

combined partial knee arthroplasty, finite element, total knee arthroplasty, unicondylar, stress shielding, strain shielding, compartmental arthroplasty

Introduction

It has been reported that, for some patients, end-stage knee osteoarthritis (OA) can result in a quality of life that is "worse than death" (Scott et al., 2019). With aging populations in many countries, the global burden of the disease is growing (Safiri et al., 2020). Arthroplasty is an efficacious, evidence-based treatment to relieve pain and restore function for people with severe OA. For at least three-quarters of people, their disease is isolated to one or two of the three knee compartments (medial, lateral, and patellofemoral) (Stoddart et al., 2021); however, total knee arthroplasty (TKA), in which all three compartments of the knee are replaced, accounts for 87% of knee arthroplasty procedures in the English and Welsh NJR (Brittain et al., 2021).

Partial knee arthroplasty (PKA), in which a single compartment of the knee is replaced and the cruciate ligaments are preserved, is a less-invasive alternative to TKA. PKA is associated with better knee function (Wiik et al., 2013; Jones et al., 2016) and lower risk of death, stroke, and myocardial infarction or blood transfusion requirement (Liddle et al., 2014). However, revision rates for cementless unicompartmental arthroplasty (UKA) are 2.7 times higher than those for cemented TKA at 15 years, while patellofemoral arthroplasty (PFA) has a revision rate in excess of five times that of TKA at 10 years (Brittain et al., 2021). In 2022, for the first time, the NJR reported on revision rates for combined (i.e., multi-compartmental) partial knee arthroplasty (CPKA). While the recorded numbers are small and should be interpreted with caution, their revision rates are more than four times higher than that for TKA at 5 years. The reasons for higher revision rates in PKA are complex and multi-factorial (Goodfellow et al., 1976); however, the progression of arthritis in an unresurfaced knee compartment remains a leading cause. CPKA allows for the preservation of a well-functioning, well-fixed PKA in these cases (Garner et al., 2021f), or an alternative primary procedure for the one-in-three patients with bicompartmental knee disease (Garner et al., 2019; Stoddart et al., 2021). CPKA is associated with favorable patient outcomes (Biazzo et al., 2018; Wada et al., 2020; Garner et al., 2021e; Garner et al., 2021f; Garner et al., 2021b), stability (Garner et al., 2021d), and function (Wang et al., 2018; Garner et al., 2021b; Garner et al., 2021) compared to TKA. However, it is not known how use of multiple PKAs in the same knee affects load transfer to bone.

Preventing arthroplasty-associated bone loss remains an unmet clinical need, with aseptic loosening being the leading cause of implant failure associated with TKA (Brittain et al., 2021). Bone remodeling is sensitive to mechanical stimulus: increased strain can lead to bone formation, bone structure optimization, and higher bone mineral density (BMD), while reduced strain leads to bone resorption and bone loss (Huiskes et al., 1987). Finite element analysis enables the quantification of the change in the strain environment and is widely used to understand how interventions and disease affect load transfer and bone remodeling (Ong et al., 2009; Dickinson, 2014; Quilez et al., 2017; Zhang et al., 2020; Anijs et al., 2022). CPKA procedures could, in theory, lead to favorable load transfer to bone, as articulating surfaces, ligaments, and bone stock are preserved compared to TKA. However, it is also possible that the regions of bone between implants could lead to unfavorable loading conditions that could, perhaps, accelerate bone loss (through strain shielding) or risk of fracture (through overstraining) (Stoddart et al., 2022).

The aim of this research was to analyze how the different knee arthroplasty options (PKA, CPKA, and TKA) affect load transfer to bone using the finite element method. It was hypothesized that preserving the intact joint surface in CPKA would result in more favorable load transfer to bone, indicative of reduced risk of bone loss following arthroplasty.

Materials and methods

Bone model preparation

An experimentally validated (Tuncer et al., 2013) subject-specific (Supplementary Table S1) finite element model (female, right-sided) of the distal femur and proximal tibia was prepared intact, with PKAs: medial (UKA-M) and lateral (UKA-L) unicondylar, PFA- CPKAs: bi-unicondylar (Bi-UKA), medial (BCA-M) and lateral (BCA-L) bicompartmental, and tricompartmental (TCA), and TKA. All implants were cemented variants from the same manufacturer (Zimmer Biomet, United States): the mobile bearing medial Oxford® and fixed lateral Oxford® (FLO) UKA implants, the Gender Solutions® PFA, and the NexGen® cruciate retaining (CR) TKA. Standard NexGen® CR implants were used and did not include the option tibial components or any combinations subject to the voluntary medical device field safety corrective action conducted by Zimmer Biomet Inc. Since the combination of implants used in the tibia was identical for UKA-M and BCA-M, UKA-L and BCA-L, and Bi-UKA and TCA, only the models for UKA-M, UKA-L, and Bi-UKA were prepared for this study.

Implants were sized and positioned using surgical planning software (Embody Orthopaedic, UK), following the senior surgical author's clinical practice (Supplementary Table S2). Boolean operations were used to prepare the bones for the implants (including a 1 mm cement layer), and the volume of bone removed was quantified for each procedure.

Bone volume meshes were created in 3-matic (Materialise NV, Belgium) with ten-noded tetrahedral elements. The cortical bone was modeled with type 127 ten-noded tetrahedral elements in MARC (MSC Software Corporation, United States). The thin tibial cortex was modeled with type 22 one-side collapsed quadratic quadrilateral 0.2 mm thick shell elements to reduce partial volume effects arising from the bone material allocation method. Mesh convergence was assessed for the accuracy of the equivalent elastic strain predicted by each bone model under toe-off in gait loading in nine regions of interest: at the tips of each peg in the distal femur implanted with TCA and around the keels of each implant in the proximal tibia implanted with Bi-UKA. An element edge length of 2 mm resulted in peak values in each region of interest that were within 5% equivalent elastic strain of those predicted by the highest-density mesh investigated.

Material properties

The bones were CT-scanned (Definition AS+, Siemens, Germany) with a slice thickness of 0.6 mm and cross-section voxels 0.5 × 0.5 mm. The scans were phantom-calibrated against air and water: the grey-scale values were calibrated as Hounsfield units (HU) such that water

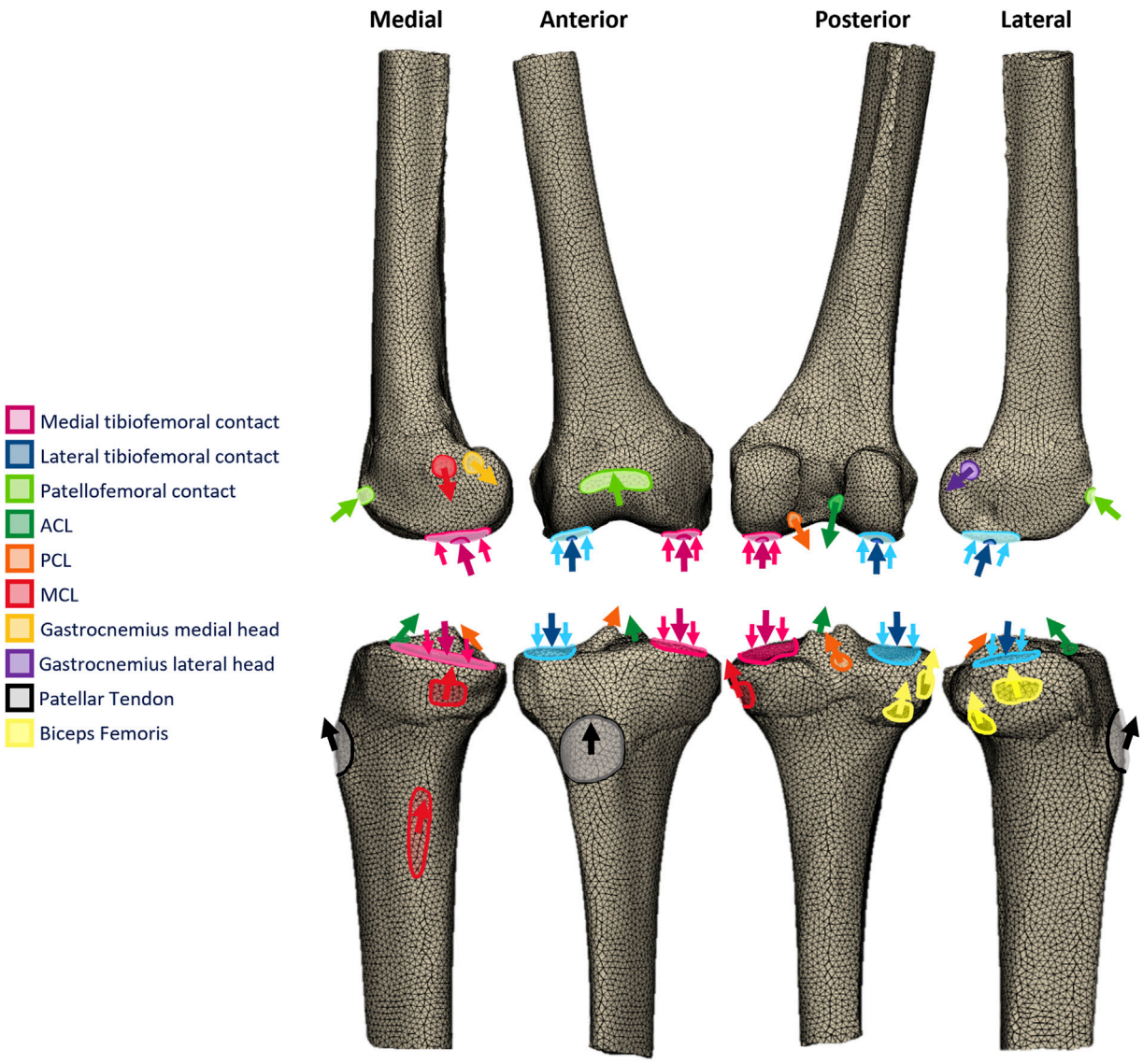

FIGURE 1
Free-body diagrams illustrating the toe-off in gait loading applied to the femoral and tibial finite element models.

corresponds to ±4 HU and air to −1,000. Cancellous bone material properties were applied heterogeneously based on empirical measures relating HU to density and elastic moduli from quantitative CT of each specimen using Mimics (Materialise NV) (Tuncer et al., 2013). All other materials were homogeneous, isotropic, and linear elastic (Supplementary Table S3).

Boundary conditions

The most proximal and distal surfaces of the femoral and tibial diaphysis, respectively, were fixed. Loading for three activities of daily living was modeled to capture the effects of load transfer for a range of contact locations: gait (toe-off, 15° flexion, when tibial contacts the distal condyles, and when patellar contacts the proximal trochlea) (Figure 1), stair ascent (weight acceptance, 50° flexion, when tibial contacts the posterior plateaux, femoral posterodistal condyles, and when patellar contacts the mid trochlea), and sit-to-stand (when leaving chair, 90° flexion, when tibial contacts the posterior plateaux, femoral posterior condyles, and when patellar contacts the distal trochlea).

The tibiofemoral joint reaction force was based on measured *in vivo* telemetric data for posterior-stabilized TKA (Bergmann et al., 2014) scaled to the bodyweight of each model specimen. The mediolateral load split was calculated according to the varus–valgus moment at the point of peak contact force (Kutzner et al., 2013). Equivalent data are not available for the native knee, PKA/CPKA, or posterior-cruciate retaining TKA. The data were, thus, adapted and applied to the models as follows: 1) The loading magnitude and medial–lateral distribution were assumed to be the same for all variants. This allowed for direct comparisons where the only change was the type of implant. 2) Equal and opposite musculoskeletally predicted ACL and PCL forces were added to the tibiofemoral contact forces appropriately for each modeling

condition, since neither were present in the orthoload data (i.e., ACL and PCL for the native, PKA, and CPKA states and PCL only for the TKA state). 3) In native knee compartments, condylar loads were distributed to simulate the effect of the menisci and cartilage, in accordance with a method that has previously been verified (Stoddart et al., 2022) with lab data (Munford et al., 2022). 4) Loading through implants was applied as point load to the implant, in accordance with the previous model validation (Tuncer et al., 2013).

Muscle and ligament forces associated with each load case were derived from the results of published musculoskeletal models (Rasnick et al., 2016; Hume et al., 2019). Muscle and ligament forces were applied directly to the bone models as point loads distributed over anatomically derived attachment areas, rather than as continuum bodies. Other than the presence or absence of the ACL, the load cases applied to the intact and implanted bones were identical. The directions of the muscle force vectors were determined by inputting the hip, knee, and ankle kinematics associated with each load case into the 2010 Lower Limb musculoskeletal (Arnold et al., 2010) model in OpenSim (SimTK, United States), using a published plugin (Van Arkel et al., 2013). Ligament force vectors were assumed to act in the same direction as the vector connecting their bony attachments. MRI studies of the ACL (Jordan et al., 2007) and PCL (Papannagari et al., 2007) bundles informed their force direction vectors, while the directions of the collateral ligaments with flexion were taken from a cadaveric study (Herzog and Read, 1993).

The patellofemoral joint reaction force was calculated from the predicted quadriceps load, using the relationship between patellar contact force and quadriceps force with flexion described by Ahmed et al. (1987). The location and contact area were estimated by translating and rotating the patella relative to the femur according to a kinematic dataset of the native knee (Garner et al., 2021; Dandridge et al., 2022), then identifying the contact area on the articulating surface of the femur according to descriptions given in a functional anatomical study (Goodfellow et al., 1976) and projecting the patellar contact area onto the femur. The resulting femoral contact area was then verified through comparison with MRI-measured contact areas at each flexion angle under weight-bearing conditions (Hungerford and Barry, 1979; Besier et al., 2005); deviations were less than 11%. Similar to the tibiofemoral loads, when patellofemoral loading occurred through an implant, a single point load was applied.

The resulting loads applied to the tibial and femoral models in the toe-off gait load case are described in Supplementary Tables S5, S6, respectively, as well as the stair ascent and sit-to-stand load cases in Supplementary Tables S6–S9.

Data analysis

The percentage difference between the equivalent elastic strain in the implanted and intact bone was calculated; strain shielding (negative percentage differences) was a term used to describe regions where the strain reduced following implantation. Conversely, overstraining (positive percentage differences) was used to denote bone that experienced increased strain following implantation. Equivalent elastic strain was defined according to the Von Mises formulation, and the percentage difference in equivalent elastic strain was calculated as $\frac{\varepsilon_{equiv,implanted}-\varepsilon_{equiv,intact}}{\varepsilon_{equiv,intact}} \times 100$.

The bone meshes were inherently different following the Boolean operations that enabled implantation. Strain data were, thus, interpolated onto the same regular grid to enable percentage difference calculation. Two interpolations were used, with grid spacing determined following a sensitivity study. First, a 2D grid with 0.1 mm spacing, using a MATLAB (MathWorks, United States) triangulation-based cubic interpolation function, was used to create visual contour maps in regions of interest. The same regions were used for all implant states, and they were defined prior to the generation of any results. For the femur: a sagittal slice through the medial condyle located at the center of the posterior fixation peg of the UKA-M, a sagittal slice through the lateral condyle at the center of the posterior fixation peg of the UKA-L, a frontal slice through the distal tail of the PFA, and a frontal slice through the condyles, at the center of the posterior fixation peg of the UKA-M. It was coincidental, yet convenient, that the surgically planned positions led to the TKA and PFA fixation pegs appearing in the condylar sagittal cross-sections. For the tibia: a frontal slice 10 mm anterior to the tibial origin that approximately bisected the ACL attachment, a transverse slice 8 mm distal to the condyles corresponding to the proximodistal midpoint of the keels of the UKA-M and UKA-L, and a transverse slice 30 mm distal to the condyles toward the distal tip of the TKA stem. Separate 2D contour plots were prepared for strain shielding (−100%–0% difference in equivalent elastic strain from intact bone) and overstraining (0%–100% difference), since this best allowed for the clear visualization of the areas of the greatest strain shielding or overstraining. In both contour plots, yellow regions ($\geq |\pm 100|$% difference) represented bones that experienced a strain state most different from the intact bone, while dark-blue regions represented the bone that either experienced no difference in the strain state or was overstrained when investigating strain shielding or *vice versa* (≤ 0% difference).

Second, a 3D grid with 5 mm spacing, using a MATLAB triangulation-based linear interpolation function, was used to capture the strain distribution throughout the entire distal femur (1,493 sample points) and proximal tibia (1,027 sample points). This allowed a quantitative comparison for all states that was independent of the *a priori* chosen 2D slices used for visual comparison. Histograms were used quantitatively and visually to evaluate the changes in load transfer throughout the bone volume. Were there no changes in load transfer, the mean and variance would be zero. A negative mean indicates that on average, the distal femur/proximal tibia was strain-shielded, and a positive mean indicates that it was overstrained. The variance is a measure of the extent to which the load transfer was changed: a spike-like distribution with a high peak is indicative of near-native load transfer throughout the bone (low variance), whereas a wide distribution with a low peak would indicate that little of the bone experienced near-native strain and much of it was either strain-shielded or overstrained (high variance) (Figure 2). Skew indicates if there was greater spread for the strain-shielded portion of the bone or the overstrained region.

Strain energy density was also calculated and plotted as histograms. In bone remodeling algorithms, typically a “lazy zone” where no remodeling occurs is included so that only the bone experiencing changes to the mechanical stimulus over a certain threshold resulted in changes to the local bone material

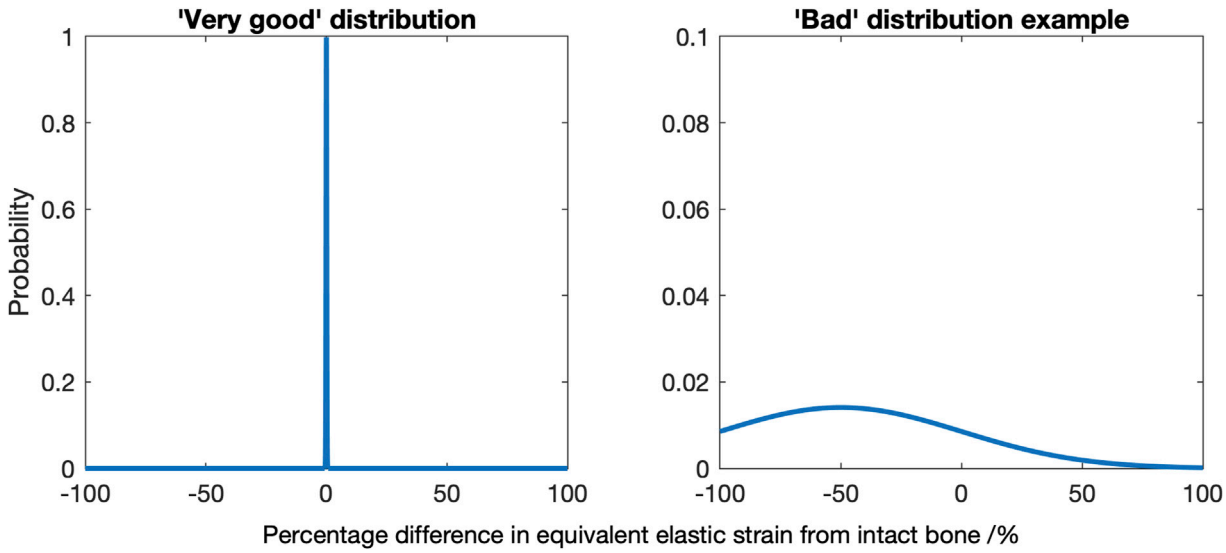

FIGURE 2
Diagrams indicating a "very good" strain difference distribution, where a mean of zero and low variance indicates most of the bone experiences near identical strains as the native bone (left), and an example of a "bad" distribution, here where there is a non-zero mean and a high variance (right).

properties going forward. Thresholds of 50% and 75% have been used (Turner et al., 2005; Cawley et al., 2012; Dickinson, 2014). The percentage of the sample points throughout the distal femur found to exceed either threshold was, thus, calculated. A negative result implied risk of resorption, and a positive result was indicative of stimulus that encourages bone formation.

In addition to the load case analyses, sensitivity of the conclusions to a second subject-specific model (male tibia, right-sided) was also assessed. This model had also been validated previously (Tuncer et al., 2013).

Results

Load transfer changes

Strain shielding during toe-off gait

For isolated PKA during toe-off in gait: UKA-M femoral strain shielding (Figure 3) was the greatest in the distal medial condyle, in the region enclosed by the implant. The same was true for the tibia (Figure 4), where strain shielding was mostly concentrated medially under the implant. Little strain shielding was observed in the femoral trochlear frontal section, the lateral condyle, or 30 mm distal to the tibial plateau, indicating near-native load transfer in these regions. The trends following UKA-L were similar but with the effects observed laterally: strain shielding was evident in the lateral condyle and plateau adjacent to the implant, with little difference in load transfer elsewhere. Strain shielding for the PFA was the greatest in the frontal slice adjacent to the implant. In the distal femur, strain shielding was greater laterally, visible in the frontal trochlear and lateral condylar slices.

Strain shielding following CPKA (Figures 3, 4) was again the greatest immediately adjacent to the implants. There were also regions where strain shielding increased between the implants (up to ~50% strain shielding). This was not the result of an interaction leading to a new load transfer phenomenon, rather was broadly like the addition of the two isolated implant strain-shielding maps leading to regions where the strain shielding became appreciable.

With TKA, almost the entire distal femur region experienced strain shielding (Figure 3). The regions of the bone that were highly strain-shielded for PKA and CPKA were even bigger following TKA. Even when compared to TCA, where a UKA-M, UKA-L, and PFA were all implanted leaving no native articular surface, the strain shielding was appreciably increased for the monolithic TKA component. The same was true in the tibia (Figure 4); TKA strain shielding was both more intense and affected more of the tibia than for Bi-UKA. The medial and proximal regions of the tibia saw the highest degree of strain shielding, while the bone closest to the stem was not strain shielded.

Overstraining during toe-off gait

For isolated PKA during toe-off in gait: femoral overstraining (Figure 5) was the greatest for the UKA-M and UKA-L implants at the peg tips, at the most anterior tip of the implant, and at the most proximal posterior region adjacent to the implant. The result was a large region of overstraining anteriorly as these effects combined. For the tibia (Figure 6), overstraining was observed in the frontal slice lateral/medial to the UKA-M/L, respectively. Overstraining was comparatively greater for the UKA-M, suggesting interaction with the ACL under its attachment. The transverse slices 8 mm distal to the implant revealed a halo-like overstraining effect that tracked the edge of the implant. It was the greatest close to the cruciate ligaments' attachments. For the PFA, overstraining was again evident at the tips of the implant (most proximally and most distally). A small portion of overstraining occurred around the peg, but this was less evident than that seen for the UKA-M and UKA-L.

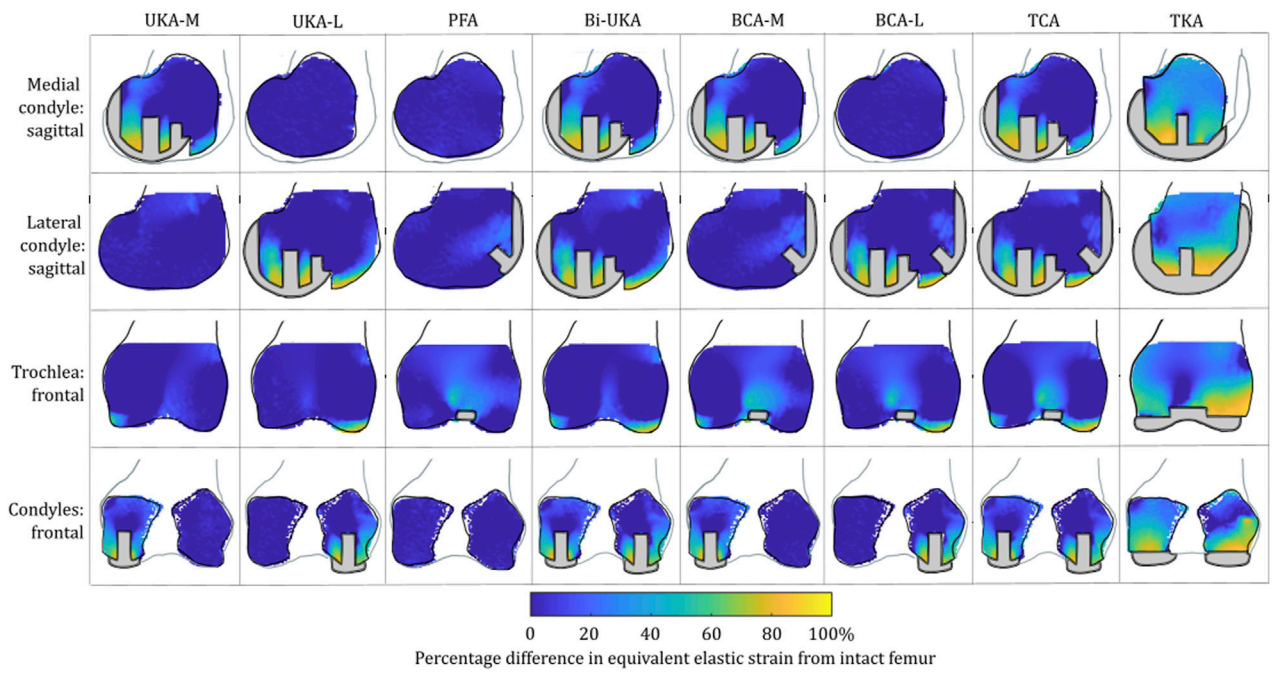

FIGURE 3
Contour plots showing the degree of strain shielding predicted during toe-off in gait, in the implanted femur compared to the intact femur. Values of strain difference have been truncated at 0% for clarity of the figure, with overstraining patterns presented separately in Figure 5.

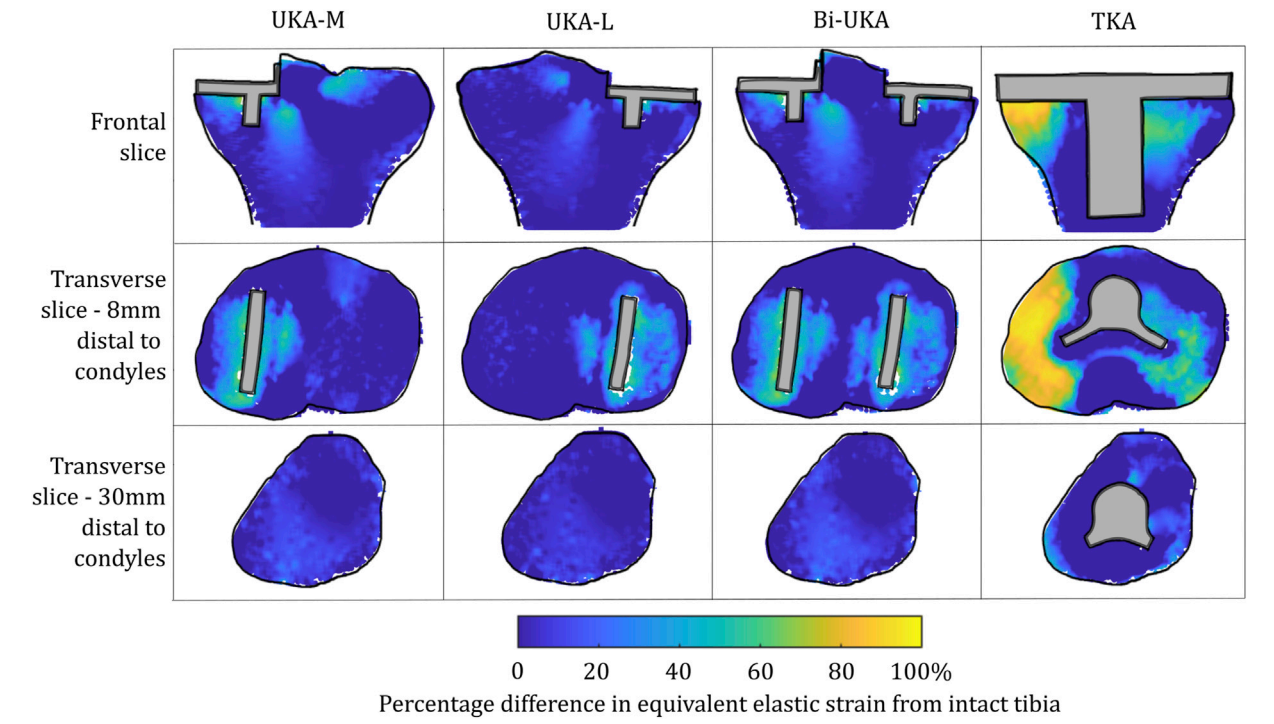

FIGURE 4
Contour plots showing the degree of strain shielding predicted during toe-off in gait, in the implanted tibia compared to the intact tibia. Values of strain difference have been truncated at 0% for clarity of the figure, with overstraining patterns presented separately in Figure 6.

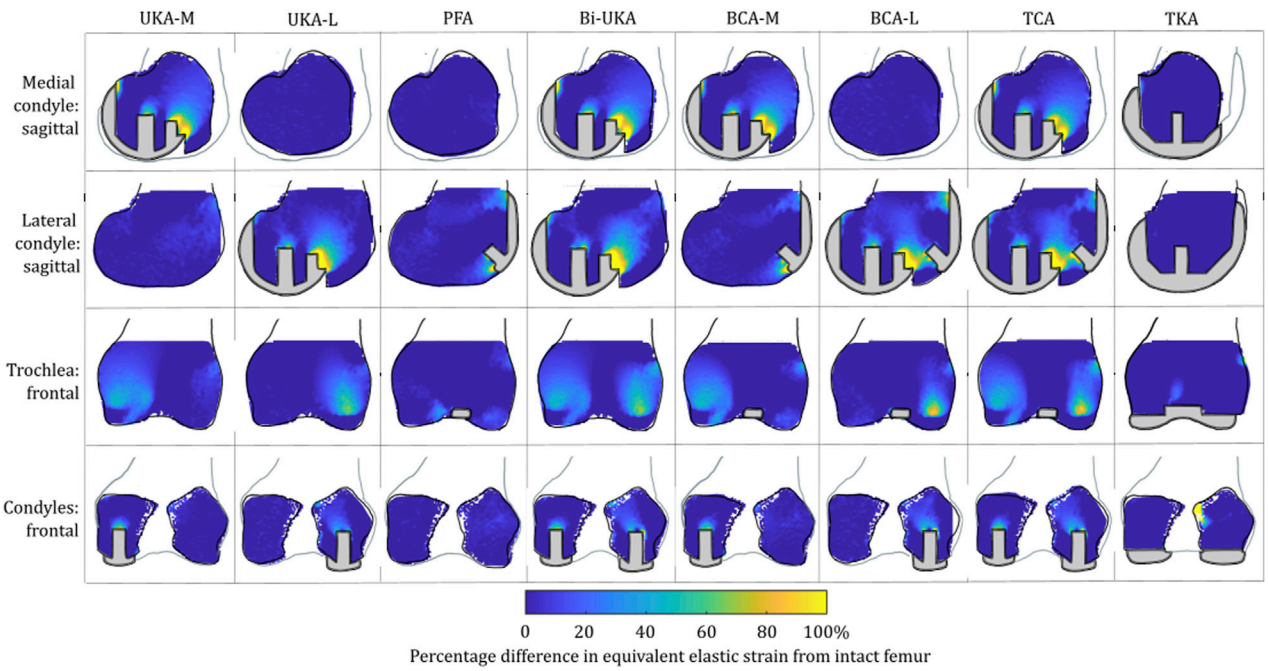

FIGURE 5
Contour plots showing the degree of overstraining predicted during toe-off in gait, in the implanted femur compared to the intact female femur. Values of strain difference have been truncated at 0% for clarity of the figure, with strain-shielding patterns presented separately in Figure 3.

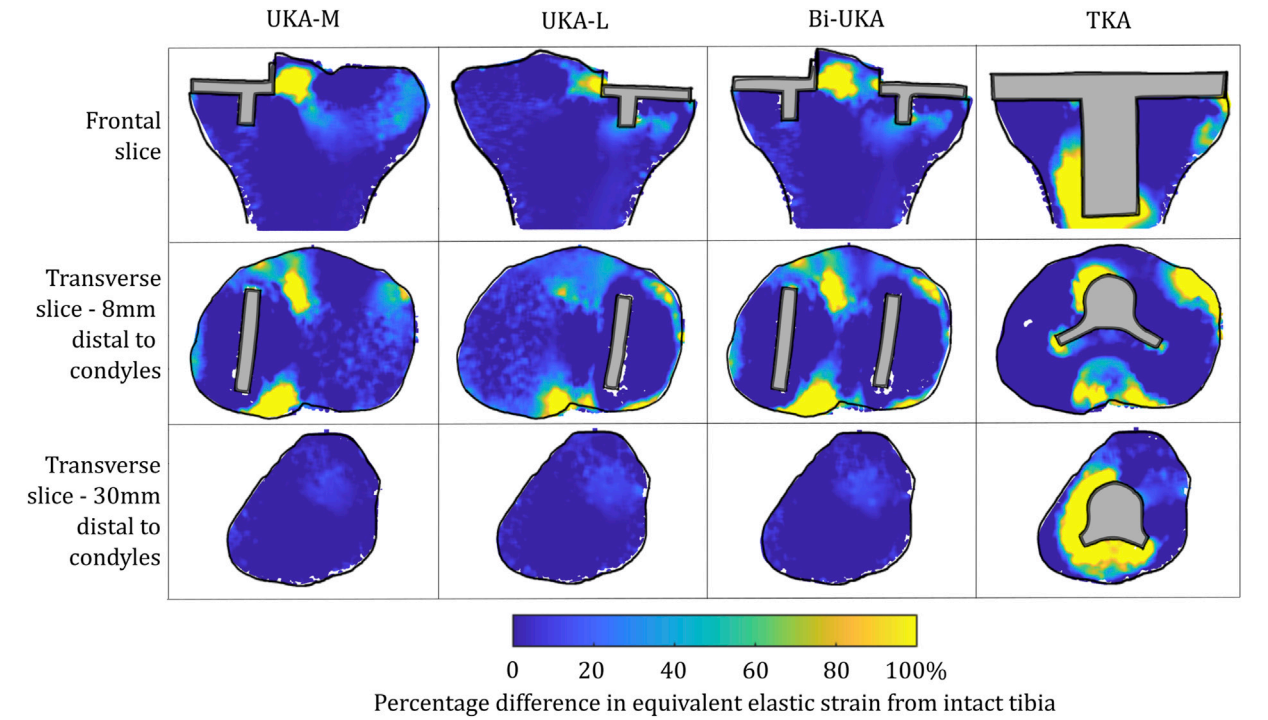

FIGURE 6
Contour plots showing the degree of overstraining predicted during toe-off in gait, in the implanted tibia compared to the intact tibia. Values of strain difference have been truncated at 0% for clarity of the figure, with strain-shielding patterns presented separately in Figure 4.

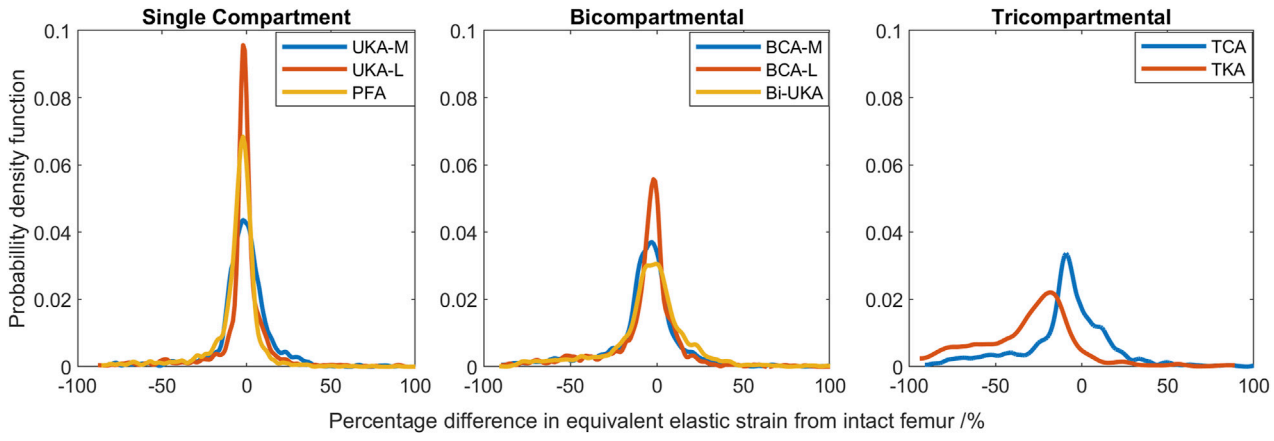

FIGURE 7
Histograms showing the distribution of strain shielding (negative x-axis) and overstraining (positive x-axis) throughout the volume of the implanted distal femur during toe-off in gait.

For the CPKA procedures, overstraining increased, but as was the case for strain shielding, this was an additive effect, rather than a new load transfer phenomenon.

For TKA, no overstraining was evident in the femoral slices (Figure 5), other than on the proximomedial corner of the lateral condyle. The 3D model was inspected for evidence of overstraining not captured in these slices, and it was observed proximal and posterior to the proximal edge of the anterior flange of the TKA (similar to the overstraining observed at the anterior tip of the UKA implants that is visible in the slices shown). In the tibia (Figure 6), overstraining was predicted anterolaterally near the implant, posteriorly under the cruciate attachment, and around the stem. Overstraining around the stem was greater medially than laterally and greater distally than proximally.

Strain distribution during toe-off gait

During toe-off in gait, the mean percentage difference in the equivalent elastic strain predicted throughout the distal femur was from −7.3% to −3.5% in the PKAs and from −8.1% to −5.2% for CPKAs affecting two compartments (Figure 7; Supplementary Table S10). In TCA, the mean strain shielding was −7.8%, while in TKA, the mean degree of strain shielding was more than three times higher, at −30%. The Bi-UKA and TKA distributions were largely symmetrical, while all the PKAs and BCA-M and BCA-L were negatively skewed, meaning that there was a wider spread of strain shielding than overstraining. The strain difference distribution was highly positively skewed for TCA. The spread of the data increased as more compartments of the knee were resurfaced; the variance σ^2 measured in the PKAs was roughly half that of the CPKAs affecting two compartments and almost a quarter of the spread in TKA; the trend was $\sigma^2_{uni} < \sigma^2_{bi} < \sigma^2_{tri}$. The distribution in TCA was most spread; the variance was about twice the value of that in TKA.

In the proximal tibia, the mean percentage difference in the equivalent elastic strain predicted was positive for all arthroplasties considered, indicating overstraining rather than strain shielding (Figure 8; Supplementary Table S10). All arthroplasties showed positive skew. The mean percentage difference in the equivalent elastic strain predicted was from 0.4% to 6.4% for the CPKAs, while it was much higher, at 21.3%, for TKA. The variance in TKA was also about ten times greater than in CPKA.

Sensitivity to the load case

Results for the PKA and CPKA implant states were largely insensitive to the load case. Similar patterns of strain shielding and overstraining were predicted during stair ascent and sit-to-stand: strain shielding occurred between pegs and in the offloaded anterior notch in the femur, and overstraining was predicted at the tips of pegs (Supplementary Figures S1–S4, S7–S10). Differences were seen according to the mediolateral condylar loading ratio and the direction of the condylar load application on the femur, which affected the direction in which the regions of strain shielding and overstraining dissipated around features.

There were notable differences in the load transfer associated with each load case in the femoral TKA model (Figure 9). For both the lower-flexion gait and stair ascent load cases, almost the whole volume of the distal femur investigated experienced strain shielding, while in contrast to this, at the higher flexion angle during sit-to-stand, the posterior femoral condyles, instead, experienced a high degree of overstraining.

Strain energy density changes

Compared to the results for the same load case with the change in equivalent elastic strain considered (Figure 7), the general trends observed for strain energy density are the same (Figure 10); PKA resulted in the tallest and narrowest distributions, while TCA and TKA had the flattest and widest change in strain energy density distributions. In addition, similar to the equivalent elastic strain results, strain energy density distributions were largely symmetrical for all PKA and CPKA variants. For TKA, however, almost all the changes in strain energy density were negative.

Given a remodeling stimulus threshold of 75%, roughly 3% of the sample points in the distal femur implanted with only PKA were predicted to experience a mechanical stimulus causing bone resorption, while this was between 5% and 9% for CPKA and 24% for TKA. With a lower threshold of 50%, the percentage of sample points that would be at risk of bone

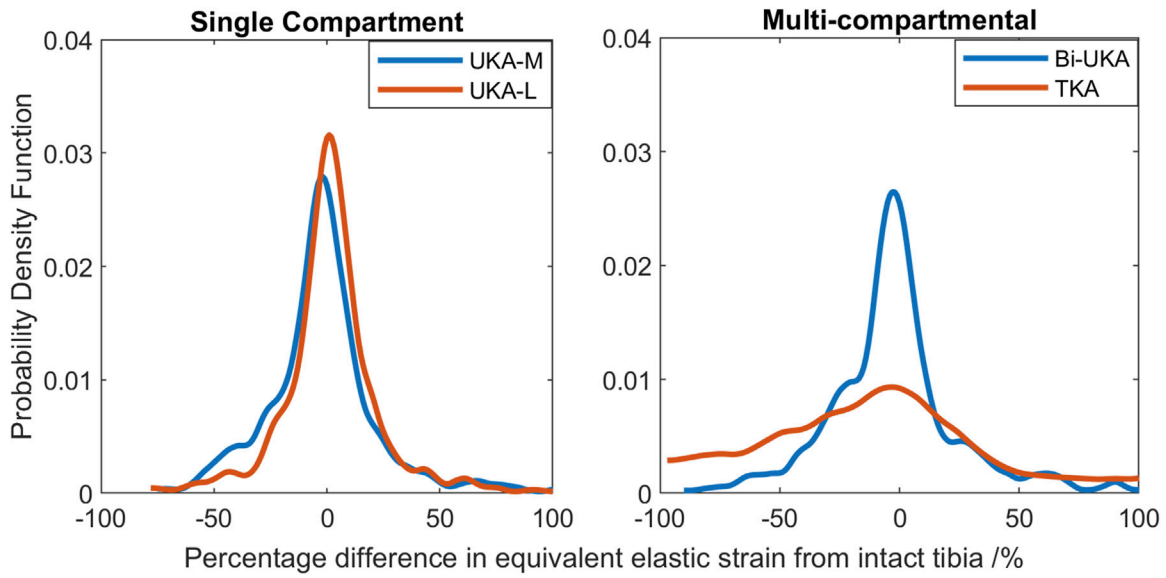

FIGURE 8
Histograms showing the distribution of strain shielding (negative x-axis) and overstraining (positive x-axis) throughout the volume of the implanted proximal tibia during toe-off in gait.

resorption in the immediate post-operative period rose to 50% in TKA (Figure 11).

Sensitivity to a second subject-specific tibial FE model

Similar strain-shielding patterns were observed in the male tibia (Figure 12) as in the female tibia. The biggest difference observed between the tibial results were in the mid-keel transverse slice of the Bi-UKA case and UKA-L, where a region of about 60% strain shielding was predicted in between the two implants, under the tibial eminence in the male model.

Similar patterns and magnitudes of overstraining were also observed for all the arthroplasties modeled (Figure 13: frontal and distal transverse slices). The most notable differences were predicted in the most proximal transverse slice investigated, in UKA-M, UKA-L, and Bi-UKA, when compared to the results of the female model.

The PKAs in the male tibia had the least-disturbed distributions, with the mean difference close to zero, and low variance (Figure 14). As more bone was removed in Bi-UKA and TKA, respectively, the distribution flattened as the variance increased, and more of the proximal tibia experienced progressively large changes to the native strain. Thus, the trends observed for the female bone were replicated.

Discussion

This study showed, for the first time, that TKA leads to mean strain shielding more than three times higher than for partial and multi-compartmental knee arthroplasty. For all eight implant combinations analyzed, the load was found to have transferred from within the implant's bone footprint to the rim of the implant and the tips of any peg/keel-like features. In TKA, the pegs, keel, and implant footprint are larger, and hence, more of the bone is shielded. The monolithic components required for TKA are, thus, doubly disadvantageous for bone biomechanics, requiring greater initial bone resection and having a larger negative effect on bone remodeling stimulus, disrupting load transfer more than any compartmental arthroplasty alternative (Figures 3–8). This change in remodeling stimulus is important as for every one standard deviation decrease in BMD, the relative risk of fracture increases by 2.6% (Prince et al., 2019).

Clinically, a meta-analysis of changes in distal femoral BMD after TKA (Prince et al., 2019) found that there was a non-recoverable and rapid decrease in BMD following TKA of 17.5% in the intracondylar regions that was maintained at 2 years. The mean strain shielding in this region in our model was predicted to be between −10.5% and −42.6% (Supplementary Table S10), and the contour plots indicated gross strain shielding throughout the distal femur (Figure 9), thus agreeing with clinical trends. The sit-to-stand load case, for which the condylar region was found to be overstrained rather than strain-shielded, suggests high-flexion activity may help protect bone stock following TKA. This may help explain why complete bone loss is not observed clinically despite the gross strain shielding predicted for stair climbing/gait. Other FE and DEXA studies have also indicated BMD loss in the femur behind the anterior flange in TKA (Petersen et al., 1995; van Lenthe et al., 1997) and PFA (Van Jonbergen et al., 2010), which also agree with our findings. In our analyses, the load was found to have transferred from the condylar region to proximal to the implant, where there were high levels of overstraining predicted. When considering a proximally extended sagittal slice through the lateral femoral condyle, a further observation was made from our results: in low-flexion activities (gait), the entire femoral slice was strain-shielded when implanted with TKA, with higher-intensity strain shielding predicted just proximal to the anterior flange of the implant (Figure 15A), which, in the long term, would be expected to weaken the bone proximal to the implant. However, when

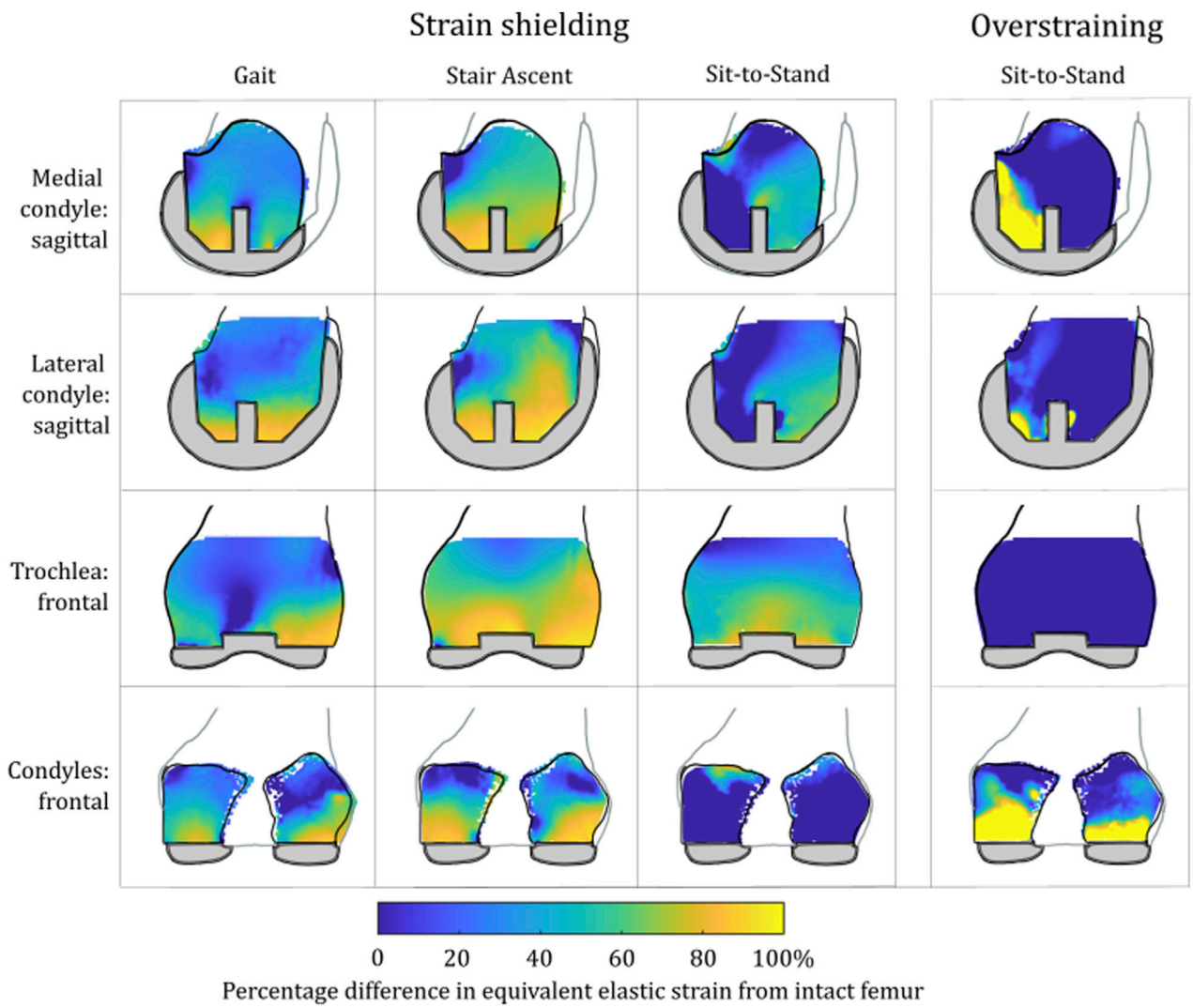

FIGURE 9
Contour plots showing the degree of strain shielding predicted during toe-off gait (left), stair ascent (middle, left), and sit-to-stand (middle, right) for the femur implanted with TKA, as well as overstraining associated with sit-to-stand (right).

higher-flexion activities (stair ascent) were modeled, this same region of bone proximal to the implant was predicted to be highly overstrained (Figure 15B). Rorabeck type II fractures (Figure 15C) have been found to be the most common type of periprosthetic fracture associated with TKA (Ebraheim et al., 2015), and their typical location coincides with the predicted overstrained region. Joint registries do not currently record many such periprosthetic fractures as causing revision, as they are typically treated with long locking plates and the TKA implants remaining *in situ*; however, such fractures are associated with substantial morbidities such as non-union and infection (Ebraheim et al., 2015).

Femoral BMD loss has also been measured in the first 3 months after UKA-M (Soininvaara et al., 2013; Tuncer et al., 2013). Our strain-shielding predictions (Figure 3) correlated with the clinical finding that the posterior region of interest had the largest reduction in BMD.

Tibial BMD following TKA has been suggested to be dependent on the nature of the preoperative varus–valgus deformity that was corrected. For a preoperative varus deformity where the medial compartment was overloaded, its correction would act to unload it and a relative decrease in BMD has been observed after arthroplasty (Deen et al., 2018; Yoon et al., 2018). The converse effect has been observed in the lateral compartment. In our study, the load case sensitivity analyses found that the mediolateral condylar loading ratio and the direction of the condylar load application on the femur affected the predicted strain shielding, agreeing with these clinical observations. Dudhniwala et al. (2016) investigated radiolucencies in 15 patients, 6 months and 1 year following monobloc BCA-M. Femoral comparisons are not appropriate as we did not model a monobloc femoral component. In the tibia, however, they found that the medial portion of the resurfaced medial tibial condyle had a reduced bone density both anteriorly and posteriorly, immediately under the tibial tray, agreeing with our prediction of strain shielding in this region (Figure 4). Others have found an increase in BMD in the medial tibial metaphysis 3 months and 7 years post-operatively (Soininvaara et al., 2013). This correlated with the positive mean of

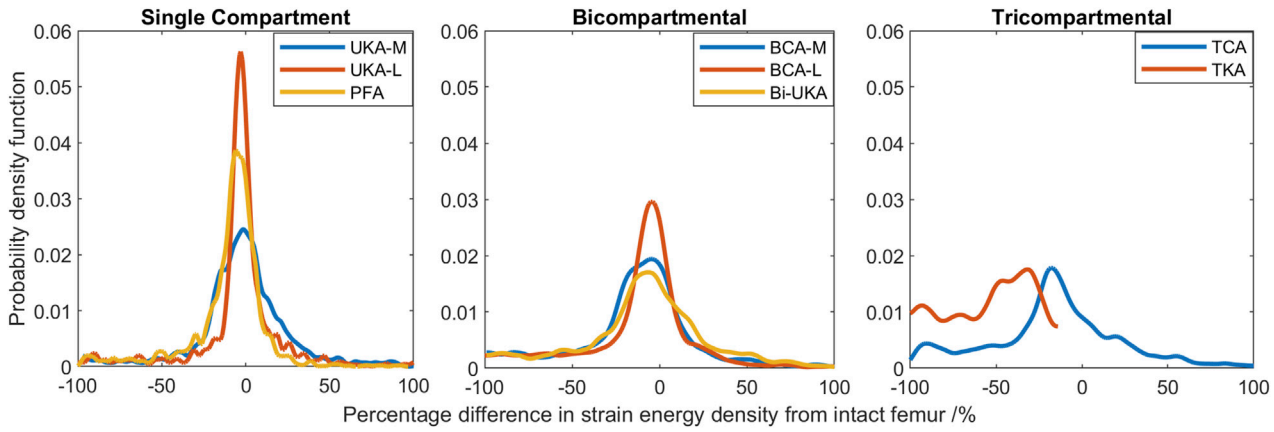

FIGURE 10
Histograms showing the distribution of changes in strain energy density predicted throughout the volume of the implanted distal femur during toe-off in gait.

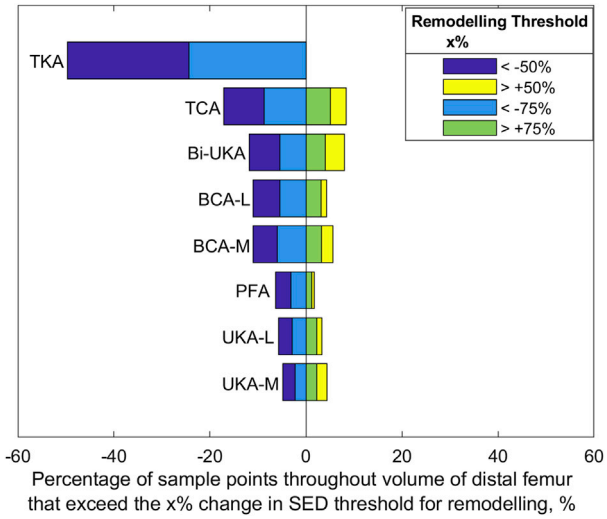

FIGURE 11
Bar chart showing the percentage of sample points in the distal femur found to exceed a change SED stimulus threshold of 50% and 75% at toe-off in gait.

the strain difference distributions predicted for each load case in the proximal tibia (Supplementary Table S10). While classically, TKA has been associated with supracondylar femoral fractures (Parvizi et al., 2008), UKA has been associated with tibial condylar fracture (Thoreau et al., 2022). Although not explicitly investigated in this study, the areas of high overstraining predicted in the tibia, namely, adjacent to the sagittal wall or under the keel of a unicondylar prosthesis, correlate with the observed fracture initiation points (Burger et al., 2022).

To our knowledge, this is the first study to present mechanical results such as bone strain differences in a volume as a histogram. This analysis approach enabled quantitative comparison across the entire bone volume, with metrics that are less sensitive than maximum stress/strain/strain energy density. It also reduces measurement bias associated with only considering regions of interest. Others have analyzed strain shielding in the lab (Correa et al., 2018) or with FE analysis (Pal et al., 2010; Chanda et al., 2015). In the lab, Completo et al. measured cortical strains at toe-off (Completo et al., 2008) and found a 65% difference following TKA, agreeing with the 60%–80% strain shielding predicted on the medial posterior cortex under the tibial tray in our FE models (Figure 4: proximal transverse slice). Their posterior cortex distal findings (20% strain shielding) also agree with our findings. However, they found 10% strain shielding anteromedially, whereas in our model, overstraining was predicted. This difference is likely due to the use of sawbones versus cadaveric tibiae and the boundary conditions where the *in vitro* experiment did not consider muscular or ligamentous contributions. An experimental analysis of strain differences following patellofemoral arthroplasty (Meireles et al., 2010) used strain gauges at locations roughly corresponding to points on the perimeter of the frontal slice

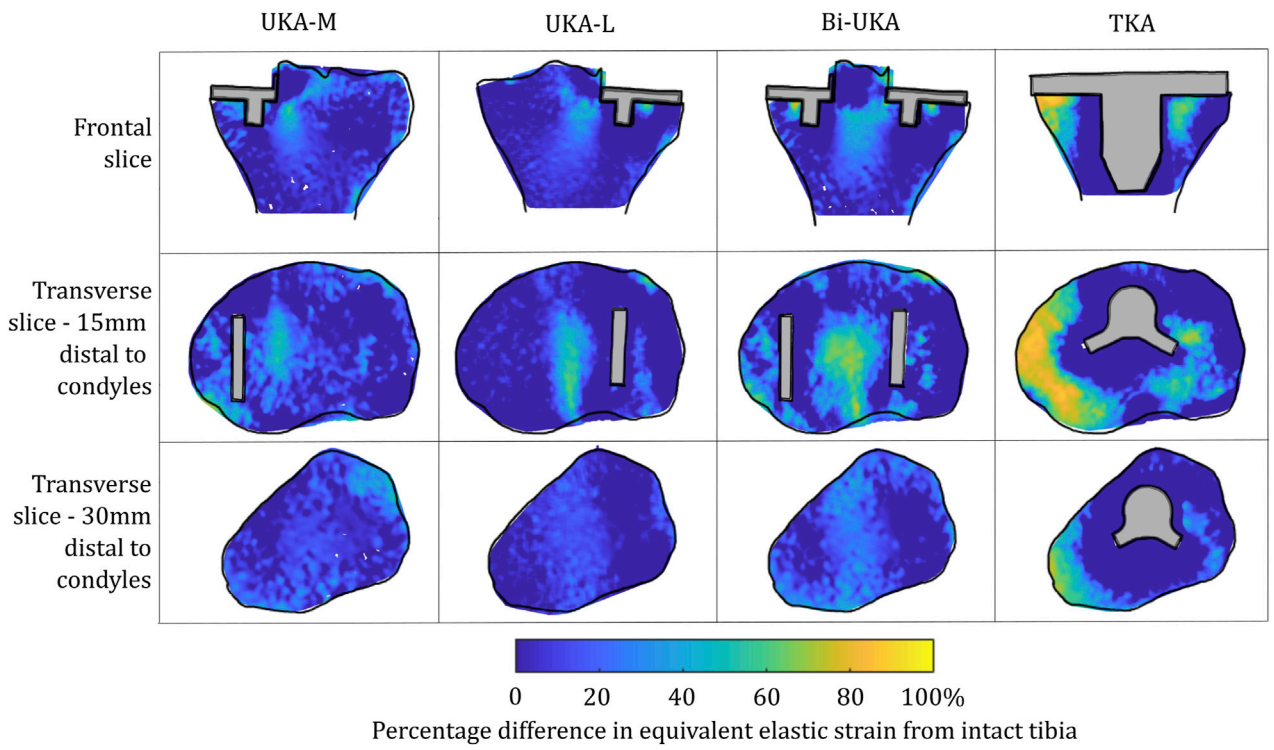

FIGURE 12
Contour plots showing the degree of strain shielding predicted during toe-off in gait, in the implanted male tibia compared to the intact male tibia.

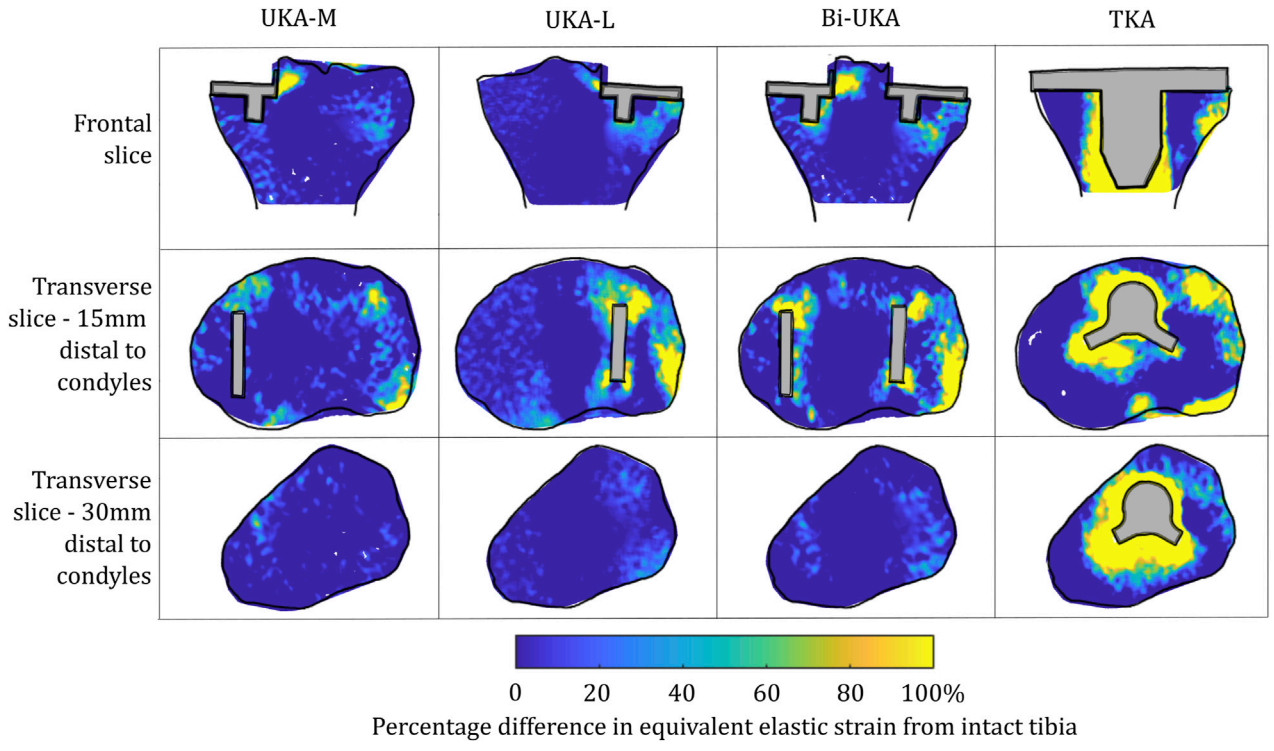

FIGURE 13
Contour plots showing the degree of overstraining predicted during toe-off in gait, in the implanted male tibia compared to the intact male tibia.

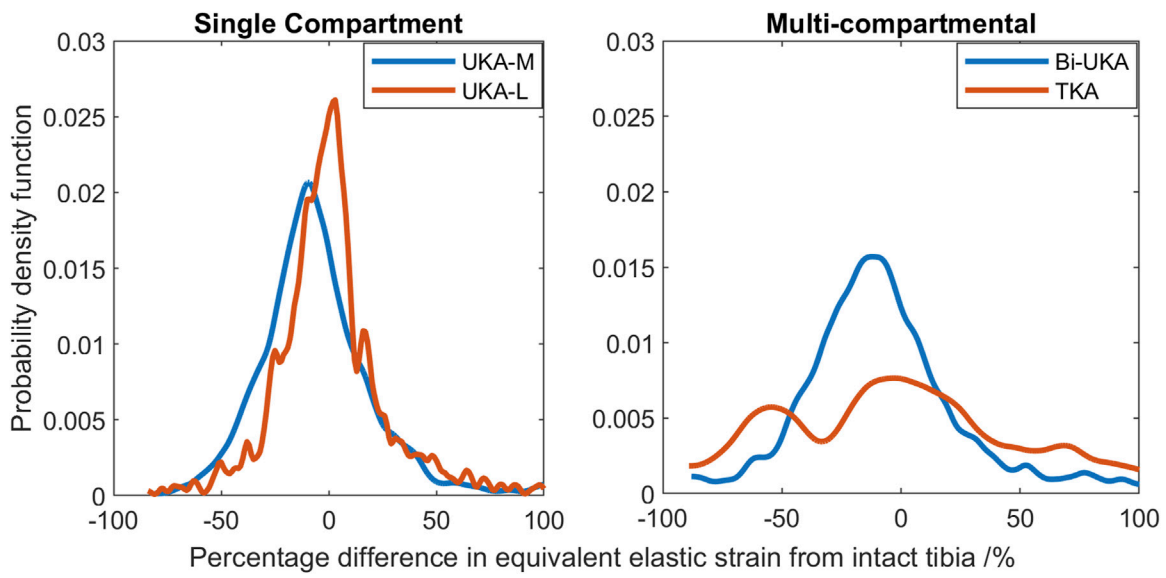

FIGURE 14
Histograms showing the distribution of strain shielding (negative x-axis) and overstraining (positive x-axis) throughout the volume of the implanted proximal male tibia during toe-off in gait.

(Figure 5). They found −43.5% to −67.5% strain shielding and −15.7% to −28.7% in the lateral and medial condyles, respectively. These data agree broadly with our predictions of 40% and 20% laterally/medially, respectively, during sit-to-stand (Supplementary Figure S7). During gait, however, near the medial epicondyle, they measured around 20% overstraining, while our model predicted close to no difference; this may be due to the absence of the medial collateral ligament from their model, which attaches at the medial epicondyle. Our models predicted increased strain shielding in the lateral distal femur in comparison to in the medial condyle. This was likely a combination of the more lateral position of the trochlear component and the increased loading on the lateral trochlea in the native knee because of the quadriceps angle. The phenomenon of remodeling-driven bone loss has been studied both in terms of strain and stress shielding. We chose to study the differences in strains developed pre- and post-implantation since bone remodeling in terms of triggering osteocyte activity has been measured to be controlled by changes in vascular and lacunar pore pressures associated with macroscopic bone strains (Scheiner et al., 2016). Further to this, the strain-related measure of strain energy density is the most commonly used mechanical stimulus when FE-based iterative bone remodeling schemes are employed. Contextualizing our results against FE studies that looked at stress shielding post-TKA, Cawley et al. predicted increased stress at the distal stem of the tibial component and stress shielding just distal to the tray (Cawley et al., 2012). This agrees with the locations within the tibia that we predicted to be overstrained or strain-shielded with TKA. An FE study investigating the stress shielding associated with PFA found some stress shielding posterior to the trochlear implant in PFA, similar to the strain shielding we predicted, but similarly predicted much higher stress shielding in the same area for TKA (van Jonbergen et al., 2012).

This study's strength lies in the number of models studied (nine femoral and five tibial), for female tibia, each with three load cases, and an additional five male tibial models. This is the first study to analyze the effects of all eight types of knee arthroplasty in the same modeling framework and with the bone models with shared open access to enable others to build on our research. There was a limitation in the development of these load cases, however, as they required mixing data from multiple sources for which there are inevitably assumptions. For example, it was assumed that TKA tibiofemoral joint reaction force data are relevant to PKA and CPKA, or that ligament forces estimated for the native knee are transferable to a PKA implanted knee. This may not be the case as differences in gait kinetics and kinematics have been observed; for example, UKA patients have been observed to walk faster than TKA patients (Wiik et al., 2013; Jones et al., 2016; Agarwal et al., 2019), as have patients with Bi-UKA (Garner et al., 2021c) and BCA-M (Garner et al., 2021e); however, the muscle loads were not changed to account for this. While these assumptions did not prevent our data replicating known clinical trends, or from correlating with prior laboratory work, there are likely subtle impacts that may have occurred. For example, in Rasnick et al.'s musculoskeletal models of healthy and TKA subjects climbing stairs, they predicted much lower quadriceps forces during weight acceptance for the TKA subjects, but higher forces produced by the knee flexors, in an apparently compensatory strategy (Rasnick et al., 2016). This may mean that the FE models have under-predicted the degree of strain shielding posterior to the anterior flange of the femoral TKA component and, correspondingly, might have under-predicted the degree of overstraining in the posterior condyles close to the gastrocnemii attachments during stair ascent. This study was also limited as we only looked at relative measures of strain, comparing the pre- and post-implantation strain states, and did not investigate absolute strain values. As such, no direct assessment of fracture risk by the comparison of peak strains to bone yield strains can be made, though the regions of high overstraining identified may correlate with periprosthetic fractures observed clinically. Detailed work using the finite element method to investigate the fracture risk associated with UKA-M has been conducted previously (Sawatari

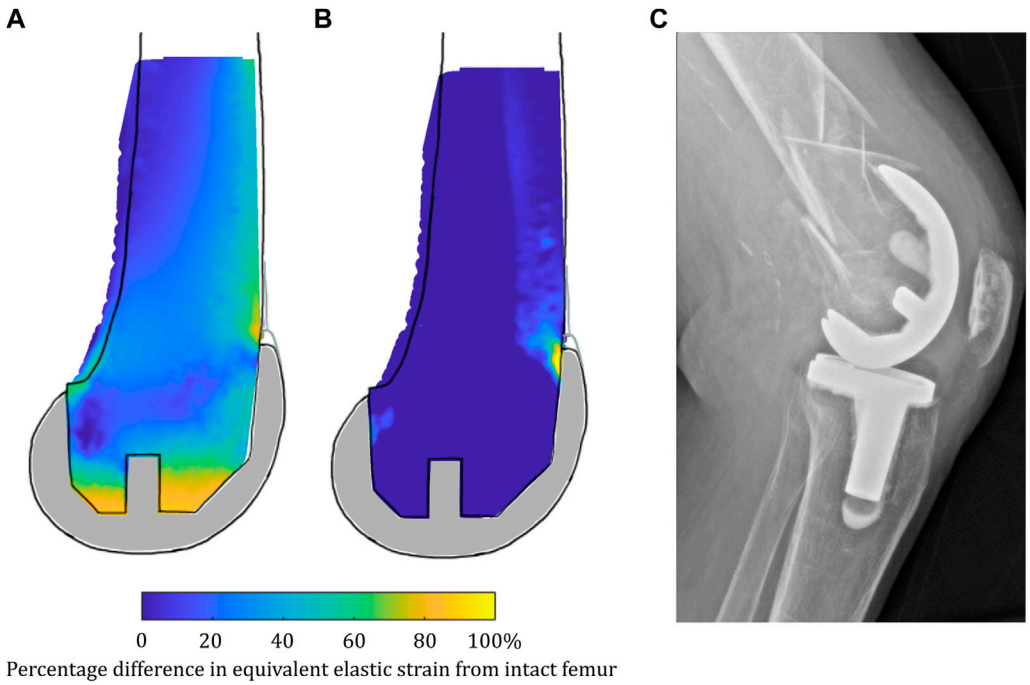

FIGURE 15
(A) Strain shielding during low-flexion gait combined with **(B)** overstraining during higher-flexion stair ascent in a sagittal slice through the lateral femoral condyle when implanted with TKA may contribute to periprosthetic femoral fractures such as that shown in **(C)** a lateral radiograph of a femoral TKA periprosthetic fracture.

et al., 2005; Dai et al., 2018; Pegg et al., 2020). Additionally, previous work by the present authors has investigated the risk of intraoperative tibial eminence avulsion fracture associated with Bi-UKA, finding that relative implant positioning was an important risk factor (Stoddart et al., 2022). There is still room for further work looking at the femoral fracture risk associated with CPKA. Another limitation was that when comparing the results to that of the additional second tibial model, the natural variations in anatomy meant it was difficult to find equivalent slices to compare the models. The male tibia was larger than the female tibia, so using the same distance would not necessarily imply that the equivalent part of bone was being considered. Efforts were made to use equivalent slice locations, for example, by choosing a different depth distal to the tibial plateau for the most proximal transverse slice, approximately halfway down the length of the implant keels. The histogram data were, thus, useful for these comparisons, with the male/female trends matching well. Finally, remodeling algorithms can be used to predict how the mechanical stimulus (strain shielding or change in strain energy density) leads to changes in BMD, as has been demonstrated by others (Pérez et al., 2010; Phillips et al., 2015; Mathai et al., 2022). In this study, we prioritized direct comparison of all the arthroplasty types, for different load cases and different anatomies, over a more detailed remodeling analysis of one or two variants. Our data are, thus, best interpreted as the stimulus for likely remodeling in the early post-operative period, and the resulting data reflect known clinical trends for the early post-operative period well (Petersen et al., 1995; Van Jonbergen et al., 2010; Prince et al., 2019). Only one brand (Zimmer Biomet) of implants was considered, so variations in geometries and materials used in other products may affect the results.

Conclusion

Arthroplasty inherently disturbs load transfer to bone around the knee joint; however, less is better when it comes to bone: PKA and CPKA lead to more normal load transfer than TKA, even when all articulating surfaces are replaced during tricompartmental arthroplasty.

The intact bone models used for this research are provided as open access Supplementary Materials to facilitate future research at other centers. The histogram analyses presented here are recommended as a quantitative way to compare multiple tests without risk of inadvertently excluding key data. The sensitivity of the results to load case highlights the need to consider multiple load cases in any future analyses using these models.

Data availability statement

The datasets presented in this study can be found in online repositories. The names of the repository/repositories and accession number(s) can be found in the article/Supplementary Material.

Ethics statement

The studies involving humans were approved by the National Research Ethics Service, London Fulham, Ref No. 09/H0711/51. This ethical approval was obtained for the development of the

original models from which this research was based. The studies were conducted in accordance with the local legislation and institutional requirements. Written informed consent for participation was not required from the participants or the participants' legal guardians/next of kin in accordance with the national legislation and institutional requirements.

Author contributions

JS: formal analysis, investigation, methodology, and writing–original draft. AG: methodology and writing–review and editing. MT: methodology, validation, and writing–review and editing. AA: supervision and writing–review and editing. JC: conceptualization, funding acquisition, supervision, and writing–review and editing. RvA: conceptualization, project administration, supervision, and writing–review and editing.

Funding

The authors declare that financial support was received for the research, authorship, and/or publication of this article. This work was funded by the Peter Stormonth Darling Charitable Trust. The implant CAD models used in this paper were provided by Zimmer Biomet in kind. The Open Access Fee was paid from the Imperial College Open Access Fund.

Acknowledgments

The authors are grateful to Zimmer Biomet, in particular Michael Malon and Christopher Friend, for supporting their modeling research.

Conflict of interest

JS is now an employee of OSSTEC Ltd., but had no conflicts during the period in which this research was carried out. AA received funding from Smith & Nephew and DePuy Synthes, paid as grants to research accounts of Imperial College London, not related to this study. JC received institutional royalties or licenses and stock or stock options (paid to Imperial College London) from Embody Orthopaedic and payment or honoraria for lectures, presentations, speakers' bureaus, manuscript writing, or educational events from Zimmer Biomet, not related to this study. RV received funding from DePuy Synthes, paid as grants to research accounts of Imperial College London, not related to this study. Author MT was employed by Alloyed Ltd.

The remaining author declares that the research was conducted in the absence of any commercial or financial relationships that could be construed as a potential conflict of interest.

Publisher's note

Supplementary material

The Supplementary Material for this article can be found online at: https://www.frontiersin.org/articles/10.3389/fbioe.2024.1274496/full#supplementary-material

References

Agarwal, A., Miller, S., Hadden, W., Johnston, L., Wang, W., Arnold, G., et al. (2019). Comparison of gait kinematics in total and unicondylar knee replacement surgery. *Ann. R. Coll. Surg. Engl.* 101, 391–398. doi:10.1308/rcsann.2019.0016

Ahmed, A. M., Burke, D. L., and Hyder, A. (1987). Force analysis of the patellar mechanism. *J. Orthop. Res.* 5, 69–85. doi:10.1002/jor.1100050110

Anijs, T., Eemers, S., Minoda, Y., Wolfson, D., Verdonschot, N., and Janssen, D. (2022). Computational tibial bone remodeling over a population after total knee arthroplasty: a comparative study. *J. Biomed. Mat. Res. - Part B Appl. Biomater.* 110, 776–786. doi:10.1002/jbm.b.34957

Arnold, E. M., Ward, S. R., Lieber, R. L., and Delp, S. L. (2010). A model of the lower limb for analysis of human movement. *Ann. Biomed. Eng.* 38, 269–279. doi:10.1007/s10439-009-9852-5

Bergmann, G., Bender, A., Graichen, F., Dymke, J., Rohlmann, A., Trepczynski, A., et al. (2014). Standardized loads acting in knee implants. *PLoS One* 9, e86035. doi:10.1371/journal.pone.0086035

Besier, T. F., Draper, C. E., Gold, G. E., Beaupré, G. S., and Delp, S. L. (2005). Patellofemoral joint contact area increases with knee flexion and weight-bearing. *J. Orthop. Res.* 23, 345–350. doi:10.1016/j.orthres.2004.08.003

Biazzo, A., Manzotti, A., and Confalonieri, N. (2018). Bi-unicompartmental versus total knee arthroplasty: long term results. *Acta Orthop. belg.* 84, 237–244.

Brittain, R., Howard, P., Lawrence, S., Stonadge, J., Wilkinson, M., Wilton, T., et al. (2021). *The national joint registry 18th annual report 2021*. London: National Joint Registry.

Burger, J. A., Jager, T., Dooley, M. S., Zuiderbaan, H. A., Kerkhoffs, G. M. M. J., and Pearle, A. D. (2022). Comparable incidence of periprosthetic tibial fractures in cementless and cemented unicompartmental knee arthroplasty: a systematic review and meta-analysis. *Knee Surg. Sport. Traumatol. Arthrosc.* 30, 852–874. doi:10.1007/s00167-021-06449-3

Cawley, D. T., Kelly, N., Simpkin, A., Shannon, F. J., and McGarry, J. P. (2012). Full and surface tibial cementation in total knee arthroplasty: a biomechanical investigation of stress distribution and remodeling in the tibia. *Clin. Biomech.* 27, 390–397. doi:10.1016/j.clinbiomech.2011.10.011

Chanda, S., Dickinson, A., Gupta, S., and Browne, M. (2015). Full-field *in vitro* measurements and *in silico* predictions of strain shielding in the implanted femur after total hip arthroplasty. *Proc. Inst. Mech. Eng. Part H. J. Eng. Med.* 229, 549–559. doi:10.1177/0954411915591617

Completo, A., Fonseca, F., and Simões, J. A. (2008). Strain shielding in proximal tibia of stemmed knee prosthesis: experimental study. *J. Biomech.* 41, 560–566. doi:10.1016/j.jbiomech.2007.10.006

Correa, T. A., Pal, B., van Arkel, R. J., Vanacore, F., and Amis, A. A. (2018). Reduced tibial strain-shielding with extraosseous total knee arthroplasty revision system. *Med. Eng. Phys.* 0, 22–28. doi:10.1016/j.medengphy.2018.09.006

Dai, X., Fang, J., Jiang, L., Xiong, Y., Zhang, M., and Zhu, S. (2018). How does the inclination of the tibial component matter? A three-dimensional finite element analysis of medial mobile-bearing unicompartmental arthroplasty. *Knee* 25, 434–444. doi:10.1016/j.knee.2018.02.004

Dandridge, O., Garner, A., Amis, A. A., Cobb, J. P., and van Arkel, R. J. (2022). Variation in the patellar tendon moment arm identified with an improved measurement framework. *J. Orthop. Res.* 40, 799–807. doi:10.1002/jor.25124

Deen, J. T., Clay, T. B., Iams, D. A., Horodyski, M., and Parvataneni, H. K. (2018). Proximal tibial resorption in a modern total knee prosthesis. *Arthroplast. Today* 4, 244–248. doi:10.1016/J.ARTD.2017.10.005

Dickinson, A. S. (2014). Activity and loading influence the predicted bone remodeling around cemented hip replacements. *J. Biomech. Eng.* 136, 041008. doi:10.1115/1.4026256

Dudhniwala, A. G., Rath, N. K., Joshy, S., Forster, M. C., and White, S. P. (2016). Early failure with the Journey-Deuce bicompartmental knee arthroplasty. *Eur. J. Orthop. Surg. Traumatol.* 26, 517–521. doi:10.1007/s00590-016-1760-4

Ebraheim, N. A., Kelley, L. H., Liu, X., Thomas, I. S., Steiner, R. B., and Liu, J. (2015). Periprosthetic distal femur fracture after total knee arthroplasty: a systematic review. *Orthop. Surg.* 7 (4), 297–305. doi:10.1111/os.12199

Garner, A. J., Dandridge, O. W., Amis, A. A., Cobb, J. P., and van Arkel, R. J. (2021b). Bi-unicondylar arthroplasty: a biomechanics and clinical outcomes study. *Bone Jt. Res.* 10, 723–733. doi:10.1302/2046-3758.1011.bjr-2021-0151.r1

Garner, A. J., Dandridge, O. W., Amis, A. A., Cobb, J. P., and van Arkel, R. J. (2021c). Bi-unicondylar arthroplasty. *Bone Jt. Res.* 10, 723–733. doi:10.1302/2046-3758.1011.BJR-2021-0151.R1

Garner, A. J., Dandridge, O. W., Amis, A. A., Cobb, J. P., and van Arkel, R. J. (2021d). Partial and combined partial knee arthroplasty: greater anterior-posterior stability than posterior cruciate–retaining total knee arthroplasty. *J. Arthroplasty* 36, 3765–3772.e4. doi:10.1016/j.arth.2021.06.025

Garner, A. J., Dandridge, O. W., van Arkel, R. J., and Cobb, J. P. (2021e). Medial bicompartmental arthroplasty patients display more normal gait and improved satisfaction, compared to matched total knee arthroplasty patients. *Knee Surg. Sport. Traumatol. Arthrosc.* 31, 830–838. doi:10.1007/s00167-021-06773-8

Garner, A. J., Dandridge, O. W., van Arkel, R. J., and Cobb, J. P. (2021f). The compartmental approach to revision of partial knee arthroplasty results in nearer-normal gait and improved patient reported outcomes compared to total knee arthroplasty. *Knee Surg. Sport. Traumatol. Arthrosc.* 31, 1143–1152. doi:10.1007/s00167-021-06691-9

Garner, A., Dandridge, O., Amis, A. A., Cobb, J. P., and van Arkel, R. J. (2021a). The extensor efficiency of unicompartmental, bicompartmental, and total knee arthroplasty. *Bone Jt. Res.* 10, 1–9. doi:10.1302/2046-3758.101.BJR-2020-0248.R1

Garner, A., Van Arkel, R. J., and Cobb, J. (2019). Classification of combined partial knee arthroplasty. *Bone Jt. J.* 101 B, 922–928. doi:10.1302/0301-620X.101B8.BJJ-2019-0125.R1

Goodfellow, J., Hungerford, D. S., and Zindel, M. (1976). Patello-femoral joint mechanics and pathology. 1: functional anatomy of the patello-femoral joint. *J. Bone Jt. Surg.* 58-B, 287–290. doi:10.1302/0301-620x.58b3.956243

Herzog, W., and Read, L. J. (1993). Lines of action and moment arms of the major force-carrying structures crossing the human knee joint. *J. Anat.* 182, 213–230.

Huiskes, R., Weinans, H., Grootenboer, H. J., Dalstra, M., Fudala, B., and Slooff, T. J. (1987). Adaptive bone-remodeling theory applied to prosthetic-design analysis. *J. Biomech.* 20, 1135–1150. doi:10.1016/0021-9290(87)90030-3

Hume, D. R., Navacchia, A., Rullkoetter, P. J., and Shelburne, K. B. (2019). A lower extremity model for muscle-driven simulation of activity using explicit finite element modeling. *J. Biomech.* 84, 153–160. doi:10.1016/j.jbiomech.2018.12.040

Hungerford, D. S., and Barry, M. (1979). Biomechanics of the patellofemoral joint. *Clin. Orthop. Relat. Res.* 144, 9–15. doi:10.1097/00003086-197910000-00003

Jones, G. G., Kotti, M., Wiik, A. V., Collins, R., Brevadt, M. J., Strachan, R. K., et al. (2016). Gait comparison of unicompartmental and total knee arthroplasties with healthy controls. *Bone Jt. J.* 98-B, 16–21. doi:10.1302/0301-620X.98B10.BJJ.2016.0473.R1

Jordan, S. S., DeFrate, L. E., Kyung, W. N., Papannagari, R., Gill, T. J., and Li, G. (2007). The *in vivo* kinematics of the anteromedial and posterolateral bundles of the anterior cruciate ligament during weightbearing knee flexion. *Am. J. Sports Med.* 35, 547–554. doi:10.1177/0363546506295941

Kutzner, I., Trepczynski, A., Heller, M. O., and Bergmann, G. (2013). Knee adduction moment and medial contact force-facts about their correlation during gait. *PLoS One* 8, e81036. doi:10.1371/journal.pone.0081036

Liddle, A. D., Judge, A., Pandit, H., and Murray, D. W. (2014). Adverse outcomes after total and unicompartmental knee replacement in 101330 matched patients: a study of data from the National Joint Registry for England and Wales. *Lancet* 384, 1437–1445. doi:10.1016/S0140-6736(14)60419-0

Mathai, B., Dhara, S., and Gupta, S. (2022). Bone remodelling in implanted proximal femur using topology optimization and parameterized cellular model. *J. Mech. Behav. Biomed. Mat.* 125, 104903. doi:10.1016/j.jmbbm.2021.104903

Meireles, S., Completo, A., António Simões, J., and Flores, P. (2010). Strain shielding in distal femur after patellofemoral arthroplasty under different activity conditions. *J. Biomech.* 43, 477–484. doi:10.1016/j.jbiomech.2009.09.048

Munford, M. J., Stoddart, J. C., Liddle, A. D., Cobb, J. P., and Jeffers, J. R. T. (2022). Total and partial knee arthroplasty implants that maintain native load transfer in the tibia. *Bone Jt. Res.* 11, 91–101. doi:10.1302/2046-3758.112.BJR-2021-0304.R1

Ong, K. L., Day, J. S., Kurtz, S. M., Field, R. E., and Manley, M. T. (2009). Role of surgical position on interface stress and initial bone remodeling stimulus around hip resurfacing arthroplasty. *J. Arthroplasty* 24, 1137–1142. doi:10.1016/j.arth.2008.08.005

Pal, B., Gupta, S., New, A. M. R., and Browne, M. (2010). Strain and micromotion in intact and resurfaced composite femurs: experimental and numerical investigations. *J. Biomech.* 43, 1923–1930. doi:10.1016/j.jbiomech.2010.03.019

Papannagari, R., DeFrate, L. E., Nha, K. W., Moses, J. M., Moussa, M., Gill, T. J., et al. (2007). Function of posterior cruciate ligament bundles during *in vivo* knee flexion. *Am. J. Sports Med.* 35, 1507–1512. doi:10.1177/0363546507300061

Parvizi, J., Jain, N., and Schmidt, A. H. (2008). Periprosthetic knee fractures. *J. Orthop. Trauma* 22, 663–671. doi:10.1097/BOT.0b013e31816ed989

Pegg, E. C., Walter, J., D'Lima, D. D., Fregly, B. J., Gill, H. S., and Murray, D. W. (2020). Minimising tibial fracture after unicompartmental knee replacement: a probabilistic finite element study. *Clin. Biomech.* 73, 46–54. doi:10.1016/j.clinbiomech.2019.12.014

Pérez, M. A., Fornells, P., Doblaré, M., and García-Aznar, J. M. (2010). Comparative analysis of bone remodelling models with respect to computerised tomography-based finite element models of bone. *Comput. Methods Biomech. Biomed. Engin.* 13, 71–80. doi:10.1080/10255840903045029

Petersen, M. M., Olsen, C., Lauritzen, J. B., and Lund, B. (1995). Changes in bone mineral density of the distal femur following uncemented total knee arthroplasty. *J. Arthroplasty* 10, 7–11. doi:10.1016/S0883-5403(05)80094-4

Phillips, A. T. M., Villette, C. C., and Modenese, L. (2015). Femoral bone mesoscale structural architecture prediction using musculoskeletal and finite element modelling. *Int. Biomech.* 2, 43–61. doi:10.1080/23335432.2015.1017609

Prince, J. M., Bernatz, J. T., Binkley, N., Abdel, M. P., and Anderson, P. A. (2019). Changes in femoral bone mineral density after total knee arthroplasty: a systematic review and meta-analysis. *Arch. Osteoporos.* 14, 23. doi:10.1007/s11657-019-0572-7

Quilez, M. P., Seral, B., and Pérez, M. A. (2017). Biomechanical evaluation of tibial bone adaptation after revision total knee arthroplasty: a comparison of different implant systems. *PLoS One* 12, e0184361. doi:10.1371/journal.pone.0184361

Rasnick, R., Standifird, T., Reinbolt, J. A., Cates, H. E., and Zhang, S. (2016). Knee joint loads and surrounding muscle forces during stair ascent in patients with total knee replacement. *PLoS One* 11, e0156282. doi:10.1371/journal.pone.0156282

Safiri, S., Kolahi, A.-A., Smith, E., Hill, C., Bettampadi, D., Mansournia, M. A., et al. (2020). Global, regional and national burden of osteoarthritis 1990-2017: a systematic analysis of the Global Burden of Disease Study 2017. *Ann. Rheum. Dis.* 79, 819–828. doi:10.1136/annrheumdis-2019-216515

Sawatari, T., Tsumura, H., Iesaka, K., Furushiro, Y., and Torisu, T. (2005). Three-dimensional finite element analysis of unicompartmental knee arthroplasty–the influence of tibial component inclination. *J. Orthop. Res.* 23, 549–554. doi:10.1016/j.orthres.2004.06.007

Scheiner, S., Pivonka, P., and Hellmich, C. (2016). Poromicromechanics reveals that physiological bone strains induce osteocyte-stimulating lacunar pressure. *Biomech. Model. Mechanobiol.* 15, 9–28. doi:10.1007/s10237-015-0704-y

Scott, C. E. H., MacDonald, D. J., and Howie, C. R. (2019). 'Worse than death' and waiting for a joint arthroplasty. *Bone Jt. J.* 101, 941–950. doi:10.1302/0301-620X.101B8.BJJ-2019-0116.R1

Soininvaara, T. A., Harju, K. A. L., Miettinen, H. J. A., and Kröger, H. P. J. (2013). Periprosthetic bone mineral density changes after unicondylar knee arthroplasty. *Knee* 20, 120–127. doi:10.1016/j.knee.2012.10.004

Stoddart, J. C., Dandridge, O., Garner, A., Cobb, J., and van Arkel, R. J. (2021). The compartmental distribution of knee osteoarthritis – a systematic review and meta-analysis. *Osteoarthr. Cartil.* 29, 445–455. doi:10.1016/j.joca.2020.10.011

Stoddart, J. C., Garner, A., Tuncer, M., Cobb, J. P., and van Arkel, R. J. (2022). The risk of tibial eminence avulsion fracture with bi-unicondylar knee arthroplasty: a finite element analysis. *Bone Jt. Res.* 11, 575–584. doi:10.1302/2046-3758.118.BJR-2021-0533.R1

Thoreau, L., Morcillo Marfil, D., and Thienpont, E. (2022). Periprosthetic fractures after medial unicompartmental knee arthroplasty: a narrative review. *Arch. Orthop. Trauma Surg.* 142, 2039–2048. doi:10.1007/s00402-021-04063-z

Tuncer, M., Cobb, J. P., Hansen, U. N., and Amis, A. A. (2013). Validation of multiple subject-specific finite element models of unicompartmental knee replacement. *Med. Eng. Phys.* 35, 1457–1464. doi:10.1016/j.medengphy.2013.03.020

Turner, A. W. L., Gillies, R. M., Sekel, R., Morris, P., Bruce, W., and Walsh, W. R. (2005). Computational bone remodelling simulations and comparisons with DEXA results. *J. Orthop. Res.* 23, 705–712. doi:10.1016/j.orthres.2005.02.002

Van Arkel, R. J., Modenese, L., Phillips, A. T. M., and Jeffers, J. R. T. (2013). Hip abduction can prevent posterior edge loading of hip replacements. *J. Orthop. Res.* 31, 1172–1179. doi:10.1002/jor.22364

van Jonbergen, H. P. W., Innocenti, B., Gervasi, G. L., Labey, L., and Verdonschot, N. (2012). Differences in the stress distribution in the distal femur between patellofemoral joint replacement and total knee replacement: a finite element study. *J. Orthop. Surg. Res.* 7, 28. doi:10.1186/1749-799X-7-28

Van Jonbergen, H. P. W., Koster, K., Labey, L., Innocenti, B., and Van Kampen, A. (2010). Distal femoral bone mineral density decreases following patellofemoral arthroplasty: 1-year follow-up study of 14 patients. *BMC Musculoskelet. Disord.* 11, 74. doi:10.1186/1471-2474-11-74

van Lenthe, G. H., de Waal Malefijt, M. C., and Huiskes, R. (1997). Stress shielding after total knee replacement may cause bone resorption in the distal femur. *J. Bone Jt. Surg.* 79 (1), 117–122. doi:10.1302/0301-620X.79B1.6808

Wada, K., Price, A., Gromov, K., Lustig, S., and Troelsen, A. (2020). Clinical outcome of bi-unicompartmental knee arthroplasty for both medial and lateral femorotibial arthritis: a systematic review—is there proof of concept? *Arch. Orthop. Trauma Surg.* 140, 1503–1513. doi:10.1007/s00402-020-03492-6

Wang, H., Foster, J., Franksen, N., Estes, J., and Rolston, L. (2018). Gait analysis of patients with an off-the-shelf total knee replacement versus customized bi-compartmental knee replacement. *Int. Orthop.* 42, 805–810. doi:10.1007/s00264-017-3622-z

Wiik, A. V., Manning, V., Strachan, R. K., Amis, A. A., and Cobb, J. P. (2013). Unicompartmental knee arthroplasty enables near normal gait at higher speeds, unlike total knee arthroplasty. *J. Arthroplasty* 28, 176–178. doi:10.1016/j.arth.2013.07.036

Yoon, C., Chang, M. J., Chang, C. B., Song, M. K., Shin, J. H., and Kang, S.-B. (2018). Medial tibial periprosthetic bone resorption and its effect on clinical outcomes after total knee arthroplasty: cobalt-chromium vs titanium implants. *J. Arthroplasty* 33, 2835–2842. doi:10.1016/J.ARTH.2018.04.025

Zhang, M., Gregory, T., Hansen, U., and Cheng, C. K. (2020). Effect of stress-shielding-induced bone resorption on glenoid loosening in reverse total shoulder arthroplasty. *J. Orthop. Res.* 38, 1566–1574. doi:10.1002/jor.24711

frontiers | Frontiers in Bioengineering and Biotechnology

TYPE Original Research
PUBLISHED 18 March 2024
DOI 10.3389/fbioe.2024.1319602

OPEN ACCESS

EDITED BY
João Manuel R. S. Tavares,
University of Porto, Portugal

REVIEWED BY
Jay Tivedi,
Rhode Island Hospital, United States
Daniel Schmitt,
Duke University, United States

*CORRESPONDENCE
Hongsheng Zhan,
zhanhongsheng@shutcm.edu.cn

RECEIVED 11 October 2023
ACCEPTED 01 March 2024
PUBLISHED 18 March 2024

CITATION
Wang Z, Lu J, Ge H, Li Z, Zhang M, Pan F, Wang R, Jin H, Yang G, Shen Z, Du G and Zhan H (2024), Morphology and transverse alignment of the patella have no effect on knee gait characteristics in healthy Chinese adults over the age of 40 years.
Front. Bioeng. Biotechnol. 12:1319602.
doi: 10.3389/fbioe.2024.1319602

Morphology and transverse alignment of the patella have no effect on knee gait characteristics in healthy Chinese adults over the age of 40 years

Zhengming Wang[1,2], Jiehang Lu[1,2], Haiya Ge[1,2], Zhengyan Li[1,2], Min Zhang[1,2], Fuwei Pan[1,2,3], Rui Wang[4], Hengkai Jin[5], Guangyue Yang[1], Zhibi Shen[1,2], Guoqing Du[1] and Hongsheng Zhan[1,2]*

[1]Shi's Center of Orthopedics and Traumatology, Shuguang Hospital Affiliated to Shanghai University of Traditional Chinese Medicine, Shanghai, China, [2]Institute of Traumatology and Orthopedics, Shanghai Academy of Traditional Chinese Medicine, Shanghai, China, [3]Department of Massage, Third Affiliated Hospital of Henan University of Chinese Medicine, Zhengzhou, China, [4]Shanghai University of Traditional Chinese Medicine, Shanghai, China, [5]The First Affiliated Hospital of Zhejiang Chinese Medical University (Zhejiang Provincial Hospital of Chinese Medicine), Hangzhou, Zhejiang, China

Background: The influence of patella morphology and horizontal alignment on knee joint kinematics and kinetics remains uncertain. This study aimed to assess patella morphology and transverse alignment in relation to knee kinetics and kinematics in individuals without knee conditions. A secondary objective was to investigate the impact of femur and tibia alignment and shape on knee gait within this population.

Patients and methods: We conducted a prospective collection of data, including full-leg anteroposterior and skyline X-ray views and three-dimensional gait data, from a cohort comprising 54 healthy individuals aged 40 years and older. Our study involved correlation and logistic regression analyses to examine the influence of patella, femur, and tibia morphology and alignment on knee gait.

Results: The patellar tilt angle or the patella index did not show any significant relationships with different aspects of gait in the knee joint, such as velocity, angle, or moment ($p > 0.05$, respectively). Using multivariate logistic regression analysis, we found that the tibiofemoral angle and the Q angle both had a significant effect on the adduction angle (OR = 1.330, 95%CI 1.033–1.711, $p = 0.027$; OR = 0.475, 95%*CI* 0.285–0.792, $p = 0.04$; respectively). The primary variable influencing the knee adduction moment was the tibiofemoral angle (OR = 1.526, 95% CI 1.125–2.069, $p = 0.007$).

Abbreviations: KOA, knee osteoarthritis; PROMs, patient-reported outcome measures; FTA, tibiofemoral angle; KL, Kellgren and Lawrence; PTVA, proximal tibia varus angle; DFVA, distal femoral valgus angle; SA, sulcus angle; PTA, patellar tilt angle; PI, patella index; TD, trochlear depth; KAM, knee adduction moment; OR, odds ratios; CI, confidence level; BMI, body mass index; PFJ, patellofemoral joint.

Conclusion: In healthy Chinese individuals aged over 40, patella morphology and transverse alignment do not impact knee gait. However, the femoral-tibial angle has a big impact on the knee adduction moment.

KEYWORDS

morphology, alignment, patella, femur, tibia, gait

1 Introduction

Anatomically, the knee joint, being the largest and most intricate joint in the body, comprises the femur, tibia, patella, and surrounding soft tissues, all working in concert to ensure knee stability within physiological limits (Zhao et al., 2021). Under normal physiological conditions, the knee joint capably fulfills its essential biomechanical functions. However, deviations in bone or soft tissue anatomy can lead to undesirable mechanical load distribution and persistent knee instability (Campos et al., 2022), ultimately paving the way for the development of knee osteoarthritis (KOA).

With the global population aging, the prevalence of KOA is estimated to be 22.9% in individuals aged 40 years and older, making it one of the leading contributors to chronic disability (Cui et al., 2020). Recognized risk factors encompass gender, genetic predisposition, obesity, aberrant gait biomechanics, joint laxity, and meniscal injuries (Heidari, 2011). Among these factors, the role of biomechanics in KOA development has consistently come to the forefront and been substantiated (Lee, 2014; Aljehani et al., 2022; Spierings et al., 2023).

Knee joint kinematics results from the intricate roto-translation movements characteristic of the tibiofemoral and patellofemoral articulations (Vasso et al., 2017). The patella functions as an articulating fulcrum, enhancing the moment arm of the extensor mechanism. Additionally, it enhances quadriceps muscle efficiency by elevating the extensor mechanisms away from the axis of rotation of the knee, thus increasing torque (Wheatley et al., 2021). Moreover, it assists in reducing frictional wear that could otherwise damage the extensor mechanism tendon. When the knee is fully flexed, the patella serves as a connection between the quadriceps and the patellar ligament. Daily activities subject the patellofemoral joint to compressive forces of 3.3 times body weight during stair climbing and 7.6 times body weight during squatting (Reilly and Martens, 1972). From 45° flexion to full extension, the patella articulates with the femur, displacing the extensor mechanism from the knee's mechanical axis, thereby enhancing torque generation for terminal extension (LeBrun et al., 2012). Gait patterns vary based on the position and orientation of the patella relative to the trochlear groove and the alignment of the tibia in relation to the femur. Within the knee joint complex, the patella, the largest sesamoid bone in the body, plays a crucial role in knee biomechanics (Suzuki et al., 2013). Early intervention is believed to facilitate timely stabilization and restoration of knee biomechanics, thereby reducing the risk of concurrent knee pathology (Bornes et al., 2014). Consequently, a comprehensive investigation into the factors influencing knee joint biomechanics, early identification of biomechanical irregularities, and prompt intervention become crucial components in slowing the progression of KOA.

Currently, the assessment of KOA involves patient-reported outcome measures (PROMs) as well as various imaging techniques, including X-ray, computed tomography, magnetic resonance imaging, and gait analysis. While PROMs provide clinical insights, their subjective nature, potential ceiling effects, and reliance on pain rather than daily life activities limit their clinical value (Bolink et al., 2015). Imaging evaluation, on the other hand, is constrained by factors such as cost, time, accessibility, and the static nature of images (Vomer et al., 2023). Fortunately, recent advancements in three-dimensional motion analysis have enabled objective, quantitative, reproducible, and standardized evaluation of knee joint kinematics (Piriyaprasarth and Morris, 2007). Prior studies (Clark et al., 2016; Hösl et al., 2018; Murakami et al., 2018) have already established the influence of patellar sagittal and coronal alignment, as well as the mechanical axis, on knee joint kinematics.

As such, this study's primary focus is to evaluate how patellar morphology and transverse alignment impact the kinetics and kinematics of the knee joint in individuals without pre-existing knee conditions. The secondary objective involves assessing the influence of femoral and tibial morphology, femoral-tibial angle (FTA), and Q angle on knee kinetics and kinematics within this specific population.

2 Materials and methods

2.1 Participants

This study received approval from the Ethics Committee, and written informed consent was obtained from all participants at our institution before their inclusion. A total of 54 eligible subjects (20 males and 34 females) were recruited from our hospital between December 2020 and December 2022. Exclusion criteria were as follows: 1) participants with a diagnosis of KOA (Zhang et al., 2010); 2) individuals younger than 40 years of age; 3) reported knee pain within the preceding year; 4) a history of lower limb injuries or knee surgery; 5) presence of tumors or tuberculosis; 6) any diseases or lower limb deformities that might impact gait patterns; 7) a Kellgren-Lawrence (K-L) radiographic disease severity scale score of grade II (Kellgren and Lawrence, 1957) or greater; 8) untreated medical conditions.

2.2 X-ray evaluation

Radiographs (AXIOM Aristos VX, Siemens, Germany) of the random knees of the participants were analyzed. Each subject's knee was imaged from two distinct perspectives: a weight-bearing full-leg anteroposterior view and a skyline view. The KL radiographic

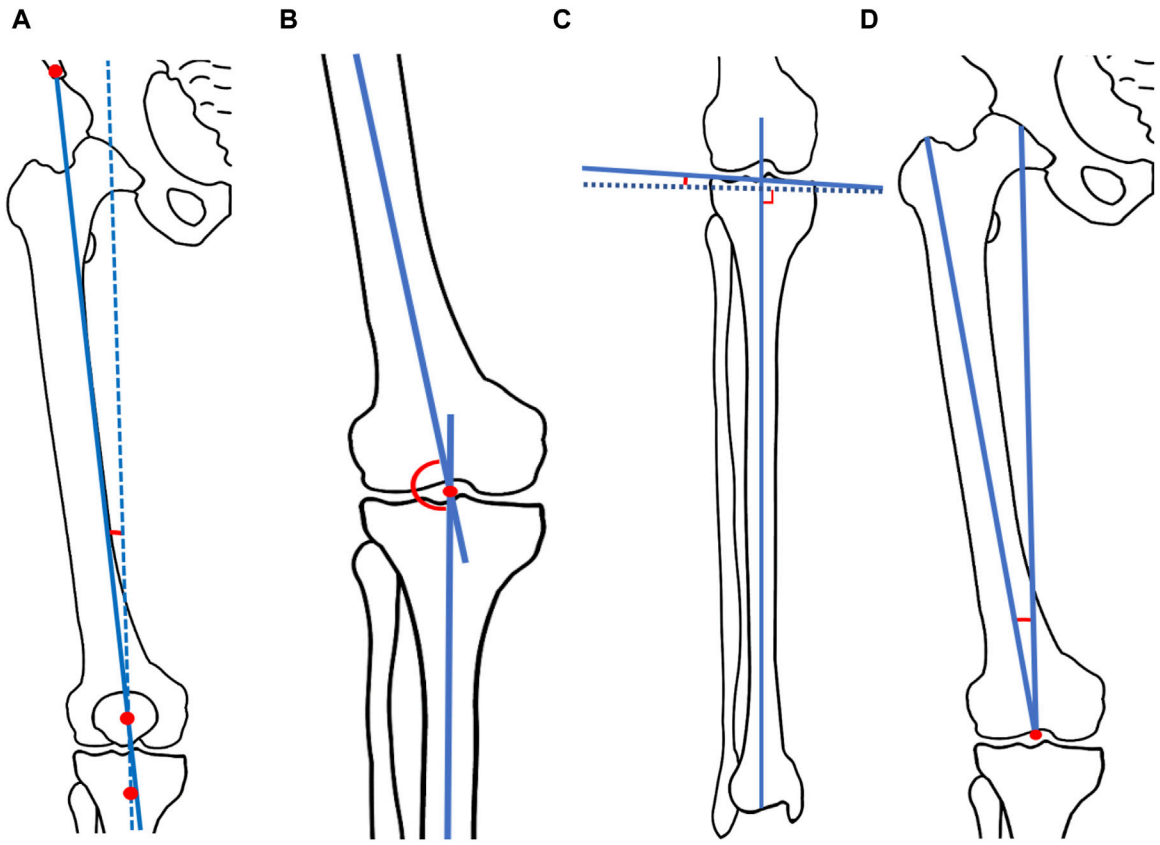

FIGURE 1
Schema of measured radiograph. **(A)** Q angle. The Q-angle represents the angle between two lines: the first drawn from the anterior-superior iliac spine to the mid-patella, and the second drawn from the mid-patella to the tibial tubercle. **(B)** Femoral-tibial angle (FTA). The FTA is defined as the lateral angle between the anatomical axes of the femur and tibia. **(C)** Proximal tibia varus angle (PTVA). The PTVA measures the angle between the tibial articular margins and a line perpendicular to the tibial mechanical axis. **(D)** Distal femoral valgus angle (DFVA). The DFVA represents the valgus angle between the femoral mechanical axis and the distal femoral anatomical axis.

grading system was employed, aligning with the criteria established by Farrokhi et al. (Farrokhi et al., 2015). Specifically, the KL grades were defined as follows: Grade 0 indicated the absence of osteophytes; Grade I denoted the presence of osteophytes approximately 1 mm in size, with an uncertain classification; Grade II signalled the presence of minimal osteophytes, along with potential joint space narrowing, cysts, and sclerosis; Grade III indicated moderate or definite osteophytes and/or moderate joint space narrowing; and Grade IV signified the presence of large osteophytes and/or severe joint space narrowing.

Alignment and bony morphology were measured using established methods from prior studies (Chhabra et al., 2011; Stefanik et al., 2013). In the anteroposterior view, we assessed several angles (Dai et al., 2019; Kokubu et al., 2022; Hao et al., 2023; Milovanović et al., 2023), including the quadriceps angle (Q-angle), FTA, the proximal tibia varus angle (PTVA), and the distal femoral valgus angle (DFVA) (Figures 1A–D). The Q-angle represents the angle between two lines: the first drawn from the anterior-superior iliac spine to the mid-patella, and the second drawn from the mid-patella to the tibial tubercle. The FTA is defined as the lateral angle between the anatomical axes of the femur and tibia. The PTVA measures the angle between the tibial articular margins and a line perpendicular to the tibial mechanical axis. The DFVA represents the valgus angle between the femoral mechanical axis and the distal femoral anatomical axis.

In the skyline view, measurements were taken for the sulcus angle (SA) (Powers, 2000), patellar tilt angle (PTA) (Sasaki and Yagi, 1986), patella index (PI) (Cross and Waldrop, 1975), and trochlear depth (TD) (Damgacı et al., 2020) Figures 2A–D). The SA was defined by lines connecting the highest points of the medial and lateral condyles and the lowest point of the intercondylar sulcus. The PTA was defined as the angle subtended by the equatorial line of the patella and the line connecting the anterior limits of the femoral condyles. The PI, a guide to the understanding and diagnosis of patellofemoral instability, was calculated by the following method: two perpendicular lines were drawn, one through the maximum width and one through the maximum height of the patella, with their intersection point labelled "X." The points where "X" met the lateral or medial cortex were labeled as "A" or "B." PI was calculated as the ratio of (XB + AX) to (XB-AX) (Cross and Waldrop, 1975). TD represented the perpendicular distance from the line connecting the most anterior parts of the medial and lateral femoral trochlear facets to the deepest part of the trochlear groove (Damgacı et al., 2020). These radiographic measurements were performed by two experienced orthopedists using ImageJ software (Version 1.52, National Institutes of Health, United States) to derive the average values for continuous variables.

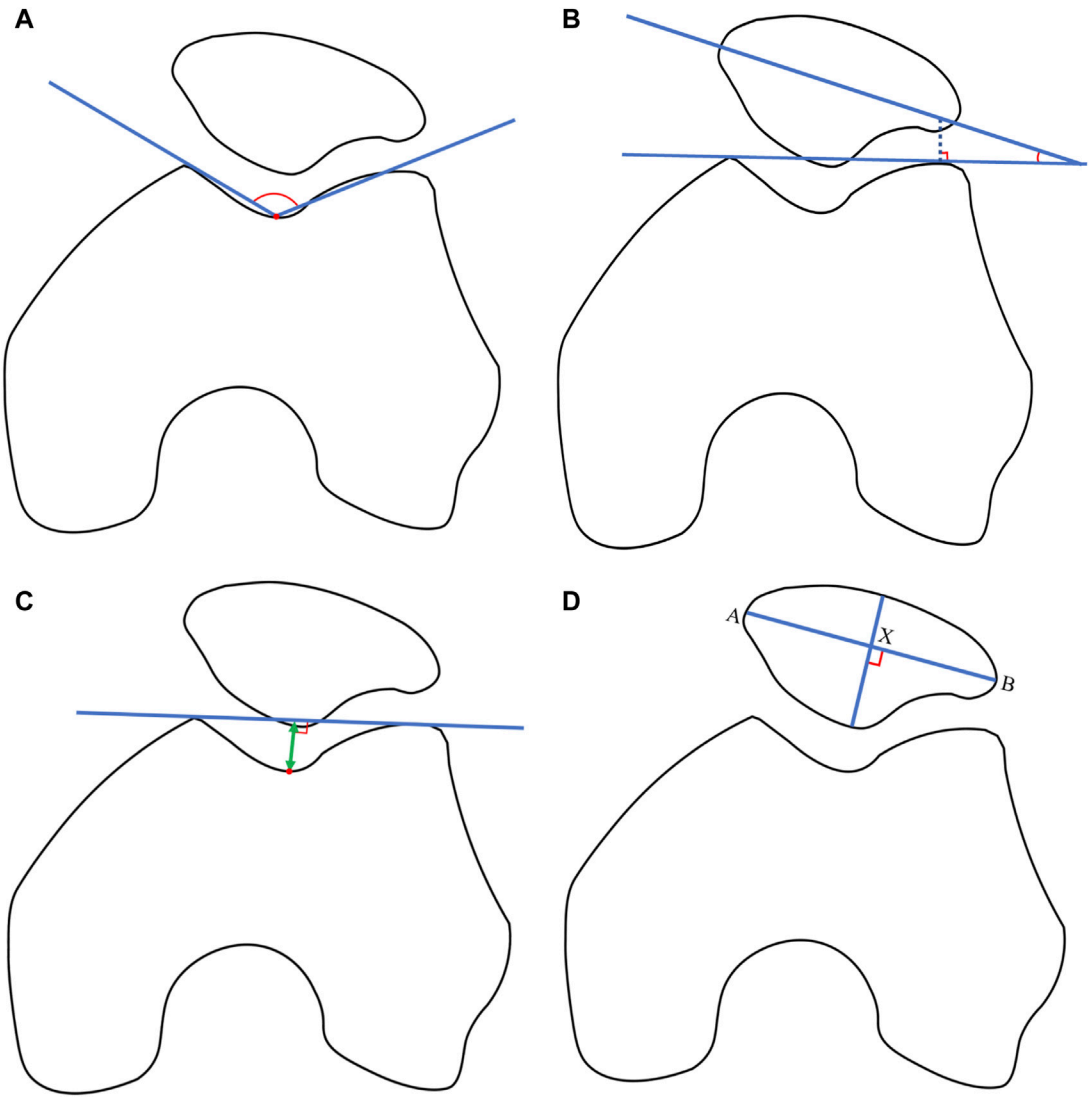

FIGURE 2
(A) Sulcus angle (SA). The SA was defined by lines connecting the highest points of the medial and lateral condyles and the lowest point of the intercondylar sulcus. **(B)** Patellar tilt angle (PTA). The PTA was defined as the angle subtended by the equatorial line of the patella and the line connecting the anterior limits of the femoral condyles. **(C)** Patella index (PI). The PI is were drawn by the two perpendicular lines, one through the maximum width and one through the maximum height of the patella, with their intersection point labelled "X." The points where "X" met the lateral or medial cortex were labeled as "A" or "B." PI was calculated as the ratio of (XB + AX) to (XB-AX). **(D)** Trochlear depth (TD). TD represented the perpendicular distance from the line connecting the most anterior parts of the medial and lateral femoral trochlear facets to the deepest part of the trochlear groove.

2.3 Gait analysis

Before each test, the instrument underwent calibration. The gait test followed the methodology detailed in our previous study (Zhang et al., 2022), offering a more comprehensive procedural explanation. In general, participants walked along an 8.6-meter-long and 6.5-meter-wide path, covered with timber and wooden flooring, at their self-selected pace. Motion data from retro-reflective markers were captured using the VICON motion capture and analysis system (VICON, Oxford, United Kingdom), operating at a sampling rate of 100 Hz and consisting of 16 cameras.

In line with a previous study (Riazati et al., 2022), quality assessments were performed using Visual 3D (Version 6.01.16, C-motion, United States) to eliminate excessively aberrant data, a crucial step in calculating kinematic and kinetic measurements (Jones et al., 2013). Both kinematic and analog data underwent filtration using a Butterworth 4th-order digital filter with cut-off frequencies set at 6 Hz for kinematics and 25 Hz for analog data. Gait speed was determined by dividing the distance walked by the time taken. Negative values are indicative of a particular direction. The external knee adduction moment (KAM) was normalized to each participant's body mass. The initial KAM peak, representing the highest value within the first half of the stance phase, was assessed. Additionally, external knee moments for flexion, extension, external rotation, and internal rotation were evaluated.

TABLE 1 Participant characteristics and gait indicators outcomes.

Variables	*N* = 54	Range	Variables	*N* = 54	Range
Age (years)	54.3 ± 7.8	40.0 to 70.0	Speed (m/s)	1.2 ± 0.1	0.9 to 1.4
BMI (kg/m^2)	22.8 ± 3.1	17.2 to 29.9	Angle of the knee (°)		
Male (*n*/%)	20/37.0%		Flexion	68.3 ± 4.8	59.0 to 77.7
Left (*n*/%)	30/55.6%		Extension	3.3 ± 3.7	−3.2 to 12.3
Alignment (°)			Abduction	9.8 ± 5.5	−0.4 to 25.7
PTA	2.0 (3.0)	−6.9 to 7.0	Adduction	−1.7 (4.6)	−13.0 to 5.0
Q angle	12.9 ± 4.0	6.0 to 22.0	External rotation	−11.9 ± 4.9	−24.0 to −1.7
FTA	173.5 (4.3)	168.0 to 179.0	Internal rotation	3.8 ± 4.6	−8.4 to 14.4
Morphology			Moment of the knee (N·m/kg)		
PI	6.8 (4.0)	2.9 to 161.0	Flexion	0.6 ± 0.2	0.2 to 1.3
SA (°)	133.0 (6.0)	120.0 to 150.0	Extension	−0.3 ± 0.1	−0.6 to −0.2
TD (mm)	4.8 (1.0)	3.8 to 8.8	Adduction	0.4 ± 0.1	0.2 to 0.7
PTVA (°)	3.0 (3.0)	0 to 7.0	External rotation	−0.1 ± 0	−0.2 to 0
DFVA (°)	6.0 (1.0)	5.0 to 8.0	Internal rotation	0.2 ± 0	0 to 0.3

BMI, body mass index; PTA, patellar tilt angle; FTA, femoral-tibial angle; PI, patella index; SA, sulcus angle; TD, trochlear depth; PTVA, proximal tibia varus angle; DFVA, distal femoral valgus angle.

2.4 Statistical analysis

All statistical analyses were performed using IBM SPSS Statistics version 16.0 (IBM, Armonk, NY, United States). The normality of continuous variables was assessed using Shapiro-Wilk tests. Normally distributed data were presented as mean ± standard deviation, while non-normally distributed data were summarized as median and interquartile range. Categorical data were expressed as counts (percentages). Spearman correlation analysis was employed to investigate the relationships between bone morphology, transverse alignment, and knee kinematic and kinetic outcomes. Generally, correlation coefficients less than 0.30 were considered indicative of weak correlations; those in the range of 0.30–0.50 were deemed moderate; and values exceeding 0.50 indicated strong correlations (McCaffrey et al., 2016). Variables with a *p*-value less than 0.1 in the Spearman correlation analysis were included in the regression model. For both univariate and multivariate logistic regression analyses, odds ratios (OR) were calculated after discretizing continuous variables based on their median values. The significance level was set at 0.05, and confidence intervals were reported at the 95% confidence level (CI).

3 Results

3.1 Participant characteristics

Table 1 presents the demographics and clinical characteristics of all study participants. The age of the participants ranged from 40 to 70, with a mean age of 54.3 ± 7.8 years. The body mass index (BMI) ranged from 17.2 to 29.9, with a mean BMI of 22.8 ± 3.1 kg/m^2. The study included 20 male participants, and the majority had left knee joint involvement. Regarding bone alignment, the values for PTA, Q angle, and FTA were recorded as 2.0 (3.0), 12.9 ± 4.0, and 173.5 (4.3), respectively. In terms of knee joint bone morphology, the measurements for SA, patella index PI, TD, proximal PTVA, and DFVA were 133.0 (6.0), 6.8 (4.0), 4.8 (1.0), 3.0 (3.0), and 6.0 (1.0), respectively.

3.2 Kinematic and kinetic outcomes of knee motion

The walking speed of the participants ranged from 0.9 to 1.4 m/s, with an average speed of 1.2 ± 0.1 m/s. During locomotion, knee joint kinematics were as follows: flexion angle, 68.3 ± 4.8 degrees; extension angle, 3.3 ± 3.7 degrees; adduction angle, 1.7 (4.6) degrees; abduction angle, 9.8 ± 5.5 degrees; internal rotation angle, 3.8 ± 4.6 degrees; external rotation angle, 11.9 ± 4.9 degrees. Kinetic information during movement included the first external KAM peak, which was 0.4 ± 0.1 N m/kg. The external knee flexion and extension moments were 0.6 ± 0.2 and 0.3 ± 0.1 N m/kg, respectively. Additionally, the external knee external and internal rotation moments were 0.1 ± 0 and 0.2 ± 0, respectively. Detailed kinematic and kinetic outcomes are provided in Table 1.

3.3 Correlation between alignment or morphology and knee kinematics or kinetics

Correlation analysis revealed no significant relationship between speed and the alignment or morphological characteristics assessed in this study ($p > 0.05$, Table 2). The adduction angle showed moderate to strong correlations with age, gender, Q angle, FTA, and PTVA

TABLE 2 Correlation of kinematics and kinetics with age, BMI, sex, PTA, Q angle, and FTA.

Variables	Age		BMI		Sex		PTA		Q angle		FTA	
	r	*P*	r	*P*	r	*P*	r	*P*	r	*P*	r	*P*
Speed	0.155	0.264	−0.121	0.385	−0.091	0.513	−0.157	0.256	0.040	0.774	0.211	0.126
Angle of the knee												
Flexion angle	0.106	0.445	0.208	0.131	0.128	0.357	0.017	0.905	−0.045	0.745	−0.063	0.653
Extension angle	0.238	0.083	−0.019	0.894	−0.007	0.958	−0.105	0.451	−0.099	0.475	0.020	0.883
Adduction angle	−0.364	**0.007**	−0.201	0.145	0.539	**<0.001**	−0.062	0.654	0.338	**0.012**	−0.614	**<0.001**
Abduction angle	−0.172	0.212	−0.278	**0.042**	0.231	0.092	−0.185	0.181	0.242	0.078	−0.388	**0.004**
External rotation	−0.245	0.074	−0.235	0.087	0.128	0.357	−0.052	0.708	0.231	0.089	−0.143	0.304
Internal rotation	−0.299	**0.028**	0.065	0.643	0.106	0.446	0.196	0.155	0.160	0.247	0.167	0.277
Moment of the knee												
Flexion moment	−0.016	0.909	−0.105	0.452	−0.015	0.916	0.051	0.714	−0.006	0.966	−0.055	0.619
Extension moment	−0.053	0.704	−0.009	0.948	0.295	**0.030**	−0.012	0.931	0.036	0.798	−0.226	0.100
Adduction moment[#]	0.201	0.145	−0.029	0.835	−0.303	**0.026**	0.009	0.946	−0.063	0.653	0.563	**<0.001**
External rotation moment	0.212	0.125	0.137	0.324	0.047	0.737	−0.028	0.839	0.033	0.814	−0.138	0.321
Internal rotation moment	0.197	0.154	−0.058	0.678	0.108	0.436	−0.055	0.694	−0.149	0.282	0.039	0.780

BMI, body mass index; PTA, patellar tilt angle; FTA, femoral-tibial angle. The boldface indicates p value < 0.05.

TABLE 3 Correlation of kinematics or kinetics with sulcus angle, patella index, trochlear depth, PTVA, and DFVA.

Variables	Sulcus angle		Patella index		Trochlear depth		PTVA		DFVA	
	r	*P*	r	*P*	r	*P*	r	*P*	r	*P*
Speed	−0.067	0.629	0.117	0.398	−0.024	0.866	−0.141	0.310	−0.166	0.229
Angle of the knee										
Flexion angle	0.008	0.955	0.121	0.382	−0.055	0.691	−0.131	0.343	−0.049	0.723
Extension angle	−0.054	0.699	−0.013	0.928	−0.057	0.682	0.025	0.860	−0.081	0.562
Adduction angle	−0.010	0.944	−0.109	0.434	−0.082	0.557	−0.334	**0.014**	0.219	0.111
Abduction angle	−0.057	0.684	0.004	0.977	−0.050	0.720	−0.287	**0.035**	0.238	0.083
External rotation	−0.104	0.452	−0.188	0.174	−0.044	0.749	−0.064	0.648	−0.033	0.814
Internal rotation	−0.014	0.921	−0.246	0.073	0.107	0.442	−0.225	0.101	0.080	0.565
Moment of the knee										
Flexion moment	−0.068	0.627	0.106	0.444	−0.009	0.951	−0.012	0.929	−0.032	0.818
Extension moment	−0.006	0.963	−0.159	0.250	−0.014	0.922	−0.190	0.168	0.092	0.510
Adduction moment	0.081	0.559	0.188	0.174	0.104	0.453	0.362	**0.007**	−0.156	0.259
External rotation moment	0.005	0.970	0.034	0.806	−0.077	0.578	−0.120	0.387	0.070	0.613
Internal rotation moment	−0.178	0.198	0.051	0.716	0.136	0.327	0.069	0.620	−0.159	0.251

PTVA, proximal tibia varus angle; DFVA, distal femoral valgus angle. The boldface indicates p value < 0.05.

(r = −0.364, p = 0.007; r = 0.539, p < 0.001; r = 0.338, p = 0.012; r = −0.614, p < 0.001; r = −0.334, p = 0.014; respectively, Table 2). However, age was not found to be related to the kinetic parameters of the knee (p > 0.05, respectively). Notably, a robust positive association was observed between FTA and the first KAM peak in knee kinetics (r = 0.563, p < 0.001, Table 2). Moderate correlations were also noted between FTA and abduction angle, as well as PTVA and the first KAM peak (r = −0.388, p = 0.004; r = −0.303, p = 0.026; r = 0.362, p = 0.007; respectively). Weak correlations were found between BMI or PTVA and abduction angle, age and internal rotation angle, and gender and external knee extension moment (r = −0.278, p = 0.042; r = −0.287, p = 0.035; r = -0.299, p = 0.028; r = 0.295, p = 0.03; respectively, Table 3). Comprehensive illustrations of the correlations between alignment or morphology and knee kinematics or kinetics are provided in Tables 2, 3.

3.4 Logistic regression analysis

Based on the correlation analysis results mentioned earlier, variables with a p-value less than 0.1 were incorporated into the regression model. In the univariate logistic regression analysis with

TABLE 4 Logistic regression analysis between adduction angle with demographics, Q angle, FTA, and PTVA.

Variables	Univariate analysis		Multivariate analysis	
	OR (95% CI)	*P*	OR (95% CI)	*P*
Age	0.893 (0.822–0.970)	**0.007**	0.895 (0.783–1.024)	0.106
BMI	0.960 (0.806–1.144)	0.650	1.057 (0.761–1.470)	0.739
Sex	0.120 (0.032–0.443)	**0.001**	0.540 (0.057–5.102)	0.591
Q angle	1.240 (1.053–1.460)	**0.010**	1.330 (1.033–1.711)	**0.027**
FTA	0.584 (0.435–0.784)	**< 0.001**	0.475 (0.285–0.792)	**0.004**
PTVA	0.704 (0.500–0.992)	**0.045**	1.281 (0.734–2.234)	0.383

BMI, body mass index; FTA, femoral-tibial angle; PTVA, proximal tibia varus angle; OR, odds ratios; CI, confidence level; Boldface indicates p value < 0.05.

TABLE 5 Logistic regression analysis between KAM with demographics, FTA, and PTVA.

Variables	Univariate analysis		Multivariate analysis	
	OR (95% CI)	*P*	OR (95% CI)	*P*
Age	1.021 (0.953–1.095)	0.551	0.977 (0.888–1.076)	0.643
BMI	0.916 (0.766–1.096)	0.338	0.865 (0.670–1.118)	0.865
Sex	2.653 (0.844–8.336)	0.095	2.602 (0.393–17.235)	0.321
FTA	1.578 (1.211–2.057)	**0.001**	1.526 (1.125–2.069)	**0.007**
PTVA	1.300 (0.936–1.807)	0.118	0.944 (0.608–1.464)	0.796

BMI, body mass index; FTA, femoral-tibial angle; PTVA, proximal tibia varus angle; OR, odds ratios; CI, confidence level; Boldface indicates p value < 0.05.

the adduction angle as the dependent variable, independent variables included age, BMI, gender, Q angle, FTA, and PTVA (Table 4). Multivariate regression analysis findings revealed that both the Q angle and FTA had significant effects on the adduction angle, even after adjusting for other variables (OR = 1.330, 95% *CI* 1.033–1.711, $p = 0.027$; OR = 0.475, 95% *CI* 0.285–0.792, $p = 0.04$; respectively).

Similarly, in univariate logistic regression analysis with KAM as the dependent variable, independent variables included age, BMI, gender, FTA, and PTVA. The results of the regression analysis demonstrated that FTA independently determined KAM, even after adjusting for other variables (OR = 1.526, 95% *CI* 1.125–2.069, $p = 0.007$, Table 5). In a univariate regression model, FTA and PTVA were observed as independent factors influencing the adduction angle (OR = 0.733, 95% *CI* 0.627–0.954, $p = 0.016$; OR = 0.683, 95% *CI* 0.482–0.967, $p = 0.032$; respectively). However, this influence became statistically insignificant after controlling for other variables, such as age, BMI, gender, Q angle, and DFVA ($p > 0.05$, respectively, Supplementary Table S1). The internal rotation angle of the knee did not exhibit any significant effect on age, BMI, gender, or PI in both univariate and multivariate regression models ($p > 0.05$, respectively, Supplementary Table S2).

4 Discussion

The knee, a pivotal component of the locomotor system, serves as a weight-bearing joint susceptible to degenerative changes primarily driven by abnormal mechanical loads (Zhao et al., 2021; Campos et al., 2022). Therefore, it is imperative to acquire a comprehensive understanding of the multifaceted factors influencing the mechanical load conditions experienced by the knee joint. Such insights can inform the tailoring of prevention strategies to mitigate inherent risks. The geometric characteristics of the knee's articular components play a pivotal role in predicting joint contact mechanics. There is a prevailing consensus that the biological function of the patella is intricately linked to the compatibility of the patellofemoral joint (PFJ), which, in turn, depends significantly on PFJ morphology and biological performance (Fox et al., 2012). Previous studies (Clark et al., 2016; Hösl et al., 2018; Murakami et al., 2018) have predominantly focused on the substantial roles played by sagittal and coronal alignments of the PFJ and the mechanical axis of the lower limbs in mediating knee joint mechanics. However, the impact of patellar morphology and transverse alignment remains an area that warrants more extensive investigation. Building on existing literature, this study is thus well justified.

Our study's findings indicated that there was no statistically significant correlation between PTA, a measure of transverse alignment in the PFJ, or the PI, an indicator of patellar morphology, and knee movement kinematics or kinetics ($p > 0.05$, respectively). Notably, an increase in PTA and PI, which play a critical role in assessing patellar stability, may suggest patellar malalignment. Such malalignment has been associated with conditions such as patellar instability, patellofemoral pain syndrome, and chondromalacia patellae. In contrast to metrics like the tibial tubercle trochlear groove distance in the coronal plane and the Insall-Salvati ratio or Caton-Deschamps index in

the sagittal plane (Verhulst et al., 2020), our distinct results underscore two key observations. On the one hand, significant variability in patellofemoral alignment suggests that the observed patellar features in our study population may not accurately represent the broader trends across all populations (Hochreiter et al., 2020). On the other hand, while patellar alignment in individuals with osteoarthritis may lead to morphological changes, subsequently affecting muscle function and mechanical loading, it is important to acknowledge that this perspective has yet to be confirmed in the general population.

Our study provided evidence supporting the idea that FTA exerted a substantial and independent influence on KAM in individuals without underlying knee conditions, even after adjusting for potential confounding factors ($p = 0.007$). The KAM, a structural risk factor for KOA, is frequently used as an indicator of medial-to-lateral knee joint load distribution during gait (Zhao et al., 2007). Previous studies (Miyazaki et al., 2002; Barrios et al., 2009) have found associations between static frontal plane knee alignment and peak KAM magnitude. Increased varus malalignment is believed to augment the knee ground reaction force lever arm, thereby increasing the KAM during gait and the risk of various knee-related conditions (Bennell et al., 2011).

Our correlation analysis revealed that among demographic factors, age, BMI, and gender did not have a statistically significant impact on the velocity of the healthy population. However, we did observe that age was associated with adduction and internal rotation angles. Additionally, BMI showed a sole association with the abduction angle, while gender was related to the adduction angle, extension moment, and KAM ($p < 0.05$, respectively). Nonetheless, the multivariate regression model did not demonstrate any significant disparities between demographic independent variables and dependent variables related to the adduction angle, or KAM. This suggested that the absence of discernible differences in dependent variables may be attributed to the unique characteristics of the normal population under investigation. Furthermore, differences in demographic factors can be linked to the Q angle and the FTA. Q angle is frequently cited as a possible predictor of knee pathology and lower limb injury (Rauh et al., 2007). The varus-valgus angulation of the knee has been associated with mediolateral distribution of loads on the knee's articular structures. Minor increases in varus alignment (approximately 5%) have the potential to greatly increase (approximately 20%) medial knee loading (Schipplein and Andriacchi, 1991). Previous research (Tran et al., 2022) has shown variations in gender, age, and BMI concerning the Q angle and FTA, which in turn affect mechanical distribution by influencing moments, ultimately increasing the likelihood of developing KOA.

The consideration and design of therapeutic interventions aimed at reducing peak KAM are of paramount importance in the effort to delay or prevent the development and/or progression of KOA in middle-aged adults. Correcting varus alignment disperses high-pressure zones, resulting in significant improvements in knee pain and other KOA symptoms. Interventions such as footwear, knee bracing, exercise, and gait retraining may be appropriate for reducing varus tibial malalignment in KOA and should be periodically evaluated (Hatfield et al., 2016).

This study provides the initial comprehensive analysis of the relationship between knee imaging evaluation and three-dimensional gait analysis, enriching our understanding of how the morphology and transverse alignment of the patella, femur, and tibia impact knee kinematics and kinetics. However, it is essential to interpret the findings considering certain limitations. Firstly, our study exclusively recruited healthy senior adults, indicating the necessity for further investigations across diverse age demographics to thoroughly validate our findings. Secondly, it is worth noting that, compared to the sagittal plane, the frontal and transversal planes exhibit smaller ranges of motion. This characteristic increases the susceptibility of skin markers to soft tissue artifacts, thereby limiting the reliability of our results. Nevertheless, it is important to acknowledge that skin markers provide a non-invasive and reproducible method for visual motion capture. Thirdly, our study did not incorporate surface electromyography of the lower limb to evaluate muscle activity. Although it is improbable for healthy individuals to display abnormal muscle co-contraction, this aspect should be considered in future studies involving individuals with KOA. Finally, this study did not explore the correlation between patellar shape, alignment, and the onset of articular cartilage degeneration and KOA. Subsequent studies should include populations with KOA for comparative analysis and subsequent conclusions.

5 Conclusion

In summary, this study found that the morphology and transverse alignment of the patella do not significantly impact knee gait characteristics in a sample of healthy Chinese adults aged 40 years and older. Notably, the FTA emerges as a pivotal determinant influencing the KAM, a crucial parameter for assessing normal mechanical knee function. Future investigations should focus on establishing threshold values for FTA, Q-angle, and PTVA that could indicate an increased risk of mechanical dysfunction in individuals. Furthermore, there is a pressing need for comprehensive studies that encompass structural, passive, and dynamic elements to formulate treatments aimed at reducing the incidence of KOA.

Data availability statement

The raw data supporting the conclusion of this article will be made available by the authors, without undue reservation.

Ethics statement

The studies involving humans were approved by the Ethics Committee of the Shuguang Hospital Affiliated to Shanghai University of Traditional Chinese Medicine. The studies were conducted in accordance with the local legislation and

institutional requirements. The participants provided their written informed consent to participate in this study.

Author contributions

ZW: Investigation, Data curation, Validation, Writing–original draft. JL: Data curation, Writing–original draft, Methodology. HG: Data curation, Writing–original draft, Formal Analysis. ZL: Writing–review and editing, Conceptualization, Investigation. MZ: Formal Analysis, Project administration, Writing–review and editing. FP: Formal Analysis, Project administration, Writing–review and editing, Methodology. RW: Formal Analysis, Data curation, Writing–original draft. HJ: Formal Analysis, Software, Visualization, Writing–review and editing. GY: Formal Analysis, Writing–review and editing, Project administration. ZS: Formal Analysis, Writing–review and editing, Methodology, Visualization. GD: Formal Analysis, Methodology, Visualization, Writing–review and editing, Supervision. HZ: Supervision, Writing–review and editing, Funding acquisition.

Funding

The author(s) declare that financial support was received for the research, authorship, and/or publication of this article. This work was supported by the Shanghai Municipal Health Commission [20MC1920600, shslczdzk03901, and ZY (2021–2023)-0209-02], the National Natural Science Foundation (82074466 and 82174403), and Shanghai University of Traditional Chinese Medicine (GJ2023017).

Conflict of interest

The authors declare that the research was conducted in the absence of any commercial or financial relationships that could be construed as a potential conflict of interest.

Publisher's note

All claims expressed in this article are solely those of the authors and do not necessarily represent those of their affiliated organizations, or those of the publisher, the editors and the reviewers. Any product that may be evaluated in this article, or claim that may be made by its manufacturer, is not guaranteed or endorsed by the publisher.

Supplementary material

The Supplementary Material for this article can be found online at: https://www.frontiersin.org/articles/10.3389/fbioe.2024.1319602/full#supplementary-material

References

Aljehani, M. S., Christensen, J. C., Snyder-Mackler, L., Crenshaw, J., Brown, A., and Zeni, J. A. (2022). Knee biomechanics and contralateral knee osteoarthritis progression after total knee arthroplasty. *Gait Posture* 91, 266–275. doi:10.1016/j.gaitpost.2021.10.020

Barrios, J. A., Higginson, J. S., Royer, T. D., and Davis, I. S. (2009). Static and dynamic correlates of the knee adduction moment in healthy knees ranging from normal to varus-aligned. *Clin. Biomech. (Bristol, Avon)* 24, 850–854. doi:10.1016/j.clinbiomech.2009.07.016

Bennell, K. L., Bowles, K. A., Wang, Y., Cicuttini, F., Davies-Tuck, M., and Hinman, R. S. (2011). Higher dynamic medial knee load predicts greater cartilage loss over 12 months in medial knee osteoarthritis. *Ann. Rheum. Dis.* 70, 1770–1774. doi:10.1136/ard.2010.147082

Bolink, S. A., Grimm, B., and Heyligers, I. C. (2015). Patient-reported outcome measures versus inertial performance-based outcome measures: a prospective study in patients undergoing primary total knee arthroplasty. *Knee* 22, 618–623. doi:10.1016/j.knee.2015.04.002

Bornes, T. D., Adesida, A. B., and Jomha, N. M. (2014). Mesenchymal stem cells in the treatment of traumatic articular cartilage defects: a comprehensive review. *Arthritis Res. Ther.* 16, 432. doi:10.1186/s13075-014-0432-1

Campos, Y., Fuentes, G., Almirall, A., Que, I., Schomann, T., Chung, C. K., et al. (2022). The incorporation of etanercept into a porous tri-layer scaffold for restoring and repairing cartilage tissue. *Pharmaceutics* 14, 282. doi:10.3390/pharmaceutics14020282

Chhabra, A., Subhawong, T. K., and Carrino, J. A. (2011). A systematised MRI approach to evaluating the patellofemoral joint. *Skelet. Radiol.* 40, 375–387. doi:10.1007/s00256-010-0909-1

Clark, D. A., Simpson, D. L., Eldridge, J., and Colborne, G. R. (2016). Patellar instability and quadriceps avoidance affect walking knee moments. *Knee* 23, 78–84. doi:10.1016/j.knee.2015.08.007

Cross, M. J., and Waldrop, J. (1975). The patella index as a guide to the understanding and diagnosis of patellofemoral instability. *Clin. Orthop. Relat. Res.* 110, 174–176. doi:10.1097/00003086-197507000-00023

Cui, A., Li, H., Wang, D., Zhong, J., Chen, Y., and Lu, H. (2020). Global, regional prevalence, incidence and risk factors of knee osteoarthritis in population-based studies. *EClinicalMedicine* 29-30, 100587. doi:10.1016/j.eclinm.2020.100587

Dai, Y., Li, H., Li, F., Lin, W., and Wang, F. (2019). Association of femoral trochlear dysplasia and tibiofemoral joint morphology in adolescent. *Med. Sci. Monit.* 25, 1780–1787. doi:10.12659/msm.913600

Damgaci, L., Özer, H., and Duran, S. (2020). Patella-patellar tendon angle and lateral patella-tilt angle decrease patients with chondromalacia patella. *Knee Surg. Sports Traumatol. Arthrosc.* 28, 2715–2721. doi:10.1007/s00167-020-06065-7

Farrokhi, S., O'Connell, M., and Fitzgerald, G. K. (2015). Altered gait biomechanics and increased knee-specific impairments in patients with coexisting tibiofemoral and patellofemoral osteoarthritis. *Gait Posture* 41, 81–85. doi:10.1016/j.gaitpost.2014.08.014

Fox, A. J., Wanivenhaus, F., and Rodeo, S. A. (2012). The basic science of the patella: structure, composition, and function. *J. Knee Surg.* 25, 127–142. doi:10.1055/s-0032-1313741

Hao, K., Niu, Y., Feng, A., and Wang, F. (2023). Coronal laxity at flexion is larger after posterior-stabilized total knee arthroplasty than with cruciate-retaining procedures. *J. Arthroplasty* 38, 1267–1272. doi:10.1016/j.arth.2022.12.041

Hatfield, G. L., Cochrane, C. K., Takacs, J., Krowchuk, N. M., Chang, R., Hinman, R. S., et al. (2016). Knee and ankle biomechanics with lateral wedges with and without a custom arch support in those with medial knee osteoarthritis and flat feet. *J. Orthop. Res.* 34, 1597–1605. doi:10.1002/jor.23174

Heidari, B. (2011). Knee osteoarthritis prevalence, risk factors, pathogenesis and features: Part I. *Casp. J. Intern Med.* 2, 205–212.

Hochreiter, B., Hess, S., Moser, L., Hirschmann, M. T., Amsler, F., and Behrend, H. (2020). Healthy knees have a highly variable patellofemoral alignment: a systematic review. *Knee Surg. Sports Traumatol. Arthrosc.* 28, 398–406. doi:10.1007/s00167-019-05587-z

Hösl, M., Böhm, H., Seltmann, M., Dussa, C. U., and Döderlein, L. (2018). Relationship between radiographic patella-alta pathology and walking dysfunction in children with bilateral spastic Cerebral Palsy. *Gait Posture* 60, 28–34. doi:10.1016/j.gaitpost.2017.11.006

Jones, R. K., Zhang, M., Laxton, P., Findlow, A. H., and Liu, A. (2013). The biomechanical effects of a new design of lateral wedge insole on the knee and ankle during walking. *Hum. Mov. Sci.* 32, 596–604. doi:10.1016/j.humov.2012.12.012

Kellgren, J. H., and Lawrence, J. S. (1957). Radiological assessment of osteo-arthrosis. *Ann. Rheum. Dis.* 16, 494–502. doi:10.1136/ard.16.4.494

Kokubu, Y., Kawahara, S., Hamai, S., Akasaki, Y., Tsushima, H., Momii, K., et al. (2022). Sagittal femoral bowing contributes to distal femoral valgus angle deviation in

malrotated preoperative radiographs. *BMC Musculoskelet. Disord.* 23, 579. doi:10.1186/s12891-022-05542-z

Lebrun, C. T., Langford, J. R., and Sagi, H. C. (2012). Functional outcomes after operatively treated patella fractures. *J. Orthop. Trauma* 26, 422–426. doi:10.1097/bot.0b013e318228c1a1

Lee, T. Q. (2014). Biomechanics of hyperflexion and kneeling before and after total knee arthroplasty. *Clin. Orthop. Surg.* 6, 117–126. doi:10.4055/cios.2014.6.2.117

Mccaffrey, N., Kaambwa, B., Currow, D. C., and Ratcliffe, J. (2016). Health-related quality of life measured using the EQ-5D-5L: south Australian population norms. *Health Qual. Life Outcomes* 14, 133. doi:10.1186/s12955-016-0537-0

Milovanović, D., Begović, N., Bukva, B., Dučić, S., Vlahović, A., Paunović, Z., et al. (2023). The influence of the Q-angle and muscle strength on idiopathic anterior knee pain in adolescents. *Med. Kaunas.* 59, 1016. doi:10.3390/medicina59061016

Miyazaki, T., Wada, M., Kawahara, H., Sato, M., Baba, H., and Shimada, S. (2002). Dynamic load at baseline can predict radiographic disease progression in medial compartment knee osteoarthritis. *Ann. Rheum. Dis.* 61, 617–622. doi:10.1136/ard.61.7.617

Murakami, K., Hamai, S., Okazaki, K., Ikebe, S., Higaki, H., Shimoto, T., et al. (2018). Preoperative tibial mechanical axis orientation and articular surface design influence on the coronal joint line orientation relative to the ground during gait after total knee arthroplasties. *Knee Surg. Sports Traumatol. Arthrosc.* 26, 3368–3376. doi:10.1007/s00167-018-4899-1

Piriyaprasarth, P., and Morris, M. E. (2007). Psychometric properties of measurement tools for quantifying knee joint position and movement: a systematic review. *Knee* 14, 2–8. doi:10.1016/j.knee.2006.10.006

Powers, C. M. (2000). Patellar kinematics, part II: the influence of the depth of the trochlear groove in subjects with and without patellofemoral pain. *Phys. Ther.* 80, 965–973. doi:10.1093/ptj/80.10.965

Rauh, M. J., Koepsell, T. D., Rivara, F. P., Rice, S. G., and Margherita, A. J. (2007). Quadriceps angle and risk of injury among high school cross-country runners. *J. Orthop. Sports Phys. Ther.* 37, 725–733. doi:10.2519/jospt.2007.2453

Reilly, D. T., and Martens, M. (1972). Experimental analysis of the quadriceps muscle force and patello-femoral joint reaction force for various activities. *Acta Orthop. Scand.* 43, 126–137. doi:10.3109/17453677208991251

Riazati, S., Mcguirk, T. E., Perry, E. S., Sihanath, W. B., and Patten, C. (2022). Absolute reliability of gait parameters acquired with markerless motion capture in living domains. *Front. Hum. Neurosci.* 16, 867474. doi:10.3389/fnhum.2022.867474

Sasaki, T., and Yagi, T. (1986). Subluxation of the patella: investigation by computerized tomography. *Int. Orthop.* 10, 115–120. doi:10.1007/bf00267752

Schipplein, O. D., and Andriacchi, T. P. (1991). Interaction between active and passive knee stabilizers during level walking. *J. Orthop. Res.* 9, 113–119. doi:10.1002/jor.1100090114

Spierings, J., van Den Hengel, M., Janssen, R. P. A., van Rietbergen, B., Ito, K., and Foolen, J. (2023). Knee instability caused by altered graft mechanical properties after anterior cruciate ligament reconstruction: the early onset of osteoarthritis? *Front. Bioeng. Biotechnol.* 11, 1244954. doi:10.3389/fbioe.2023.1244954

Stefanik, J. J., Zumwalt, A. C., Segal, N. A., Lynch, J. A., and Powers, C. M. (2013). Association between measures of patella height, morphologic features of the trochlea, and patellofemoral joint alignment: the MOST study. *Clin. Orthop. Relat. Res.* 471, 2641–2648. doi:10.1007/s11999-013-2942-6

Suzuki, T., Motojima, S., Saito, S., Ishii, T., Ryu, K., Ryu, J., et al. (2013). Osteoarthritis of the patella, lateral femoral condyle and posterior medial femoral condyle correlate with range of motion. *Knee Surg. Sports Traumatol. Arthrosc.* 21, 2584–2589. doi:10.1007/s00167-013-2508-x

Tran, D. H., Hoshino, H., and Matsuyama, Y. (2022). Relationship of lower limb geometrics with femorotibial osteoarthritis in the toei cohort. *Sci. Rep.* 12, 12342. doi:10.1038/s41598-022-16081-x

Vasso, M., Corona, K., Toro, G., Rossini, M., and Schiavone Panni, A. (2017). Anatomic double-bundle medial patellofemoral ligament reconstruction with autologous semitendinosus: aperture fixation both at the femur and the patella. *Joints* 5, 256–260. doi:10.1055/s-0037-1607192

Verhulst, F. V., van Sambeeck, J. D. P., Olthuis, G. S., van der Ree, J., and Koëter, S. (2020). Patellar height measurements: Insall-Salvati ratio is most reliable method. *Knee Surg. Sports Traumatol. Arthrosc.* 28, 869–875. doi:10.1007/s00167-019-05531-1

Vomer, R. P., Boggess, S., and Boggess, B. (2023). Ultrasound evaluation of knee osteoarthritis. *Cureus* 15, e39188. doi:10.7759/cureus.39188

Wheatley, M. G. A., Thelen, D. G., Deluzio, K. J., and Rainbow, M. J. (2021). Knee extension moment arm variations relate to mechanical function in walking and running. *J. R. Soc. Interface* 18, 20210326. doi:10.1098/rsif.2021.0326

Zhang, M., Pang, J., Lu, J., Kang, M., Chen, B., Jones, R. K., et al. (2022). The immediate effect of backward walking on external knee adduction moment in healthy individuals. *J. Healthc. Eng.* 2022, 1–8. doi:10.1155/2022/4232990

Zhang, W., Doherty, M., Peat, G., Bierma-Zeinstra, M. A., Arden, N. K., Bresnihan, B., et al. (2010). EULAR evidence-based recommendations for the diagnosis of knee osteoarthritis. *Ann. Rheum. Dis.* 69, 483–489. doi:10.1136/ard.2009.113100

Zhao, D., Banks, S. A., Mitchell, K. H., D'Lima, D. D., Colwell, C. W., and Fregly, B. J. (2007). Correlation between the knee adduction torque and medial contact force for a variety of gait patterns. *J. Orthop. Res.* 25, 789–797. doi:10.1002/jor.20379

Zhao, Q., Ridout, R. P., Shen, J., and Wang, N. (2021). Effects of angular resolution and b value on diffusion tensor imaging in knee joint. *Cartilage* 13, 295s–303s. doi:10.1177/19476035211007909

Frontiers in
Bioengineering and Biotechnology

Accelerates the development of therapies, devices, and technologies to improve our lives

A multidisciplinary journal that accelerates the development of biological therapies, devices, processes and technologies to improve our lives by bridging the gap between discoveries and their application.

Discover the latest Research Topics

See more →

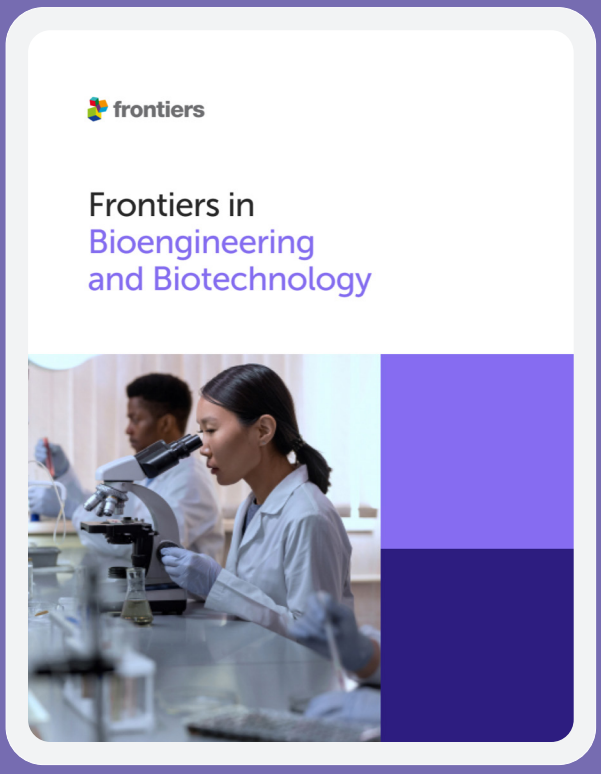

Frontiers

Avenue du Tribunal-Fédéral 34
1005 Lausanne, Switzerland
frontiersin.org

Contact us

+41 (0)21 510 17 00
frontiersin.org/about/contact